

GEOCHRONOLOGY OF ANCIENT COASTAL DEPOSITS OF
GEORGIA, USA

TIMING OF THE EMPLACEMENT OF ANCIENT COASTAL DEPOSITS OF
GEORGIA AIDED BY GROUND PENETRATING RADAR AND DETERMINED BY
OPTICALLY STIMULATED LUMINESCENCE AND ELECTRON SPIN
RESONANCE OPTICAL DATING

By Robert Rombuck Hendricks, B.S., M.Sc.

A Thesis Submitted to the School of Graduate Studies in Partial Fulfillment of the
Requirements for the Degree of Doctorate of Philosophy

McMaster University © Copyright by Robert Rombuck Hendricks, December 2015

McMaster University DOCTORATE OF PHILOSOPHY (2015) Hamilton, Ontario
(Earth Science)

TITLE: Timing of the Emplacement of Ancient Coastal Deposits of Georgia Determined
by Optically Stimulated Luminescence and Electron Spin Resonance Optical Dating

AUTHOR: Robert Rombuck Hendricks, B.S. (Centenary College of Louisiana), M.Sc.
(South Dakota School of Mines and Technology) SUPERVISOR: William Jack Rink

NUMBER OF PAGES: xix, 198

Lay abstract

ESR, OSL and TT-OSL dating methods were applied to samples collected from six of the Ancient Coastal Deposits (ACDs) along the southern Georgia Coastline with the goal of determining the age of formation of these features. Ground Penetrating Radar (GPR) was used to determine the subsurface morphology and target lithologies for age determination. A number of low additive dose points were added to the ESR dose plan to attempt to create a better dose response curve for the low-dose saturation of the Ti-H signal in attempt to better utilize the signal.

While the geochronological methodology did not prove useful for determining the age of all of the ACDs, it did result in depositional age estimates for the Cypresshead Formation at 433-2978 ka and Satilla Formations at 243-417 ka. The GPR, ESR, and core data all point to the conclusion that the ACDs of the Georgia Coast are geomorphic features without unique depositional events.

Abstract

ESR, OSL and TT-OSL dating methods were applied to samples collected from six of the Ancient Coastal Deposits (ACDs) along the southern Georgia Coastline. Samples were collected from the Princess Anne (the youngest and most seaward ACD), Pamlico, Talbot, Penholoway, Wicomico, and Okefenokee ACDs with the goal of determining the age of formation of these features. Ground Penetrating Radar (GPR) was used to determine the subsurface morphology and target lithologies for age determination. OSL and TT-OSL dating was attempted on samples collected from the youngest two ACDs, the Pamlico and Princess Anne, at McMaster Universities AGE Lab. ESR samples collected from all of the ACDs studied were measured at Florida State University as well as Osaka University. ESR analysis measured the Al signal, the Ti-Li signal, measured using two different methods, as well as the Ti-H signal. A number of low additive dose points were added to the ESR dose plan to attempt to create a better dose response curve for the low saturating Ti-H signal in attempt to better utilize the signal.

While the geochronological methodology did not prove useful for determining the age of all of the ACDs it did result in depositional age estimates for the Cypresshead Formation at 433-2978 ka and Satilla Formations at 243-417 ka using the Ti-Li ESR signal as a maximum age estimate. The GPR, ESR, and core data all point to the conclusion that the ACDs of the Georgia Coast are geomorphic modifications and not the result of a unique depositional process. Based on the discrepancy between the depositional age of the Cypresshead and Satilla Formations as determined by ESR in this study and the ages of the ACDs published by others from Georgia (Markewich et.al., 2013) or other areas of the Atlantic Coast (Wehmiller, 2004; Willis, 2006) it can be concluded that paleo sea-levels modified the Cypresshead and Satilla Formations in to the morphology seen today at some point after their initial deposition.

Acknowledgements

I would first like to thank my adviser Dr. W. Jack Rink and my Thesis Committee members Dr. Joe Boyce and Dr. Edward Reinhardt for their guidance and time, especially under tight deadlines. I would like to thank Dr. Amanda Keen-Zebert and Dr. David Mallinson for their efforts in GPR collection and coring as well as Dr. Clark Alexander for logistical help in Georgia. My thanks to Rob Pasuta and the others at the McMaster Nuclear Reactor for their training and hosting me in the Reactor. My thanks to Dr. Shin Toyoda for his efforts in dosing samples and ESR measurements when our equipment malfunctioned. I would like to thank the Physics Department at FSU for hosting me during my ESR measurements.

My thanks to McMaster University and the government of Canada for giving me the opportunity to live and study in Canada. I would like to thank the staff at McMaster University's Department of Earth Science who made me feel welcome in a foreign country and helped in countless logistical and administrative issues. I would like to thank Shannon Mahan and Dr. Amanda Keen-Zerbert for their guidance in the world of luminescence dating (and in general). My thanks to Dr. Maureen Padden as a sounding board and inspiration. I would like to thank Dr. Foster Sawyer at SDSMT for getting me through my Masters (so I could do this) and Dr. David Bieler at Centenary for setting me on this path.

I would like to thank all of my family and friends (including the people mentioned above) who have been so supportive and helpful to me during this endeavor.

I would finally like to thank my wife and kids, Theodore and Roberta, who are the greatest result accomplished in the timeframe of this thesis. Sarah there is no way I could have done this without your support, thank you. I love you .

Table of Contents

<u>Section:</u>	<u>Page number:</u>
Lay abstract.....	iii
Abstract.....	iv
Acknowledgements.....	v
Table of contents.....	vi
List of Figures.....	x
List of tables.....	xiii
List of equations.....	xv
List of abbreviations and symbols.....	xvi
Declarations of academic achievement.....	xix
Chapter 1: Introduction.....	1
Section 1.1: Introduction to the geochronology of the ancient southern Georgia coastline project.....	1
Section 1.1.1: Project outline.....	1
Section 1.1.2: Research objectives.....	2
Section 1.2: Geologic setting of eastern Georgia.....	3
Section 1.3: Morphology, sediment characteristics and age of the ancient coastal deposits of Georgia and the Atlantic coasts.....	7
Section 1.4: Ground Penetrating Radar.....	16
Section 1.4.1: Introduction to GPR.....	16
Section 1.4.2: GPR in coastal sites and in conjunction with geochronology.....	22
Section 1.4.3: Georgia GPR surveys and core sampling.....	23
Section 1.5: Electron spin (Paramagnetic) resonance.....	24
Section 1.5.1: Introduction to ESR.....	24
Section 1.5.2: Physics of ESR.....	25
Section 1.5.3: ESR of quartz.....	30

Table of Contents

<u>Section:</u>	<u>Page number:</u>
Section 1.5.4: Quartz ESR-OD of coastal deposits.....	35
Section 1.6: Optically stimulated luminescence dating.....	36
Section 1.6.1: Introduction to optically stimulated luminescence.....	36
Section 1.6.2: Theory.....	37
Section 1.6.2.1: OSL theory.....	37
Section 1.6.2.2: TT-OSL theory.....	41
Section 1.6.3: Previous works in the Georgia coastal setting.....	41
Chapter 2: Methodology.....	43
Section 2.1: Locations of GPR transects and cores.....	43
Section 2.2: GPR methodology.....	44
Section 2.2.1: GPR survey methods.....	44
Section 2.2.2: GPR collection.....	44
Section 2.2.3: Software and processing.....	45
Section 2.3: Coring and sediment analysis.....	46
Section 2.3.1: Coring strategy.....	46
Section 2.3.2: Core collection.....	46
Section 2.3.3: Core logging.....	47
Section 2.4: ESR dating.....	48
Section 2.4.1: Sample targeting.....	48
Section 2.4.2: Sample prep methodology.....	48
Section 2.4.3: ESR spectrometry.....	50
Section 2.4.4: Signal processing.....	51
Section 2.4.5: Dose rates.....	53
Section 2.4.6: Sample age determination.....	54

Table of Contents

<u>Section:</u>	<u>Page number:</u>
Section 2.5: OSL dating.....	54
Section 2.5.1: Sample targeting.....	54
Section 2.5.2: Sample prep methodology.....	55
Section 2.5.3: OSL equipment and measurement conditions.....	55
Section 2.5.4: Data analysis.....	57
Section 2.5.5: OSL De models.....	57
Section 2.5.6: Dose rates.....	58
Chapter 3: Results.....	59
Section 3.1: Results of GPR survey.....	59
Section 3.2: Sediment analysis.....	69
Section 3.3: ESR results.....	71
Section 3.3.1: Use of correlation tables.....	82
Section 3.4: OSL results.....	90
Chapter 4: Discussion and conclusions.....	98
Section 4.1: GPR discussion and interpretation.....	98
Section 4.2: Sediments and nature of the ACDs morphology.....	101
Section 4.2.1: Georgia sediments.....	101
Section 4.2.2: Morphology of the ACDs.....	102
Section 4.3: ESR discussion.....	103
Section 4.3.1: ESR ages.....	103
Section 4.3.2: Incomplete bleaching remediation test.....	120
Section 4.3.3: Ti-H (Yoshida, 1986) signal.....	123
Section 4.3.4: Ga ages vs Fl ages.....	124
Section 4.4: OSL discussion.....	127
Section 4.4.1: Standard OSL.....	127
Section 4.4.2: OSL saturation work.....	127

Table of Contents

<u>Section:</u>	<u>Page number:</u>
Section 4.4.3: TT-OSL.....	128
Section 4.5: Summary and conclusions.....	129
Section 4.5.1: Ages of ACDs based on ESR and OSL (objective 1).....	129
Section 4.5.2: GPR stratigraphy and sediment analysis (objective 2).....	130
Section 4.5.3: Georgia and Florida deposit correlations (objective 3).....	132
Section 4.5.4: Suitability of OSL and ESR-OD in Georgia (objective 4).....	132
Section 4.5.4.1: Using OSL in Georgia.....	133
Section 4.5.4.2: Using ESR in Georgia.....	133
Section 4.5.5: Future work.....	135
Section 4.5.6: Closing Remarks.....	135
References cited.....	137
Appendix 1: Locations.....	145
Appendix 2: Core logs.....	147
Appendix 3: ESR data.....	154
Appendix 4: OSL result statistics.....	191
Supplemental data.....	198

List of Figures

<u>Figure:</u>	<u>Description</u>	<u>Page number:</u>
Figure 1	Location of Georgia	4
Figure 2	ACDs of Georgia	5
Figure 3	Cross section of Georgia coast	6
Figure 4	Upper and lower ACDs	8
Figure 5	Changes in coastal sequence elevation	12
Figure 6	GPR system	17
Figure 7	GPR anomalies	21
Figure 8	Groundwater in the coastal environment	23
Figure 9	Electrons reaction to radiation	26
Figure 10	Zeeman splitting	27
Figure 11	Absorption of microwave energy spectra	28
Figure 12	ESR spectrometer	29
Figure 13	Quartz defect sites	31
Figure 14	Quartz ESR spectra	31
Figure 15	The Yoshida (1986)/ Ti-H signal	33
Figure 16	ESR De determination	34
Figure 17	OSL traps	37
Figure 18	SAR and DRC of OSL	40
Figure 19	Study site	43
Figure 20	GPR collection setup	45
Figure 21	Core liners	47
Figure 22	Quartz ESR signals measured	52
Figure 23	GPR of Princess Anne ACD	64
Figure 24	GPR of Pamlico ACD	65
Figure 25	GPR of Talbot ACD	66
Figure 26	GPR of Penholoway and Wicomico ACD	67
Figure 27	GPR of Okefenokee ACD	68

List of Figures

<u>Figure:</u>	<u>Description</u>	<u>Page number:</u>
Figure 28	Core locations in the Ga cross section	69
Figure 29	Quartz ESR spectra (Osaka University)	71
Figure 30	ESR spectra response to dose (Osaka U.)	72
Figure 31	ESR spectra response to dose (FSU)	73
Figure 32	DRC of gp1422c (Princess Anne)	74
Figure 33	DRC of gp124e (Penholoway)	75
Figure 34	OSL DRC	92
Figure 35	Modern and paleo deposit GPR	99
Figure 36	Princess Anne ACD ages	109
Figure 37	Pamlico ACD ages	110
Figure 38	Lower Georgia ACD ages	111
Figure 39	Talbot ACD ages	114
Figure 40	Penholoway and Wicomico ACD ages	115
Figure 41	Okefenokee ACD ages	116
Figure 42	Upper Georgia ACD ages	117
Figure 43	Georgia ACD ages	119
Figure A1-F2	Locations on the Georgia geological map	145
Figure A2-F1	Core log gp1422 (Princess Anne)	148
Figure A2-F2	Core log gp1421 (Pamlico)	149
Figure A2-F3	Core log gp129 (Talbot)	150
Figure A2-F4	Core log gp124 (Penholoway)	151
Figure A2-F5	Core log gp123 (Wicomico)	152
Figure A2-F6	Core log gp127 (Okefenokee)	153
Figure A3-F1	DRC gp1422d (Princess Anne)	156
Figure A3-F2	DRC gp1422g (Princess Anne)	157
Figure A3-F3	DRC gp1421c (Pamlico)	158
Figure A3-F4	DRC gp1421d (Pamlico)	159

List of Figures

<u>Figure:</u>	<u>Description</u>	<u>Page number:</u>
Figure A3-F5	DRC gp1421f (Pamlico)	160
Figure A3-F6	DRC gp129b (Talbot)	161
Figure A3-F7	DRC gp129c (Talbot)	162
Figure A3-F8	DRC gp124b (Penholoway)	163
Figure A3-F9	DRC gp123c (Wicomico)	164
Figure A3-F10	DRC gp123d (Wicomico)	165
Figure A3-F11	DRC gp123f (Wicomico)	166
Figure A3-F12	DRC gp127b (Okefenokee)	167
Figure A3-F13	DRC gp127c (Okefenokee)	168
Figure A3-F14	DRC gp127e (Okefenokee)	169
Figure A3-F15	Anatol dose rate calculation	170
Figure A4-F1	TT-OSL data gp1422g (Princess Anne)	192
Figure A4-F2	OSL data gp1422g (Princess Anne)	193
Figure A4-F3	TT-OSL data gp1422d (Princess Anne)	194
Figure A4-F4	OSL data gp1421f (Pamlico)	195
Figure A4-F5	OSL data gp1421d (Pamlico)	196
Figure A4-F6	TT-OSL data gp1421d (Pamlico)	197

List of Tables

<u>Table:</u>	<u>Description</u>	<u>Page number:</u>
Table 1	Correlation of coastal deposits	13
Table 2	TT-OSL procedure	56
Table 3	GPR facies	61
Table 4	ESR Do values	76
Table 5	Natural ESR signal intensities	77
Table 6	Dose rates	79
Table 7	ESR samples D_E and ages	80
Table 8	ages of gp1421f (Pamlico)	85
Table 9	ages of gp124e (Penholoway)	86
Table 10	Georgia sample age agreement Ti-Li option D (SSE)	88
Table 11	sample gp1422d (Princess Anne) OSL/TT-OSL	94
Table 12	Sample gp1422g (Princess Anne) OSL/TT-OSL	95
Table 13	Sample gp1421d (Pamlico) OSL/TT-OL	96
Table 14	Sample gp1421f (Pamlico) OSL/TT-OSL	97
Table 15	Relic intensity removal ages	122
Table 16	Georgia and Florida age correlations	125
Table A1-T1	Locations of sample sites	146
Table A3-T1	ESR measurement conditions	155
Table A3-T2	ages of gp1422c (Princess Anne)	171
Table A3-T3	ages of gp1422d (Princess Anne)	172
Table A3-T4	ages of gp1422g (Princess Anne)	173
Table A3-T5	ages of gp1421c (Pamlico)	174
Table A3-T6	ages of gp1421d (Pamlico)	175
Table A3-T7	ages of gp129b (Talbot)	176
Table A3-T8	ages of gp129c (Talbot)	177
Table A3-T9	ages of gp124b (Penholoway)	178
Table A3-T10	ages of gp123c (Wicomico)	179

List of Tables

<u>Table:</u>	<u>Description</u>	<u>Page number:</u>
Table A3-T11	ages of gp123d (Wicomico)	180
Table A3-T12	ages of gp123f (Wicomico)	181
Table A3-T13	ages of gp127b (Okefenokee)	182
Table A3-T14	ages of gp127c (Okefenokee)	183
Table A3-T15	ages of gp127e (Okefenokee)	184
Table A3-T16	Georgia sample age agreement Al (SSE)	185
Table A3-T17	Georgia sample age agreement Al (Exp+Lin)	186
Table A3-T18	Georgia sample age agreement Ti-Li option A (SSE)	187
Table A3-T19	Georgia sample age agreement Ti-Li option A (Ti2)	188
Table A3-T20	Georgia sample age agreement Ti-Li option D (Ti2)	189
Table A3-T21	Georgia sample age agreement T-H (SSE)	190

List of Equations

<u>Equation:</u>	<u>Description</u>	<u>Page number:</u>
Equation 1	R value (GPR)	18
Equation 2	Zeeman energy (ESR)	25
Equation 3	Zeeman split conditions (ESR)	25
Equation 4	Resonance absorption conditions (ESR)	26
Equation 5	Single Saturating Exponential (part a & b)	33
Equation 6	Age equation	34

List of Abbreviations and Symbols

<u>Abbreviation or Symbol</u>	<u>Explanation</u>
ACD	Ancient coastal deposit
Al	Aluminum
AAR	Amino acid racemization
CAM	Central age model
D	dose
D _E	Equivalent dose or dose equivalent
D ₀	Characteristic saturation dose
D _r	Dose rate
DRC	Dose recovery curve
DRT	Dose recovery test
EM	Electromagnetic (wave)
ESR	Electron spin resonance
ESR-OD	Electron spin resonance optical dating
Exp+Lin	Exponential + linear equation
Fl	Florida (state)
FSU	Florida State University
g	Londe factor (g value)
Ga	Georgia (state)
Ge	Germanium
GPR	Ground penetrating radar
Gy	Gray (radioactive dose)
H	external magnetic field
H	Hydrogen
h	Planck's constant
H ₂ O ₂	Hydrogen peroxide
HCL	Hydrochloric acid
HF	Hydrofluoric acid

List of Abbreviations and Symbols (cont.)

<u>Abbreviation or Symbol</u>	<u>Explanation</u>
I	ESR signal intensity
Imax	ESR signal intensity maximum based on curve fitting
Isat	Saturation intensity of OSL signal
K	Potassium
LED	Light emitting diode
Lx	Luminescence intensity at a given stage of the SAR procedure
MAA	Multiple aliquot additive dose
MAM	Minimum age model
MRI	Magnetic resonance imaging
N-	low energy electrons
N+	high energy electrons
NAA	Neutron activation analysis
NMR	Nuclear magnetic resonance
OSL	Optically stimulated luminescence
R	reflection coefficient
s/n	signal to noise ratio
SAR	Single aliquot regeneration
Si	Silicon
Sr	Strontium
SSE	Single saturating exponential equation
T	Temperature (Kelvin)
Th	Thorium
Ti	Titanium
Ti2	Fit for Ti ESR signals by Duval and Guiliarte (2014)
TL	Thermoluminescence
TT-OSL	Thermal transfer optically stimulated luminescence

List of Abbreviations and Symbols (cont.)

<u>Abbreviation or Symbol</u>	<u>Explanation</u>
T _x	Test dose luminescence intensity
U	Uranium
ν	frequency
Y	Yttrium
β	Bohr magneton
ΔE	Zeeman energy levels
ϵ	Dielectric permittivity
λ	Wavelength
μ	magnetic permeability
σ	electrical conductivity (GPR) or error value (ESR/OSL)
σ_b	over-dispersion
PA	Princess Anne ACD
Pam	Pamlico ACD
Tal	Talbot ACD
Pen	Penholoway ACD
Wic	Wicomico ACD
Oke	Okefenokee ACD

Declaration of Academic Achievement

This project was planned by the student (R.R. Hendricks) under the supervision of the academic advisor (Dr. W.J. Rink). Samples were collected by the student under the supervision of the academic advisor as well as the Dr. D. Mallinson and Dr. A. Keen-Zebert. GPR processing was conducted with the supervision of Dr. J. Boyce and Dr. D. Mallinson. Sample preparation was conducted on the instruction of the advisor by the student. Samples were irradiated and measured by the student as well as Dr. S. Toyoda (those samples measured at Osaka University, Japan). Processing of the ESR and OSL data was conducted by the student. This thesis was written and compiled by the student with editorial advice from the advisor as well as the Thesis Committee members Dr. J Boyce and Dr. E. Reinhardt.

Chapter 1

1.1 Introduction to the Geochronology of the Ancient Southern Georgia Coastline Project

1.1.1 Project Outline

There are a number of ancient coastal deposits (ACDs) deposited along the eastern portion of Georgia, USA. These deposits are of great interest due to their economic heavy mineral deposits and as a record of past sea levels of the Atlantic Ocean. Few attempts at dating the ancient coastal deposits of Georgia have been carried out and deposit ages are assigned by correlating the deposits found in Georgia deposits to those found in Florida, South Carolina and further north along the Atlantic Coast (McMartan et.al., 1982; Cronin et.al., 1984; Wehmiller, 2012, and others). Methods used to determine the age of these Atlantic Coast deposits (with few studies taking place in Georgia specifically) include paleomagnetism amino acid racemization, fossil biostratigraphy, cosmogenic nuclide dating, optical luminescence dating, and uranium series dating. The Georgia ancient coastal deposits lack abundant preserved fossils limiting the use some of the above geochronological techniques. A dating method that does not rely on fossil material, such as luminescence dating (OSL), thermally-transferred optical luminescence dating (TT-OSL), or electron spin resonance optical dating (ESR-OD) methods is needed to provide wide spread age determination of these deposits.

This project focuses on determining the age of emplacement of coastal deposits in southern Georgia in order to better understand the history of the Georgia coast in the Pliocene and Pleistocene. It links research conducted in Florida and further north (South and North Carolina, Virginia, etc.) (McCarten et.al., 1982; Szabo, 1985; Krantz, 1991; Whemiller, 2004; Willis, 2006; Whemiller et.al., 2010; Burdette etl.al, 2012) and sought to provide a better understanding of the evolution of the Atlantic Coastal Plain and local Plio-Pleistocene sea level change. In addition this project assesses the suitability of using quartz ESR-OD, OSL, and TT-OSL on the ancient coastal deposits of southern Georgia and makes recommendations for their use in this location.

ESR-OD is conducted on quartz grains to determine the depositional age of the ancient coastal deposits of southern Georgia. In addition OSL and TT-OSL dating of quartz is attempted on some of the deposits expected to be younger in age in order to provide independent age control for the ESR ages. While both of these methods have been used numerous in coastal settings (see sections 1.5.4 and 1.6.3) this study is the first attempt at ESR-OD on the ancient coastal deposits of Georgia.

The results of this study have implications for the history of the Georgia coastline: specifically, how sea-level has changed locally in Georgia over time as compared to other locations along the Atlantic coast as well as in relationship to local sea-level variations in Georgia which have in the past been associated with global shifts in climate. The emplacement age and morphology of the Georgia ACDs could also contribute to knowledge about the timing of changes in the bathymetric profile of the continental shelf off Georgia, specifically related to development and modification of the Georgia Bight. This data would provide information for further research into the neo-tectonics of passive margins.

1.1.2 Research Objectives

- 1) Determine the age of the ancient coastal deposits of Eastern Georgia using geochronologic techniques including OSL, TT-OSL, and ESR-OD. Some focus on the intercomparison of ESR-OD and OSL as well as explore the suitability of a little used Ti-H quartz ESR signal at a g value of 1.9162 (Yoshida, 1986) to determine the age of younger (>1Ma) deposits, and the use of Thermally Transferred OSL (TT-OSL) to investigate some of the samples.
- 2) Use detailed ground penetrating radar (GPR) to explore the stratigraphy of the deposits, as a guide to select coring locations. Use analyses of sediment core lithology to characterize the suitability of the deposits as they apply to the use of OSL and ESR dating techniques.
- 3) Use the geochronologic and stratigraphic data to refine the correlations between the ancient coastal deposits of southern Georgia and those found in Florida, specifically

those studied by Burdette et.al (2012), and other Atlantic coast deposits. Hypotheses on the nature of the relationships between these deposits will be explored as they relate to the timing of formation, geomorphological classification (i.e. are these depositional features or those affected by erosion after deposition) and their relationship with various sea level highstands.

4) Determine the suitability of quartz OSL, TT-OSL and ESR-OD for future projects on dating the ancient coastal deposits of Georgia. Issues leading to deposits that were found to be problematic for dating are explored and recommendations for future research are made.

1.2 Geologic Setting of Eastern Georgia

The state of Georgia is located on the eastern seaboard of the southern United States and makes up part of the Atlantic Coastal Plain. This region is composed of eastward (seaward) dipping deposits of Cretaceous to Holocene age that lie uncomfortably over Pre-Cambrian to Triassic rocks (Herrick and Vorhis, 1963; Georgia Geological Survey, 1979; Kellam et. al., 1991). The coast of Georgia is located to the west of the Georgia Bight, an area of the continental shelf that is broad and shallow (Figure 1). As a result the modern coast is dominated by tidal processes resulting in short, stubby, and dissected modern barrier islands with extensive back barrier marshes and tidal flats (Hayden and Dolan, 1979; Howard and Frey, 1985; Rhea, 1986; Kellam, 1986; Huddleston, 1988; Kellam et.al., 1991). In contrast the barriers islands found to the south in Florida as well as northward in and past North Carolina consist of elongated barriers that are continuous and constructed by wave dominated processes (Hayden and Dolan, 1979; Kellam et.al., 1991). While waves dominantly strike the Georgia coast from the south or southeast, fewer but stronger waves strike the coast from the north and northeast. This results in a net-southern longshore transport along the modern Georgia coastline (Kellam, 1986).

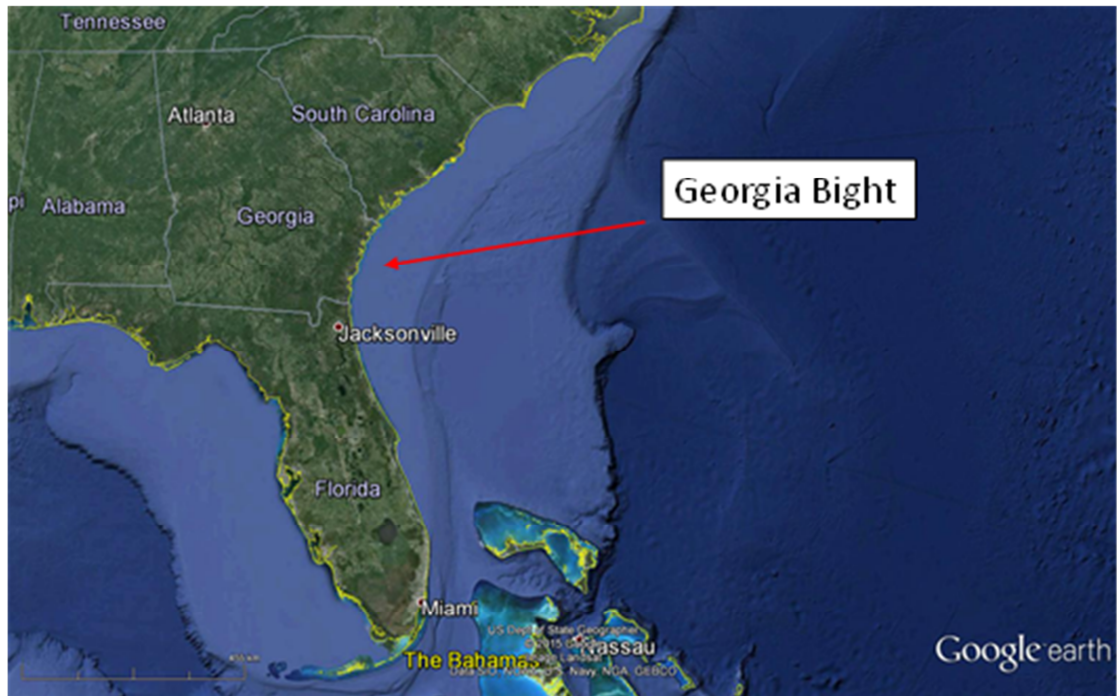


Figure 1: Location of state of Georgia and the associated morphology of the Georgia Bight.

A total of 13 complex paleo-shoreline deposits (ancient coastal deposits, ACDs) ranging in elevation from 0-79 m can be found overlying the Tertiary bedrock in the Georgia Coastal Plain (Huddlestun, 1988; Kellam et.al., 1991). While the most recent mapping of these deposits was done by Rhea (1986) the deposits were mapped by the Georgia Geological Survey (1979) as well. The Rhea mapping (1986) differs from the Georgia Geological Survey in the classification of the ACDs. Rhea's classification is closer to that of Huddlestun (1988) and the Rhea map shows more detail as it focused on these features. The location of the ACDs according to the Georgia Geological Survey map of 1979 as well as the sample locations of this study can be found in Appendix 1 (Figure A1-F1). The paleo-shoreline deposits are thought to have been deposited and stranded during times of sea level standstill or regression (Kellam et.al., 1991). As such they represent an important record of the sea level change along the coast of Georgia through time. These deposits have been extensively mapped and sedimentary characteristics analyzed (Hoyt and Hails, 1967; Hails and Hoyt 1969a; Hails and Hoyt, 1969b; Hails and Hoyt, 1972; Oertel, 1975; Georgia Geological Survey, 1979; Howard and Frey., 1985; Rhea, 1986; Huddlestun, 1988; Kellam et.al., 1991). Each paleo-

shoreline consists of barrier island deposits, characterized by sandy sediments, and back barrier deposits, consisting of fine sediments associated with lagoon and marsh environments.

Of the 13 ACDs this project will focus on the barrier island deposits found between 4-46 m elevation (relative to mean modern sea level) of which there are 6 (Figure 2). These ACDs are, from east to west, the Princess Anne, at approximately 4m above modern sea level, the Pamlico, at approximately 7.5 m above modern sea level, the Talbot, at 12-14 m about modern sea level, the Penholoway, at 21-23 m above modern sea level, the Wicomico, at 29-31 m above sea level, and the Okefenokee, at 35-46 m

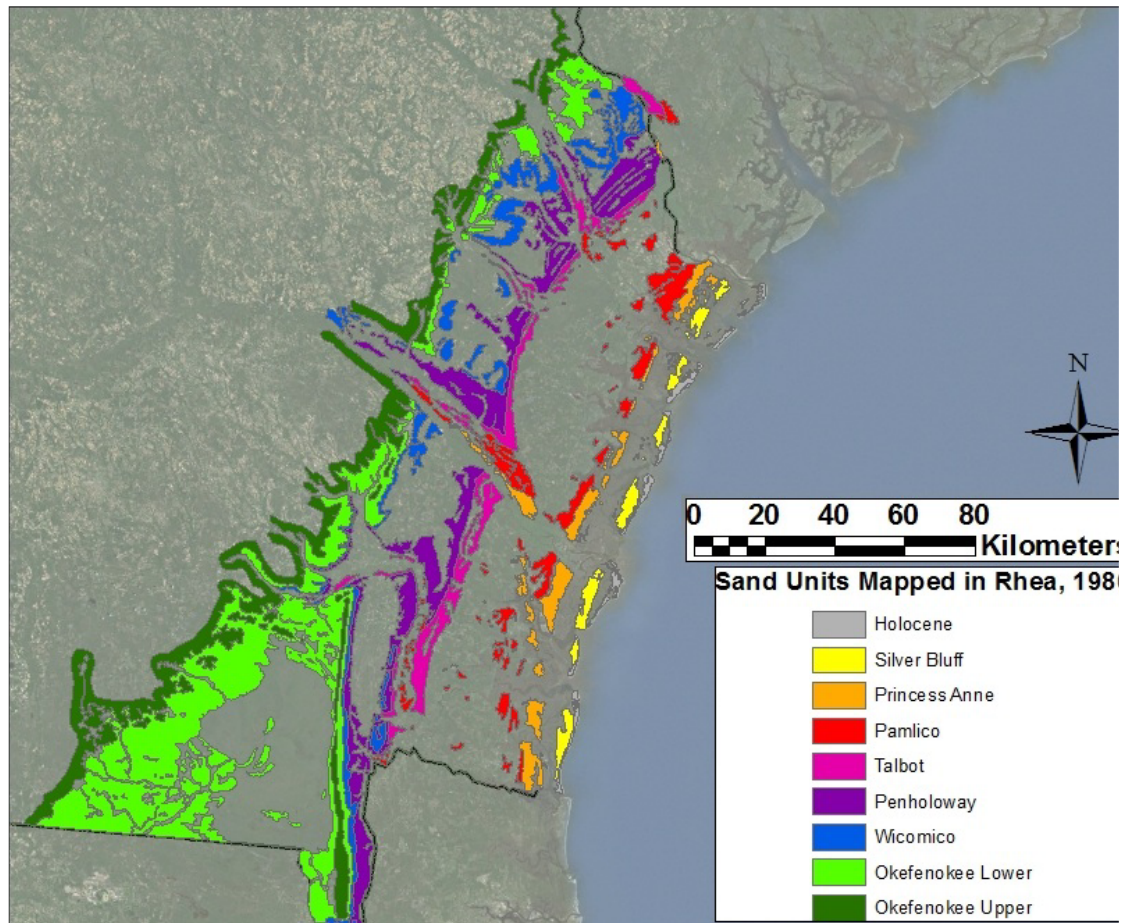


Figure 2: Sand units mapped as paleo barrier islands by Rhea (1986). Shown are the ACDs studied in this project. Also included are the younger Silver Bluff and Holocene barriers. These were not associated with this project but are included to show a complete map of the Georgia ACDs.

above sea level (Hails and Hoyt, 1969b; Rhea, 1986; Huddleston, 1988). For the remainder of this work the Talbot through Okefenokee ACDs will be referred to collectively as the “upper ACDs” while the Princess Anne and Pamlico ACDs will be referred to as the “lower ACDs”.

The upper ACDs overlie the Cypresshead Formation, a lithologically diverse, quartz-rich, fine to pebbly sand that is massive to planar to cross bedded, deposited during the early Late Pliocene to Late Pleistocene in a shallow marine environment (Huddleston, 1988). The Satilla Formation underlies the lowermost ACDs and is generally a fine quartz sand with variable clay content deposited during the Late Pleistocene to Holocene in a marine environment (Huddleston, 1988). Huddleston (1988) states that based on limited evidence from core and outcrops the Satilla Formation disconformably overlies the Cypresshead Formation (Figure 3).

The ACDs of the Georgia coast are not distinct lithostratigraphic units but are instead strictly geomorphic features. As such their relationship with the underlying formations is variable. Huddleston (1988) concludes that while the creation of the lower ACDs may have been contemporaneous with the deposition of the Satilla Formation, the upper ACDs are post depositional modifications of the Cypresshead Formation by paleo-sea levels. In either case the sediments of the ACD and the underlying formation are similar, making identification of the ACDs from the underlying formations difficult.

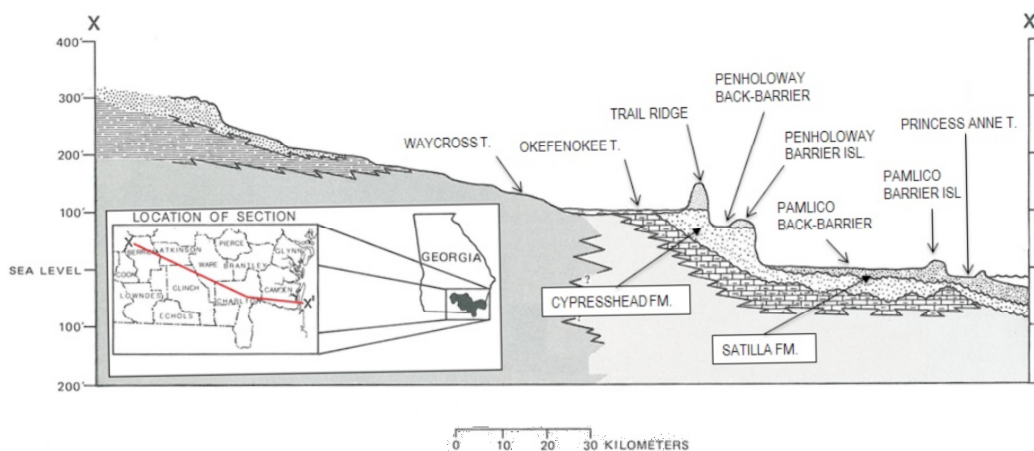


Figure 3: Cross section of the southern coast of Georgia showing the ACDs and their underlying geological formations (modified from Huddleston, 1988).

1.3 Morphology, Sediment Characteristics and Age of the Ancient Coastal Deposits of Georgia and the Atlantic Coast

As mentioned above the Georgia ACDs are geomorphic features and lack a unique lithology to differentiate them. The ACDs are mapped using topography and the identification of “scarps” interpreted as the paleo-shorelines marking the seaward edge of the feature. ACDs are correlated based on similar surface elevations (Hails and Hoyt, 1967; Georgia Geological Survey, 1976; Rhea 1986, Huddleston, 1988). As a result there is a lack of detail in the available maps of the features and field checking is necessary to locate the scarp of a particular ACD (Kellam et.al, 1991). The Wicomico to Holocene ACDs have been most extensively mapped and studied due to their importance as economic sources of heavy minerals (Kellam et.al., 1991).

Hayden and Dolan (1979) compared barrier island shape and their associated lagoon and marsh characteristics of the Atlantic coast of the U.S as well as the offshore bathymetry in effort to determine the cause of regional variation in barrier island type and controls on barrier island morphology. They concluded that offshore continental slope and concavity controlled the morphology of the Atlantic barrier islands with shallow slopes and convex slope creating small barriers with extensive marshes dominated by tidal processes. Steeper concave continental slopes were in contrast dominated by waves and currents and developed elongated barriers with narrower lagoons.

The modern barriers of Georgia (as well as southern South Carolina and northernmost Florida) are classified as short with large marshes, the result of the shallow shelf morphology of the Georgia Bight. To the north, in northern South Carolina, and south, in Florida, the barrier islands are elongated and their lagoons shrink as a result of the diminished influence of the Georgia Bight and increasing wave energy (Hayden and Dolan, 1979).

The Pleistocene barrier islands of Georgia stand out as anomalous features in that they do not seem to follow the morphological patterns observed on the modern Atlantic coast, as noted by Hayden and Dolan (1979). This would indicate that other processes

may have controlled the morphology of the Pleistocene barriers of Georgia or that they were formed under different bathymetric slope configurations.

A morphological difference between the upper and lower ACDs can be observed from the maps of the deposits (Figure 4). Most of the upper ACDs exhibit limited back barrier marsh deposits with elongated, continuous morphology attributed to deposition under wave dominated conditions and a large sediment supply (Rhea, 1986; Huddleston, 1988; Kellam et.al., 1991). Barrier island morphology can only be seen in the northern most Penholoway. The morphology of most of the upper ACDs is similar to the modern coastlines of North Carolina and southern Florida where the depositional conditions are

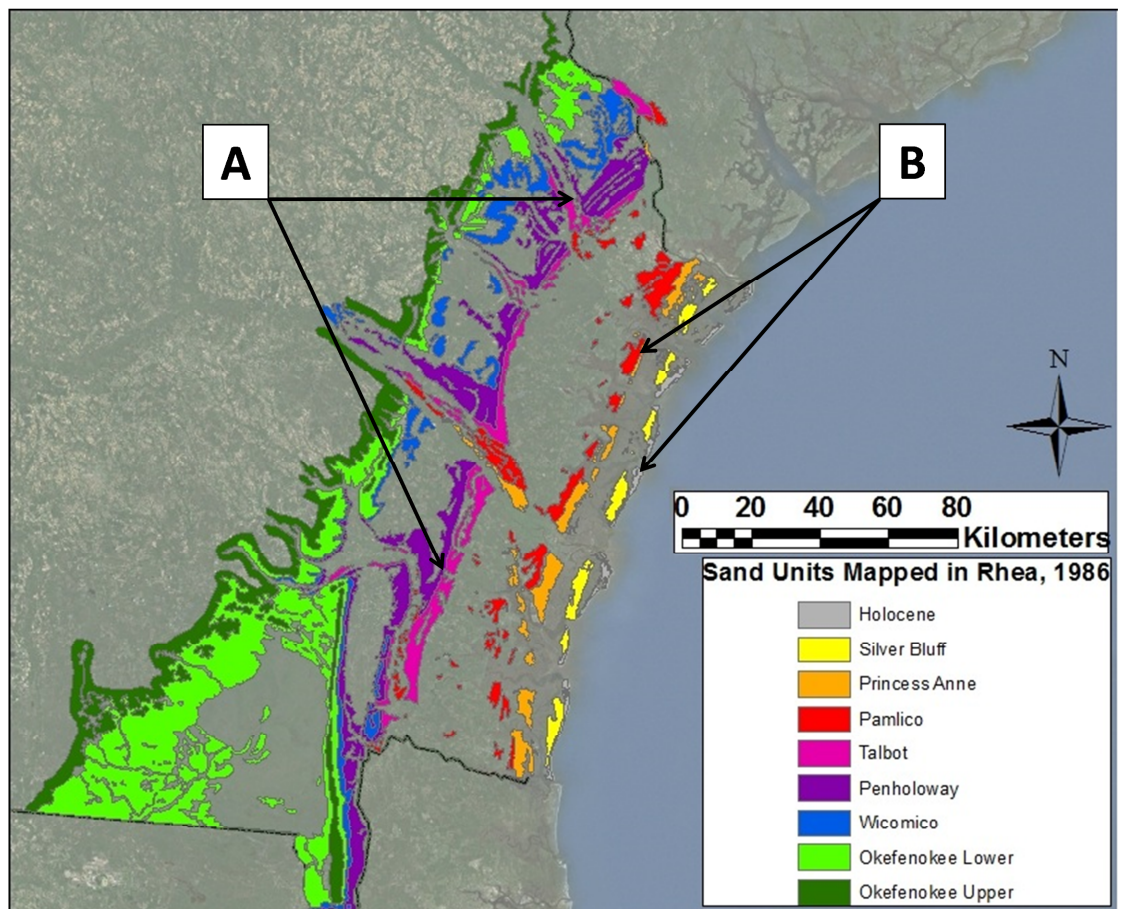


Figure 4: Map of the Georgia ACDs. The upper ACDs display an elongated morphology as highlighted by A while the lower ACDs and the modern barrier islands have a shorter discontinuous morphology shown by B.

wave dominated as well (Hayden and Dolan, 1979; Kellam et.al., 1991). The continental shelf in these locations is significantly steeper than that found in modern Georgia (Hayden and Dolan, 1979) and Keller et.al. (1991) implicate this as possible reason (along with sediment supply) for the elongated paleo-barriers. This morphology is much different than the modern Georgia barrier islands (Figure 4).

In contrast the lower (eastern) ACDs exhibit a morphology similar to that of the modern Georgia coast with highly dissected short barrier islands with an extensive back barrier marsh developed (Rhea, 1986; Huddleston, 1988; Kellam et.al., 1991). The formation of these barrier types, and the modern coast of Georgia, is attributed to tide dominated processes in a sediment starved environment as well as shallow continental shelf that dampens wave energy (Hayden and Dolan, 1979; Howard and Frey, 1985; Rhea, 1986; Kellam et.al., 1991). The back barrier region of these ACDs may have been shared and reoccupied during the deposition of the younger coastal deposits. While the marshes dissect the ACDs preserved scarps of the Pamlico and younger ACDs can be found to be generally located directly west of (ie. behind) the modern barrier islands.

Both the upper and lower ACDs exhibit a “welded” morphology in which a younger ACD is in direct contact with the eastern edge of the successively older ACD. This morphology is seen extensively in the upper ACDs and to a lesser extent in the lower ACDs. This is the result of the younger ACD reoccupying or partially reoccupying the previous ACD’s environment allowing for the formation of a new scarp by reworking a portion of the older ACD with limited deposition of new material. This, as well as post depositional reworking, makes identifying the boundary between ACDs difficult (Kellam et.al., 1991).

Sediment that composes the Georgia ACDs, as well as the paleo-shoreline deposits further south in Florida is derived from igneous and metamorphic rocks that make up the Georgia Piedmont and Blue Ridge Provinces (Martens, 1935; Clark and Zisa, 1976; Kellam et.al., 1991). As implicated above reworking of other ACD material is another source of sediment for younger paleo-coastal deposits (Martens, 1935; Hails and Hoyt, 1969b). It has been noted by many that the subsurface sediments of the ACDs

of the Georgia coast exhibit a distinct lack of primary sedimentary features (Hails and Hoyt, 1969b; Howard and Scott, 1983; Rhea, 1986; Huddleston, 1988; Kellam et.al., 1991). This has been attributed to bioturbation, groundwater flow, dissolution of originally deposited minerals and the deposition of clay minerals, and other pedogenic processes.

The coastal sediments of Georgia (and the entire Atlantic coast) have been extensively explored as they are a valuable source of economic heavy minerals (Martens, 1935; Neiheisel, 1962; Hoyt and Hails, 1967; Hails and Hoyt, 1969a; Hails and Hoyt 1969b, Kellam et.al., 1991). As such their sediments have been studied in great deal in order to determine depositional environment and mineralogy to aid exploitation.

Martens (1935) compared the sedimentary characteristics of modern beach sands collected from southern South Carolina to south Florida. It was found that generally grain rounding increased to the south and the ratio of feldspar to quartz decreased from north to south from 0.062 in South Carolina to less than 0.006 in southern Florida. The feldspar to quartz ratio in the modern beaches of Georgia ranged between 0.038-0.007. It was also discovered that the average grain size increased from north to south, though this is attributed to winnowing of fines due to a steeper shelf further south and not as a primary condition of the sediments. The author notes that the mineralogy of the quartz grains within the study area lack flint, chert, and other microcrystalline forms of silica indicating that the quartz is primary and derived from the metamorphic and igneous rocks of the Piedmont. Finally it is noted that the quartz grains in South Carolina and Georgia are often coated with Illite while this is not the case in Florida as increased transport abrades the coating away. Martens (1935) concludes that the sand grains of Florida have undergone more modification since their erosion from the source than those of Georgia.

Within the coastal deposits of Georgia there is significant variation in the mineral and structural characteristics of the modern barrier islands and the ACDs. Neiheisel (1962) discovered that while the modern beach sands of Georgia contain 4-6% (by weight) feldspar while the Holocene barrier deposits contain 2-5% feldspars. The Pleistocene barriers (Sliver Bluff, Princess Anne and Pamlico ACDs) had feldspar

contents of 0.5-2.5% feldspar. It was noted that the feldspars appear to be more weathered in the older deposit (Neiheisel, 1962). Feldspar content in the Talbot-Wicomico ACDs ranges between 0.3-1% (Hails and Hoyt, 1969b). Based on this information and information from heavy mineral weathering profiles it is concluded that post depositional processes account for the lack of feldspars in the ACDs of Georgia and that this variation does not reflect a change in source sediments but in the age of the deposits (Neiheisel, 1962; Hails and Hoyt, 1969b).

Correlation of the deposits of the Atlantic Coastal Plain has been of interest to geoscientists since the mid-1800s as the deposits record evidence of sea level fluctuations and has implications to coastal neo-tectonics, with notable works including: Winker and Howard (1977), Cornin et.al. (1984), Hollin and Hearty (1990), Krantz (1991), Wehmiller et.al. (2004) and Markewich et.al. (2013). While early attempts at correlation made use of deposit elevation, lithology, and micro-paleontology (Cornin et.al., 1984) there are many challenges to this objective. The deposits are subject to erosion and modification by subsequent coastal processes during times of sea level transgression as well as erosion by fluvial processes during sea level regressions. As a result the deposits are highly dissected or even none existent in some locations. This has resulted in an Atlantic Coast depositional record that is incomplete. Reworking of a deposit incorporates material, including fossils, into younger deposits making lithologic and paleontological studies difficult (Cornin et.al., 1984; Szabo, 1988). As mentioned above the morphology of the barriers and lagoons along the Atlantic Coastal Plain is varied and the depositional environments of the deposits are varied as a result (Hayden and Dolan, 1979; Cornin et.al., 1984). Glacisostatic movement along the Atlantic coast that occurred throughout history hamper correlation efforts (Winker and Howard, 1977; Szabo, 1985; Marple et.al., 2000; Scott et.al., 2010). Erosion, depositional environment, and isostatic shifts all result in variable elevations for that could be considered the same deposit (Figure 5). Many of the deposits have regional names that are state or regionally specific and what defines an ancient coastal deposit, how it is recognized in the field and reported in text, is equally varied. All of these factors make correlation among the

Atlantic coastal deposits challenging. Table 1 shows the history of the Georgia coastal deposit evolution as well as historical correlations within the entire Atlantic Coastal Plain by elevation. The classifications in the final four columns are of particular importance. They represent the regional terms of the deposits used in South Carolina (DuBar et.al, 1974), Florida (Winker and Howard, 1977) as well as those used in Georgia (Rhea, 1986) and this study.

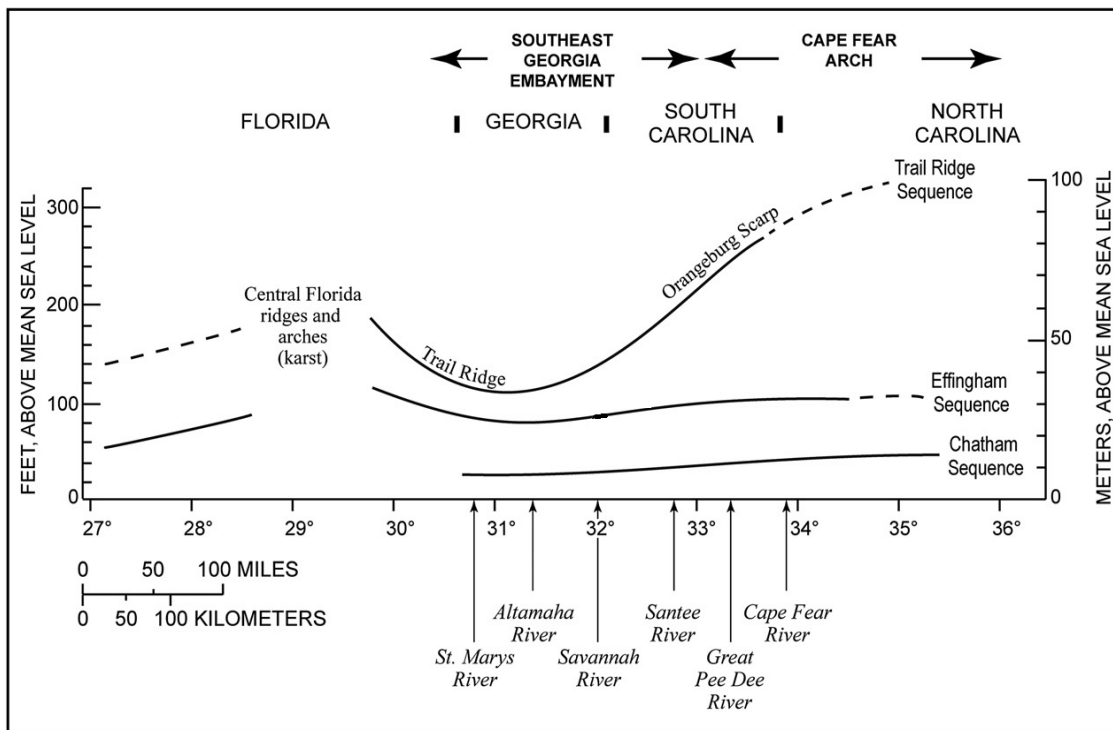


Figure 5: Modified from Markewich et.al. (2013) and Winker and Howard (1977) showing the change in elevation of the Trail Ridge, Effingham, and Chatham sequences along the Atlantic Coast. Note the large change in elevation along the coast of the oldest sequence, the Trail Ridge. The younger Effingham and Chatham sequences display a more consistent elevation along the coastline.

As stated above determination of the depositional age of the Georgia ACDs has been limited by the lack of material suitable for dating by isotopic methods (^{14}C , U-series) and biochemical techniques (amino acid racemization). Elevation-based correlations with deposits found in South Carolina and Florida and limited fossil evidence the Upper ACDs of Georgia, are used to assign ages of Late Pliocene to Pleistocene, while the lower ACDs are assigned ages of Pleistocene to Late Pleistocene (Hoyt and Hails, 1967; Colquhoun, 1969; Huddleston, 1988). More recently researchers have been attempting to refine these ages.

McCartan et.al. (1982) determined the age of the South Carolina deposits using AAR and U-series. They concluded that the age of the Socastee to be 202-203 ka, the Canepatch 300-580 ka, and the Waccamaw to be greater than 1000 ka. Cornin et.al. (1984) compiled the results of paleomagnetic and paleontological studies along the Atlantic Coastal Plain from Virginia to South Carolina. They placed the Socastee and Canepatch Formations in South Carolina as well as the Princess Anne, Pamlico, and Talbot (of southern South Carolina) in the Brunhes Chron and the Middle Pleistocene. The Waccamaw and Penholoway were assigned to the Matuyama Chron and the Early Pleistocene. The Wicomico formation was also placed in the Matuyama Chron but within the Late Pliocene (though modern stratigraphy has moved the Plio/Pleistocene boundary back since this time and this unit would still be part of the Early Pleistocene by modern standards (Cohen et.al., 2013)). Szabo (1985) refined the age of the Canepatch, using U-series, to 460 \pm 100 ka (a younger deposit, the Wando correlated from deposits in North Carolina, was also dated in this work with ages between 87 \pm 4 ka to 129 \pm 10 ka). In an attempt to better understand differences found between the AAR and U-series ages within the region Hollins and Hearty (1990) reanalyzed McCarten et.al. (1982) work. They criticized the correlations used by McCarten et.al. suggesting that the Socastee of the McCarten et.al. (1982) paper was in fact the Socastee and Canepatch Formation and that the Canepatch was in fact the Waccamaw based on AAR amino zones. They provide a U-series age of the Canepatch Formation at 125 ka or MIS 5e. Krantz (1991) used data from high resolution Marine Isotope Stage cores along with the

available age data of the Atlantic Coastal Plain in an effort to further refine the age of the deposits by correlating them to periods of high sea level within their age range. The Waccamaw Formation was correlated to MIS 75, 73, or 71 (1875-1990 ka) and found it difficult to correlate younger deposits due to the number of low amplitude variations in the Marine Isotope Stage record. Wehmiller (2004) reanalyzed the U-series ages of the Atlantic Coastal Plain deposits in an attempt to rectify the 80 ka ages of depositional events that do not seem to correspond to a sea level rise to the elevation needed to deposit them according to the global sea level curve. They confirm these ages, though note that there is potential for open system behavior and cite regional sea level effects for the discrepancy with the global sea level curve. Willis (2006) used OSL on the Talbot, Pamlico, and Princesses Anne deposits of South Carolina concluding that the Talbot was deposited during MIS 7, the Pamlico during MIS 5e, and the Princess Anne 80-90 ka confirming the U-series ages of previous works of Szabo (1985) and Wehmiller et.al. (2010). These ages are stated as “preliminary” and “minimum ages” as few aliquots yielded useable equivalent dose (D_E).

The most recent work in Florida by Burdette et.al. (2012) and in Georgia by Markewich et.al (2013) and Turck and Alexander (2014) have provided ages independent of the traditional U-series and AAR that have been used extensively in the past in this area. Burdette et.al. (2012) made use of ESR-OD to determine the age of the Trail Ridge, Effingham and Chatham deposits in Florida. They concluded that Trail Ridge was deposited 2,200 \pm 400 ka but has remained active through reworking of the deposit up until 6ka. The Effingham was deposited between 1,430-1,580 ka while the Chatham was deposited 860-1,090 ka. Markewich et.al. (2013) used both OSL and ^{10}Be to determine the age of deposits in inland sections westward of the northern coast of Georgia. Using this combined approach they determined that the Princess Anne was deposited during MIS 5e (109-123 ka), the Pamlico during MIS 7 (191-243 ka), the Talbot and Penholoway during MIS 9 (300-337 ka), and the Wicomico as being less than 360 ka. OSL and radiocarbon dating of the Silver Bluff ACD (not explored in this study) (Table 1) and Holocene barrier islands of Georgia by Turck and Alexander (2014) determine the

earliest age of deposition for these features to be between 45.8 \pm 10.2 ka and 62.3 \pm 13.0 ka. These ages provide a minimum age of deposition for the older Princess Anne ACD.

1.4 Ground Penetrating Radar

1.4.1 Introduction to GPR

Ground-penetrating radar (GPR) uses pulsed electromagnetic (EM) energy waves to detect and image subsurface stratigraphy and buried objects. It achieves this by creating EM waves and propagating them through the subsurface and measuring their refraction and reflections. This non-invasive and relatively cheap tool has many applications in the fields of geology, archeology, and geotechnical analysis (Neal, 2004). The following is an introduction to GPR and GPR theory, those already familiar with GPR should proceed to Section 1.4.2.

GPR theory and application has grown out of the field of seismic geophysical surveys and many of the terms and data processing and management techniques are borrowed from that field. Like seismic surveys GPR measures the two-way travel time of an energy wave through a medium, in this case, the earth. Unlike seismic, GPR makes use of EM waves in the MHz range allowing for greater resolution of subsurface features while reducing the effectiveness of the techniques to the upper 50 m of the earth's surface (Neal, 2004).

The GPR system consists of a transmitting and receiver antenna and a controlling/recording device (Figure 6) (Neal, 2004). The EM pulse is directed into the subsurface by the transmitting antennae, travels through the subsurface and is reflected back where it is detected by the receiving antennae. The time it takes for a signal to make this journey is the two-way travel time (Figure 6). The resulting two-way travel data is recorded and then processed. The processing phase consists of several steps that filter signals and apply gain to the data in an attempt to remove features created by the EM pulse and not lithology. Corrections are also made for surface topographic changes and the two-way

travel times converted to distance from the surface. The completed radargram provides an accurate representation of the subsurface morphology (Neal, 2004).

As the EM wave travels through the subsurface its velocity is modified by the materials it encounters. A materials dielectric permittivity (ϵ), electrical conductivity (σ), and magnetic permeability (μ) effect the velocity of the EM wave. The permittivity (ϵ) of a material is a measure of how the material stores EM energy compared to the energy storage ability of free spaces. Conductivity (σ) is the ability of a material to transport charge within a static electrical field. Both permittivity and conductivity are dependent

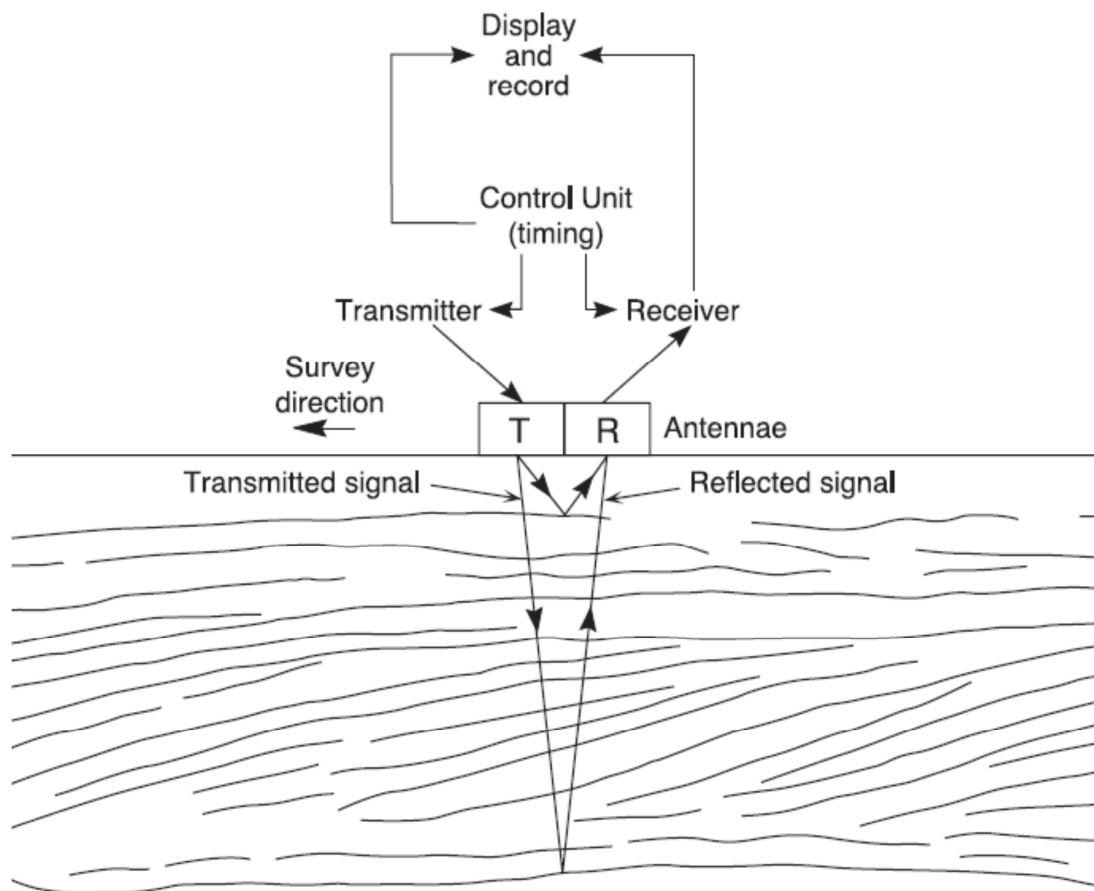


Figure 6: From Neal (2004), a schematic diagram of the GPR system and signals produced from the subsurface.

on the frequency of the EM wave and limit the useful frequencies of GPR to between 50 MHz-1 GHz due to energy scattering and polarization (Neal, 2004). Permeability measures the net magnetic field energy of a material within an induced magnetic field with respect to free space (Powers, 1997; Neal, 2004). These properties change with a materials composition, grain size and shape, orientation and packing of the grains, as well as pore fluid material. This allows for changes in the EM properties of a material to be a proxy for changes in subsurface lithology (Neal, 2004). While some materials have EM properties that are ideal for transmitting the EM pulse of a GPR others are less than ideal due to their chemical composition, for example, while clean sand and fresh water transmit the EM pulse well, clay minerals and salt water do not as their ionic charges cause loss of energy due to conduction (σ) (Olhoeft, 1998). For this reason the GPR pulse is not able to travel through these materials resulting in a loss of signal (Neal, 2004).

Where the EM properties of a material change there is the potential for reflection of the GPR wave. The reflection coefficient (R) is a measure of how strong a reflection between two materials is likely to be and is determined by either the (ϵ) of the materials or the velocity of the materials through which the wave is traveling. The R value is between -1 and +1, representing the polarity of the reflected wave, and can be calculated by equation 1 (Neal, 2004):

$$(1) \quad R = \frac{\sqrt{\epsilon_1} - \sqrt{\epsilon_2}}{\sqrt{\epsilon_1} + \sqrt{\epsilon_2}} = \frac{V_2 - V_1}{V_2 + V_1}$$

Where ϵ_1 is the relative permittivity of the upper medium and ϵ_2 is the permittivity of the lower medium and V_1 and V_2 are the radar wave velocities in the upper and lower layers respectively.

Resolution with GPR is concerned with two questions, 1) can a transition between materials be detected? and 2) is this transition in the correct location on the radargram in relationship to the subsurface? These questions have to be answered in vertical and horizontal components.

Vertical resolution depends on the frequency of the EM pulse used by the GPR, the EM properties of the material the wave travels through (ϵ , σ , μ), the size of the

material beds, and the topography of the surface on which the GPR unit transverses during its measurements.

The material through which the radar wave travels can affect where the reflections occur. GPR measures two way travel time to a feature, not depth to a feature, in the subsurface. In order to convert this time in to depth the velocity of the EM wave in the material must be known. This property can be calculated for different materials and for a specific frequency each material will have a unique velocity. The materials within a vertical GPR profile can change frequently and as such the velocity of the EM wave as it travels through each material is changing. This has an effect on the two way travel time and can lead to an error in the depth estimation for a reflection (Neal, 2004). The use of sediment cores within a GPR profile can help to correlate GPR facies with lithological facies encountered in the profiles increasing the confidence in the vertical resolution (Mallinson et.al. 2010).

While the differences in the EM properties of two materials affect the strength of the reflection the rate at which the EM properties change between the materials as well as the thickness of the material unit determines the clarity of the reflections and therefore the ability of the GPR to detect this boundary at a given frequency. Generally transitions between two materials must be on the order of 3x larger than the wavelength of the GPR EM pulse in order to be resolved while the thickness of the unit must be greater than one-quarter of the EM pulse wavelength (Sheriff, 1977; Neal, 2004) for a unit to be resolved (Neal, 2004). As both of these factors are depended on the frequency of the EM pulse it is important that the selected antenna to be used in a GPR survey reflect the level of detail a research requires. Unfortunately, while high frequency antennae can be used to resolve finer features, they have limited penetration depth due to attenuation of the EM wave. The opposite applies to low frequency antennae (Davis and Annan, 1989).

Surface topography must also be accounted for in order for vertical resolution to be accurate. Any change in the elevation of the antenna and receiver must be accounted for so that the two way travel time to subsurface structures remains independent of

surface morphology. This is done in the processing phase of developing a complete radargram.

It is important that the elevation profile of the GPR line be recorded in the field using GPS or during processing uses other forms of elevation tracking (DEMs or LiDAR).

Horizontal resolution is affected by the nature of the propagation of the EM wave in the subsurface. Normally EM waves travel outward in all directions, but GPR units are shielded so that most of the wave energy is directed downward toward the ground. The EM wave propagates as a cone outward from the bottom of the GPR unit into the ground. The further away from the GPR unit (ie. the deeper in to the subsurface) the wider the wave cone becomes. A return signal can be received and recorded from any part of this curved wave front. This can lead to reflections that show up in the GPR profile that do not accurately represent the subsurface morphology (Figure 7a) (Neal, 2004). This is taken into consideration in the processing of a GPR profile.

The results of this propagation cone, in some cases, are features that appear on the radargram but are not an accurate representation of the subsurface. Figure 7b shows how a reflections of the propagation cone on a down dip surface result in a radar boundary that is shallower than the real facies boundary in the in the subsurface. One of the more common distortions is what is known as a “point reflector”. These occur when the GPR transect encounters a larger isolated object in the subsurface such as a cobble or pipe (running perpendicular to the survey). Multiple EM pulses bounce off this object with the first pulses (being further way form the object) record it being deeper than the object is in the subsurface. The pulses from the when the GPR unit is directly over top of the object record its true depth. The final pulses again record it being deeper than its true depth (again due to its distance from the GPR unit) (note the term “depth” is used here in place of two way travel time in order to allow the reader to visualize this concept better). The results is a reflection that appears like that in Figure 7c. As stated above the processing phase of making a complete radargram attempts to correct for these objects. Though attempts are made to remove these features, the presence of these objects provide insight into subsurface lithology and EM velocity. Areas of like reflection types are

grouped into radar facies which borrows its definition from the seismic geophysical school's seismic facies term. Radar facies is used to describe the configuration, amplitude, continuity, frequency, and internal velocity of a 2D or 3D set of radar reflections bounded by a radar surface (Baker, 1991; Neal, 2004). It is similar to sedimentary facies in that it is used to describe, characterize, and separated unique packages of reflections within a GPR profile (while a sedimentary facies does the same task with rocks). The types of and boundaries between radar facies can be used to hypothesize a depositional environment or subsurface structures. Once a radargram is complete the researcher can pick these facies out by their traits.

As mentioned above change in the type and amount of pore fluid also change the ϵ , σ , and μ of the materials and as a result create a reflection of the EM wave within a homogeneous material. The water table can also be the site of

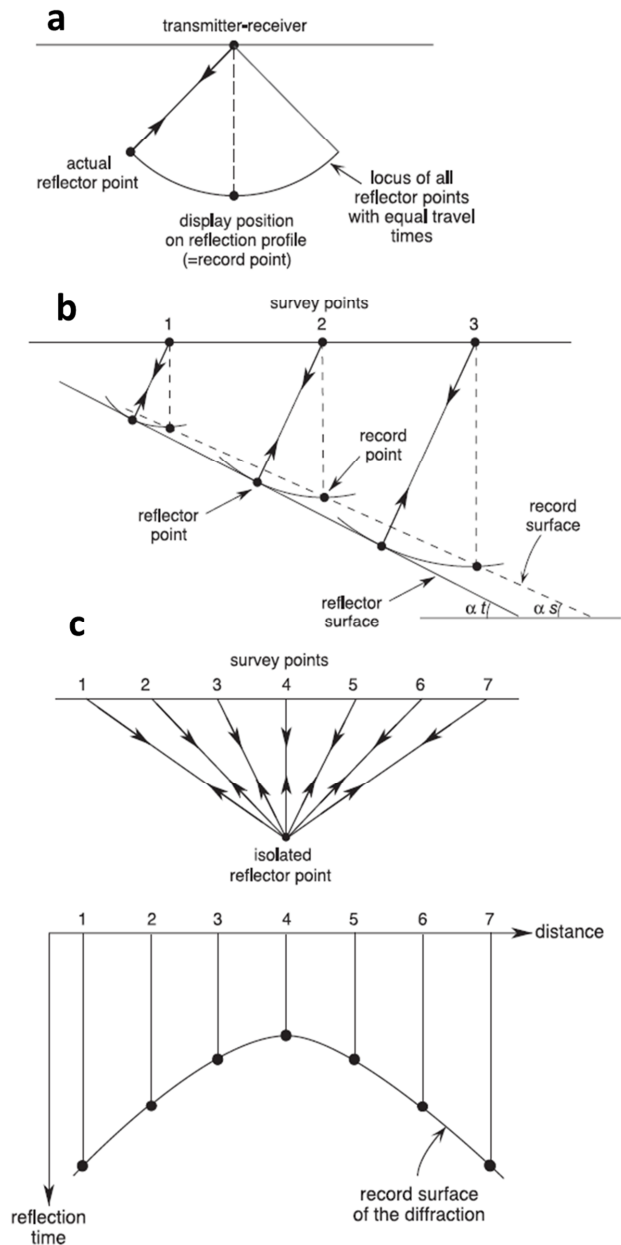


Figure 7: From Neal (2004). Diagram a) depicts the curved radar wave front locating a reflection at the wrong position in the subsurface, directly under the transmitter/antenna. Part b) shows how this type of reflection can affect the apparent dip of a stratigraphic surface in the radargram. Isolated point reflections, such as large boulders or pipes, appear as convex up signals due to the signals generated by the curved wave front as shown in c.

dissolution and precipitation of minerals within the subsurface. This process can also occur outside of the water table through the concentration of minerals by downward percolating meteoric water. These precipitated mineral deposits can be the source of a reflecting surface as well and likewise do not represent primary bedding structures. These features are not grouped into their own radar facies as they are not diagnostic of the original morphology.

1.4.2 GPR in Coastal Sites and in Conjunction with Geochronology

GPR has been used extensively in coastal environments (see Neal, 2004 and references therein) as a tool for profiling the internal architecture of sand deposits, including coastal dunes and barrier systems (Jol, 1996). GPR studies in barrier islands has shown that GPR has the ability to resolve fine-scale bedding, deposit architecture and morphology (e.g. bedforms, channels) as well as the freshwater/saltwater interface and channel features within the coastal deposits (Baker, 1991; Jol, 1996; Jol et.al., 2002; Mallinson et.al., 2008; Mallinson et.al., 2010).

The application of GPR in coastal environments it is not without its challenges. The sands that compose the barrier islands allow for transmission of the radar pulse but clay materials, often found in the back barrier environment or marshes, attenuate the signal and making penetration through that layer impossible (Baker, 1991; Neal, 2004). The coast is also the location of the groundwater/seawater interface and fluctuations in groundwater head and tidal motions can allow for seawater to invade the freshwater table within coastal deposits (Johannes, 1980) (Figure 8). The freshwater table can be seen on the radargrams, often cross cutting stratigraphy, but saltwater attenuates the GPR signal similar to clay materials (Baker, 1991; Jol, 1996; Neal, 2004). GPR has been applied to the coastal deposits of the Florida (Burdette et.al., 2012), Georgia (Schultz, 2001; Hergott, 2011), South Carolina (Willis, 2006) and North Carolina (Mallinson et.al., 2008; Mallinson et.al., 2010) as well as the modern beaches of Georgia (Jol, 1996) with success.

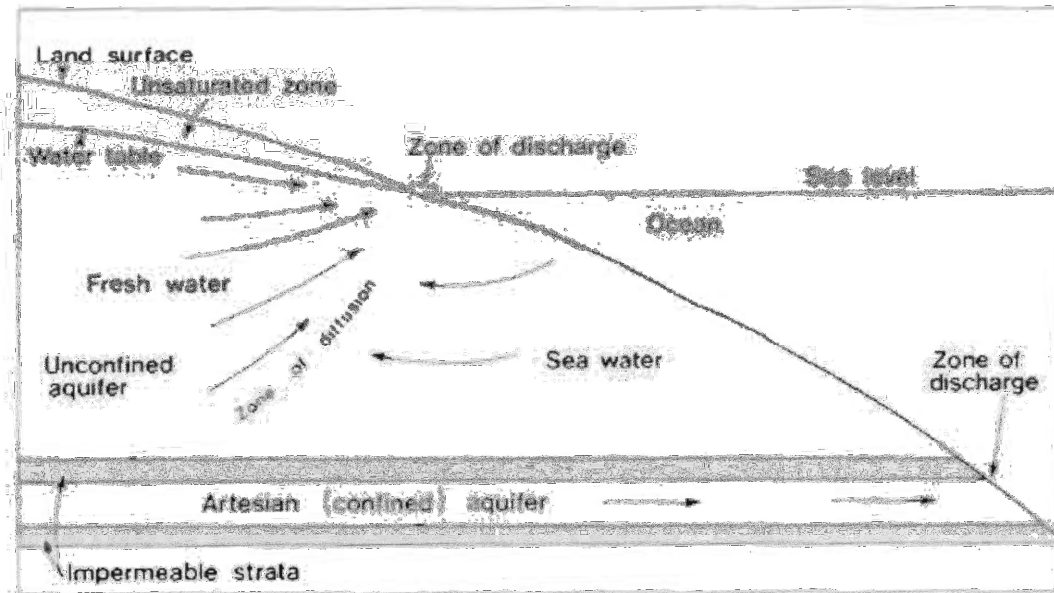


Figure 8: Diagram of the interaction between salt and fresh water at the coast. This interaction affects GPR's ability to resolve structures in the near shore as the saltwater attenuates the GPR EM waves. Figure from Johannes (1980).

Willis (2006), Mallinson et.al. (2008) and Burdette et.al. (2012) employed GPR as well as optical dating in their studies in South Carolina, North Carolina, and Florida respectively. GPR was used to target core sample locations for dating as well as assist in interpretation of depositional environments. This is particularly useful in optical dating where variations in age can occur within a sediment core.

1.4.3 Georgia GPR Surveys and Core Sampling

The goal of the GPR surveys in this study were to aid in selecting coring locations, selection of samples for age determination and to determine the subsurface stratigraphy of the Georgia ACDs and their relationship to one another. Shore perpendicular features within the ACDs are the focus of this work and GPR transects are run west to east over the ACDs as a consequence. After GPR processing the core locations were selected based on the features observed in the radargrams. Sediment cores were taken as close to the GPR transect as possible with two cores being taken at each

site. One core is used for sedimentary logging and the other used for the optical dating. The exact procedure is discussed further in sections 2.2 and 2.3.

1.5 Electron Spin (Paramagnetic) Resonance

1.5.1 Introduction to ESR

Electron spin resonance (ESR), also known as electron paramagnetic resonance (EPR), measures the absorption of microwave energy at a particular resonance frequency by unpaired electrons contained within an object in a magnetic field (Ikea,1993). It was discovered in 1945 and is very similar to Nuclear Magnetic Resonance (NMR) commonly used in the medical field as a MRI machine (Ikea, 1993; Blackwell, 1995). ESR is used in the fields of biochemistry, chemistry, and physics as well as in the fields of geology and archeology (Ikea, 1993; Blackwell, 1995; Rink, 1997). The following sections are included to educate the reader in the use of ESR in geochronology and are by no means a complete review of the physics and application of ESR.

When used as a geological or archeological dating method ESR measures the signal proportional to the number of unpaired electrons in an object, created by exposure radioactive doses, since the time of an event that removes all (or most) of the previous unpaired electrons (Grün, 1989; Blackwell, 1995). An equivalent dose to the one accrued nature is obtained by adding laboratory doses to multiple subsamples carrying the burial dose followed by curve fitting of the dose response behavior. Comparing the equivalent dose to the radiation dose rate of the environment the object was exposed to during burial yields a time length in which that object resided in that radiation field (Hennig and Grün, 1983; Ikea, 1993; Jonas, 1997). A plethora of geological and anthropological materials have been dated using ESR ranging from carbonate speleothems and shells, to teeth, blood, and skins of various mammals, to geological sediments and rocks (Henning and Grün, 1983; Grün, 1989; Ikea, 1993; Blackwell, 1995; Rink, 1997). Unlike a great many geochronological methods ESR can be done in a non-destructive manner and measurements can be repeated.

1.5.2 Physics of ESR

At its most basic, ESR measures a signal proportional to the number of paramagnetic electrons in the application of age determination of a material. Due to an electron's charge and spin, each electron has a very small magnetic field. In most cases electrons are paired within a crystal structure with the magnetic field of one electron canceling the magnetic field of another electron with the opposite spin direction resulting in a zero net field (Ikea, 1993; Blackwell, 1995). Ionizing radiation excites the electrons, energizing them, allowing them to split from their partner and travel through the crystal's conduction band energy states. After a time they lose energy and can become trapped by defects within the crystal. Some sites, known as "trapped electron sites", have an excess electron while others, "trapped holes", are missing an electron. As a result these electrons do not have an oppositely spinning electron to counteract their magnetic field and a net magnetic field is present (Figure 9) (Ikea, 1993). An increasingly larger radiation dose received by an object results in more and more electrons becoming energized, traveling, and becoming trapped at defect sites.

When exposed to an external magnetic field the unpaired electrons align themselves with the field and split into two energy levels known as Zeeman energies (Henning and Grün, 1983; Ikea, 1993; Blackwell, 1995) (Figure 10). The difference between the energy levels, ΔE , is defined by the equation (equation 2):

$$(eq. 2) \quad \Delta E = g\beta H$$

Where β is the Bohr Magnetron (9.27401×10^{-24} Joule/Tesla), H is the external magnetic field (in Teslas but commonly reported in Gauss), and g is the Lande's Factor commonly referred to as the "g value" (Henning and Grün, 1983; Ikea, 1993; Blackwell, 1995). The number of high energy "up spin" electrons versus the number of lower energy "down spin" electrons can be calculated using the equation (equation 3):

$$(eq. 3) \quad N/N_+ = e^{0.048(v/T)}$$

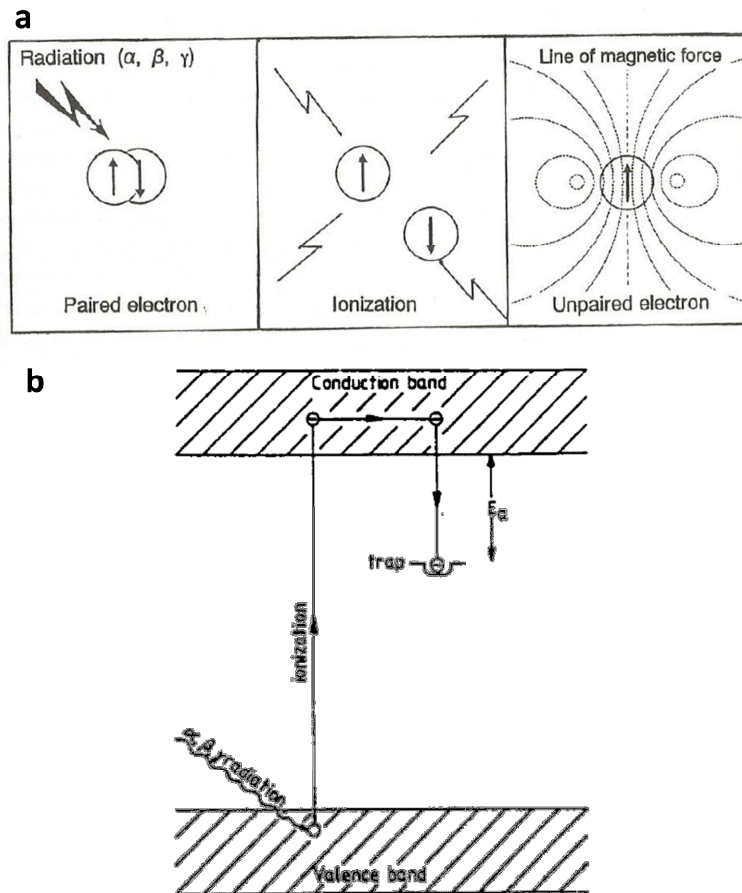


Figure 9: Diagram a) illustrating the process of creating an unpaired electron and the resulting magnetic field. After Ikea (1993). Part b) depicts and electron, energized by irradiation, leaving the valence band energy state, traveling through the conduction band before losing energy and becoming trapped in a region between the valence and conduction band (from Grün, 1989). These trapped electrons are responsible for the ESR signals.

Where N_- is the number of low energy electrons, N_+ the number of high energy electrons, ν is the frequency of the microwave field (GHz) and T is temperature (K) (Henning and Grün, 1983; Blackwell, 1995). The addition of microwave energy will cause the down spin electrons to absorb some of the microwave energy and become excited into the up spin state. This resonance absorption occurs when (equation 4):

$$(eq. 4) \quad g\beta H = h\nu$$

where ν is the microwave frequency in Hz and h is Planck's Constant (6.62554×10^{-34} J/s). After a period of time electrons that have transitioned to the upper energy level the return to the lower energy level by distributing their energy through the

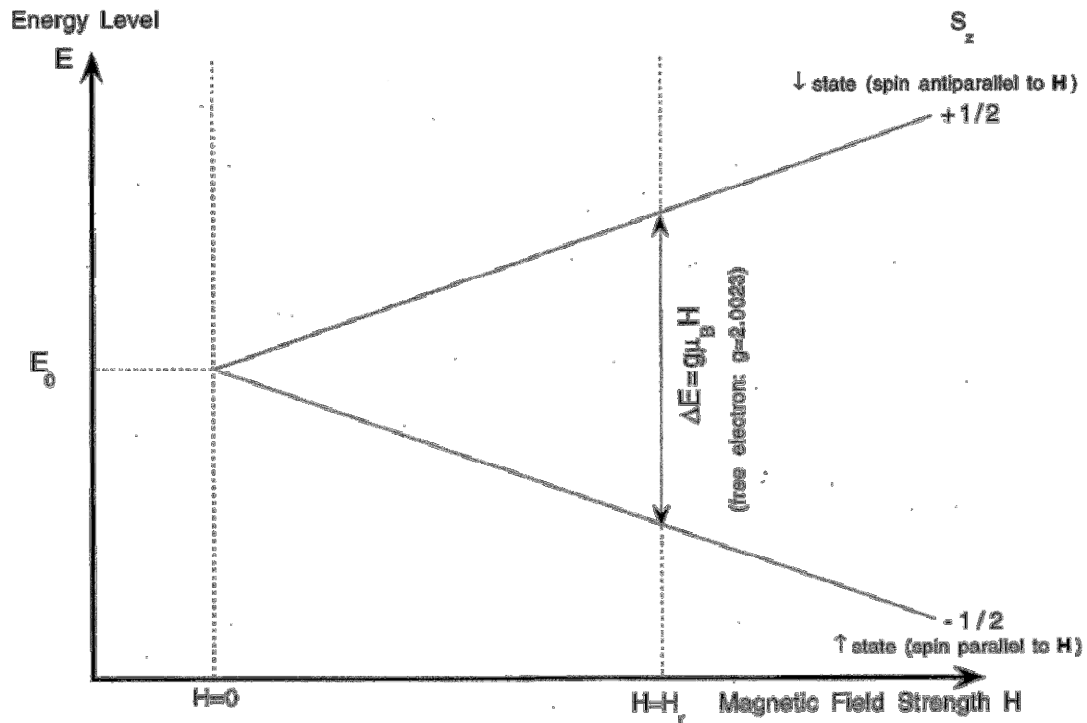


Figure 10: From Jonas (1997) showing the Zeeman Split of the energy levels of an electron in a magnetic field. The magnetic field is needed to split the energy states of the spinning electrons.

crystal lattice, characterized by their “spin-lattice relaxation time” or through interactions with other spinning electrons through “spin-spin relaxation time”. Given that these periods of time are long enough a signal can be measured (Ikea, 1993; Blackwell, 1995). Absorption spectra are generally displayed as the first derivative of the absorption peak (Figure 11) (Henning and Grün, 1983; Ikea, 1993; Blackwell, 1995; Jonas, 1997).

The g value of a free electron is $g = 2.0023$ but when that electron is within a crystal structure the orbit of the electron in the crystal and the atoms near the electron create a variation in the g value that is specific to the location of the electron within the crystal (Blackwell, 1995). Given this, specific defects within a crystal structure will have unique g values and as such absorb microwave energy at a particular combination of magnetic field strength and microwave frequency. This allows for measurement of the detection of a signal that is proportional to the number of electrons present at a specific trap or hole within the crystal.

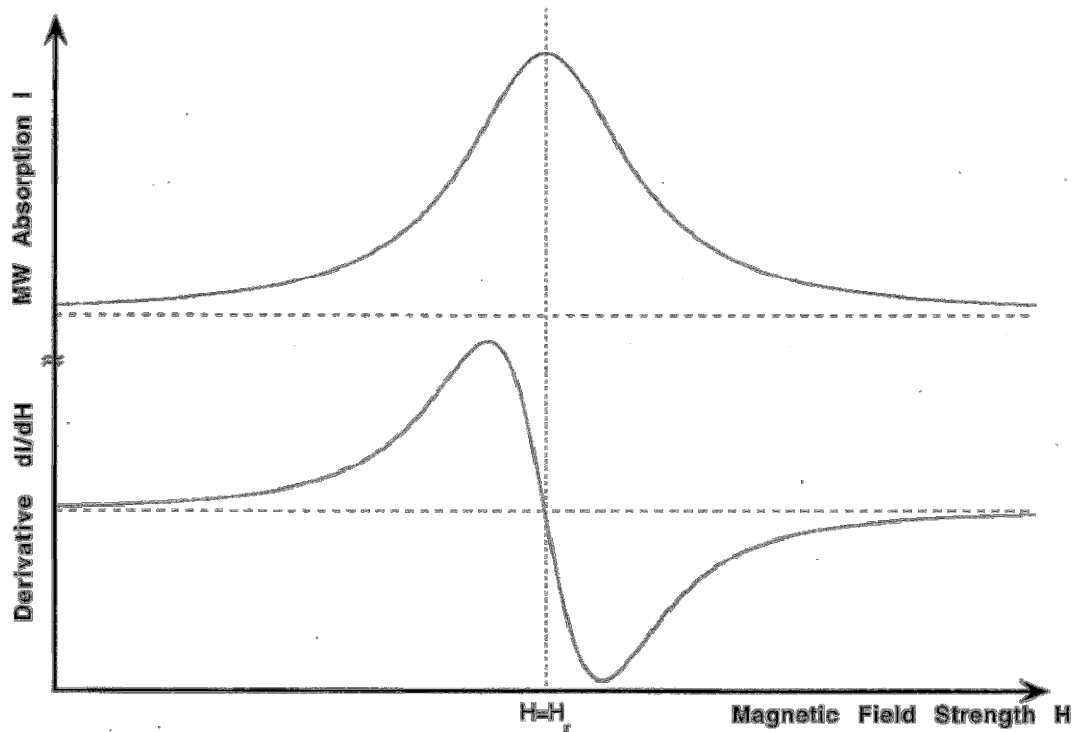


Figure 11: A schematic of an ESR microwave absorption spectrum. The upper spectrum represents the absorption of the microwave energy (defined as intensity, I) with varying magnetic field strength (H). The lower spectrum is the first derivative of the spectrum. The first derivative is typically used when working with ESR to determine signal location and intensity. From Jonas (1997).

An ESR spectrometer is used to obtain the ESR spectrum of an object. The spectrometer consists of a microwave source (Klystron or Gunn-diode oscillators), a wave guide connecting the microwave source to the sample resonance cavity (tuned to a specific band of microwave frequencies), large electromagnets surrounding the cavity to provide the static magnetic field, microwave field detectors to detect energy absorption and relaxation, as well as associated control computers and power supplies (Figure 12), (Henning and Grün, 1983; Ikea, 1993). With a sample in the resonance cavity and the microwave energy directed in to the cavity, the magnetic field is varied to cause resonance at selected range of g values (the tuned cavity prevents the varying of the microwave frequency thus allowing a resonance condition) (Henning and Grün, 1983; Grün, 1989; Ikea, 1993). Absorption of the microwave energy is recorded by the detectors. As shown by equation 3, the signal strength is dependent on frequency and temperature, with lower temperatures increasing the lower energy electron population

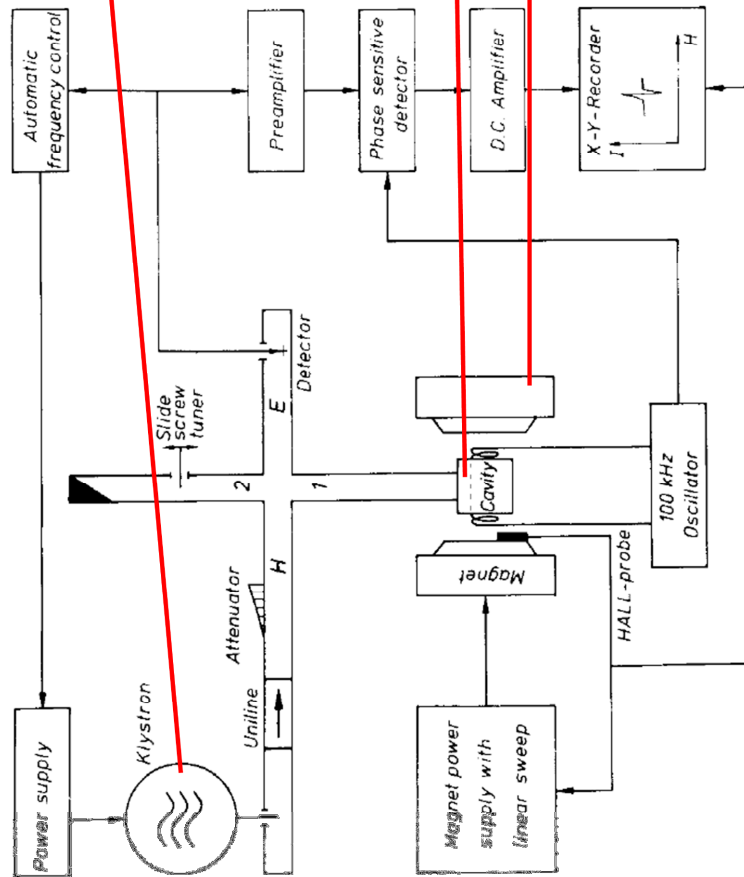
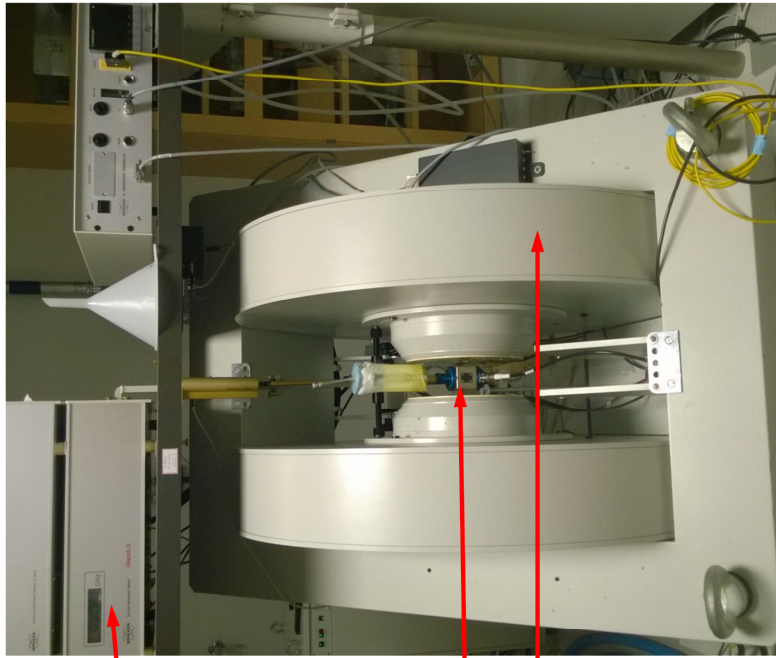


Figure 12: A schematic of an ESR spectrometer (from Henning and Grün, 1983) and a photo of one of the ESR spectrometers used in this research located at Florida State University. A few features are identified on the photo from the schematic to orient the reader. Many of the elements in the schematic cannot be seen in the photo.

yielding better signal to noise ratios (s/n) and high frequencies saturating the ESR signal (Grün, 1989; Ikea, 1993). As stated above the first derivative of the energy absorption curve is displayed and the signal intensity is measured either from the high peak to the low peak or from a peak to a known base line.

1.5.3 ESR of Quartz

There have been many studies using ESR on quartz for geochronological measurements, using a variety of defects whose paramagnetic condition has been reset, or whose paramagnetic condition is introduced from a zero state, using numerous methods. An extensive list can be found in Blackwell (1995) and Rink (1997).

For optically bleached quartz geochronology (ESR-OD) being used in this research, the primary defect sites are the Al (Yokomata, et.al., 1985), Ti (Yoshida, 1996; Toyoda et.al., 2000), and Ge (Buhay et.al., 1988; Walther and Zilles, 1994).

The Ge site defect is easily bleached by sunlight in a matter of hours (Walther and Zilles, 1994) but due to its low signal intensity it is rarely used for dating purposes (Rink, 1997).

The Ti defect is a site in which the element Ti has replaced Si in the quartz crystal structure. The presence of a trapped unpaired electron at this defect creates a net negative charge that attracts positive cations, the most common of these are H, Na, and Li (Ikea, 1993; Rink, 1997) (Figure 13). As a result the Ti defect in quartz has multiple peaks related to g values associated with each of the different cations present (Toyoda et.al., 2000; Duval and Guilarte, 2014) (Figure 14). The Ti signal is fully bleached by exposure to sunlight for 10-20 days (Yoshida, 1996; Toyoda et.al., 2000; Rink et.al, 2007). Due to low signal intensity ESR of the Ti centers is done at low temperature (less than 100°K) (Grün, 1989; Ikea, 1993). The Ti signal grows in intensity up to 10,000 Gy after which intensity becomes unstable with respect to dose and can be considered saturated (Duval and Guilarte, 2014).

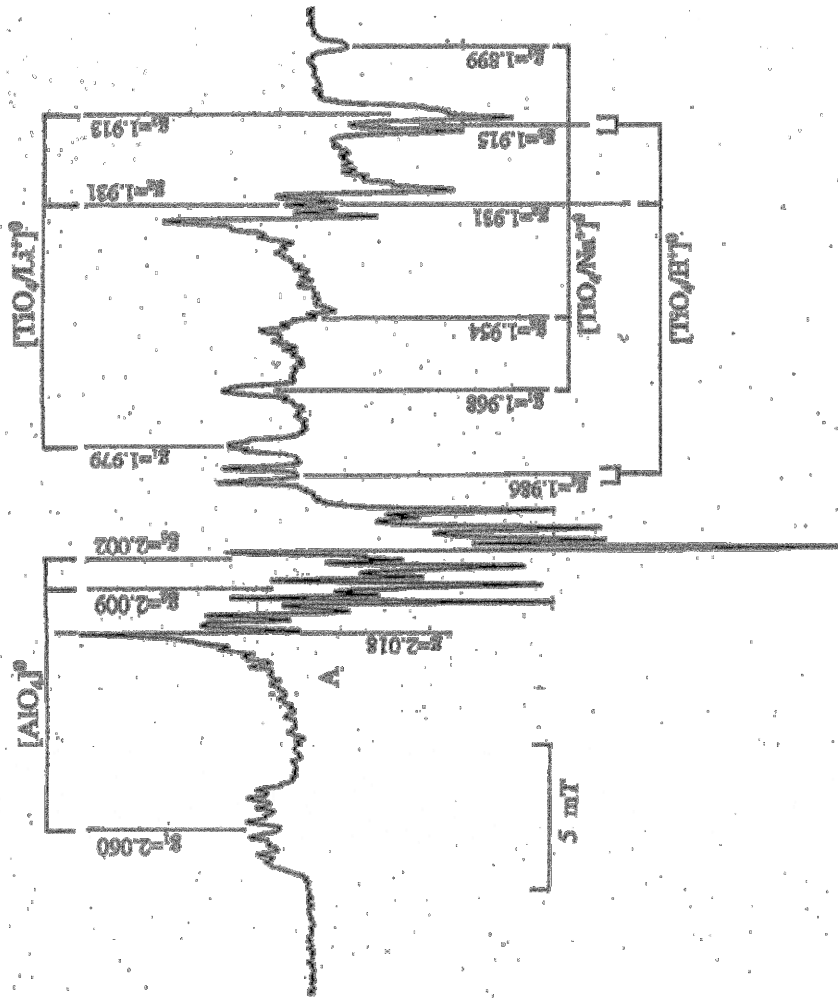


Figure 14: Ideal quartz ESR spectrum taken at 77K showing both the Al defect signals as well as the Ti-Li, Ti-H, and Ti-Na signals and their associated g values. Note the hyperfine splitting within the Al signal and the overlap between the Ti-Li and Ti-H signals in many locations. Modified from Toyoda et.al. (2000).

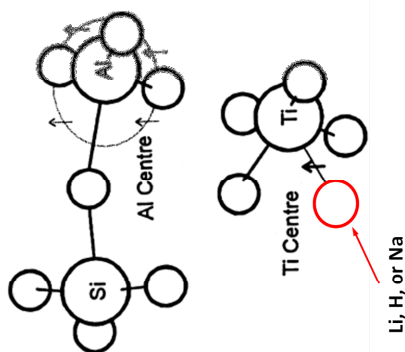


Figure 13: ESR defect sites in quartz of interest in this research. Note that the Ti replacement of Si attracts an alkali element (shown in red): Li, H, or Na. The nature of the alkali element associated with the Ti replacement gives rise to multiple Ti ESR signals each associated with a particular alkali element. Modified from Rink (1997).

The Al quartz ESR signal arises from the replacement of Al for Si in the quartz crystal that when irradiated results in an electron trapped hole (Rink, 1997) (Figure 13). Due to the interactions of the electron's spin at the Al site with the nuclear spin of ^{27}Al the Zeeman split described in section 1.5.2 is complicated resulting in numerous peaks (known as 'hyperfine splitting' (Henning and Grün, 1983; Ikea, 1993; Blackwell, 1995; Jonas, 1997)) at a range of g values for this defect (Figure 14). The Al signal is unable to be fully bleached by sunlight (ie. sunlight cannot reduce the signal to zero intensity) but signal intensity will be reduced to a residual level of between 40-60% of the initial (natural) signal with approximately 100 days of sun exposure (Walther and Zilles, 1994; Yoshida, 1996; Rink et al., 2007). As a result of this the residual "unbleachable" portion of the Al signal must be measured and removed to yield an accurate paleodose in a sample that had been bleached to a residual level in nature. Like the Ti signal the Al center is measured at low temperature (Grün, 1989; Ikea, 1993) but unlike Ti the Al signal does not saturate at doses higher than 10,000 Gy (Duval and Guilarte, 2014).

Yoshida (1996) describes another light sensitive defect in quartz that can be found at a g value of 1.9162. This signal is bleached fully within 20 hours exposure to sun light and saturates around 1000 Gy (Yoshida, 1996; Rink, 1997) (Figure 15). Yoshida showed that this ESR signal yielded ages that were in agreement with independent chronology established by ^{14}C , OSL, and TL while the Al and Ti signal ages significantly over estimated independent chronology. This signal is studied by Tissoux et al. (2007) and described it as one of the Ti-H signals at $g = 1.917$. In this work it is shown that this signal is completely bleached in half the time required of the Ti-Li signal. Like the above Ti and Al signal, this signal is measured at low temperature.

In the case of quartz optical ESR dating, the paleodose received, known as the equivalent dose (D_E), is determined using the additive dose method. The sample is split into numerous aliquots; one aliquot is retained as the "natural" (containing the dose experienced since the bleaching event) and at least one other used to determine the unbleachable portion of the ESR signal (in the case of the Al signal). The remaining aliquots are exposed to known radioactive doses, each greater than the previous, so that

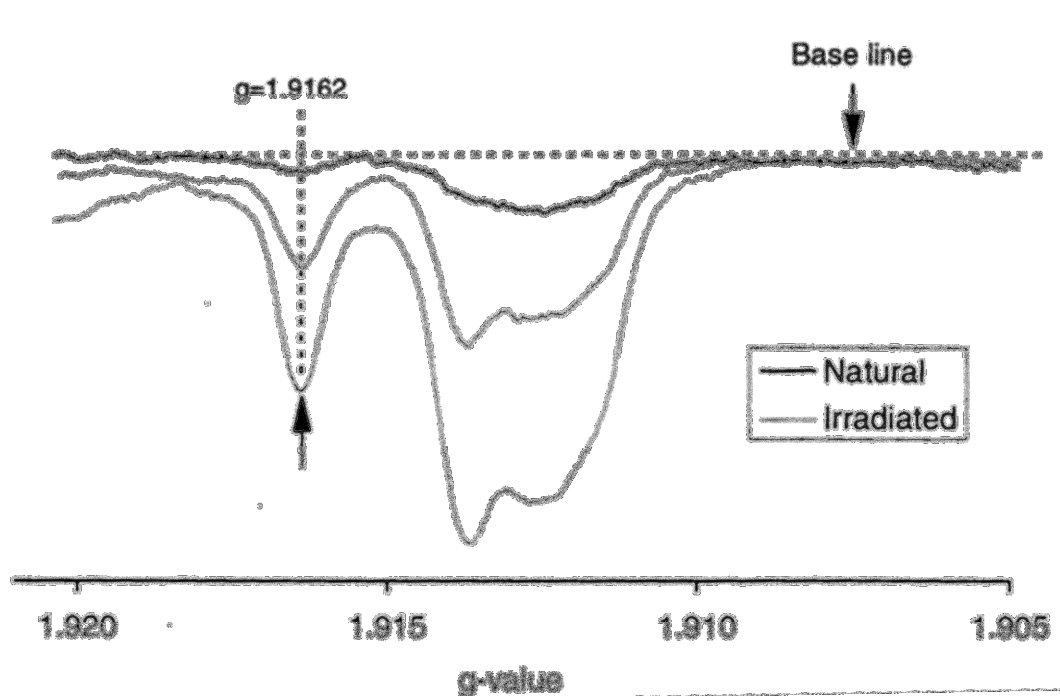


Figure 15: A schematic of an ESR microwave absorption spectrum of the light sensitive signal described by Yoshida (1996), shown at a g value of 1.9162. Note the signals proximity to the Ti-Li signals. From Yoshida (1996).

the total dose recorded by the aliquot is the “natural” + given known dose. The ESR signal intensity of all aliquots is measured and a curve is used to extrapolate the intensity of the signal to zero dose. The position of this point on the x-axis of a graph yields the D_E of the sample (Henning and Grün, 1983) (Figure 16).

Generally these data points do not fit a linear regression so a nonlinear fit is needed (Grün and MacDonald, 1989). A Single Saturating Exponential (SSE) curve defined by (equation 5a) is generally used to fit quartz ESR:

$$(eq. 5a) \quad I = I_{max} * (1 - e^{-(D/D_0)})$$

I is the ESR signal intensity (in arbitrary units), I_{max} is the maximum intensity the ESR signal approaches, D is the dose in Gy, and D_0 is the characteristic saturation dose (Gy) describing the dose at which ESR signal intensity is equal to (equation 5b):

$$(eq. 5b) \quad I = (1 - (1/e)) * I_{max}$$

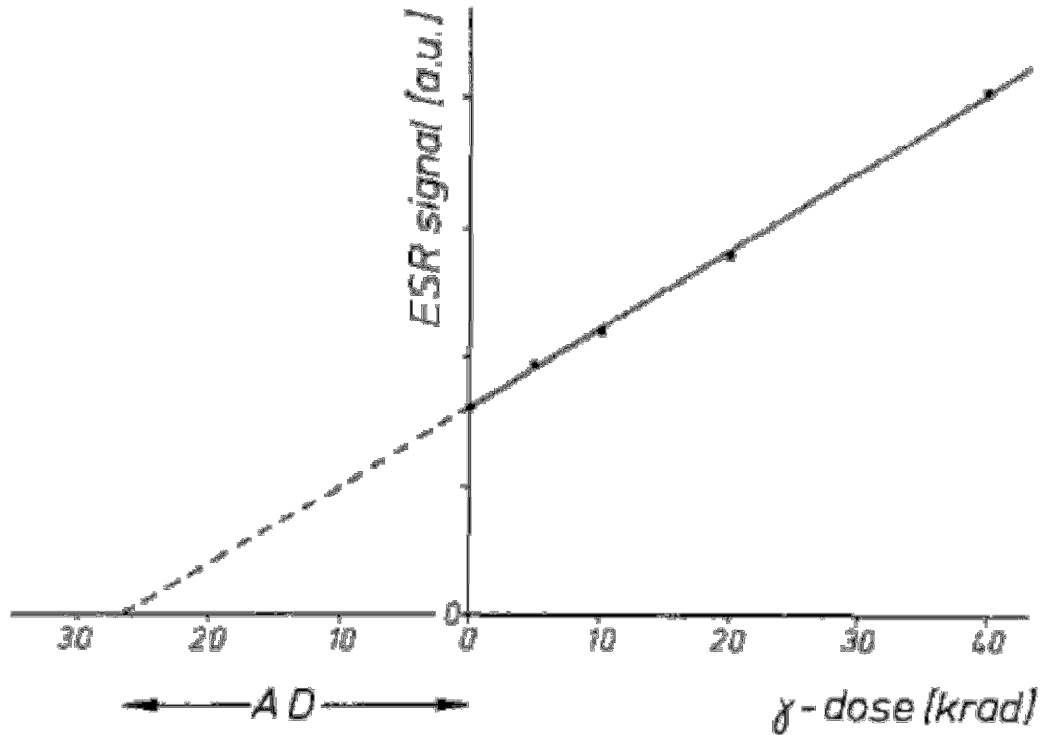


Figure 16: Determining the paleodose of the ESR signal through back extrapolation. The intersection of the fitted curve with the x-axis corresponds the paleodose. From Henning and Grün (1983).

The D_0 value is equal to the dose at which the ESR signal intensity is at approximately 60% of the saturation (I_{max}) value (Rink et.al., 2007). While other types of curves have been suggested, the SSE curve seems to approximate the behavior of both the quartz ESR signal at least up to 10,000 Gy (Duval and Guilarte, 2014).

To determine an age of the sample the D_E is divided by the annual radioactive dose rate (D_r) the sample receives (equation 6);

$$(eq. 6) \quad \text{Age} = D_E / D_r$$

The D_r of a sample is calculated using the concentrations of radioisotopes (generally, U, Th, and K) within and surrounding the sample, by directly measuring the radiation flux of the environment surrounding the sample, or a combination of both (Grün, 1989; Blackwell, 1995). In addition to the radioisotopes, the radioactive dose

contributed by cosmic rays is calculated as well as the shielding effect caused by water in the sediments. Both of these factors contribute to the total dose rate (Grün, 1989).

While an individual ESR signal can provide an age for a sediment, it has been suggested by Toyoda et.al (2000) and Rink et.al. (2007) that a “multiple center method” (Tissoux et.al., 2008) be used to counteract the effects of incomplete bleaching of the ESR signals and provide a robust age estimate of the sample. If the D_E derived from two separate signals (with different bleachabilities) are approximately equivalent then the age is considered robust. Toyoda et.al (2000) suggests using the D_E estimates from two Ti signals, Ti-Li and Ti-H, to provide a robust age. Rink et.al. (2007), Tissoux et.al. (2007) and Duval et.al. (2015) suggest the use of the Al center signal and the Ti-Li signal to insure an accurate estimate of the D_E .

1.5.4 Quartz ESR-OD of Coastal Deposits

ESR has been used as a geochronological method in coastal environments in many studies. This is due to the wide variety of materials that can be dated with ESR (coral, shells, etc.) that can also be found within this environment. The reader is referred to Blackwell (1995) and Rink (1997) for a list of materials and example of these studies. This project focuses on the use of quartz ESR within the coastal environment.

Tanaka et.al. (1997) used ESR, Thermoluminescence (TL), and OSL to date a number of marine terraces in Japan with independent age control provided by tephra. While the TL and OSL agreed with the tephra ages the Ti-Li signal of the ESR measurement resulted in a large age overestimate. While there was agreement of the ESR signal with the OSL and TL within a 1σ error, the D_E error was approximately 60% of the D_E value. It was concluded that the Ti-Li signal was not fully bleached prior to deposition.

Tissoux et.al. (2008) attempted to date marine terraces using ESR of quartz. It was found that Ti-Li signal D_E was larger (more than 50% larger) than the D_E obtained from the Al signal and the Ti-H signal. The Ti-H signal, though yielding larger D_E errors, showed agreement with the Al signal and better agreement to the expected age

than the Ti-Li signal. A series of bleaching tests showed that the Ti-Li signal was not bleached fully by UVA (315-400 nm) light alone and needs a full spectrum of sunlight to be bleached. The Al signal on the other hand can be bleached by just UVA light. They conclude that the Ti-Li signal was not completely bleached due to its deposition in water and suggest using the Ti-H and Al signal in these cases.

Burdette et.al. (2012) used quartz ESR to date ancient shoreline deposits of Florida. Following the methodology of Rink et.al., (2007) the Ti-Li and Al signals were used to determine the ages of the Trail Ridge, Effingham, and Chatham sequences (see section 1.2). 85% of the samples dated yield agreement between the Ti and Al signals with D_E errors between 15-25%. A study of modern beach sands was done to determine if the Ti-Li signal was bleached during its deposition. The results indicate that modern Florida beach sands show no Ti-Li signal indicating that the Ti-Li signals along Florida shorelines can be fully bleached at deposition.

1.6 Optically Stimulated Luminescence Dating

1.6.1 Introduction to Optically Stimulated Luminescence

Optically Stimulated Luminescence (OSL) dating is very similar to ESR in that both methods involve signals that are proportional to the number of electrons within defects in a crystal structure which were trapped there due to the effects of ionizing radiation from the surrounding environment. OSL generally makes use of quartz and feldspar minerals ability to release these stored electrons when exposed to light. This exposure to light becomes the bleaching event and restarts the geochronometer. Once the minerals have been buried ionizing radiation can again energize electrons and electrons begin to accumulate in traps (Murray and Olley, 2002; Preusser et.al, 2008; Preusser et.al., 2009; Duller; 2015). As quartz is the most common mineral in earth's sedimentary deposits this technique has been applied to a number of geological and anthropological applications within the Quaternary (Preusser et.al., 2009). The following sections are a brief review of OSL physics and commonly used methods. Extensive review on OSL

and its application can be found in Duller (2008), Preusser et.al. (2009), and Rink and Thompson (2015).

1.6.2 Theory

1.6.2.1 OSL Theory

The most accepted model of the creation of the luminescence in OSL is known as the “energy band model” (Preusser et.al., 2009) (Figure 17). It states that when the mineral (quartz in this case) is exposed to ionizing radiation electrons are energized and escape the valance band energies and travel through the crystal at conduction band energies. Most electrons will return to the valance band releasing their energy as photons, but a few will become trapped in energy levels between the valance and conduction band. These traps are formed by defects within the crystal structure. The

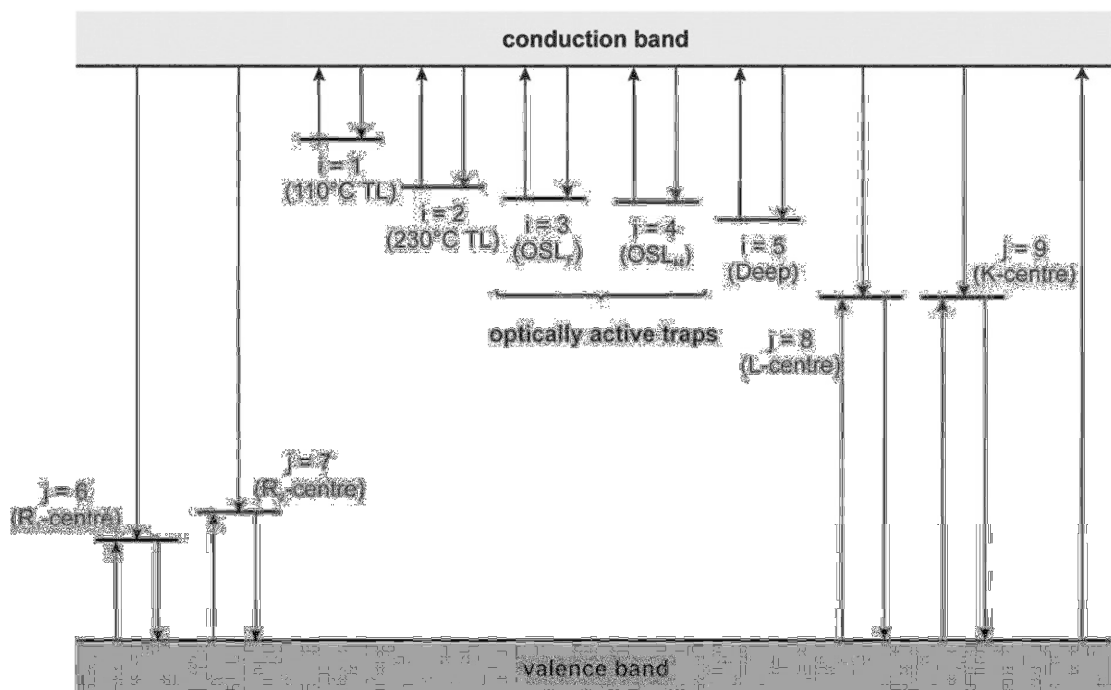


Figure 17: The energy band model of the source of the OSL signal. Electrons trapped in the optically active centers can be stimulated by light. Recombination of the electron with radiative holes (L-centre) can lead to the emission of a photon. From Preusser et.al. (2009).

trapped electrons leave holes in the valance band energy level. When these holes occur at negatively charge crystal defects within the crystal structure they create a condition that is attractive to free electrons. These negatively charged defect holes are known as recombination centers. When the mineral is exposed to light the electrons trapped in between the valance and conduction band can escape their traps and travel through the crystal. They are attracted to the recombination centers where they release their energy either radiatively in the form of a single photon or non-radiatively (Preusser et.al., 2009). The photons released from the luminescent recombination centers are those measured during OSL dating. OSL measurements cannot be repeated on a sample as the light exposure used to measure the signal also bleaches the quartz destroying the natural OSL signal.

Just like in ESR, OSL uses the comparison between the luminescence intensity of known radiation doses to those found in the naturally derived signal to determine the equivalent dose or D_E . The Single Aliquot Regenerative-dose (SAR) procedure developed by Murray and Wintle (2000, 2003) is used to construct the dose response curve in OSL (Figure 18). In the protocol each sample is subdivided into a number of aliquots (usually 48). The natural luminescence signal of each aliquot is measured completely bleaching the sample as well. The aliquots are then given a small known dose of radiation, known as the test dose, and the luminescence responses measured. The aliquots are then given a larger known dose of radiation call a regeneration dose. The OSL signal is measured and the test dose procedure is repeated. The aliquots are given a number of successively larger regeneration doses (each followed by the same test dose). The signal intensity of the natural and the regeneration doses (L_x) is divided by the intensity of their respective test doses (T_x) to correct for any changes in the minerals sensitivity to laboratory radiation doses that could occur throughout the SAR procedure. A single saturating exponential (SSE) is often fitted to the dose intensity (L_x/T_x) to create a dose response curve (Preusser et.al., 2009). The natural signal D_E is then interpolated from the curve (Figure 18). An age is then calculated using the D_E divided by the dose rate of the surrounding material (see section 1.5.3 and equation 6).

As in ESR there are a finite number of traps for the electrons to fill within an ionizing environment. A quartz grain whose traps have been completely filled is said to be saturated. When saturation occurs the mineral no longer acts as a geochronometer giving an upper limit to the ages that OSL can be used effectively. This generally occurs with quartz after exposure to between 100-200 Gy of radiation (Duller, 2015). The D_0 value calculated in the building of the SSE dose response curve (equation 6) can be used to estimate the saturation dose. Saturation occurs at a dose of $2 * D_0$ (Wintle and Murray, 2006; Duller, 2015). Typical D_0 values found in quartz are between 50-100 Gy (Wintle and Murray, 2006). By dividing the saturation dose ($2 * D_0$) by the dose rate of a sample the hypothetical maximum possible OSL age of the sample can be found.

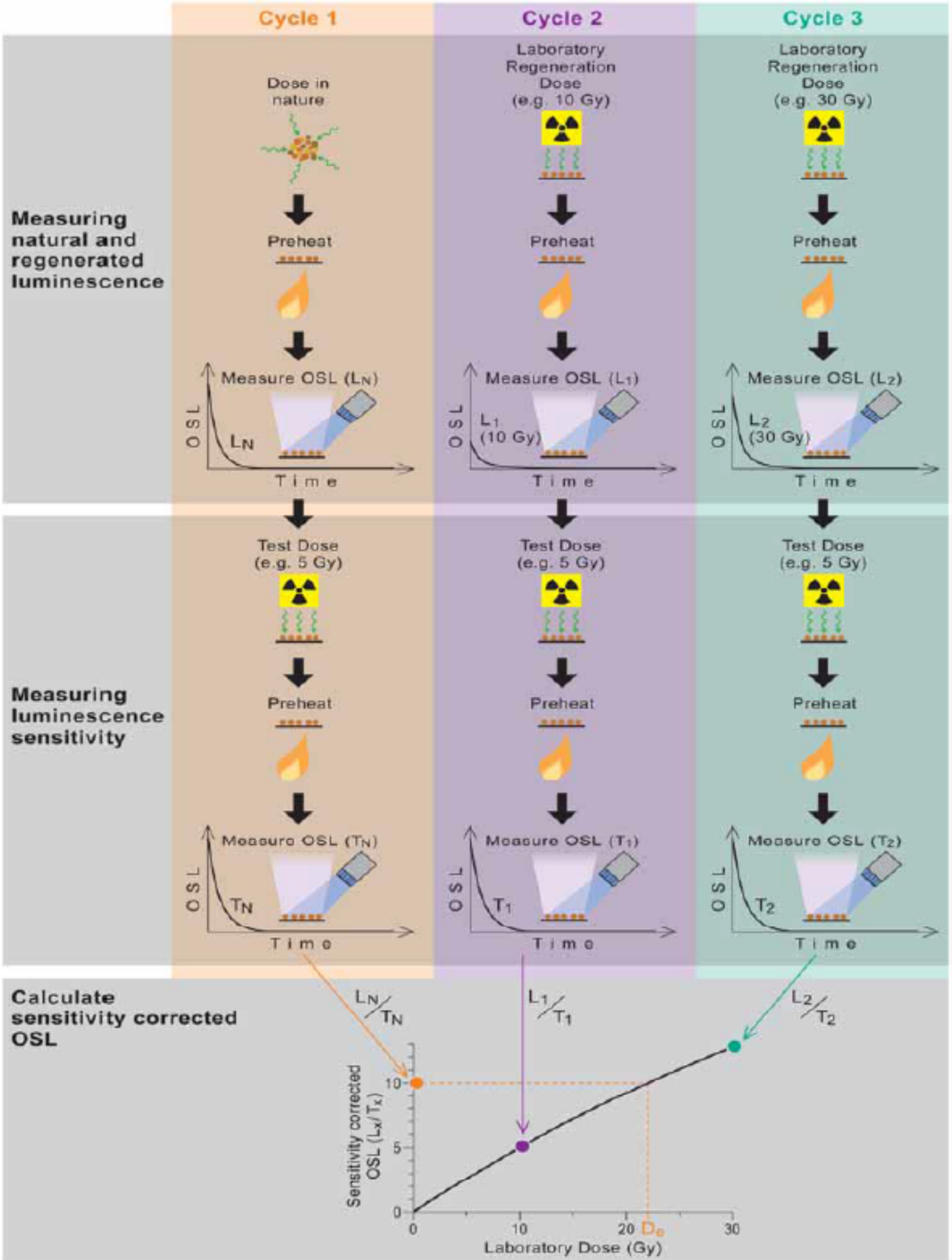


Figure 18: The Single Aliquot Regeneration method of OSL measurement. The lower portion of the figure depicts the creation of the dose response curve from the test dose normalized luminescence intensity. From Duller (2008).

1.6.2.2 TT-OSL Theory

Aitken and Smith (1988) noted that the OSL signal of bleached samples “recovers” after exposure to heat or long storage time. Wang et.al. (2006) first used this thermal transfer in an effort to extend the range of OSL. Since that time a number of researchers (Wang et.al., 2007; Porat et.al., 2009; Stevens et.al., 2009) have modified and improved the protocols of TT-OSL.

The TT-OSL signal is measured after the OSL signal has been bleached by optical stimulation within the laboratory. The origin of the TT-OSL signal is still unknown at this time but two hypotheses have been proposed. The first postulates that during the OSL bleach stored electrons are released, some recombine at luminescence centers (giving rise to the OSL signal) while others are stored in “refuge traps (Aitken, 1988)” (Adamiec et.al, 2010). Heat then transfer these electrons from the refuge traps in to the now empty optically active traps allowing for a second stimulation and release of electrons. The second hypothesis is that the heating transfers charge from optically insensitive traps in to the OSL traps (Adamiec et.al., 2010). Based on the work of Adamiec et.al (2008) and Pagonis et.al. (2008) the second hypothesis is favored as the TT-OSL transfer method (Adamiec etl.al., 2010).

TT-OSL is a new luminescence dating technique but has shown the potential to determine the age of quartz as old as the Plio-Pleistocene boundary. Do values of TT-OSL dose response curves routinely reach in to the 100-10000 Gy. The TT-OSL ages presented in this research are the first to be applied to the coastal deposits of Georgia and to be directly compared to quartz ESROD.

1.6.3 Previous Works in the Georgia Coastal Setting

OSL has been used with success in Georgia in both fluvial dunes (Leigh et.al., 2004) and coastal environments (Markewich et.a., 2013; Turak and Alexander, 2014; Alexander et.al., unpublished data). Markewich et.al. (2013) was able to use OSL to recover doses up to 170 Gy with saturation of the quartz occurring between 175-320 Gy. They used these ages to determine the age of the Wicomico, Penholoway, Talbot,

Pamlico, and Princess Anne deposits as well as a number of younger coastal deposits in along the northern coast of Georgia. OSL has also been used on South Carolina coastal deposits (Willis, 2006) as well as in Florida (Burdette et.al., 2010, Burdette et.al., 2012). Burdette et.al. (2012) found all of the OSL signals measured within the Trail Ridge, Effingham, and Chatham sequences in Florida to be saturated at a value close to 200 Gy and unusable for that particular study. Burdette et.al.'s 2010 work on Merritt Island, Florida recovered OSL doses ranging from 5-60 Gy. Willis (2006) recovered OSL doses ranging from approximately 120-160 Gy for a sequence of sample representing the Talbot through Princess Anne deposits in South Carolina.

Chapter Two: Methodology

2.1 Locations of GPR Transects and Cores

This study was focus on the southern portion of the Georgia coast USA. The study region contains the Princess Ann, Pamlico, Talbot, Penholoway, Wicomico, and Okefenokee ACDs in close proximity to one another. Figure 19 shows the study area and locations of the GPR profiles, core locations, and the location of the ACDs as mapped by Rhea (1986) (Table A1-T1 provides the latitude and longitude of the sample locations).

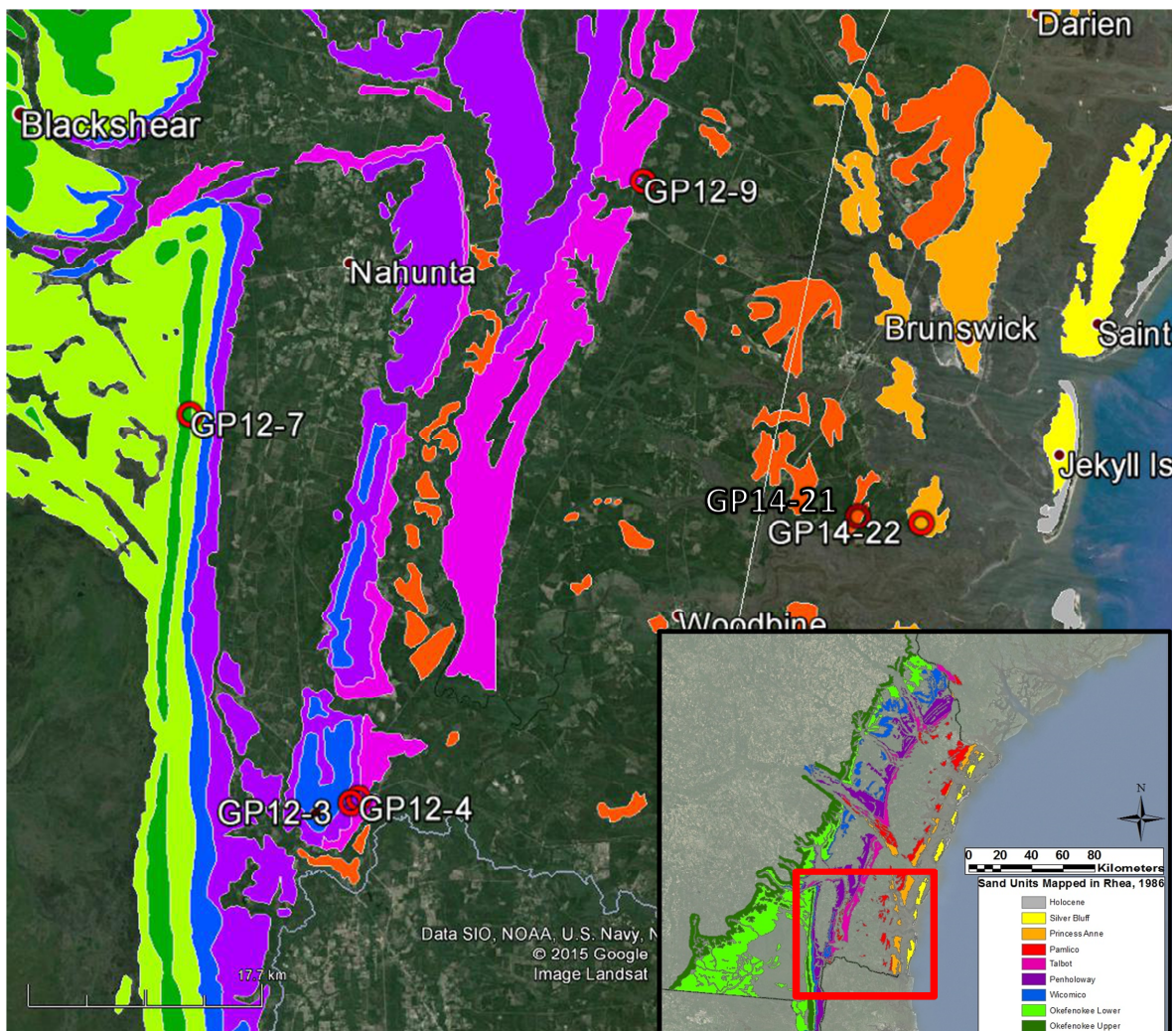


Figure 19: South Georgia coastline showing the locations of the core sample locations (red circles). The GPR Figures in Chapter 3 are sections of the total lines centered around the core locations.

2.2 GPR Methodology

2.2.1 GPR Survey Methods

The GPR surveys were conducted using a Geophysical Survey Systems Inc. (GSSI) SIRS 2000 200 MHz ground-penetrating radar system (Figure 20). One of the systems is owned by East Carolina University and operated with the supervision of Dr. David Mallinson (GPR collected in 2012) the other is owned by Murray State University and was operated with the supervision of Dr. Amanda Keen-Zebert (2013 GPR surveys). The 200 MHz GPR frequency provided penetration of up to 20 meters in sandy coastal deposits and a decimetric vertical resolution. The 200 MHz antenna was towed at a distance of 4 m behind a truck at a speed of 4-6 km/hr. One field member drove the truck and the other operated the GPR system (Figure 20). The GPR system was set to collect data at 16 bits/sample, 512 samples/scan and 20 scans/meter. In line positioning was provided with the GPR odometer wheel.

2.2.2 GPR Collection

A total of 43 line km of GPR profiles were acquired on paved or dirt roads. This allowed easy access for the vehicle as well as providing a very flat, smooth, and stable surface for the GPR antenna. Each GPR profile was split into a number of lines approximately 1km long. GPS was used to locate the start and end points of the individual GPR lines and to locate waypoints along the survey path. These points were verified using Google Earth imagery in the field via cellular internet access. Figure 20 shows the typical GPR survey set up and equipment.



Figure 20: Set up of the GPR survey with a truck pulling the GPR unit behind it.

2.2.3 GPR Processing and Interpretation

GPR data were processed using RadExplorer 1.41. Raw GSSI files underwent 10 processing steps that included DC and background removal, bandpass filtering and amplitude correction. Radar profiles were depth converted using an average radar velocity of 11cm ns^{-1} determined by analysis of hyperbolic reflections throughout the GPR profiles. The resulting processed lines were then corrected for topography using elevation information from Google Earth.

Processed GPR profiles were then interpreted and radar facies identified based on radar reflection patterns and attributes (Neal, 2004). Radar facies were determined based on the reflector dip (both direction and magnitude), shape, continuity, strength (amplitude), and the relationship of the reflection to those around it. Radar facies were

then used in conjunction with core lithofacies and the deposit context (i.e. landform-sediment assemblages) to interpret the depositional environments (see section 2.3).

2.3 Coring and Sediment Analysis

2.3.1 Coring Strategy

Sites for sediment coring were targeted using the GPR survey results. Sandy deposits identified in radargrams were selected for coring and targeted for age dating. Strong reflections that would indicate coarse (sand) material and the absence of mud or clay were targeted. As sand size material is need for the dating processes there was a need to collect this specific lithology. Also targeted were locations with numerous radar facies as this would allow for many features to be dated.

While there were many locations that had the above required GPR features the ultimate location for sampling resulted from a combination of GPR targeting and site access. As the GPR was conducted on roads the coring process had to be mindful of utilities and infrastructure in close proximity.

2.3.2 Core Collection

The cores were collected using a direct push Geoprobe rig owned and operated by East Carolina University. The probe used 1.22 m coring sections and barrel. Two cores were collected from each of the locations (refer to Figure 19). The first core used standard clear plastic core liners within the core barrel. These samples were used to construct the lithologic logs of the stratigraphy. The second core was drilled adjacent to the location of the clear liner core (between 15 and 20 cm away) and used a black opaque core liners (Figure 21). The sediments from the black core liners were used for the OSL and ESROD dating.



Figure 21: Core liners used to collect the core for lithologic logging (clear) and geochronology (opaque black).

2.3.3 Core Logging

All of the cores were shipped to McMaster University for analysis. Each of the 120 cm sections was split and visually logged on a standard core log. Logging consisted of observations on mineral content, grain size, sorting, color, other materials present (charcoal or other organic matter), and condition of the grains. Samples from each lithologic unit identified in the cores were studied under a microscope and the sediment composition and grain size characteristics (average grain diameter, sorting, roundness) determined. The results of each of the individual 1.22 m cores were then compiled into a total composite core section for each site. The composite cores were then compared to the GPR radargram.

2.4 ESR dating

2.4.1 Sample Targeting

Sediment to be used in the ESR dating was selected using the sedimentary core log and GPR radargrams. The GPR profiles were consulted first and radar facies of interest, representing interpreted coastal deposition, were considered as potential candidates for dating. After radar facies of interest were selected the lithologic core was examined in the region of the above mentioned facies. Lithological units closest to the boundaries of the radar facies were targeted to provide an age for the beginning/end of that facies deposition. Sediment from the clear core was also analyzed to insure that the potential horizon had desirable properties for dating (primarily the desired grain size and type). Samples were selected from core segment locations that contained sand, lacked high heavy mineral concentrations, and that were homogenous over distances of 30 cm above and below the chosen core segment. This was done to best approximate from core an homogeneous 30 cm sphere from which the core segments' gamma dose came from. See Appendix 2 Figures A2-F1 through A2-F6 for sample collection location within each of the cores.

2.4.2 Sample Prep Methodology

The black cores were taken to the dark room at the AGE Lab at McMaster University in Hamilton, Ontario. Here they were opened under low intensity orange light that does not bleach ESR or OSL signals in the samples. The sand used for the ESR sample was then removed from a volume along the central axis of the core tube, weighed and placed in a drying oven (approx. 60° C). Over the course of a week the samples were re-weighed until their weight stabilized indicating that all of the moisture had been removed (this data is used later to determine the moisture content of the sample for dose rate estimation). A representative fraction of the dried samples was then removed for measurement by Neutron Activation Analysis (NAA) to determine the concentration of uranium, thorium, and potassium in the sample's surroundings.

All of the samples were then treated with 10% Hydrochloric acid (HCl) overnight to remove all carbonate minerals. Any sample that still appeared to be reacting after 24 hours was re-treated with fresh HCl for another 24 hours (this process was repeated until all reaction ceased). The samples were rinsed with de-ionized water and subsequently treated with 30% Hydrogen peroxide (H_2O_2) for 24 hours. This was repeated for any sample that appeared to be reacting after 24 hours. The samples were then rinsed with de-ionized water, dried and weighed.

After weighing, the samples were sieved with 212 μm , 150 μm , and 90 μm nylon meshes. Each of these size fractions ($>212 \mu\text{m}$, 212-150 μm , 150-90 μm , and $<90 \mu\text{m}$) were then weighed. The size fraction that contained the most material across all the samples was chosen to undergo the quartz isolation process (excluding the $>212 \mu\text{m}$ size fraction).

The selected size fraction for each of the samples was added to ~10mL of Lithium Polytungstate heavy liquid with a specific gravity of 2.70 g/mL and mixed thoroughly in 15 mL conical Falcon tubes. After 20 minutes, the quartz floats to the top of the tube while heavy minerals sink to the bottom. Liquid nitrogen was then used to freeze the bottom portion of the tube (trapping the heavy minerals) and the quartz at the top was subsequently poured off (Mahan, personal communications). Both the quartz fraction and the heavy mineral fraction were dried and weighed.

The quartz samples were treated in 40% Hydrofluoric acid (HF) for 40 minutes. This process dissolves any remaining feldspars and etches the quartz grain (needed to remove the part of the grain that received external alpha radiation doses). Samples were then rinsed four times with de-ionized water and treated for 15 minutes in 10% HCl to remove any fluorides that may have precipitated. The samples were rinsed for a final time with de-ionized water and then dried and weighed.

ESR dating uses the multiple aliquot additive dose method (MAA) to determine the equivalent dose of the sample (see section 1.5.3). The resulting quartz for each sample was then split into 19 0.100 ± 0.01 g aliquots for dosing. One aliquot of the 19

was used as the “natural” receiving no additional dose, and other was used for the Al bleaching experiment (see below).

The remaining aliquots were given a dose of radiation on top of their inherited natural signal (ie. an “added dose”) in the McMaster University Nuclear Reactor’s Gamma Hot Cell or at a facility in Japan with the help of the Okayama University of Science Department of Applied Physics. The McMaster Hot Cell makes use of a ^{60}Co source to provide gamma radiation at very high dose rates (up to 1000+ Gy/hour). The aliquots were placed in 6x50 mm borosilicate disposable culture tubes and then wrapped in a monolayer of aluminum foil to provide protection from light. These tubes were then placed in the hot cell in a semicircle of uniform distance from the radiation source to insure uniform doses to all the samples. Two dose fields were established, one at 250 Gy/h and the other at 1000 Gy/h. Samples were rotated through these fields to achieve a desired total additive dose. The additive doses ranged from +250 Gy to +6500 Gy for samples dosed at McMaster and +200 Gy to +10000 Gy for those dosed at Osaka University. The dose received during the raising and lowering of the ^{60}Co source was accounted for as well and added to the total dose received to the aliquots. A similar experimental set up was used in Japan.

The aliquot to be used for the Al bleaching experiment was placed in a monolayer in a small glass dish in a Dr. Honle SOL 2 solar simulator. This device exposes the sample to high intensity filtered UV light, which simulates daylight exposure. Exposure for one hour within the simulator is equal to approximately 7 hours of natural light. Following the procedure of Voinchet et.al. (2003) for Al bleaching the samples were left in the simulator for 800 hours to insure complete bleaching of the Al signal to its minimum. A new bulb was used for every bleaching cycle to insure constant power of the bulb.

2.4.3 ESR Spectrometry

Measurements on the sample from the lower ACDs (Princess Anne and Pamlico ACDs, as well as a sample from the Talbot and Penholoway each) were measured with

Florida State University's (FSU) Bruker ELEXSYS spectrometer, while the upper ACDs (Talbot, Penholoway, Wicomico, and Okefenokee, as well as the upper most Pamlico and Princess Anne) were measured at Osaka University (Japan) on a JEOL Re-1X spectrometer, both fitted with a X-band microwave source.

In both cases measurements were conducted at liquid nitrogen temperature, 77°K through the use of a fused quartz dewar attached to the ESR sample cavity (all FSU and approximately half of the Osaka University samples were measured in this fashion). In addition a number of samples measured at Osaka University were measured using a nitrogen gas system at 83° K. Measurements were conducted at a power of 5 mW with a modulation frequency of 100 kHz, time constants of 1.28 mT/min (FSU) and 0.03 mT/min (Osaka) and modulation amplitudes of 1.6 mT. At FSU measurement time was 4 minutes and both the AL and Ti portions of the signal we measured using the same conditions, in the same measurement run. Samples measured at Osaka measured the AL and Ti signals separately changing the gain respectively. In addition samples measures at Osaka University underwent 5 rotation measurements (of 60°) to ensure signal homogeneity due to grain ordinations variations. Table A1-T2 in Appendix 1 provides that details of the measurement conditions at both FSU and Osaka University.

For all samples the bleached aliquot was measured first, followed by the natural, and then lowest additive dose aliquot followed by the next highest dose and so forth. This was done to prevent contamination of the low dose aliquots with any high dose quartz grains that may have not been removed completely from the ESR measurement tube.

2.4.4 Signal Processing

ESR spectra were imported in to Origins 8.1 to measure peak to peak intensities. The AL signal was measured from the first to the last (16th) peak (Lin et.al, 2006). The Ti-Li signal was measured using two methods described in Duval and Guilarte (2014). The first method, known as option A in Duval and Guilarte (2014) as well as in this work, is measured from the Ti-Li peak at $g=1.979$ to the peak at $g=1.913$. The second

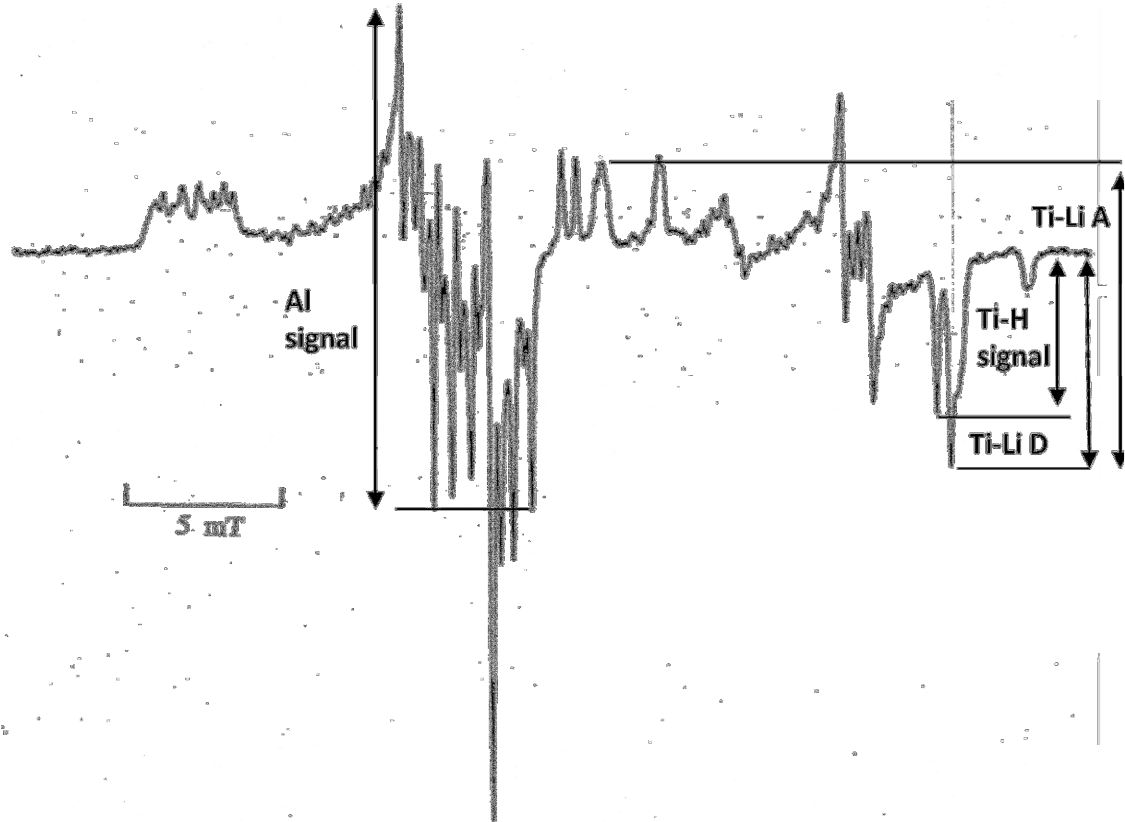


Figure 22: ESR spectrum showing the location of the signals measured in this study. The Al and Ti-H/Yoshida signal are each measured using one method. The Ti-Li is measured using two methods, option A and option D, so named after Duval and Guilarte (2014). Modified from Tissoux et.al. (2008).

method, known as option D, is measured from the $g=1.913$ peak to a baseline (Tissoux et.al, 2008; Duval and Guilarte, 2014). The Yoshida $g=1.9162$ peak (Tissoux et.al. (2007) $g=1.917$ Ti-H peak) was measured from the peak at $g=1.9162$ to the same baseline used to measure the Ti-Li peak (Yoshida, 1986; Tissoux et.al., 2007; Duval and Guilarte, 2014) (Figure 22).

The resulting peak to peak intensities and aliquot given doses were input in to the Origins 8.1 program and plotted as a scatter plot with $1/I^2$ weighing on the signal intensity (Grün and Brumby, 1994). The Al signal was modified by subtracting the signal intensity of the bleached aliquot (see above) from the intensity of the natural and added dose aliquots. This was done to remove the unbleachable component of the Al

signal (see section 1.5.3). Single saturating exponential curves (see equation 5) were fitted to the Al, Ti-Li, and Yoshida $g=1.9162$ signal data to determine a D_e , I_{sat} , and D_0 for the signals and their associated errors. In addition an exponential + linear curve was fitted to the Al signal as suggested by Duval (2012) and the Ti_2 fit of Duval and Guilarte (2014) was fitted to the Ti signal of the samples measured at Osaka University (the FSU samples did not receive a high enough additive dose to make use of this fit).

Modern samples collected from the most seaward modern beach dune as well as the active swash zone on Jekyll Island, Georgia (due east of the many of the samples sites) were also studied. The modern samples were prepared as the ancient ones described above and the natural and bleached ESR signals measured. This was done to determine whether the materials in these coastal environments had the potential to be fully bleached at deposition (Burdette et.al., 2012). The measurements were conducted at 77° K at McMaster University as well as at Osaka University. In these samples only the natural and bleach were measured and no aliquots were dosed.

2.4.5 Dose Rates

The D_E value of the samples signals calculated from the dose response curve as well as the results of the NAA elemental concentration measurements of each sample were imported in to Anatol (Mercier, 1998). Anatol uses the elemental concentrations, grain size information, as well a burial depth (to calculate the cosmic dose component), and moisture content of the sample to calculate a yearly dose rate in μGy . A global systematic error of 5% was incorporated in the dose rate contribution to the age calculation (Appendix 3 Figure A3-F15). The program then divides the D_E by the dose rate to determine the age of the sample's signal (Ti-Li, Al, etc.). Due to the sampling technique (from sediment cores) *in-situ* dose rate measurements could not be obtained. As mentioned in section 2.4.2 samples were selected from homogenous units (with 30 cm of homogenous material above and below them in core) in an effort to reduce uncertainty in dose rate layered over distances smaller than 30 cm away from the ESR sample for dating.

2.4.6 Sample Age Determination

Dose response curves to determine an equivalent dose were considered reliable if the DRC of the signal had an r^2 value (as calculated in Origins) of greater than 0.95. DRC's with r^2 values below 0.95 were considered to be unreliable (Duval et.al., 2013). Excluded from this condition were the Ti-H ESR DRC's, the reason for this will be discussed further in Chapter 4.

Following the procedure of Rink et.al (2007) and Burdette et.al. (2012) samples that showed agreement between the Ti-Li and Al signal were considered well bleached and reliable ages. If the Ti-Li and Al signals were in agreement the ages were analyzed by two methods. The first used by Burdette et.al. (2012) in which the age of the signals and their errors are averaged and the resulting age and error considered the age of the deposit. The second method used is to determine the age range in which the Ti-Li and Al signals overlap. This is done by calculating the maximum and minimum age of each signal based on the error in the age. The oldest minimum age is considered to be the samples minimum age while the youngest maximum age between the two signals is considered the maximum age of the sample. This method has the advantage of displaying the entire age range in which the Ti-Li and Al signal agree and the possible depositional ages assuming complete bleaching.

2.5 OSL Dating

2.5.1 Sample Targeting

Only samples from the lower ACDs were selected to be dated by OSL. As these are potentially the youngest samples it was most likely that they would yield OSL ages while those of the older ACDs would almost certainly be saturated. The same material that was used for the ESR measurements was used for the OSL dating process.

2.5.2 Sample Preparation Methodology

Sample preparation methodology is identical for the OSL and ESR samples (see section 2.4.2). Once the quartz was isolated the sample was separated with half going toward the ESR preparation (see above) and the other half being used for OSL dating.

2.5.3 OSL Equipment and Measurement Conditions

OSL measurements were conducted at McMaster University's AGE Lab. McMaster University AGE Lab runs all of its OSL samples on a RISØ TL-DA-15 automated OSL reader with blue (470 ± 30 nm) LEDs as a light source, a single 6mm Hoya U-340 (280-370 nm) detection window filter and a $^{90}\text{Sr}/^{90}\text{Y}$ Beta radiation source. 1mm aliquot size was selected for all samples. The pure quartz samples were first run in an "initial D_E " measurement to insure that all feldspar minerals were removed and to provide an estimate of their D_E . A dose recovery test (DRT) was then performed to insure that the quartz reacted to radioactive dose in a stable manner. The DRT bleaches the samples natural signal away and replaces it with a known artificial dose which is then measured. This dose recovery is performed under a range of pre-heat temperatures ($160^\circ\text{C} - 260^\circ\text{C}$) to assess pre-heat based sensitivity changes (ie. thermal transfer). The pre-heat temperature that provided a measured dose closest to the given dose for each sample was used for subsequent measurements of the natural signal (Madsen et al., 2005).

The Single Aliquot Regeneration (SAR) protocol was used on 1mm aliquots of all samples to obtain a final D_E determination. A complete explanation of the SAR protocol can be found in Murray and Wintle (2000; 2003) (see section 1.6.2.1). Regeneration doses of 50 Gy, 100 Gy, and 150 Gy were selected with the addition of a 0 Gy dose regeneration point and a replicate 50 Gy regeneration dose at the end of the cycle. A test dose of 25 Gy was used on all samples.

The TT-OSL methodology used in this research is based on Stevens et.al. (2009) which uses the TT-OSL signal response to a test dose to normalize the SAR cycles. A high temperature (280°) blue LED bleach for 400s was applied after both the dose

(including the natural and 0Gy) and the test dose measurements. Regeneration doses of 75 Gy, 175 Gy, 375 Gy, 475 Gy were selected as well as a 0 Gy and a repeated 75 Gy dose. A test dose of 50 Gy was used. A 260° heat was used to induce thermal transfer based on the results of previous TT-OSL works (Wang et.al., 2007; Tsukamoto et.al., 2008; Stevens et.al., 2009; Mercier personal communications, 2015). The TT-OSL was measured on 8 mm aliquots to ensure that signal strength (Table 2).

Prior to the TT-OSL measurements a bleaching test was done on each sample. 3 aliquots were exposed to 7.5, 15, and 22.5 hours of stimulation in a SOL simulator (9 aliquots total from each sample). These exposures correspond to 1, 2, and 3 days, respectfully, of natural sunlight exposure. This was done to determine the length of time needed to bleach the TT-OSL signal to a residual.

Table 2: TT-OSL Sequence

Step	Measurement Cycle	Step Information
1	Dose	Natural and regeneration doses
2	Pre-heat 10 s (260° C)	
3	Blue stimulation at 125° C for 100 s	Empty the OSL traps
4	Pre-heat 10 s (260° C)	Induce thermal transfer
5	Blue stimulation 125° C for 100 s	Measure TT-OSL signal
6	Blue stimulation 260° C for 400 s	Bleach of residual signal
7	Test dose (25 Gy)	
8	Pre-heat 10 s (260° C)	
9	Blue stimulation at 125° C for 100 s	Empty the OSL traps
10	Pre-heat 10 s (260° C)	Induce thermal transfer
11	Blue stimulation 125° C for 100 s	Measure TT-OSL signal
12	Blue stimulation 260° C for 400 s	Bleach of residual signal
13	Return to 1	Sequence repeated for all regeneration doses

2.5.4 Data Analysis

The SAR data from each aliquot of a sample (both OSL and TT-OSL) were then analyzed in the Analyst 4.14.6 program by Duller (2013) to determine a D_E and error (using 100 Monte Carlo repeats) for each aliquot. The initial signal (0-0.4 seconds) consisting of the “fast component” was used for the OSL signal, while the “late background” signal was collected at the end of the measurement time (96-100 seconds) as per Banerjee et al. (2000) (OSL) and Tsukamoto et.al. (2008) (TT-OSL). An exponential fit was applied to all of the samples.

Analyst was also used to calculate the D_0 value of each of the aliquots within a sample for estimation of the saturation dose (see section 1.6.2.1). While not all of the aliquots may provide a D_E (samples could be saturated or bleached) all aliquots that yield acceptable dose recovery curves (ie passes the acceptance criteria) were used to analyze the saturation conditions (Jakob Wallinga, personal communication). The saturation dose of the sample was calculated as two times the average of the D_0 of all the aliquots in the sample.

2.5.5 OSL D_E Models

Each sample's aliquot D_e results were then entered in to the numOSL package for R (Jun, 2014). This package uses criterion from Bailey and Arnold (2006) and Arnold et al. (2007) to determine the best age model to use, Central Age Model (CAM) or Minimum Age Model (MAM) (Galbraith et al., 1999). This is done by analyzing the skewness and kurtosis of the aliquot D_E dose distributions (Bailey and Arnold, 2006; Arnold et.al., 2007). Probability plots of the D_E distributions as well as histograms of the dose equivalents were created using this package. After the most appropriate model was identified by the numOSL package, the sample D_E and its error were calculated using the selected model in the Luminescence package for R (Kreutzer, 2014). In order to obtain the best possible age estimate for a sample, an over-dispersion (σ_b) was introduced into the selected model (CAM or MAM) (Galbraith et al., 1999; Arnold and Roberts, 2009; Cunningham et al., 2011). This value can be measured and calculated using single grain

measurements. In the event that single grain measurements are not available (as was the case for these samples) a σ_b can be estimated using the σ_b of similar depositional environments and a correction for the aliquot size (the number of grains measured in each aliquot, approximately 33 grains per aliquot for the OSL samples, 2090 grains for the TT-OSL in this project) (Cunningham et al., 2011). Furthermore an estimation of the samples over-dispersion can be made using the results of the DRT test (Bateman et.al., 2010; Guhl et.al., 2013). Using both the σ_b results from the DRT and σ_b values published previously a σ_b for the samples was determined. This value was used for all of the samples due to their similar depositional environment and proximity. The σ_b value of 0.10 was used for these samples based on the σ_b values presented in Arnold and Roberts (2009), Anderson et.al. (2006) and Carr et.al. (2007) for material in a coastal environment and the conversion factor of Cunningham et.al. (2011).

2.5.6 Dose Rate

The resulting D_E and error calculated by the Luminescence package was then used to calculate an age for the sample. The D_E as well as the results of the NAA elemental concentration measurements was imported in to Anatol (Mercier, 1998). The same dose rates found in the determination of the age of the ESR samples were used to determine the age of the OSL samples.

The dose rates of the samples were also used with the saturation dose ($2 \cdot D_0$) to determine the maximum OSL age the quartz can reliably record.

Chapter Three: Results

3.1 Results of GPR Survey

GPR data imaged the subsurface to depths of approximately 12 to 20 m, depending on the dielectric properties of the sediments. At some sites the GPR penetration was limited to <3 m due to attenuation by near-surface sediments. Figures 23-27 show the portions of the radargrams of the GPR profiles closest to the core locations. Also shown in these figures is a simplified core log showing general grain size variations within the core. Finer grain materials are shown by the log shifting to the left while coarse grains are depicted by a shift to the right of the log. Radar reflections are generally continuous and medium to high amplitude. Radar facies (after Neale, 2004) of the radargrams can be found in Table 3.

Two types of radar facies were recognized in the shore perpendicular GPR transects. The first facies was defined by west (landward) dipping ($>5^{\circ}$ - 10°) clinoformal reflections (defined as Element A) and the second (defined as Element C) by east (seaward) dipping reflections with a slightly higher dip (5° - 10°) than Element A. Both of these facies are present in the upper and lower ACDs. In addition to the above facies the lower ACDs contain an additional facies of high angle (approx. 20° apparent dip) shoreward-dipping sigmoidal reflectors (Element D). Other radar facies observed include clusters of numerous point reflections (Element B), as well as two facies that obscured other reflections. The first (Element F) consist of highly chaotic reflections, which do not allow for further radar penetration and the second facies (Element E) appears to attenuate the radar but which allow for further penetration.

The Princess Anne GPR radargrams (Figure 23) show the upper portion of the ACD is composed of two element C regions separated by a weak boundary layer. The bottom portion of the radargram is dominated by element A reflections that are obscured by element F reflections.

Figure 24 shows the GPR radargram of the Pamlico ACD. Element C composes the upper portion of the ACD. This overlies another element C region in the east and a

region defined by element D type reflections in the west. The lower portion of the radargram is composed of reflections conforming to element A.

The Talbot ACD radargram (Figure 25) shows three distinct facies. The shallowest is composed of element C type reflections. This unit is nearly completely obscured by element E type reflections. Below this is a region defined by element B type reflections. The lowermost region is composed of element F type reflections obscuring element A reflections.

Figure 26 shows the radargram of the Wicomico and Penholoway ACDs. These ACDs are composed of two element C regions separated by a weak bounding surface. A significant portion of the units reflections are of element F type. These reflections seem to occur in regions (noted on the radargram). Between the Wicomico (left) and Penholoway (right) there appears to be a paleo-channel. This feature is defined by dipping synclinal reflections.

The Okefenokee ACD radargram (Figure 27) is similar to that of the Talbot ACD in that it features three facies. Element C type reflections dominate the upper unit, while element A type reflections compose the unit below. The element A unit is significantly obscured by element E type reflections. The lower most portion of the radargram is composed of element B type reflections.

Table 3: GPR Facies

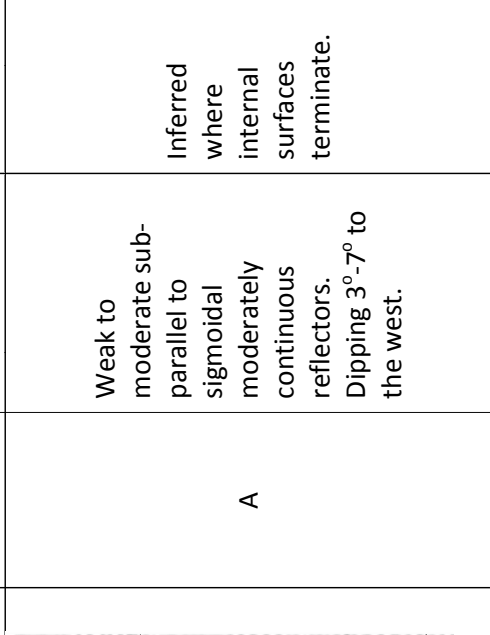
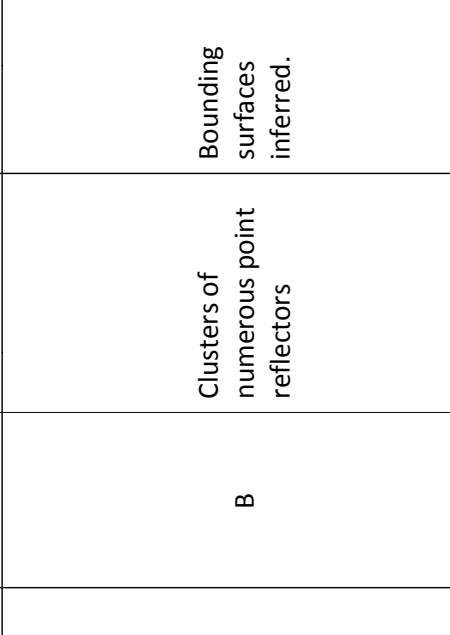
Radar Example	Element	Reflection Pattern	Bounding Surface	Interpretation
	<p style="text-align: center;">A</p>	<p>Weak to moderate sub-parallel to sigmoidal moderately continuous reflectors. Dipping 3°-7° to the west.</p>	<p>Inferred where internal surfaces terminate.</p>	<p>Barrier over-wash deposits</p>
	<p style="text-align: center;">B</p>	<p>Clusters of numerous point reflectors</p>	<p>Bounding surfaces inferred.</p>	<p>Gravelly deposits (possibly Cypresshead or Satilla Fm)</p>

Table 3: GPR Facies

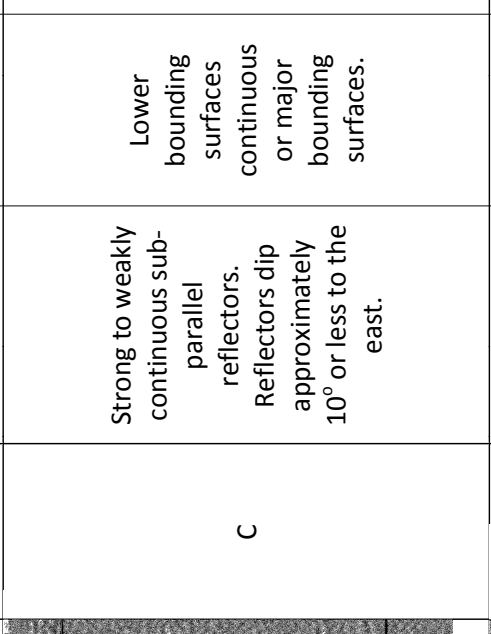
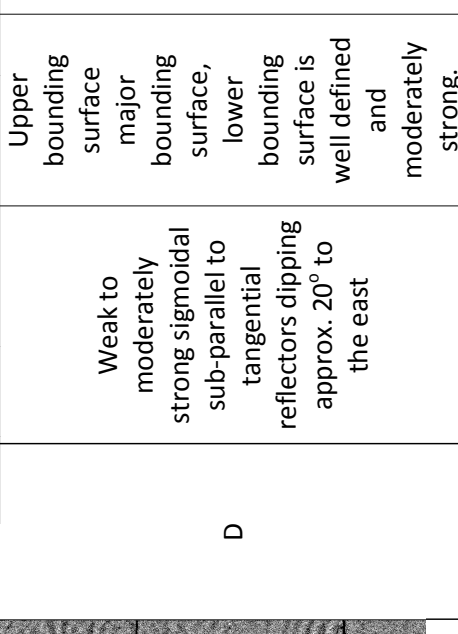
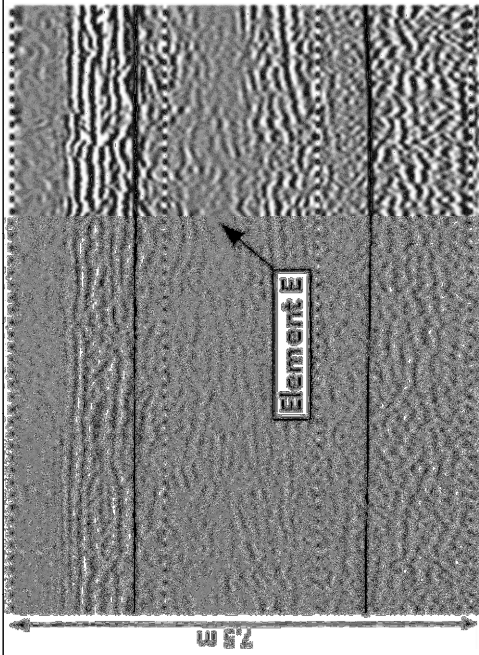
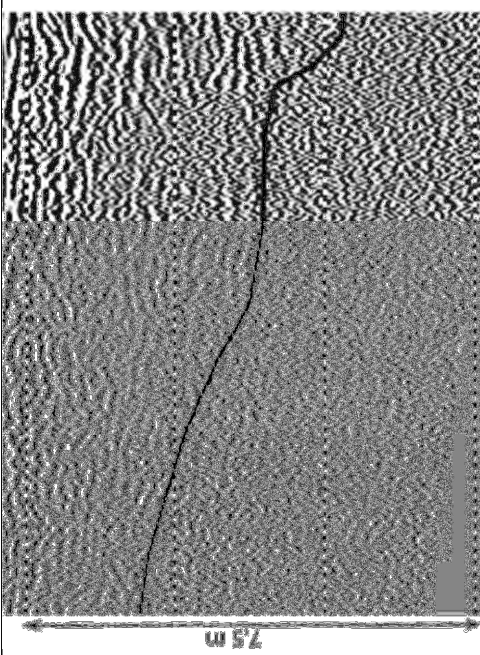
Radar Example	Element	Reflection Pattern	Bounding Surface	Interpretation
	C	<p>Strong to weakly continuous sub-parallel reflectors. Reflectors dip approximately 10° or less to the east.</p>	<p>Lower bounding surfaces continuous or major bounding surfaces.</p>	<p>Barrier progradation beach face.</p>
	D	<p>Weak to moderately strong sigmoidal sub-parallel to tangential reflectors dipping approx. 20° to the east</p>	<p>Upper bounding surface major bounding surface, lower bounding surface is well defined and moderately strong.</p>	<p>Aeolian dunes and associated deposits or beach face.</p>

Table 3: GPR Facies

Radar Example	Element	Reflection Pattern	Bounding Surface	Interpretation
	E	Reflection free. Often obscuring other reflections.	Irregular bounding surfaces.	Humate rich region.
	F	Chaotic weak reflectors. Often appear to be obscuring other reflections.	Irregular bounding surfaces.	Homogeneous sands or clay layers attenuating signal

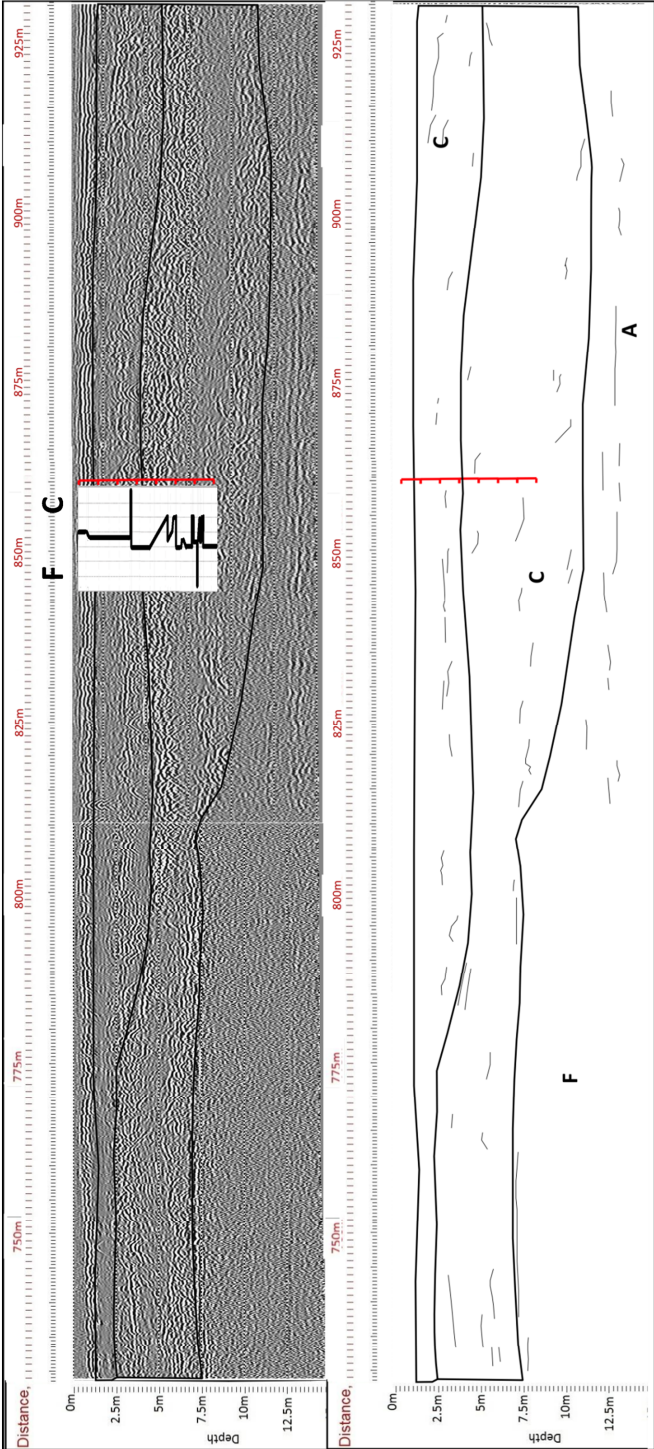


Figure 23: GPR radargram and interpretation of the Princess Anne ACD. The location of the core gp1422 is shown in red with a sketched core log to the left. In the core log coarser lithology is to the right noted by a “C” and finer lithology to the left indicated by a “F”. Two seaward dipping units are separated by a boundary of strong reflections. Below the element C region is a region of eastward dipping element A facies. This unit is interpreted as overwash deposits. Note the region displaying element F where few reflections are resolved.

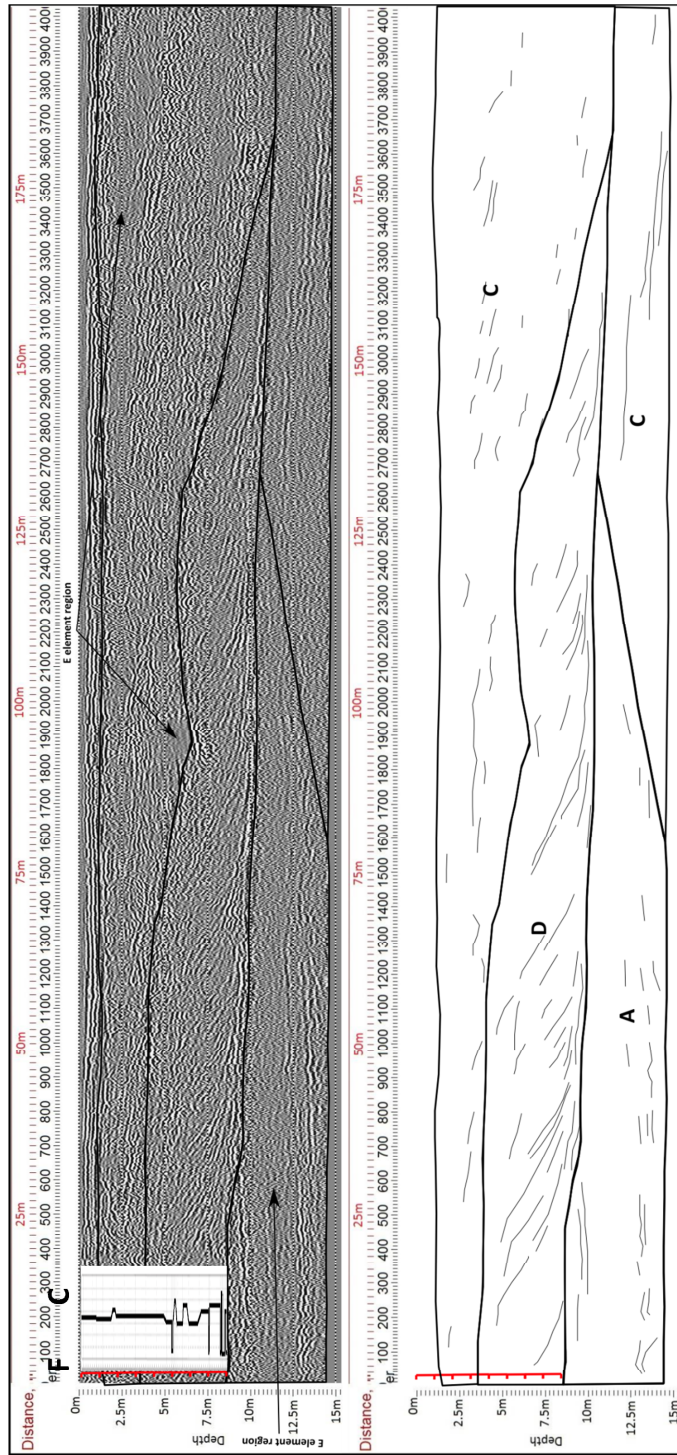


Figure 24: GPR radargram and interpretation of the Pamlico ACD. The location of the core gp1421 is shown in red with a sketched core log to the left. In the core log coarser lithology is to the right noted by a “C” and finer lithology to the left indicated by a “F”. The radargram shows a large area interpreted as element C. This ACD is unique in that it contains high angle sigmoidal reflectors (element D) interpreted as possible dune or beach facies. The lower part of the radargram shows both element C and A (seaward and landward dipping elements respectively). This is interpreted to be beach front elements overlain by overwash deposits. The boundary between element D and the elements A/C is sharp and possibly erosional. Note the regions indicated as element E. These are interpreted as regions of humate development.

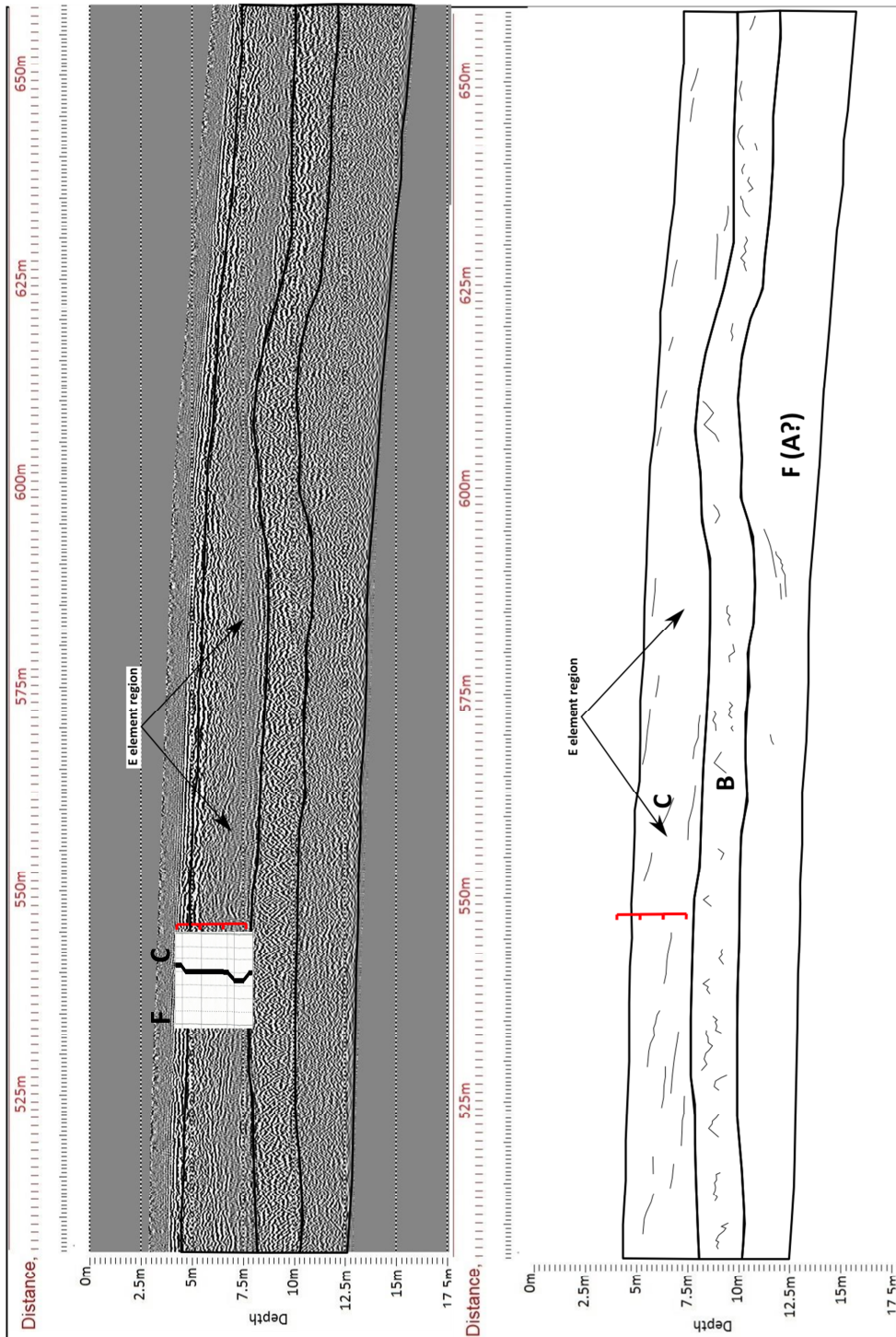


Figure 25: GPR radargram and interpretation of the Talbot ACD. The location of the core gp129 is shown in red with a sketched core log to the left. In the core log coarser lithology is to the right noted by a “C” and finer lithology to the left indicated by a “F”. This ACD shows the element C facies interpreted as a beach face. Below this unit is a region of element B characterized by numerous point reflections. The lower most region of the radargram is obscured by element F but is hypothesized to be element A based on a few landward reflections. Note the extensive element E region of humate development. This hindered coring of this ACD and resulted in a short core being taken at this location. As such lithologic details on element B facies is not possible.

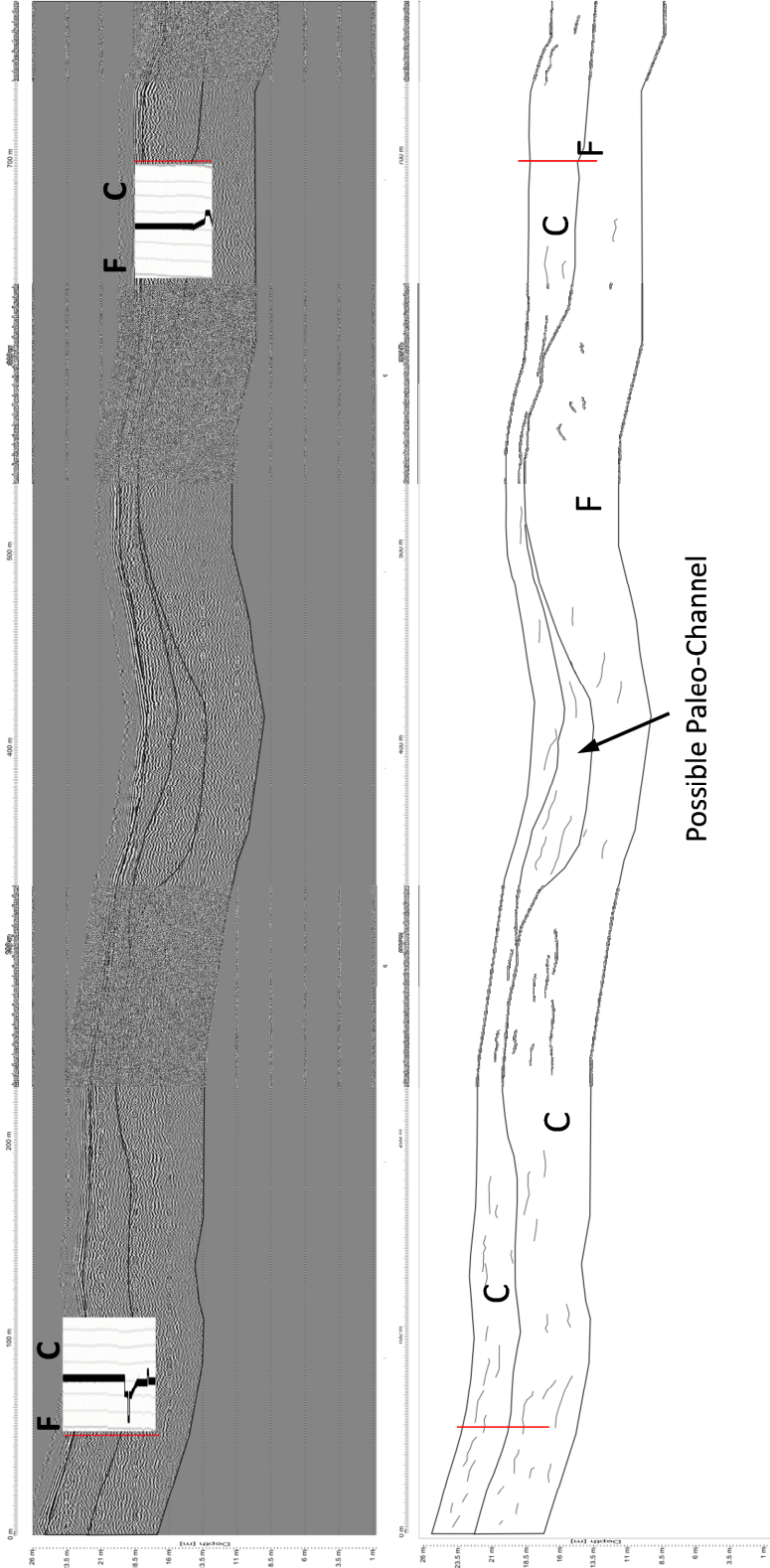


Figure 26: GPR radargram and interpretation of the Penholoway and Wicomico ACD. The location of the core gp124 (right) and core gp123 (left) are shown in red in a sketched core log to the left. In the core log coarser lithology is to the right noted by a “C” and finer lithology to the left indicated by a “F”. This ACD is composed of facies of element C primarily. Significant areas are masked by element F type reflections. Note the possible channel feature in the center of the radargram. There is no significant boundary between the Wicomico(left) and Penholoway (right) ACDs suggesting that they are in fact one depositional event.

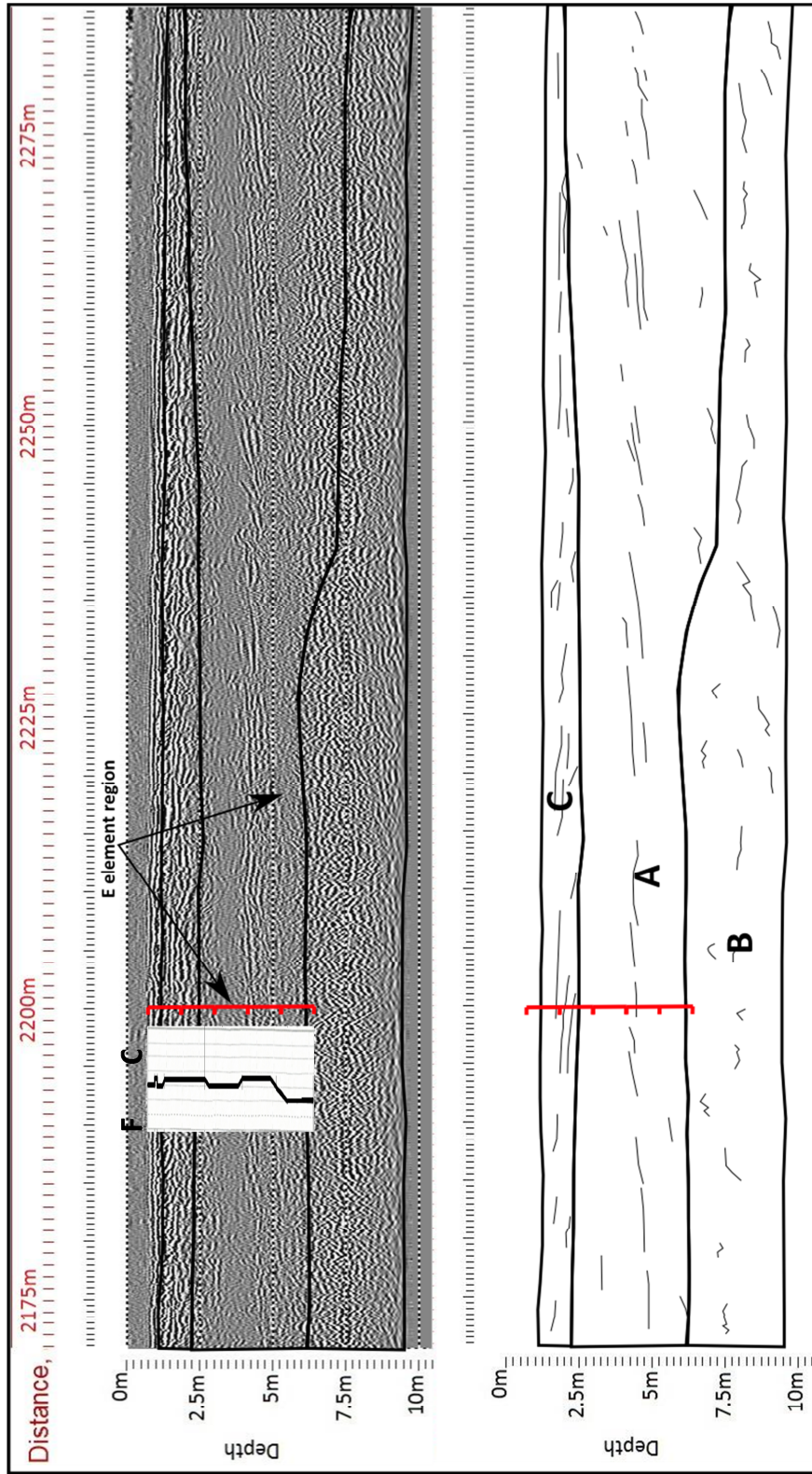


Figure 27: GPR radargram and interpretation of the Okefenokee ACD. The location of the core log 127 is shown in red with a sketched core log to the left. In the core log coarser lithology is to the right noted by a "C" and finer lithology to the left indicated by a "F". This ACD is composed of facies of element C in the upper portion of the radargram, element A in the middle, and element B in the lower portion of the radargram. This ACD has excellent landward dipping reflections (element A) that are obscured by a significant quantity of element E. This element is interpreted as a humate that impeded the coring process. The lowermost, element B region is composed of numerous point reflectors interpreted as large grains. The core from this site penetrates the upper few centimeters of this unit and is composed of poorly sorted sediments, although no materials that could cause point reflections were found, this could be due to the coring process or the limited penetration.

3.2 Sediment Analysis

Core drilling reached a depth of between 3.5-7.5 m in the upper ACDs and 7.5-8.5 m in the lower ACDs. Core recovery was generally good (25-100%) with an average recovery of approximately 75%, although challenges were encountered during sediment coring. At all core locations, coring was slowed by a highly compact and pressurized layer of sediments. This layer would, to varying degrees at each location, prevent penetration and effectively stops the core process. Once this layer was penetrated sediment would expand in the core line locking the core liner in the core barrel. Expansion of this layer would hamper extraction of the core stem and upon removal of the drill stem this layer would collapse the borehole requiring further drilling to reach the desired depth. Figure 28 shows the approximate location of the cores within a cross-section of the Georgia Coastal Plain (modified from Huddleston, 1988).

Detailed core logs are presented in Appendix 2. Cores from the upper ACD sites contain generally homogeneous well to moderately sorted quartz sand while the lower ACDs have a more varied lithology, including clay beds in the lower sections. The sands range from very fine to coarse quartz sand in discrete layers (mm-cm in thickness). The quartz in the cores has medium to high sphericity and is sub-angular to sub-rounded. Quartz grains are smooth or pitted but not frosted. Other minerals such as feldspar and

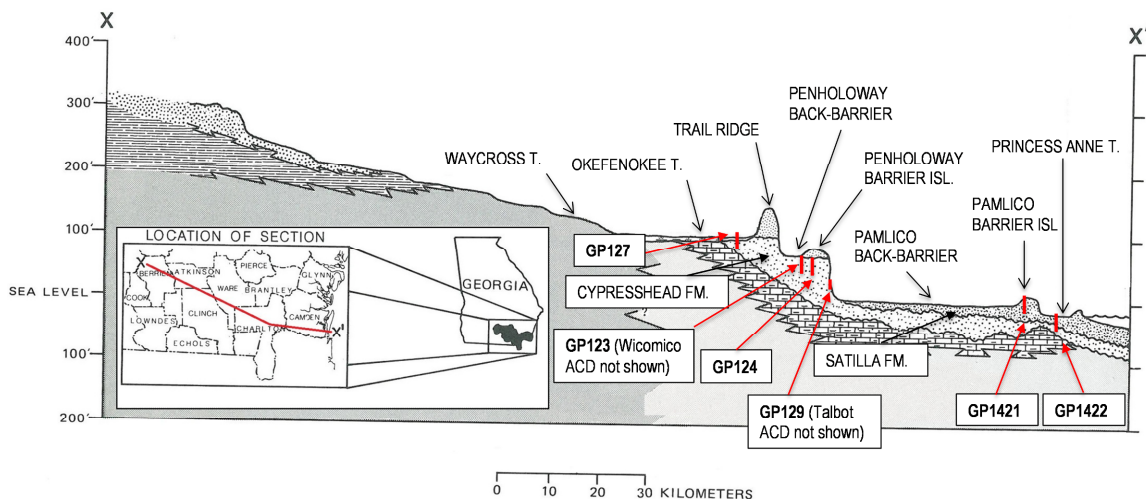


Figure 28: Location of the cores within the Georgia profile (modified from Huddleston, 1988).

muscovite are observed but were rare in all the cores (1% or less). Heavy minerals were found in small amounts in all the cores (1% or less), but heavy mineral rich beds are found in all cores with heavy mineral concentrations of up to approximately 20% in some cases. Generally organic material (roots, plant fragments, etc.) are found in the tops of the cores. Further down charcoal could be found in many cores.

Upper ACD cores contain clay with in the core averaging around 5% but increasing to 20% in locations. Furthermore cores GP12-3 and GP12-4 (Wicomico and Penholoway ACD respectively) contain clay concretions that resemble internal molds of shells. These concretions are generally small (1-2 mm) with few (<1%) reaching 2 cm in size. Few (<1%) feldspar grains are observed in all upper ACD cores. Heavy mineral concentrations in the cores range from <1% to approximately 2% on average. Laminations of heavy mineral rich horizons less than a millimeter in diameter and containing up to 20% heavy minerals are found in the lower 4 to 5.5 meters of the core GP12-4 (Penholoway ACD). These laminations are slightly parabolic concave down core; this is assumed deformation due to the coring process and not as a primary structure. The upper ACDs contain almost exclusively sand rich lithologies. The exception is the Wicomico core (GP12-3) in which a clay rich layer is found in the lower 1/3 of the core. This clay layer appears to be composed an amalgamation of clay concretions within a matrix of sand. This layer is tan in color.

The upper 5 m of cores GP14-21 and GP14-22 (Pamlico and Princess Anne ACDs respectively) show many of the same lithologies (heavy mineral bands, clay concretions) as the upper ACD cores. In the lower sections of these cores clay layers become more abundant and sorting decreases. Clay layers range from 1 cm to 10s of cm in scale and are composed of sticky grey/green clay. The clay rich region in the Pamlico core (GP14-21) can be found in the lower most section of the core and shows alteration between clay layers and coarse poor sorted sand layers. In the Princess Anne core (GP14-22) the clay rich lay occurs as a discrete layer bounded by medium-coarse sands above and coarse sands followed by fine sands below.

All of the cores contain units of coated or stained grains that varied with depth and from core to core. This staining ranged from a bright orange coating to a very dark black/brown stain (described as “black organic?” or just “organic?” in the core logs) that nearly cements the sediments. Based on the location within the core and the depths in which field coring became difficult the dark black material is the lithology that made trouble for coring.

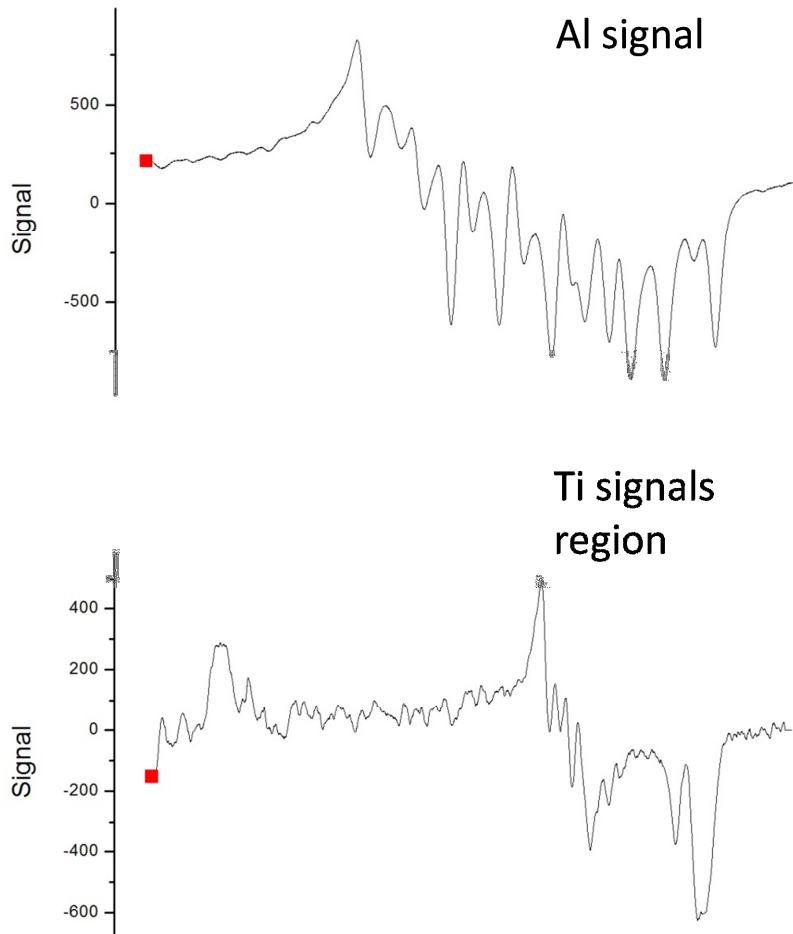


Figure 29: Examples of the typical ESR spectrum measured at Osaka University. Note that the signal gain between the two signals has been changed so that the Ti signal region is measurable.

3.3 ESR Results

Figure 29 shows an example of a sample ESR spectrum (measured at Osaka University). All of the samples show signal intensity growth with respect to dose for the Al signal with a decrease in the Ti-Li signal intensities at high added doses (>+5000 Gy).

Figures 30 and 31 shows the ESR spectrum of a bleached, natural and additive dose aliquots with noticeable growth in the ESR intensity of all signals studied.

All signals, Al, Ti-Li (option A and D), and Ti-H (Yoshida $g=1.9162$) signal intensities are fitted with a SSE curve. In addition the Al signals were fitted with an exponential + linear (exp+lin) fit. The Ti-Li option A and D of samples measured at Osaka University are fitted with the Ti₂ fit of Duval and Guiliarte (2014) as well. Examples of the plots of the signal intensity with respect to dose for samples gp1421f

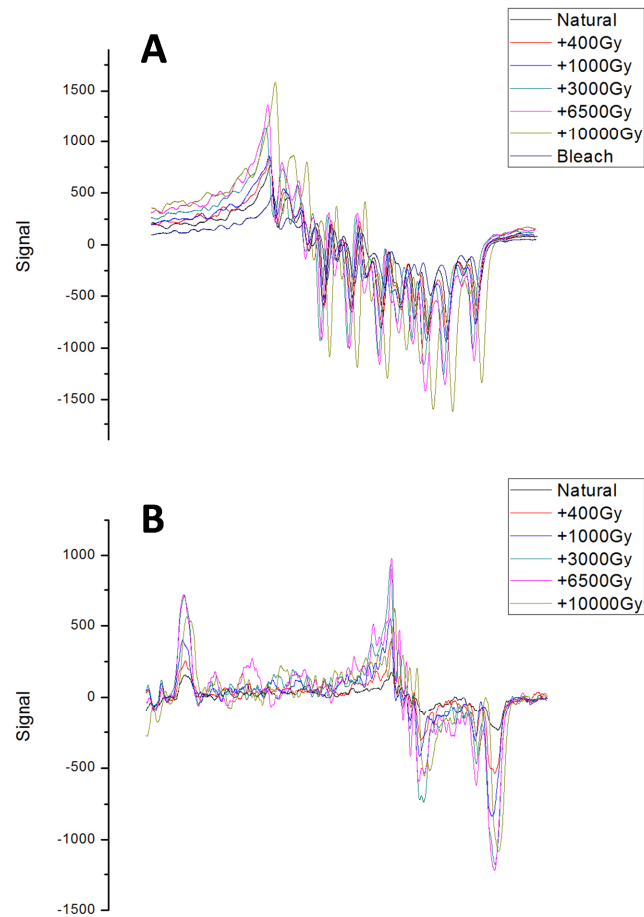


Figure 30: Examples of the typical ESR signal growth with dose measured at Osaka University. The Al signal is shown in A and the Ti signal in B. All samples showed similar growth. Note that signal intensity of the Ti signals decrease at high additive dose (+6500Gy, +10000Gy) while the Al signal continues to show growth.

and gp124e can be found in Figures 32 and 33. The plots for the remaining samples can be found in Appendix 3 (Figures A3-F1 to A3-F14). For the SSE fits all the additive dose aliquots are used to build the Al curve while only the aliquots up to +6500 Gy and +3000 Gy were used to fit the Ti-Li and Ti-H signals respectively. This is to exclude the part of the dose response curve where the SSE fit no longer models the behavior of the samples. For the Ti-H (Yoshida $g=1.9162$) signal only the dose up to +3000 Gy are used due to the

fact that the signal saturates around 1000 Gy. The characteristics of this signal are somewhat unstable (Duval and Guilarte; 2014) and a maximum accepted dose higher than the typical saturation value of this signal was chosen to fully capture the signal. For the Ti2 fit all of the additive doses aliquots are used to construct the dose response curve. The Do of all of the signal curves can be found summarized in table 4. The Do values of the Al signal range from 1555 \pm 265 Gy to 10197 \pm 4729 Gy (note that Do values for samples with DRC r^2 values over 0.95 are not included in this range). Ti-Li option A Do values range from 803 \pm 353 Gy to 2149 \pm 201 Gy, Ti-Li option D ranges from 912 \pm 83 Gy to 2207 \pm 232 Gy (note that Do values for Ti-Li signals with DRC r^2 values over 0.95 are not included in these ranges), and the Ti-H Do values range between 192 \pm 73 Gy and 1054 \pm 287 Gy.

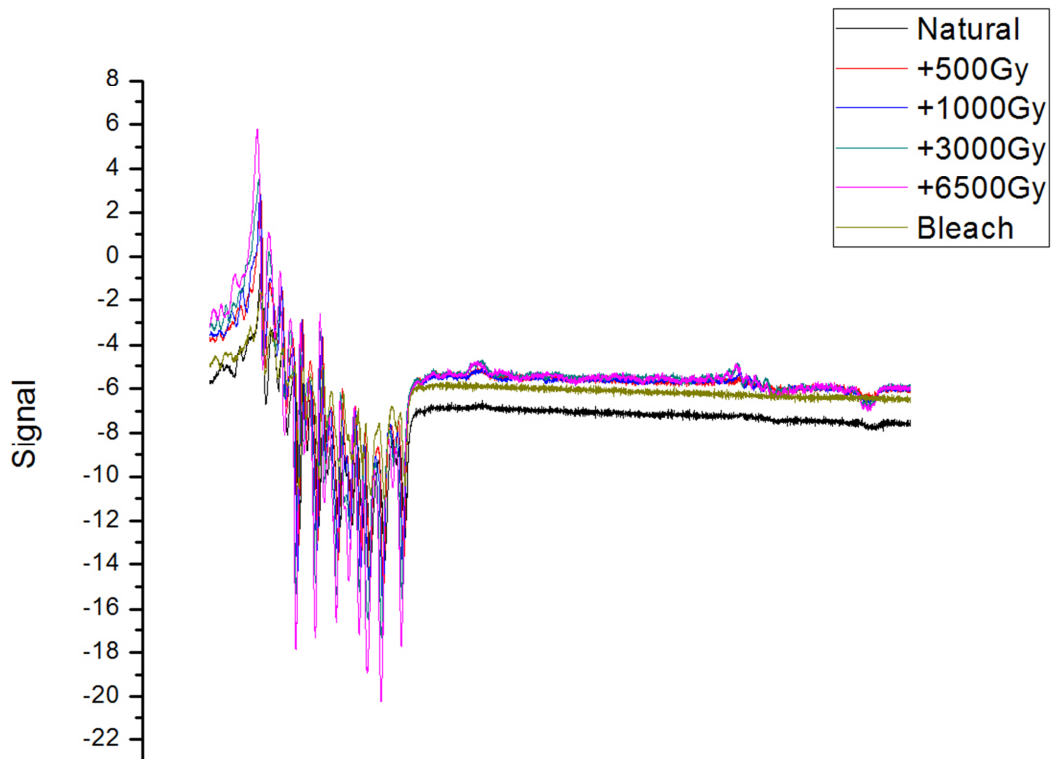


Figure 31 ESR signal growth with dose as measured at FSU.

Princess Anne: GP1422c

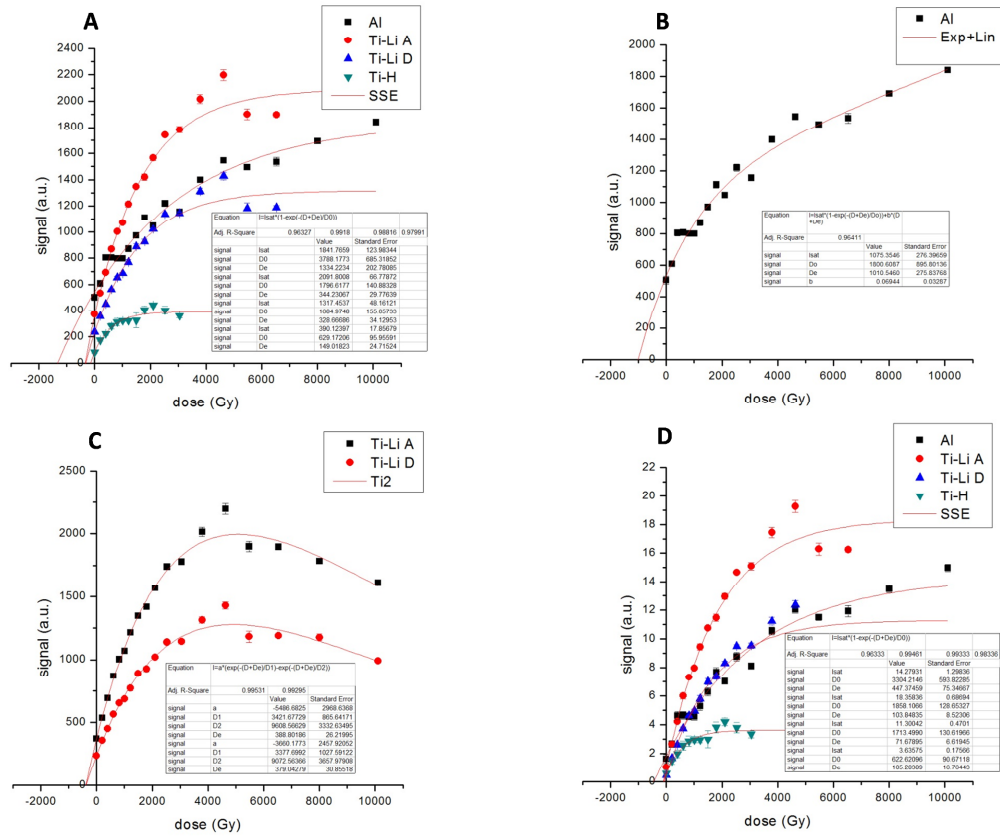


Figure 32: Dose response curve (DRC) of sample gp1422c of the Princess Anne ACD measured at Osaka University. Part A shows the AI, Ti-Li option A and option D signals, as well as the Ti-H signal fitted with a Single Saturating Exponential (SSE) fit. Shown in B is the Exponential plus Linear (Exp+Lin) fit of the AI signal. C is the DRC of the Ti-Li (option A and D) including points at additive doses over +6500 Gy and fitted with the Ti2 curve of Duval and Guilarte (2014). D shows the SSE fit of all the ESR signals, fitted with a SSE, that have had the calculated relict signal intensity removed (see part 4.3.3.1). Included in each graph is the I_{max}, D₀, D_e, and R squared fit of the curve.

Penholoway: GP124e

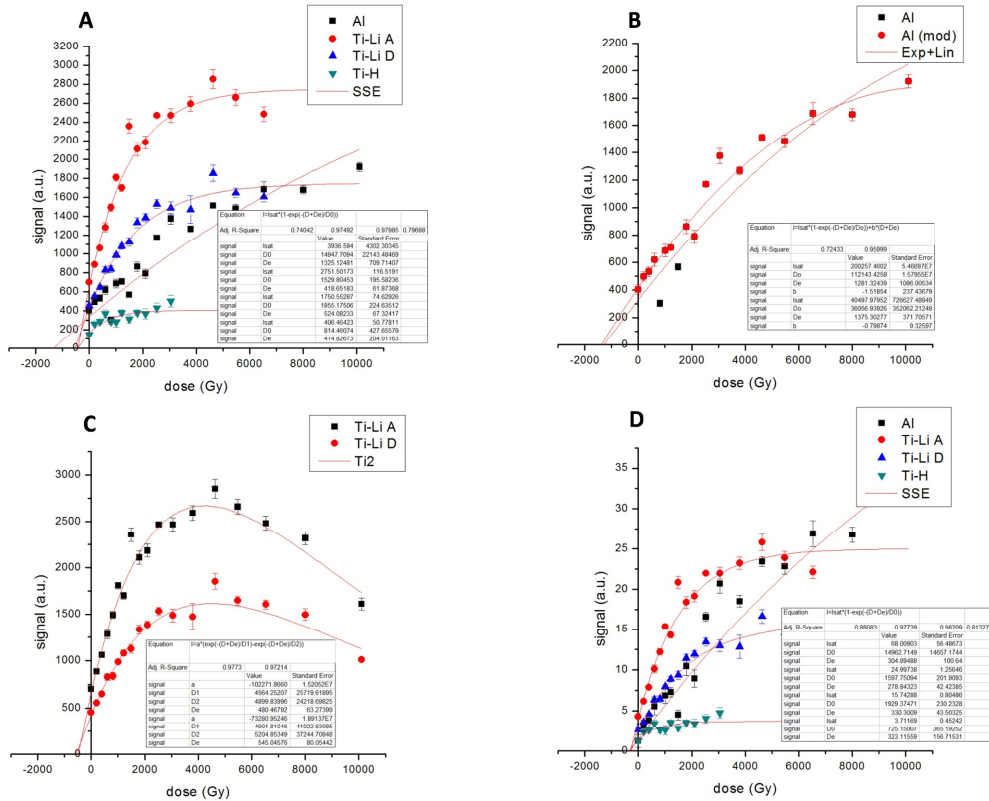


Figure 33: Dose response curve (DRC) of sample gp124e of the Penholoway ACD measured at Osaka University. Part A shows the AI, Ti-Li option A and option D signals, as well as the Ti-H signal fitted with a Single Saturating Exponential (SSE) fit. Shown in B is the Exponential plus Linear (Exp+Lin) fit of the full AI signal as well as modification were outlying dose points were dropped. C is the DRC of the Ti-Li (option A and D) including points at additive doses over +6500 Gy and fitted with the Ti2 curve of Duval and Guilarte (2014). D shows the SSE fit of all the ESR signals, fitted with a SSE, that have had the calculated relict signal intensity removed (see part 4.3.3.1). Included in each graph is the I_{max}, D₀, D_E, and R squared fit of the curve. Note that the AI (SSE) and (Exp+Lin) have r² values over 0.95 and are considered unreliable.

Table 4				
Sample	Do (SSE fit) (Gy)			
	<u>Al</u>	<u>Ti-Li A</u>	<u>Ti-Li D</u>	<u>Ti-H</u>
gp1422c	3788+/-685	1797+/-141	1685+/-155	629+/-96
gp1422d	2125+/-799*	1732+/-303	1788+/-233	1054+/-287
gp1422g	2900+/-877*	2019+/-410*	2200+/-399	854+/-283
gp1421c	6336+/-2661*	1736+/-108	1640+/-122	424+/-70
gp1421d	4858+/-2131*	7225+/-8435*	2207+/-232	598+/-259
gp1421f	1555+/-265	2149+/-201	1506+/-115	664+/-226
gp129b	2520+/-345	1423+/-119	1557+/-164	389+/-95
gp129c	7158+/-1442	1342+/-166	1439+/-161	192+/-73
gp124b	2543+/-597	1761+/-219	1818+/-121	359+/-284
gp124e	14948+/-22143*	1530+/-196	1855+/-225	814+/-428
gp123c	17758+/-20720*	2003+/-166	2089+/-171	591+/-134
gp123d	6228+/-2368*	1706+/-283	1723+/-317	883+/-235
gp123f	4781+/-1197	1885+/-237	2037+/-230	799+/-215
gp127b	6.70E8+/-4.09E13*	883+/-62	912+/-83	442+/-164
gp127c	10197+/-4729	1922+/-248	1504+/-167	866+/-231
gp127e	13257+/-9833*	803+/-353*	898+/-338*	452+/-94

Table 4: Do values of the various ESR signals from the Georgia ACD samples when fitted with a SSE fit. Samples with DRC r^2 values over 0.95 are indicated with an asterisk. Note the low Do values for the Ti-Li signals and the large error on the Ti-H values.

The natural signal from sample 0s and 0d collected from the active coast of Georgia are measured as well as a bleached aliquot for each of these samples (measured at Osaka University). The natural aliquots of these samples showed an appreciable natural signal in both the Al and Ti (Li and H) portions of the spectrum relative to the bleached aliquots (Table 5).

Dose rate information can be found in Table 6. Dose rates were calculated using a linear accumulation for the cosmic dose component (calculated assuming the burial depth was on average 50% of the present day burial depth). Doses rates varied from 0.26-1.2 Gy/ka for the ACDs, with the modern swash zone sample being significantly more radioactive, with a dose rate of 2.5 Gy/ka). The most significant variations in dose rates between samples collected in the same core occur in the Penholoway, Wicomico, and Okefenokee ACDs. The Talbot, Pamlico, and Princess Anne samples have more

Table 5: Natural signal intensity (a.u.)				
Sample	Al (natural-bleach)	Ti-Li (A)	Ti-Li (D)	Ti-H
0s	385+/-17	268+/-11	196+/-13	21+/-28
0d	300+/-37	275+/-7	184+/-5	30+/-33
gp1422c	505+/-25	374+/-5	236+/-6	81+/-8
gp1422d	na	na	na	na
gp1422g	na	na	na	na
gp1421c	509+/-30	419+/-9	261+/-10	58+/-9
gp1421d	na	na	na	na
gp1421f	na	na	na	na
gp129b	na	na	na	na
gp129c	407+/-19	996+/-20	580+/-5	95+/-16
gp124b	na	na	na	na
gp124e	403+/-33	702+/-19	453+/-13	148+/-13
gp123c	613+/-28	964+/-9	617+/-13	193+/-15
gp123d	698+/-37	778+/-17	526+/-7	157+/-17
gp123f	655+/-17	824+/-16	539+/-14	166+/-14
gp127b	252+/-13	659+/-6	417+/-9	120+/-8
gp127c	614+/-21	975+/-12	596+/-15	169+/-19
gp127e	483+/-3	832+/-9	517+/-5	111+/-8

Table 5: Signal intensity of the natural aliquot of the samples measured at Osaka University. The samples measured at FSU are not included due to the differences in measurement conditions prevents direct comparison.

consistent dose rates both within the cores and between them. All dose rates are consistent with Georgia deposits measured by other luminescence researchers (Markewich et.al., 2013; Alexander, personal communications). Variations in heavy mineral content are also consistent with other Georgia deposits (Kellem et.al., 1991).

Results of the ESR dating of the Georgia ACDs can be found summarized in Table 7. Of the 16 samples measured using ESR no agreement is found between the Ti-Li option D and Al signals of any of the samples using a single saturating exponential (SSE) fit. Only 7 samples yielded Al (SSE) DRCs with r^2 values over 0.95, 13 samples had DRC r^2 values were over 0.95 for the Ti-Li option A, and 15 samples had DRC r^2 values were over 0.95 for Ti-Li option D (see Table 7). Two samples, gp129b, and gp124b, (measured at FSU), show agreement between the Al and Ti-Li option A signal using a SSE fit but the option A and option D signals of these samples do not agree (more

on this in Chapter 4). When an exponential + linear fit is applied to the Al signals, two samples (gp1421f and gp129b) show agreement with the Ti-Li option D SSE fit (an additional 3 samples also show agreement, but r^2 values under 0.95 for the Al age excluded these from being considered reliable) . No agreement was found between the Ti-H or Ti-Li signals (A or D) with the Ti-H D_E being consistently smaller than the Ti-Li D_E (SSE fit).

Table 6 Dose Rates

ACD	sample	depth (m)	U (ppm)	Th (+/-) (ppm)	K (+/-) (ppm)	Water content	cosmic dose (µGy/a)	total dose rate (Gy/Ka)	total dose rate (Gy/Ka)	total dose rate (+/-)
J.I. swash	Ga120s	0	0.77	1.24	0.04	0%	287	2.462	2.462	0.021
J.I. dune	Ga120d	0	4.4	12.72	0.22	15%	287	0.872	0.872	0.017
P. Anne	Gp1422c	2.7	1.3	4.79	0.09	23%	174	0.909	0.909	0.015
P. Anne	GP1422d	4.6	1.21	3.67	0.07	18%	154	0.842	0.842	0.016
P. Anne	Gp1422g	7.9	1.31	3.29	0.07	19%	125	1.227	1.227	0.018
Pamlico	Gp1421c	2.7	1.04	2.99	0.06	20%	174	0.819	0.819	0.016
Pamlico	Gp1421d	4.4	1.05	0.89	0.02	19%	156	0.713	0.713	0.016
Pamlico	Gp1421f	5.2	0.95	1.55	0.04	18%	148	0.831	0.831	0.017
Talbot	Gp129b	2	0.74	1.76	0.04	17%	183	0.469	0.469	0.015
Talbot	Gp129c	3.5	0.63	1.78	0.11	15%	165	0.444	0.444	0.016
Penholoway	Gp124b	2	1.18	4.27	0.08	15%	183	0.74	0.74	0.016
Penholoway	Gp124e	5	0.41	1.51	0.1	11%	150	0.375	0.375	0.017
Wicomico	Gp123c	3	2.13	11.39	0.19	20%	171	1.581	1.581	0.018
Wicomico	Gp123d	3.7	1.86	4.91	0.31	22%	163	1.112	1.112	0.021
Wicomico	Gp123f	6.7	0.47	1.46	0.09	12%	134	0.43	0.43	0.016
Okefenokee	Gp127b	1.9	1.98	2.85	0.07	43%	184	0.683	0.683	0.013
Okefenokee	Gp127c	3.2	0.24	0.47	0.03	14%	169	0.262	0.262	0.015
Okefenokee	Gp127e	5.7	1.6	5.16	0.33	16%	143	0.81	0.81	0.021

Table 6: Uranium (U), Thorium (Th), Potassium (K) and Dose rate data for the Georgia ACD samples.

Table 7: D_E and Ages

Sample	Name	Dr(lin)	SSE												avg		
			D _E						Age (ka)								
			Al	Ti-Li (optA)	Ti-Li (optD)	Ti-H	Al	Ti-Li (optA)	Ti-Li (optD)	Ti-H							
0s	J.I. swash	2.462+/- 0.021															
0d	J.I. dune	0.872./- 0.017															
gp1422c	PA	0.909+/- 0.015	1334.22+/- 202.78	344.23+/- 29.78	328.67+/- 34.13	149.02+/- 24.72	1468.09+/- 237.34	378.77+/- 39.39	361.65+/- 42.87	163.97+/- 28.62	na						
gp1422d	P A	0.842+/- 0.016	1151.06+/- 433.51*	975.62+/- 185.95	433.70+/- 66.62	95.96+/- 23.73	1367.12+/- 514.71	1158.75+/- 227.02	515.11+/- 82.92	113.97+/- 28.54	na						
gp1422g	P A	1.227+/- 0.018	1446.68+/- 374.24*	1217.39+/- 250.27*	797.11+/- 144.67	358.70+/- 113.81	1179.09+/- 309.87	992.21+/- 209.90	649.67+/- 122.51	292.35+/- 93.53	na						
gp1421c	Pam	0.819+/- 0.016	2201.40+/- 570.89*	416.70+/- 27.96	391.47+/- 31.71	78.61+/- 14.28	2686.98+/- 705.38	508.62+/- 43.99	477.82+/- 46.56	95.95+/- 18.05	na						
gp1421d	Pam	0.713+/- 0.016	1426.50+/- 399.54*	2367.49+/- 1383.15*	523.27+/- 81.09	147.71+/- 71.91	2001.37+/- 564.78	3321.57+/- 1925.89	734.14+/- 119.54	207.24+/- 100.33	na						
gp1421f	Pam	0.831+/- 0.017	562.50+/- 106.54	1253.41+/- 117.15	285.04+/- 26.76	62.35+/- 22.53	676.67+/- 132.06	1507.82+/- 161.78	342.90+/- 36.91	75.01+/- 27.13	na						
gp129b	Tal	0.469+/- 0.015	728.16+/- 91.65	758.24+/- 72.65	481.87+/- 61.55	105.53+/- 29.72	1552.06+/- 213.57	1616.17+/- 180.81	1027.09+/- 143.02	224.93+/- 63.66	na						
gp129c	Tal	0.444+/- 0.016	1431.00+/- 165.74	712.94+/- 98.63	763.00+/- 92.81	55.87+/- 23.05	3223.38+/- 415.78	1606.42+/- 238.98	1719.22+/- 230.38	125.89+/- 51.50	na						
gp124b	Pen	0.740+/- 0.016	1184.59+/- 247.08	1114.73+/- 146.15	702.04+/- 50.03	209.87+/- 184.57	1600.81+/- 339.77	1506.40+/- 209.51	948.71+/- 82.23	283.61+/- 246.93	na						
gp124e	Pen	0.375+/- 0.017	1325.12+/- 709.71*	418.65+/- 61.87	524.08+/- 67.32	414.83+/- 204.01	3531.47+/- 1862.30	1115.71+/- 176.86	1396.68+/- 197.67	1105.53+/- 536.09	na						
gp123c	Wic	1.581+/- 0.018	4651.88+/- 1758.77*	1146.81+/- 92.12	1178.17+/- 91.32	388.64+/- 94.15	2942.02+/- 1118.36	725.29+/- 70.68	745.12+/- 70.91	245.79+/- 60.79	na						
gp123d	Wic	1.112+/- 0.021	2505.70+/- 620.25*	690.42+/- 123.10	741.97+/- 145.83	421.37+/- 109.10	2233.20+/- 564.42	615.33+/- 114.86	661.28+/- 134.84	375.54+/- 99.04	na						
gp123f	Wic	0.430+/- 0.016	2232.00+/- 420.77	836.56+/- 106.74	913.09+/- 101.06	425.43+/- 113.28	5195.48+/- 390.29	1947.28+/- 268.98	2125.42+/- 262.12	990.28+/- 264.85	na						
gp127b	Oke	0.683+/- 0.013	3006.19+/- 1709.42*	395.30+/- 33.61	416.21+/- 45.70	230.56+/- 92.31	4400.88+/- 2498.92	578.69+/- 69.06	609.31+/- 83.87	337.53+/- 136.47	na						
gp127c	Oke	0.262+/- 0.015	2316.57+/- 491.68	846.47+/- 108.99	679.77+/- 82.25	429.47+/- 110.33	8846.52+/- 1980.68	3232.50+/- 495.57	2595.91+/- 382.32	1640.06+/- 433.05	na						
gp127e	Oke	0.810+/- 0.021	3629.84+/- 1068.03*	1221.23+/- 590.50*	1327.93+/- 544.97*	389.86+/- 88.69	4481.76+/- 1326.79	1507.85+/- 725.88	1639.59+/- 671.54	481.36+/- 111.40	na						

Table 7: D_E and age results of the Georgia ACD ESR dating. SSE fits are shown here. Signals with DRC r² values less than 0.95 are noted with an asterisk.

Sample	Exp+Lin		Ti2 fit				agreement	avg
	D _E		D _E		Age (ka)			
	Al	Age (ka)	Ti-Li (optA)	Ti-Li (optD)	Ti-Li (optA)	Ti-Li (optD)		
0s								
0d								
gp1422c	1010.55+/- 275.84	1111.94+/- 307.69	388.80+/-26.22	379.04+/-30.86	427.81+/-38.11	417.07+/-41.66	na	
gp1422d	1185.93+/- 595.79*	1408.54+/- 54					na	
gp1422g	798.28+/- 442.63*	650.62+/- 360.04					na (Al Exp+Lin err over 50%)	
gp1421c	735.29+/- 330.41*	897.48+/- 402.13	460.26+/-31.78	429.67+/-36.03	561.78+/-49.43	524.45+/-52.33	na (Al Exp+Lin err over 50%)	
gp1421d	807.75+/- 641.5*7	1133.27+/- 891.44					na (Al Exp+Lin err over 50%)	
gp1421f	262.87+/- 61.93	316.23+/- 75.71					AL (Exp+Lin)/TiD (SSE)	329.57+/-42.11
gp129b	379.45+/- 60.50	808.79+/- 135.74					Al (Exp+Lin)/TiD (SEE)	917.94+/-98.59
gp129c	1220.38+/- 289.13	2749.80+/- 660.52	939.17+/-101.11	937.61+/-117.13	2116.17+/-258.09	2112.65+/-289.17	na (Ti SSE)	
gp124b	404.92+/- 148.70	547.19+/- 200.52					na	
gp124e	1375.30+/- 371.71*	3665.20+/- 997.11	480.47+/-63.27	545.05+/-80.05	1280.46+/-184.82	1452.57+/-229.07	na (Ti SSE)	
gp123c	538.55+/- 385.12*	340.60+/- 242.98	1314.19+/-100.17	1309.63+/-113.41	831.14+/-78.23	828.26+/-85.00	na	
gp123d	1765.44+/- 684.20*	1573.44+/- 612.31	715.05+/-228.09*	760.39+/-263.30*	637.29+/-205.26	667.70+/-236.33	na	
gp123f	1456.85+/- 272.38*	3391.15+/- 652.42	946.96+/-116.75	999.94+/-118.20	2204.26+/-296.09	2327.59+/-302.27	na (Ti SSE)	
gp127b	no fit		517.07+/-49.92	534.68+/-49.78	756.96+/-96.58	782.74+/-97.90	na	
gp127c	no fit		856.13+/-160.76	837.34+/-125.47	3269.39+/-661.79	3197.64+/-544.52	na	
gp127e	no fit		2285.92+/-714.78	2401.86+/-766.64	2822.42+/-886.27	2965.57+/-950.00	na	

Table 7 continued: D_E and age results of the Georgia ACD ESR dating. Al Exp+Lin and Ti-Li (option A and D) Ti2 fits shown here. Agreements shown include the stated fits used. Signals with DRC r² values less than 0.95 are noted with an asterisks.

3.3.1 Use of Correlation Tables

The ages resulting from each of the signals (Al, Ti-Li A and D, Ti-H) and their different fits (SSE, Exp+Lin, Ti2) can be found in Correlation Tables 8 and 9, and Appendix 3 (Tables A3-T2 through A3-T15). A summary of the results of these tables is included below. These tables use a homogeneity test developed by Galbraith (2003; Galbraith and Roberts, 2012; Arnold et.al., 2014) to determine if the age values of each of the fits agree with one another. For determining age agreement of the set of signals within a given sample, a P number critical value of 0.32 was chosen. This indicates that the signals agree at the 1σ confidence level and values above this number indicate agreement between the two signals/fits. Included in this table is the percent error of the age estimate as well as the R squared value of the fit.

Decisions on the value and use of certain signals in each sample was determined using the correlation tables. A summary of these correlations is given here.

Sample gp1422c (Princess Anne ACD) (Table A3-T2) shows agreement at the 1σ level between the Al (SSE) and the Al (Exp+Lin) ages. Both of the Al signals (SSE and Exp+Lin) show no agreement with any of the Ti-Li (option A or D, SSE or Ti2) ages as well as no agreement with the Ti-H age. The Ti-Li option A (SSE) age shows agreement with the Ti-Li option A (Ti2) and the Ti-Li option D (both SSE and Ti2) ages at 1σ , no agreement is found with the Ti-H signal. The Ti-Li option A (Ti2) age shows 1σ agreement with the Ti-Li option A (SSE) and the Ti-Li option D (Ti2) age estimate, no agreement is found with the Ti-H age. Likewise the Ti-Li option D (SSE) shows agreement with the Ti-Li option D (Ti2) and the Ti-Li option A (SSE) but not the Ti-Li option A (Ti2) or the Ti-H ages. The Ti-Li option D (Ti2) age agrees with all of the Ti-Li ages estimates. There is no age agreement between the Ti-H age and any of the other age estimates.

Sample gp22d (Princess Anne ACD) (Table A3-T3) shows 1σ age agreements between the Al (SSE) age and the AL (Exp+Lin) and Ti-Li option A (SSE), but as both of the Al signals have DRC r^2 values under 0.95 this is correlation is not accepted. No

other agreements at the 1σ level were found. Note that this sample was run at FSU and therefore has no Ti2 fit to the Ti-Li data.

Sample gp1422g (Princess Ann ACD) (Table A3-T4) shows an age correlation at the 1σ level between the Al (SSE) and Ti-Li option A (SSE). The Al (Exp+Lin) age correlates at the 1σ level to both the Ti-Li option A (SSE) as well as the Ti-H age. All of the above signals have DRC r^2 values over 0.95 and are considered unreliable. No further correlations were found.

Gp1421c (Pamlico ACD) (Table A3-T5) shows no correlation of the Al (SSE) age with any other signals age. The Al (Exp+Lin) age correlates at the 1σ level with all of the Ti-Li signal ages except the Ti-Li option D (SSE) age. Both of the Al signals have DRC r^2 values under 0.95 and are considered unreliable. There is correlation between all of the Ti-Li signals with the exception of between the Ti-Li option A (Ti2) and the Ti-Li option D (SSE). The age of the Ti-H signal shows no correlations.

Gp1421d (Pamlico ACD) (Table A3-T6) shows correlation between the Al (SSE) signal and the Al (Exp+Lin) and Ti-Li option A (SSE) ages at the 1σ level. The Al (Exp+Lin) age agrees with the Ti-Li option D (SSE). Only the Ti-Li option D (SSE) signal has a DRC r^2 value over 0.95 and is considered reliable. This correlation will be discussed in detail in Chapter 4.

Sample gp1421f (Pamlico ACD) shows only one age correlation between the Al (Exp+Lin) and the Ti-Li option D (SSE) ages (Table 8). This sample will be discussed further in Chapter 4.

Similarly sample gp129b (Talbot ACD) (Table A3-T7) shows only one 1σ correlation between the Al (SSE) and the Ti-Li option A (SSE) age.

Gp129c (Talbot ACD) (Table A3-T8) shows 1σ level correlations between the Al (SSE) and the Al (Exp+Lin) ages. Furthermore the Al (Exp+Lin) age agrees at the 1σ level with both the Ti-Li option A (Ti2) and the Ti-Li option D (Ti2) ages. There is a correlation at the 1σ level between the Ti-Li option D (SSE) age and the Ti-Li option A (SSE) and (Ti2) ages.

Sample gp124b (Penholoway ACD) (Table A3-T9) shows 1σ age correlation between the Al (SEE) and the Ti-Li option A (SSE) as well as between the Al (Exp+Lin) and Ti-H (SSE) ages, though due to the DRC r^2 value the AL (Exp+Lin) is considered unreliable. No further correlations are observed.

Sample gp124e (Penholoway ACD) (Table 9) shows a 1σ correlation between the Al (SSE) and the Al (Exp+Lin) ages, though both have DRC r^2 values under 0.95. There are 1σ age correlations between all of the Ti signal ages, including the Ti-H signal age, with the exceptions of between the Ti-Li option A (SSE) signal and the Ti-Li option D (SSE) and (Ti2).

Gp123c (Wicomico ACD) (Table A3-T10) shows 1σ level agreement between the Al (Exp+Lin) age and the Ti-H age, though both of the Al signals have DRC r^2 values under 0.95 and are considered unreliable. There is agreement at 1σ between all Ti-Li signals with the exception of between the Ti-Li option A (SSE) and the Ti-Li option A (Ti2) ages.

Sample gp123d (Wicomico ACD) (Table A3-T11) shows a 1σ correlation between the Al (SSE) and (Exp+Lin) ages though both have DRC r^2 values under 0.95 and are considered unreliable. All of the Ti-Li ages agree at the 1σ level but the Ti2 fits of the Ti-Li data have DRC r^2 values under 0.95 and are therefore unreliable. No correlations are seen to the Ti-H signal age.

Gp123f (Wicomico ACD) (Table A3-T12) shows 1σ correlations between all of the Ti-Li signals ages. No further correlations are seen. The Al (Exp+Lin) has an DRC r^2 value under 0.95.

Sample gp127b (Okefenokee ACD) (Table A3-T13) shows correlation at the 1σ level between the Ti-Li option A (SSE) and the Ti-Li option D (SSE). Also seen is a correlation between the Ti-Li option A (Ti2) and the Ti-Li option D (Ti2). The Al (SSE) DRC r^2 value for this sample is under 0.95. No further correlations are noted.

21f		% Age err	20%	24%	11%	na	11%	na	36%
	Age (ka)	Age err (ka)	676.67	316.23	1507.82	na	342.90	na	75.01
	Age err (ka)		132.06	75.71	161.78		36.91		27.13
R squared		AI (SSE)	AI (SSE)	AI (Exp+Lin)	Ti-Li A (SSE)	Ti-Li A (Ti2)	Ti-Li D (SSE)	Ti-Li D (Ti2)	Ti-H (SSE)
0.9551	676.67	132.06	1.00						
0.9791	316.23	75.71	0.02	1.00					
0.9876	1507.82	161.78	0.00	0.00	1.00				
		Ti-Li A (Ti2)	na	na	na	na			
0.9913	342.90	36.91	0.01	0.75	0.00	na	1.00		
		Ti-Li D (Ti2)	na	na	na	na	na	na	
0.9294	75.01	27.13	0.00	0.00	0.00	na	0.00	na	1.00

Table 8: Age correlation table for Pamlico gp1421f. Note a strong correlation between the AI (Exp+Lin) and the Ti-Li option D (SSE). This correlation has been confirmed on account of the relatively low error of the AI (Exp+Lin) age estimate. There is also a lack of agreement between the Ti-Li option A and option D age determinations. This is counter to the results of Duval and Guiliarte (2014). Note that the words “na” denote a lack of data due to the absence of a particular ESR signal(s) due to the measurement conditions.

R squared		4e		% Age err	53%	27%	16%	14%	14%	16%	48%
		Age (ka)	Age err (ka)								
0.7404	3531.47	1862.30	AI (SSE)	3531.47	1.00	3665.20	1115.71	1280.46	1396.68	1452.57	1105.53
0.9600	3665.20	997.11	AI (Exp+Lin)	1862.30	0.95	997.11	176.86	184.82	197.67	229.07	536.09
0.9749	1115.71	176.86	Ti-Li A (SSE)	AI (SSE)	1.00	0.01	1.00				
0.9773	1280.46	184.82	Ti-Li A (Ti2)	AI (Exp+Lin)	0.20	0.02	0.52	1.00			
0.9799	1396.68	197.67	Ti-Li D (SSE)	Ti-Li A (SSE)	0.25	0.03	0.29	0.67	1.00		
0.9721	1452.57	229.07	Ti-Li D (Ti2)	Ti-Li A (Ti2)	0.27	0.03	0.24	0.56	0.85	1.00	
0.7968	1105.53	536.09	Ti-H (SSE)	Ti-H (SSE)	0.21	0.02	0.99	0.76	0.61	0.55	1.00

Table 9: Age correlation table for Penholoway gp124e. Note a lack of correlation between the AI signals and the Ti signals. There is agreement between the Ti-Li option A and D in both the SSE and Ti2 fits as to be expected (Duval and Guiliarte, 2014). The agreement in the Ti-H and Ti-Li signals is discounted due to the large error in the Ti-H age estimate.

Gp127c (Okefenokee ACD) (Table A3-T14) shows 1σ correlation between all of the Ti-Li ages with the exception of between the Ti-Li option A (SEE) and the Ti-Li option D (SSE). No further correlations are seen.

Sample gp127e (Okefenokee ACD) (Table A3-T15) shows 1σ correlations between the Ti-Li option A (SSE) and the Ti-Li option D (SSE). Also seen is correlation between the Ti-Li option D (Ti2) age and the Al (SSE) and Ti-Li option A (Ti2) ages. All signals for this sample have DRC r^2 values under 0.95 and thus these DRC's are considered unreliable. This sample will be excluded from formulation of conclusions but included in tables as a point of discussion.

Table 10 shows the correlation of the ages between each of the samples the Ti-Li option D (SSE) fit. The correlation tables for the other signals can be found in Appendix 3 (Tables A3-T16 through A3-T21). These tables use the same test but the critical value of agreement is lowered to 0.05 (agreement at the 2σ level). Sample with a P value of 0.06-0.32 are considered to agree while samples with P values greater than 0.33 are considered to show stronger agreement. The results of these tables will be discussed further in chapter 4.

Ti-Li D (SSE)																		
Elev (m)	Age (ka)	Age err (ka)	22c	22d	22g	21c	21d	21f	9b	9c	4b	4e	3c	3d	3f	7b	7c	7e
0.3	361.65	42.87	22c	1.00														
-1.6	515.11	82.92	22d	0.10	1.00													
-4.9	649.67	122.51	22g	0.03	0.36	1.00												
3.3	477.82	46.56	21c	0.07	0.69	0.19	1.00											
1.6	734.14	119.54	21d	0.00	0.13	0.62	0.05	1.00										
-0.8	342.9	36.91	21f	0.74	0.06	0.02	0.02	0.00	1.00									
11	1027.09	143.02	9b	0.00	0.00	0.05	0.00	0.12	0.00	1.00								
9.5	1719.22	230.38	9c	0.00	0.00	0.00	0.00	0.00	0.01	1.00								
17	948.71	82.23	4b	0.00	0.00	0.04	0.00	0.14	0.00	0.63	0.00	1.00						
14	1396.68	197.67	4e	0.00	0.00	0.00	0.00	0.00	0.13	0.29	0.04	1.00						
21	745.12	70.91	3c	0.00	0.04	0.50	0.00	0.94	0.08	0.00	0.06	0.00	1.00					
20.3	661.28	134.84	3d	0.03	0.36	0.95	0.20	0.69	0.06	0.00	0.07	0.00	0.58	1.00				
17.3	2125.42	262.12	3f	0.00	0.00	0.00	0.00	0.00	0.00	0.24	0.00	0.03	0.00	0.00	1.00			
40.1	609.31	83.87	7b	0.01	0.42	0.79	0.17	0.39	0.01	0.00	0.00	0.00	0.22	0.74	0.00	1.00		
38.8	2595.91	382.32	7c	0.00	0.00	0.00	0.00	0.00	0.00	0.05	0.00	0.01	0.00	0.00	0.31	0.00	1.00	
36.3	1639.59	671.54	7e*	0.06	0.10	0.15	0.08	0.18	0.05	0.37	0.31	0.73	0.19	0.15	0.50	0.13	0.22	1.00

Table 10: Age agreement between the Ti-Li option D (SSE) signals of the Georgia ACD samples. P values are shown. Those shown in green are correlations at the 1σ level (strong correlations), while those in yellow are less strong correlations at the 2σ level. Due to the general lack in agreement between the Al and Ti-Li signals the Ti-Li signal is considered to be the maximum age and is used for correlation analysis. The lack in agreement between the Ti-Li option A and D in the FSU samples results in the use of the Ti-Li option D being used to compare the samples as it is the signal that is most likely bleached. The Ti-Li option A signal is not used due to the irregularities of this signal in the ESR samples measured at FSU. Correlation charts of the other signals can be found in appendix 3. Note that sample 7e (*) is included but is to be considered unreliable due to its low r^2 value.

Table 10 shows a number of correlations between the Ti-Li option D (SSE) signals of the samples studied.

Sample gp1422c (Princess Anne ACD) shows a 1σ correlation to sample gp1421f (Pamlico ACD) and 2σ correlations between gp1422d (Princess Anne ACD) and gp1421c (Pamlico ACD).

Gp1422d (Princess Anne ACD) shows 1σ correlations with gp1422g (Princess Anne ACD), gp1421c (Pamlico ACD), gp123d (Wicomico ACD) and gp127b (Okefenokee ACD). This sample shows 2σ correlations with gp1421d and gp1421f (both Pamlico ACD).

The final Princess Anne ACD sample, gp1422g, shows 1σ correlations to gp1421d (Pamlico ACD), gp123 c and d (Wicomico ACD) and sample gp127b (Okefenokee ACD). 2σ correlations are observed between gp1422g and gp1421c (Pamlico ACD).

Sample gp1421c (Pamlico ACD) shows a 1σ correlation with gp1422d (Princess Anne ACD). 2σ correlations are found with gp1422 c and g (Princess Anne ACD), gp123d (Wicomico ACD), and gp127b (Okefenokee ACD).

Gp1421d (Pamlico ACD) shows 1σ correlations with gp1422g (Princess Anne ACD), gp123 c and d (Wicomico ACD) and gp127b (Okefenokee ACD). Correlations at the 2σ level are found with gp1422d (Princess Anne ACD), gp129b (Talbot ACD) and gp124b (Penholoway ACD).

Sample gp1421f has a 1σ correlation with sample gp1422c (Princess Anne ACD) and a 2σ correlation with gp1422d (Princess Anne ACD). No other correlations are observed.

Gp129b (Talbot ACD) displays a 1σ correlation with gp124b (Penholoway ACD). Correlations at the 2σ level are seen with gp1421d (Pamlico ACD), gp124e (Penholoway ACD) and gp123 c and d (Wicomico ACD).

Sample gp129c (Talbot ACD) shows 2σ level correlations with samples gp124e (Penholoway ACD) and gp123f (Wicomico ACD).

Gp124b (Penholoway ACD) displays a 1σ correlation gp129b (Talbot ACD). Correlations at the 2σ level are seen with gp1421d (Pamlico ACD) and gp123c and d (Wicomico ACD).

Sample gp124e (Penholoway ACD) shows 2σ correlations with sample gp129b and c (Talbot ACD). No further correlations are noted.

Gp123c (Wicomico ACD) shows 1σ correlations with gp1422g (Princess Anne ACD), gp1421d (Pamlico ACD) and gp123d (Wicomico ACD). Correlations at the 2σ level are displayed with gp129b (Talbot ACD), gp124b (Penholoway ACD) and gp127b (Okefenokee ACD).

Sample gp123d (Wicomico ACD) displays 1σ correlations with samples gp1422 d and g (Princess Anne ACD), gp1421d (Pamlico ACD), gp123c (Wicomico ACD) and gp127b (Okefenokee ACD). 2σ level correlations are seen with gp1421c (Pamlico ACD), gp129b (Talbot ACD) and gp124b (Penholoway ACD).

Gp123f (Wicomico ACD) correlations at the 2σ level are observed with gp129c (Talbot ACD) and gp127c (Okefenokee ACD). No further correlations are displayed.

Sample gp127b (Okefenokee ACD) shows 1σ correlations with gp1422 and g (Princess Anne ACD), gp1421 (Pamlico ACD), gp123d (Wicomico ACD). 2σ correlations are seen with gp1421c (Pamlico ACD) and gp123c (Wicomico ACD).

Gp127c (Okefenokee ACD) displays no 1σ level correlations with any of the other ACDs. Correlations at the 2σ level are observed with gp123f (Wicomico ACD).

Though included on the table for completion of the data set due to the low DRC r^2 value of the Ti-Li option D signal for sample gp127e this sample is considered unreliable and is excluded from further analysis.

3.4 OSL Results

Standard OSL dating of the Pamlico and Princess Anne ACDs yields the following results. In all samples the number of aliquots that gave a D_E was low with $n = <13$ and the other aliquots being saturated. Table 11-14 summarize the results of the OSL dating experiments. While few aliquots gave D_E nearly all aliquots from the

samples display dose response curves that allow for an estimation of the saturation dose to be made and a minimum age of the deposit to be estimated.

Due to the few aliquots to yield standard OSL D_E in this study the analysis of the standard OSL results of the of the samples is limited. Statistical information on the D_E distribution can be found in Appendix 4.

Based on the character of the samples and the criterion proposed by Bailey and Arnold (2006) and Arnold et.al. (2007) the Minimum Age Model (MAM) (Galbraith et.al., 1999) was determined the best fit for samples gp1421d and gp1421f. The Central Age Model (CAM) (Galbraith et.al., 1999) was determined as the best fit for sample gp1422d. Sample gp1422g is omitted as only one aliquot yielded a D_E . Reported in Tables 11-14 is the D_E value of the samples calculated using the CAM as well. Also included is the mean D_E of the samples and its 1σ error.

The D_0 value for the samples can be found in Table 11-14. This value was calculated using all aliquots that have acceptable growth curves (see section 1.6.1) (Figure 34). D_0 values range between 40-47 Gy calculated from $n = 46-48$ aliquots.

Thermal Transfer OSL (TT-OSL) was attempted on samples gp1422d, gp1422g, and gp1421d. In all samples TT-OSL results in more aliquots being accepted than with standard OSL. The results of the TT-OSL when fit to Bailey and Arnold (2006) and Arnold et.al. (2007) criterion determined that the CAM is the best fit all of the TT-OSL samples. Results of the TT-OSL dating can be found in Tables 11-14. The D_0 values of the TT-OSL test can be found in Tables 11-14. The D_0 values of the TT-OSL test were determined using the same technique as the standard OSL (see above). The TT-OSL D_0 values are within error of the standard OSL D_0 values. A TT-OSL bleaching test shows that the TT-OSL signal is completely bleached after 24 hours in a SOL simulator. This is equivalent to 3-4 days of natural sunlight exposure.

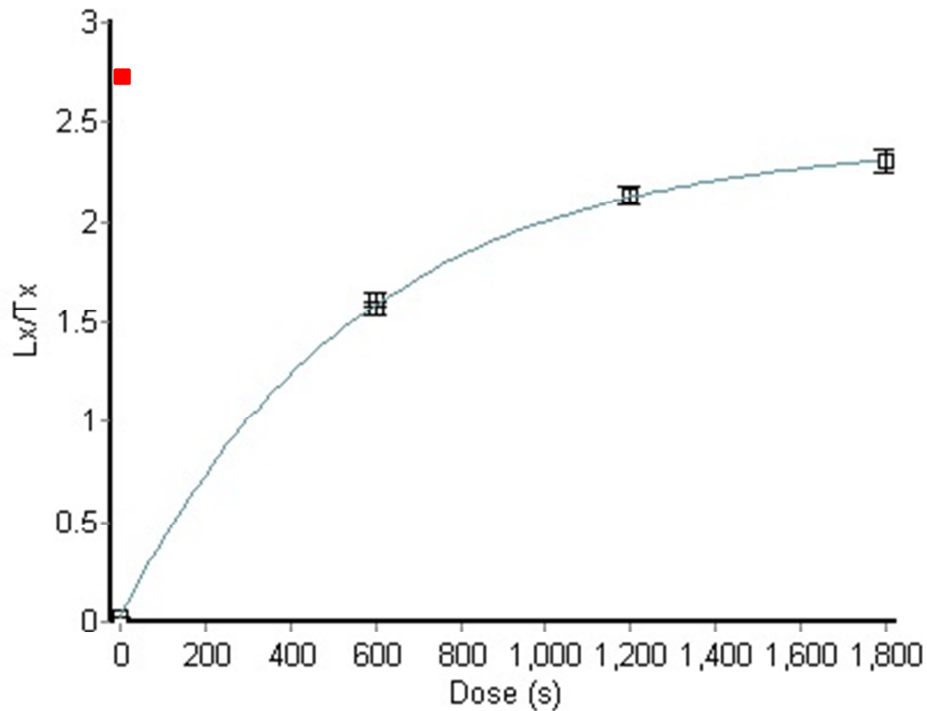


Figure 34: Typical OSL dose response curve (DRC) of a Georgia ACD measured at McMaster University. Dose in time of exposure to the source is shown on the x axis with each 100 seconds correlating to roughly 12 Gy. The regeneration points are shown as white boxes at 50, 100 and 150 Gy. The red box shows the natural luminescence of the signal. Note that this is beyond the range of the dose points and very close at the saturation point making this aliquot unusable to determine a D_E . The good fit of the DRC is still usable for determining the Do of the OSL signal.

Included in tables 11-14 is an analysis of the OSL, TT-OSL, Ti-H, and Ti-Li option D (SSE) ESR results. This analysis uses Galbraith (2003) homogeneity test (explained in section 3.3.1) to determine the age agreement between the above D_E . In all cases OSL did not agree with the Ti-Li D (SSE) ESR D_E . Sample gp1421f shows agreement at 1σ between the OSL D_E and the Ti-H ESR D_E . Gp1421d shows agreement between the OSL D_E and the Ti-H ESR D_E at 2σ while the TT-OSL and Ti-H ESR D_E show agreement at 1σ . Sample gp1422d shows the best agreement with OSL, TT-OSL, and Ti-H ESR all agreeing at 1σ . Gp1422g shows no agreement according to the test.

Dose rates used to calculate the age of the OSL sample are the same as those used to calculate the age of sample with the ESR D_E . See section 3.3 for a review of the dose rates.

The ages of the Pamlico OSL samples (gp1421d and gp1421f) agree stratigraphically with one another, with ages of 55.43 ± 4.39 ka and 91.49 ± 8.38 ka respectively. While the Princess Anne deposits is stratigraphically younger than the Pamlico the OSL age from the upper sample yield an age of 121.72 ± 15.48 ka. This age is older than both of the Pamlico ages. The significance and reliability of these ages will be discussed in Chapter 4.

The calculated standard OSL saturation dose ($2 \cdot D_0$) of these samples range from 80-94 Gy (Tables 11-14). Based on the dose rates observed in these samples this would indicate that the maximum age that could be measured with standard OSL would be approximately 150 ka (highest $2 \cdot D_0$ /lowest dose rate).

Princess Anne GP1422d			
		(Gy)/(Ka)	er(Gy)/(Ka)
OSL	N	7/48	
	Model (suggested)	CAM	
	D_E	102.48	11.98
	CAM D_E	NA	
	Avg D_E (STDV)	108.18	31.79
	Age	128.49	37.98
D0	AVG	47.14	35.27
	SD	13.47	
	Max	60.61	
	Min	33.67	
2xD0 (Sat.)	Max sat	121.22	
	Min sat	67.34	
	Avg sat	94.28	26.94
Ti-H	D0	957.45	217.58
	D_E	91.6	21.53
	Age	108.79	25.95
TT-OSL	N	13/24	
	Model (suggested)	CAM	
	D_E	93.83	6.54
	Do (avg)	47.24	0.78
	Age	111.44	9.69
	D_E stats	P value	
	OSL v. TT-OSL	0.53	
	OSL v. Ti-H	0.66	
	TT-OSL v. Ti-H	0.92	
	OSL v. Ti-Li (D SSE) ESR	0.00	

Table 11: OSL and TT-OSL results of the Princess Anne ACD sample gp1422d. Agreement between the OSL, TT-OSL, and ESR Ti-H are shown. Note the strong agreement between all of the age estimates.

Princess Anne GP1422g			
		(Gy)/(Ka)	er(Gy)/(Ka)
OSL	N	1/48	
	Model (suggested)	NA	
	D_E	Na	
	CAM D_E	NA	
	Avg D_E (STDV)	123.83	11.37
	Age		
D0	AVG	46.15	28.00
	SD	4.04	
	Max	50.19	
	Min	42.11	
2xD0 (Sat.)	Max sat	100.39	
	Min sat	84.22	
	Avg sat	92.31	8.08
Ti-H	D0	783.92	209.88
	D_E	336.55	97.75
	Age	274.3	80.56
TT-OSL	N	24-Jul	
	Model (suggested)	CAM	
	D_E	114.67	14.52
	Do (avg)	48.56	1.62
	Age	93.46	12.85
	D_E stats	P value	
	OSL v. TT-OSL	na	
	OSL v. Ti-H	na	
	TT-OSL v. Ti-H	0.02	
	OSL v. Ti-Li (D SSE) ESR	na	

Table 12: OSL and TT-OSL results of the Princess Anne ACD sample gp1422g. Due to the lack of accepted aliquots, OSL results of this sample are not available. In addition there is no agreement between the TT-OSL and Ti-H ESR age estimates.

Pamlico Gp1421d			
		(Gy)/(Ka)	er(Gy)/(Ka)
OSL	N	13/48	
	Model (suggested)	MAM	
	D_E	39.51	2.26
	CAM D_E	70.5	10.41
	Avg D_E (STDV)	81.72	44.05
	Age	55.43	4.39
D0	AVG	41.40	2.45
	SD	8.85	
	Max	50.25	
	Min	32.55	
2xD0 (Sat.)	Max sat	100.49	
	Min sat	65.10	
	Avg sat	82.80	17.70
Ti-H	D0	598.1	258.61
	D_E	147.71	71.91
	Age	207.24	100.33
TT-OSL	N	19/24	
	Model (suggested)	CAM	
	D_E	99.66	5.91
	Do (avg)	50.25	1.31
	Age	139.82	11.28
	D_E stats	P value	
	OSL v. TT-OSL	0.00	
	OSL v. Ti-H	0.13	
	TT-OSL v. Ti-H	0.51	
	OSL v. Ti-Li (D SSE) ESR	0.00	

Table 13: OSL and TT-OSL results of the Pamlico ACD sample gp1421d. Note the strong agreement between the TT-OSL and Ti-H ESR age estimates and the agreement between the OSL and Ti-H ESR age estimates.

Pamlico Gp1421f			
		(Gy)/(Ka)	er(Gy)/(Ka)
OSL	N	7/48	
	Model (suggested)	MAM	
	D_E	76.05	5.67
	CAM D_E	91.32	10.94
	Avg D_E (STDV)	96.96	32.26
	Age	91.49	8.38
D0	AVG	40.00241	19.28
	SD	7.361987	
	Max	47.36439	
	Min	32.64042	
2xD0 (Sat.)	Max sat	94.72878	
	Min sat	65.28084	
	Avg sat	80.00481	14.723974
Ti-H	D0	620.58	196.99
	D_E	62.35	22.53
	Age	75.01	27.13
	D_E stats	P value	
	OSL v. TT-OSL	na	
	OSL v. Ti-H	0.56	
	TT-OSL v. Ti-H	na	
	OSL v. Ti-Li (D SSE) ESR	0.00	

Table 14: OSL results of the Pamlico ACD sample gp1421f. TT-OSL was not conducted on this sample. Shown are the results on correlation of the OSL age and the ESR signals. Note the agreement between the OSL and Ti-H ESR age estimates.

Chapter 4: Discussion and Conclusion

4.1 GPR Discussion and Interpretation

The GPR analysis of the Georgia ACDs provides deep penetration into the subsurface and allowed for imaging of subsurface features. The younger ACDs appear to show more detail, clearer and more defined reflections, than the older ACDs. This observation is consistent with those of Hails and Hoyt (1969b), Howard and Scott (1983) and Huddleston (1988) that there is a lack of structure in the outcrops of the various ACDs. They attribute this to post depositional modification. Older ACDs will have experienced a longer period of modification and therefore greater post depositional modification. The GPR reflection differences in the older versus younger GPR profiles support this conclusion.

Table 3 provides a depositional environment interpretation to the radar facies presented in section 3.1. Figures 23-27 (section 3.1) show the depositional environment of the GPR profiles.

The two main radar facies found in the upper ACDs GPR transects are interpreted to represent washover deposition (westward, landward dipping facies, element A, washover fan) and beach deposition (eastward, shoreward dipping facies, element C, beach face) (Costas et.al, 2006). The landward dipping facies also indicate a period of barrier vertical accretion (Costas et.al, 2006). The element C east-dipping radar facies are nearly identical to modern barrier beach progradation observed by Jol et.al. (1996) on Jekyll Island, Georgia (Figure 35). GPR10 (Okefenokee ACD) shows significant washover deposition (characterized by element A) while GPR1 (Talbot ACD) and GPR4 (Wicomico and Penholoway ACD) contain more east-dipping beach progradation facies (characterized by element C). This could indicate a longer period of stability, increased sediment supply, and slower abandonment of the Okefenokee ACD. The lack of significant washover deposition in the Wicomico, Penholoway and Talbot ACDs would indicate that these surfaces experienced a low sediment flux during deposition and were abandoned quickly during regression. The lack of a clear boundary on the land surface

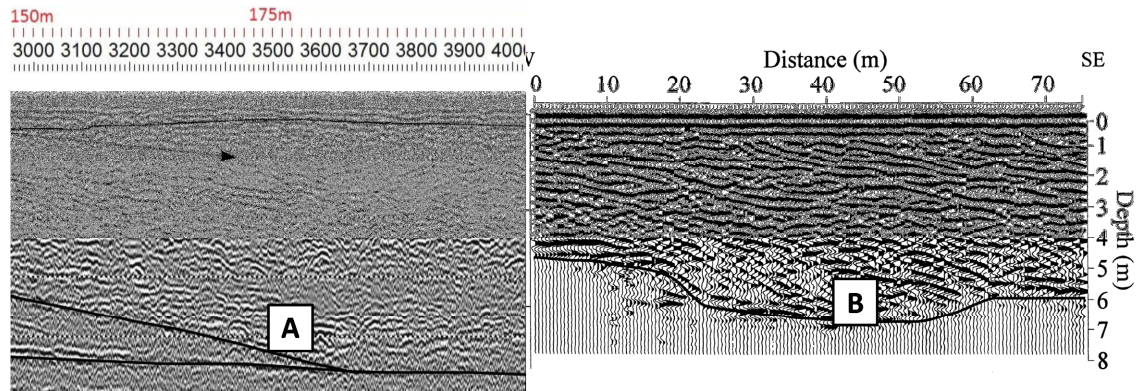


Figure 35: Comparison between the GPR radargram seen the Georgia ACDs (element c, most common element) shown in A and GPR radargram of the modern Georgia barrier island, Jekyll Island, as shown by Jol et.al. (1996) shown in B. Note the similar dip and character of the reflections. Black arrow denotes humate development.

between the Wicomico, Penholoway and Talbot ACDs suggest that they were deposited quickly one after the other without a major erosional period. These conditions support the conclusions of Huddleston (1988) that the Penholoway modified and reoccupied the Wicomico in southern Georgia and that the Talbot is a modification of the Penholoway.

The lower ACDs contain three major facies, the two found in the higher ACDs (element C, east dipping beach facies, and element A, west dipping washover facies) and an additional higher angle sigmoidal facies, element D. This latter facies is interpreted as dune front type deposit. The apparent dip of approximately 20° would be a minimum dip angle for these deposits with the true dip being steeper. This high angle facies D is found only in GPR21 on the Pamlico ACD. Above the high angle D facies is a bounding surface between it and the shoreward dipping facies of element A. This situation is not observed on the Princess Anne ACD radargrams, nor on those of the upper ACDs. It is interpreted that facies D is a preserved dune facies and has been covered with material from a subsequent transgression (element C, beach facies). This evidence supports Huddleston's (1988) hypothesis that the Pamlico back barrier region has been occupied many times in the Pleistocene to Recent. It is possible that this facies is observed in the lower ACDs as a result of their younger age with well-preserved reflectors in comparison to the older upper ACDs.

The boundary mentioned above (between facies D and facies C in the Pamlico) would be a useful sea level indicator as it represents a possible ravinement surface (see

Figure 24). This surface would indicate that sea level was between -4 to 2.25 m above the current sea level. Two other possible ravinement surfaces are found in the Talbot ACD between facies B and C (see Figure 25) and the Okefenokee ACD between facies B and A (see Figure 27). Facies B has been interpreted to represent a strata that contains a number of large pebbles (based on the numerous point reflections observed) unfortunately in both cases this interpretation could not be confirmed as sediment cores did not penetrate these units. In the case of the Talbot the ravinement surface would indicate a sea level of approximately 9.5 m above current sea level and the Okefenokee surface a sea level 37 m above modern sea level. It is possible other ravinement surfaces like those found in the Pamlico exist in the upper ACDs but due to the reduced structure seen in the older ACDs they are difficult to observe with GPR.

In all cores except core gp124, a number of units contain sediment grains that are coated with a brown to black surface coating noted as “black organic?”. This phenomenon has been observed by other workers as well (Swanson and Palacas, 1965; Hails and Hoyt, 1969; Parham et.al., 2013). The coating is caused by humate leached into the groundwater from decaying surficial plant materials (Hails and Hoyt, 1969). The presence of this material indicates a significant amount of groundwater flow through the ACDs and is consistent with other data indicating the highly weathered condition of these ACD deposits. This humate can interfere with the coring process as it is well cemented and expands when cored, resulting in a foamy liquid that can lock core liners within the core barrels and render penetration impossible (at least by the coring equipment used in this study). Comparison of GPR data and the location of humate, based on lithological logs and refusal depth during coring, now provides a method of identifying the humate rich regions with GPR. The humate can be identified by a GPR facies with very low amplitude and little structure but which allows for the EM pulse to travel through it and image the strata below the humate region. An example of this can be found in core gp1421 in GPR21 (Figure 35). Note that the GPR signal becomes very weak (attenuated) in the region containing abundant humate.

4.2 Sediments and Nature of the ACDs Morphology

4.2.1 Georgia Sediments

The dominance of quartz and lack of feldspar in these deposits has been noted by several previous works (see Chapter 1.) and confirmed in this study. Hails and Hoyt (1969b) noted the lack of feldspars and attributed this to pedogenic and groundwater processes. The hydrolysis of feldspars would provide the source of clay minerals found in the core which consists otherwise of moderately to well sorted quartz sands.

The clay concretions found in cores gp124 and gp123 resemble shell castings. Dissolution of carbonate shells by groundwater movement in southern Georgia is discussed in Markewich et.al. (2013). Significant clay or mud in the deposit (from weathered feldspars in this case) can infill the void left by the shells (Parham et.al., 2013). Parham et.al. (2013) noted the presence of these types of trace fossils in their work in Virginia and North Carolina in similar depositional environments as here in Georgia. These trace fossils hint at a marine or near shore depositional environment for their associated lithological unit. This is especially true for the Wicomico core which contains a layer rich in these concretions.

In addition to the shell casts the condition of the quartz grains suggests deposition in a subaqueous environment. The rounded and pitted conditions of the grains suggest significant transport but the lack of frosted grains suggest that this transport was not subaerial. This indicates that the deposits are not subaerial aeolian near shore dunes.

Heavy minerals layers in the core gp124 are common in foreshore and backshore beach environments (Howard and Scott, 1983). Pirkle et.al. (2013) studied the heavy mineral deposits of Georgia and concluded that most of them found in with the sandy barrier deposits of the ACDs. While distinct laminations sequences were not found in the cores of this study, fine isolated laminations and disseminated heavy minerals were. The thick bands of heavy minerals noted by Pirkle et.al. (2013) and others could have been destroyed during post-depositional process or during coring (as we see occurring in the gp124 core where the layer appeared to be disturbed). This combined with the shell casts

provides significant evidence that sea level was at the elevation of the ACD at one time. Previous works discussed in Chapter 1 also support this conclusion.

The clay-rich lithologies found in the lower ACDs indicate a variable depositional environment. The lower units of the Pamlico core (gp1421) contain beds of alternating clay and sands, consistent with descriptions of the Satilla Formation (Huddlestun, 1988). These clays are organic rich and sticky, and seem to be most similar to the marsh-type clays described by Huddlestun (1988). This would indicate then that the sands above these clays were deposited on top of the paleo-marsh in a regressive or progradational environment.

The core and GPR of the Princess Anne deposit appear to show a more complex history. The core sediments show a number of fining upward sequences with coarse sand bases. While the marsh-type clay is found in this core as well, it is much more isolated and appears higher in the core. In terms of absolute elevation the clay units found in the Pamlico and Princess Anne ACDs occur within 1m of each other. The upper portion of this cores lithology is again consistent with the description of the Satilla Formation by Huddlestun (1988). Fine sands are found under the marsh-type clay in this cores. This material could be of Satilla Formation or underlying Cypresshead Formations. The lowest GPR facies found in this ACD is radar facies A similar to that found in the Pamlico GPR. The numerous graded sequences found in this ACD and limited marsh-type clay indicates that the Princess Anne may have been formed from a number of sea level occupations. Its low elevation would allow for relatively small variations in sea level to flood the ACD.

4.2.2 Morphology of the ACDS

Rhea (1986) and Kellam et.al. (1991) note that the morphology of the upper and lower ACDs is different, with the upper ACDs appearing more continuous and elongated and the lower ACDs shorter and dissected similar to the modern barrier islands.

The modern barriers of Georgia (as well as southern South Carolina and very northern Florida) are classified as short with large marshes, the result of the shallow shelf

morphology of the Georgia Bight. To the north in northern South Carolina and south in Florida the barrier islands become elongated and their marshes shrink as a result of the diminished influence of the Georgia Bight and increasing wave energy (Hayden and Dolan, 1979).

The Pleistocene barrier islands of Georgia “stand out clearly as anomalous feature” (Hayden and Dolan, 1979) in that they do not seem to follow the morphological patterns seen throughout the modern Atlantic coast. Furthermore the modern Georgia barriers do fit the patterns discovered by Hayden and Dolan (1979). This would indicate that processes not explored by authors controlled the morphology of the Pleistocene barriers of Georgia or that they were formed under different bathymetric conditions than the present. Bathymetric changes associated with the formation of the Georgia Bight could account for a shift in barrier morphology through time. In this case the ages of formation of the upper and lower ACDs would provide the timing of such a change.

4.3 ESR Discussion

The average percent error for each of the samples (including all signals and fits except the Ti-H signal) ranges from 13-45%. The larger error percentages are generally found in the Al signal age estimates and in the Ti-Li option A values measured at FSU. While most of the signals had DRC r^2 values that were above 0.95, those that didn't were generally the Al signals and the Ti-Li option A signals.

4.3.1 ESR Ages

The lack of agreement between the Al and Ti-Li option D signal ages in this study suggest that the sediments were not exposed to enough light to fully reset the ESR signal during deposition. This is supported by the ESR signals found in the modern dune and swash zone on Jekyll Island, Georgia. In this case the Ti-Li would better approximate the true age of the deposition due to the shorter exposure time needed to bleach the Ti-Li than the Al signal, allowing for more of the residual signal to be removed.

In this study the Ti-Li D_E is determined using two methods, option A and option D (Tissoux et.al, 2008; Duval and Guilarte, 2014). Duval and Guilarte (2014) state that the D_E value of these two measurements should be equivalent. In the samples measured at Osaka University this is the case, while samples measured at FSU yield a larger D_E for the Ti-Li option A. As mentioned in Chapter 3 option A Ti signals in some cases agree with the Al signals seeming to indicate a robust age but due to the r^2 value of the Al signals this age is unreliable. The reason for this apparent agreement in the FSU data could be result of interference from the Al signal resulting in an overestimate of the first Ti-Li peak. This issue was eliminated by using measurement conditions at Osaka which isolated the Ti-Li signal, that is conditions that more accurately measured the Ti-Li signal. For this reason Ti-Li option A ages that do not agree with the option D ages should be disregarded as inaccurate in this study no matter the r^2 values of the DRCs. Ti-Li option D ages are therefore the closer approximation of the depositional age of the samples.

When the exponential+linear fit is applied to the Al signal (Table 7 continued) five samples show age agreement between the Ti-Li D (SSE) D_E and the Al (Exp+Lin) signals. Three of these samples are disregarded as the Al Exp+Lin fit results in a DRC r^2 value of under 0.95 and a D_E error estimate that was close to or greater than 50%. Sample gp1421f (Pamlico ACD) shows agreement between the Ti-Li D (SSE) and Al (Exp+Lin) signals (both with r^2 values over 0.95) with an average age of 329.57 \pm 86.51 ka with the Al signal age being reduced to allow for agreement (when compared to the Al (SSE) fit). The other sample that shows agreement is gp129b (Talbot ACD) (both signals r^2 values are over 0.95), though not at a 1σ level, with an average age of 917.94 \pm 200.18 ka. In addition to these samples, sample gp129c shows agreement between the Al (Exp+Lin) and the Ti-Li D (Ti2) (as well as the Ti-Li A (Ti2)) at a confidence level of 1σ with an average age of 2431.23 \pm 672.15 ka with all signals r^2 values over 0.95.

Based on all of the ESR data, it seems best to proceed with an analysis which makes the assumption that comparisons among samples where good agreement between Al and Ti-Li signals does not occur can still be made using an assumption that the Ti-Li

D signal option provides the best age estimate. Though it is acknowledged that these may be significant overestimates, the shorter zeroing time relative to the Al signal leads to the use of this assumption. The SSE fit of the Ti-Li option D signal is chosen to make the comparisons as all samples have the additive dose range to fit this curve while only the samples measured at Osaka University can fit the Ti₂ curve.

The above assumption is complicated by the discovery of a non-zero Ti-Li signal in the modern shoreface. The reworking of the Satilla and Cypresshead Formations during formation of the ACDs would result in sediments that received variable zeroing of their Ti-Li signals depending on the amount of exposure experienced during the reworking. Some samples could have experienced an exposure time long enough to completely bleach the Ti-Li signal but too short to completely bleach (or bleach to the residual level) the Al signal. In this case the Ti-Li signal age would be accurate. Other samples may have been exposed for less time than sufficient to completely bleach the Ti-Li signal as well as the Al signal. Here the Ti-Li signal age would be an over estimate of the age deposit.

Evidence of variable bleaching is characterized by age inversions which can be seen in the Ti-Li option D signals seen in the Pamlico, Wicomico (the lower most sample of the Okefenokee, which has an age that would lead to an inversion, has been rejected due to the low r^2 value of its Ti-Li option D DRC). Problems with the local dose rate estimates (associated with true moisture content or local heterogeneity in the 30cm radius around the sample) could also contribute to these age inversions but we attempted to be minimized by the sampling strategy. In the case of the age inversion in the Pamlico ACD (gp1421 c, d and f) the variability in the dose rates among the samples is approximately 15% indicating that the age inversion is caused by the D_E of the signal not the dose rate (Table 5). The Ti-Li ages of these samples do not agree with one another at either the 1σ or 2σ level. This is evidence of variable bleaching of the sediments of this ACD. This will be discussed further below. In the Wicomico ACD the age inversion occurs between sample gp123c and gp123d. In this case, while dose rate variation is approximately 30%, the samples do agree within error and no conclusion can be made about the source of the

inversion (ie. dose rate variability of variable bleaching) (Table 5). In addition the overall trend for the Ti-Li D option ages is found to be as expected to some extent, due to considerations of the geomorphological landscape (from east to west) and from the underlying mapped geology, as seen below.

As mentioned above inaccurate estimates of the true long-term burial dose rates may be responsible for age inversions in this study. In addition to this, previous works that have concluded that the ACDs of Georgia have been modified post-depositional (Neiheisel, 1962; Hails and Hoyt, 1969b), specifically with respect to feldspar content (a major source of K and radiation dose), would indicate that the dose rate measured using the modern sediments may not be representative of the dose rate conditions experienced by the sediments in the past. As noted in section 1.3, it appears that the removal of feldspars from the ACDs occurred rapidly over geological time with significant reduction in the feldspar content seen between ACDs of Holocene age and those of late Pleistocene. This would expose the sediment samples to a brief period of high dose during their initial deposition (perhaps approximately 10,000 years) as the feldspars present were slowly removed, followed by a dose rate more similar to those measured in this study for their remainder of their burial. This situation would result in a true age of the material that is overestimated by the ages given in this study (ie. the true age of the deposits would be younger than the ages given), which in many cases are only maximum age estimates anyway. The modeling and determination of the dose rate of these samples over geological time is a complex endeavor requiring research and experimentation outside the realm of this project. As such the modern sediment dose rates are used to estimate the maximum age of the deposits.

Using the Ti-Li option D (SSE) and the homogeneity chart a number of correlations using their P-values between the ESR sample ages within core and among ACD's in this study can be seen.

The Princess Anne ACD shows strong correlation (at 1σ uncertainty) between the lower most samples gp1422d and gp1422g. The correlation between the upper two samples gp1422c and gp1422d is less robust (2σ). Based on the GPR results (Figure 36)

and the ESR correlation data it is interpreted that samples gp1422 d and g represent one depositional age and gp1422c represents a younger depositional event.

Samples collected from the Pamlico ACD (gp1421 c, d, f) show an age inversion with the youngest sample, gp1421f, being the stratigraphically lowest sample collected (Figure 37). There is no correlation between any of these samples at a value greater than 2σ . These results are interpreted to be the result of more incomplete bleaching of the ESR signal (see section 4.3.2 for more about incomplete bleaching) in the upper two samples as discussed previously. As stated above when the Exp+Lin fit is applied to the Al signal there is an age correlation at 330 ± 87 ka in the sample gp1421f. This sample is therefore the most reliable age of the Pamlico ACD. As this is the lower most sample this would indicate that the samples above gp1421f (samples gp1421 d and c) were deposited after 330 ± 87 ka and the ages indicated by the Ti-Li option D (SSE) signals are over estimates. Any age correlations based on the upper two samples are discounted based on this evidence. This would indicate that the possible ravinement surface observed in the Pamlico GPR would be younger than a maximum age of 330 ± 87 ka based on sample gp1421f. As the sample above the surface is rejected due to other criteria, a minimum age of this surface is not obtainable.

Age correlation in the lower ACDs show that the sample gp1422c correlates with sample gp1421f. This would indicate that all the samples for the Pamlico ACD correlate with the upper most sample of the Princess Anne ACD being deposited between 243-417 ka (Figure 38). This time range covers Marine Isotope Stages MIS 11, MIS 9, and MIS 7. These ages estimates are in agreement with those made by Hoyt and Hails (1967), Colquhoun (1969), and Huddelstun (1998) of these ACDs being formed during the deposition of the Satilla formation during the Pleistocene to Late Pleistocene. While ESR ages agree with the above mentioned estimate from fossil assemblages, they do not agree with the ESR ages of the FL correlative unit, the Chatham Formation, as published by Burdette et.al. (2012) of 860-1090 ka. While the lower end of the age estimates determined by ESR of the Pamlico agrees with the Pamlico ages published by Markewich

et.al. (2013) (191-243 ka), the ESR age Princess Anne deposits appear to be much older than the range stated by Markewich et.al.

The lower samples of the Princess Anne (gp1422 d and g), while correlating well to each other, do not correlate with the above mentioned previous works. They do show strong correlation (at 1σ) to upper ACD samples gp123 c and d (Wicomico ACD) and gp127b (Okefenokee ACD). These deposits cover a depositional time frame ranging between 429-816 ka. Due to the strong correlation between these lower ACD units and those of the upper ACDs these deposits are considered to be the same deposit. This hypothesis will be explored further below.

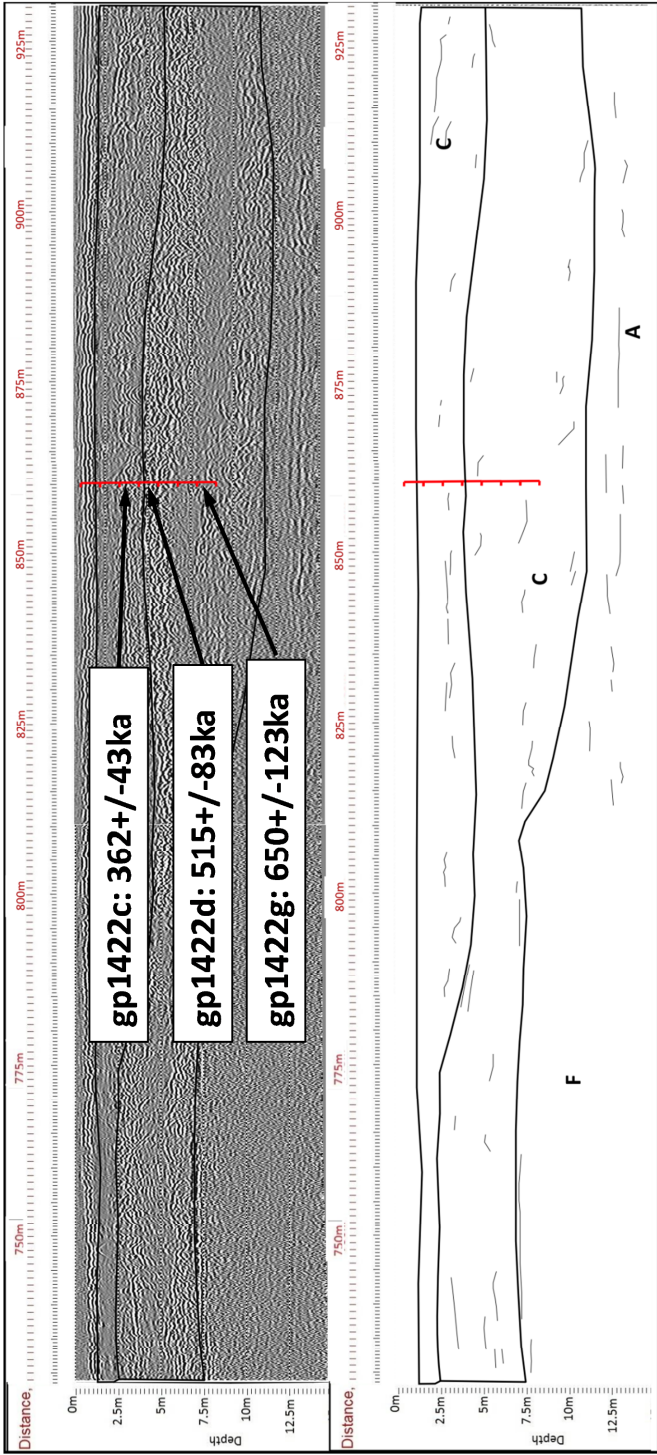


Figure 36: GPR radargram and ESR ages of the Princess Anne ACD. The location of the core gp1422 is shown in red. Bases on the GPR and ESR data this radargram shows two depositional units. The first is defined by the lower element C region deposited between 432-773ka. The second is defined by the upper element C region and was deposited between 319-405ka. The lower units are consistent with the depositional period and lithological character of the Cypresshead Formation while the upper deposits are consistent with the age and lithology of the Satilla Formation (Huddleston, 1988).

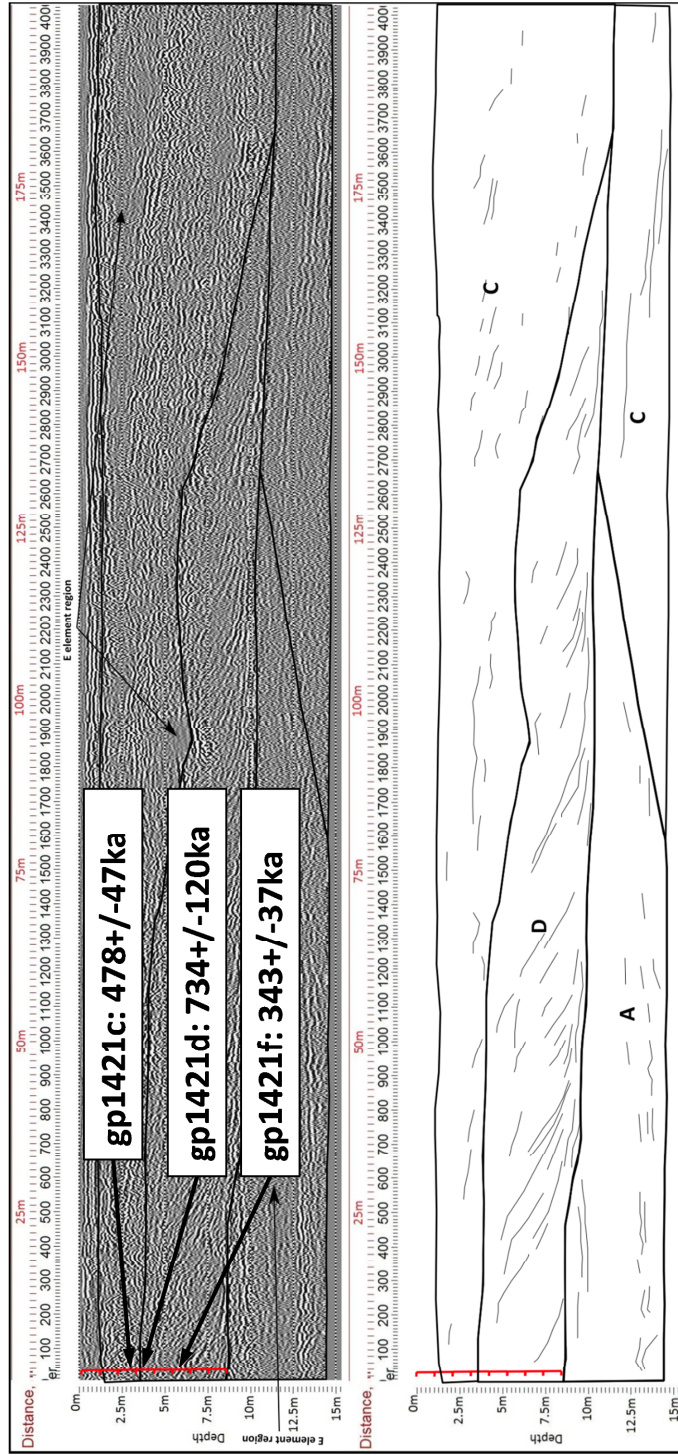


Figure 37: GPR radargram and ESR ages of the Pamlico ACD. The location of the core gp1421 is shown in red. An age inversion is apparent in this ACD. Due to the lower -most sample being determined to be the youngest age and the robustness of the age estimate of this sample (see above), the maximum age of the deposit is constrained by age of this sample (gp1421f). Therefore the age of deposition for this ACD is 306-380ka. The lithological and geochronological data suggest that the deposit defined by the element D region is the Satilla Formation (Huddleston, 1988).

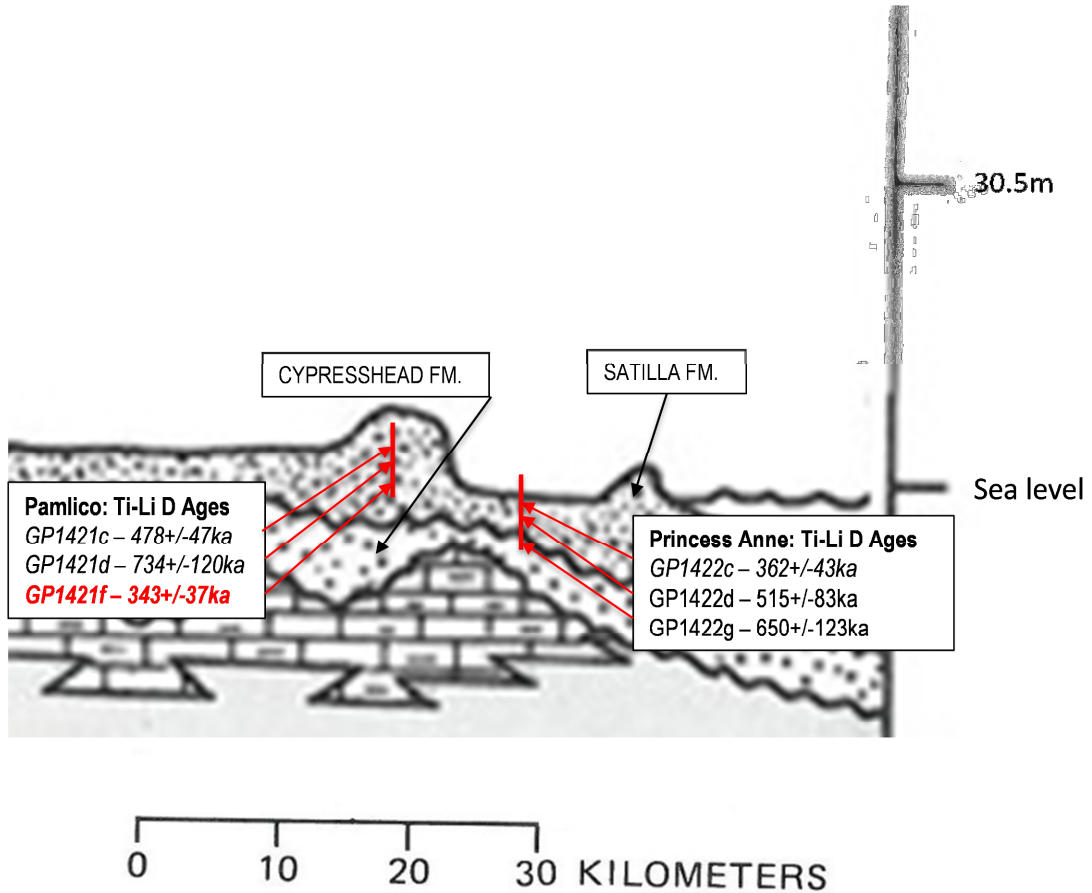


Figure 38: Ti-Li option D (SSE) ESR ages of the lower ACDs of Georgia. Shown in italics are those samples attributed to the Satilla Formation, while those that are un-italicized are attributed to the Cypresshead Formation. The sample shown in red has agreement between the AI (Exp+Lin) age and the Ti-Li option D (SSE) and is considered a more robust age estimate.

No correlation exists between the Talbot samples gp129b and gp129c. This result is interesting as these samples were collected very close together (Figure 39) with no GPR boundary between them. Sample gp129b shows a strong correlation to sample gp124b (Penholoway) and less robust correlations between samples gp124e (Penholoway) and pg123 c and d (Wicomico). Sample gp129c correlates at the 2σ level with gp124e (Penholoway) and gp123f (Wicomico). Although sample gp129b is one of the samples that yield an age agreement between the Ti-Li D (SSE) and Al (Exp+Lin) (918 \pm 99 ka, average age), the age disagreement between the upper and lower sample still stands. Unlike the situation in the Pamlico where the age agreement could shed light on the status of the samples above, gp129b is the upper most sample and the age provides a lower bound for the depositional age, not an upper. These ages indicate that the possible ravinement surface observed in the GPR radargram of the Talbot ACD would have to be older than the maximum age of 1719 \pm 230 ka.

Like the Talbot ACDs, the Penholoway ACD samples show no agreement between the upper and lower samples measured. Gp124b with an age of 949 \pm 82 ka does show agreements at the 2σ level with gp123c (age of 745 \pm 71 ka) and d (Wicomico ACD) (age of 661 \pm 135 ka) (Figure 40). No agreements are found when using Ti₂ or Exp-Lin fits instead of SSE fits. Sample gp124b estimated age falls in the range of ages assigned to the Chatham Sequence (Burdette et.al., 2012) while gp124e coincides with the Effingham Sequence age range (Burdette et.al., 2012). A GPR boundary between the two samples (see Figure 40) further supports that these two samples do not come from the same depositional time period.

Samples gp123 c, d, and f, of the Wicomico formation show a slight age inversion between the uppermost sample, gp123c, and gp123d. (Figure 40) These samples agree within a 1σ range and therefore the samples can be considered the same age. As mentioned above these two samples have strong correlations to the lower Princess Anne samples. They also correlate to sample gp127b (Okefenokee) at both the 1σ (gp123c) and 2σ (gp123d) confidence levels. Sample gp123f, while not correlating to the above samples, does correlate at the 1σ with sample gp127e and at the 2σ gp129c (Talbot) and

gp127c (Okefenokee) at the 1σ level. In this the Wicomico ACD it appears that there are two depositional events one characterized by the deposition of gp123f and the other by the deposition of gp123d and c. GPR from this ACD supports this conclusion (Figure 40). The ages of the upper samples of this ACD do not correlate any of the previous ages estimates while the lower sample does correlate to the Trail Ridge age estimate of 2210-6ka- from Burdette et.al. (2012).

The Okefenokee ACD ESR samples (gp127 b, c, and e, Figure 41)) show an age inversion similar to that of the Wicomico ACD. In this case sample gp127c is estimated to be older than sample gp127e below it. Sample gp127e has been rejected on that grounds that none of its ESR signal DRC r^2 values are over 0.95. This negates the age inversion for this ACD. Gp127b does not agree with gp127c. There is a GPR boundary between these two samples (Figure 41) supporting the conclusion that they represent two different depositional events. This would allow for this sample to correlate to the deposition of the Trail Ridge in FL dated to as old as 2200 ka by Burdette et.al. (2012). Furthermore the possible ravinement surface located below sample gp127e would have to be older than a maximum age of 2596 \pm 382 ka.

The upper ACDs show 2 distinct age groups. The first consist of gp123 c and d as well as gp127b that range from 526-796 ka. The second is a group that consists of gp129 b and c, gp124 b and e, gp123f, and gp127 c. This group has an age range of 867-2978 ka. If the Exp+Lin Al fit is used to confirm the age of the sample gp129c (with the Ti-Li D (Ti2) age, 2431 \pm 672 ka) the sample would still fall into this group and age range. Including this sample age pushes the maximum age range of the deposition to 3103 ka (Figure 42).

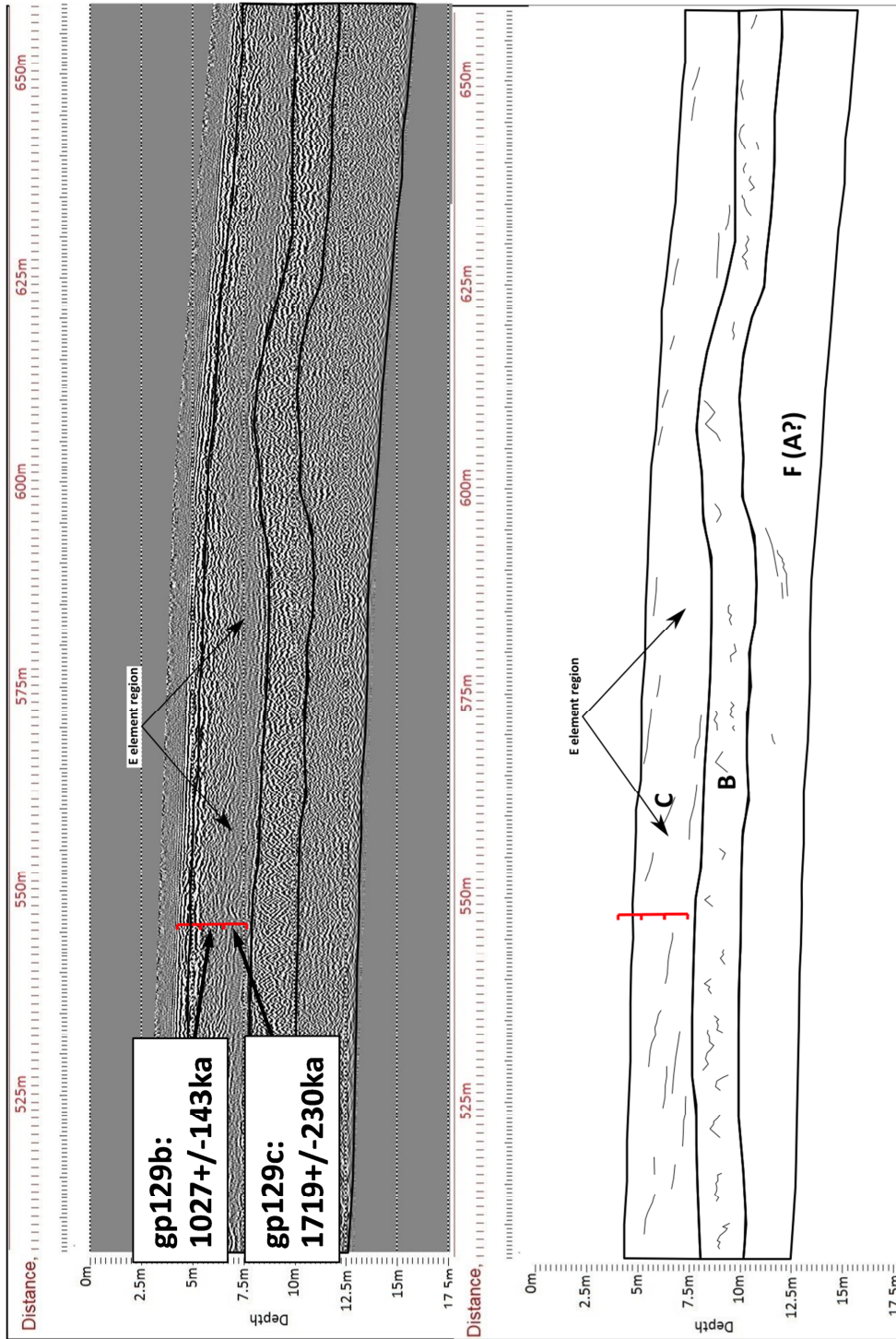


Figure 39: GPR radargram and ESR ages of the Talbot ACD. The location of the core gp129 is shown in red. This ACD shows a depositional age between 884-1949ka. The depositional age and lithology of the sediments are consistent with the Cypresshead Formation.

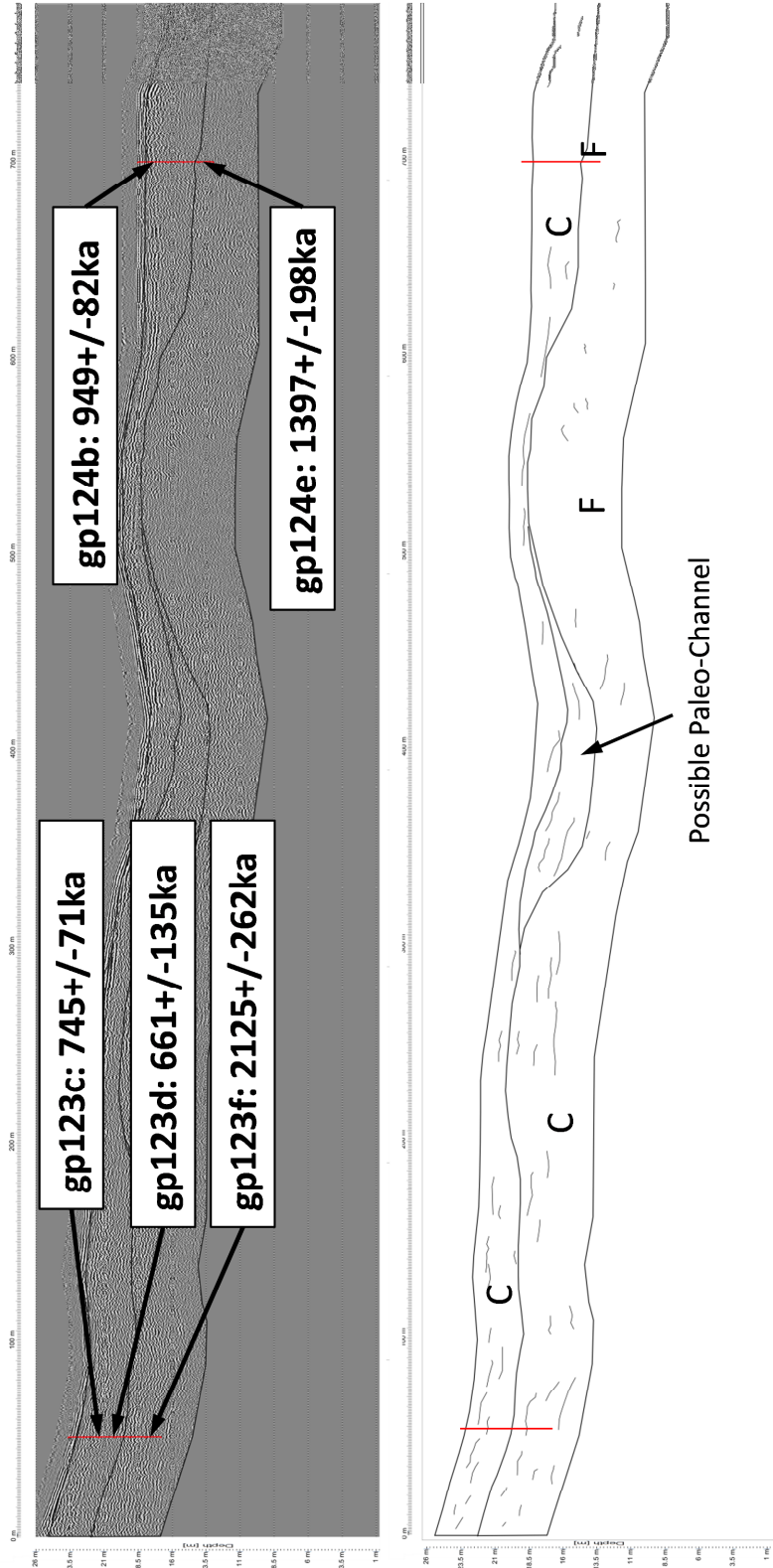


Figure 40: GPR radargram and ESR ages of the Penholoway and Wicomico ACD. The location of the core gp124 (right) and core gp123 (left) are shown in red. The radargram and ESR data point out that both the Penholoway and Wicomico cores each show two closely related depositional units. The first unit is characterized by the lower element C region and older ESR ages, while the second deposit is defined by the upper element C region and younger ESR ages. Both of the deposits are consistent with the age and lithological description of the Cypresshead Formation as described by Huddleston (1988).

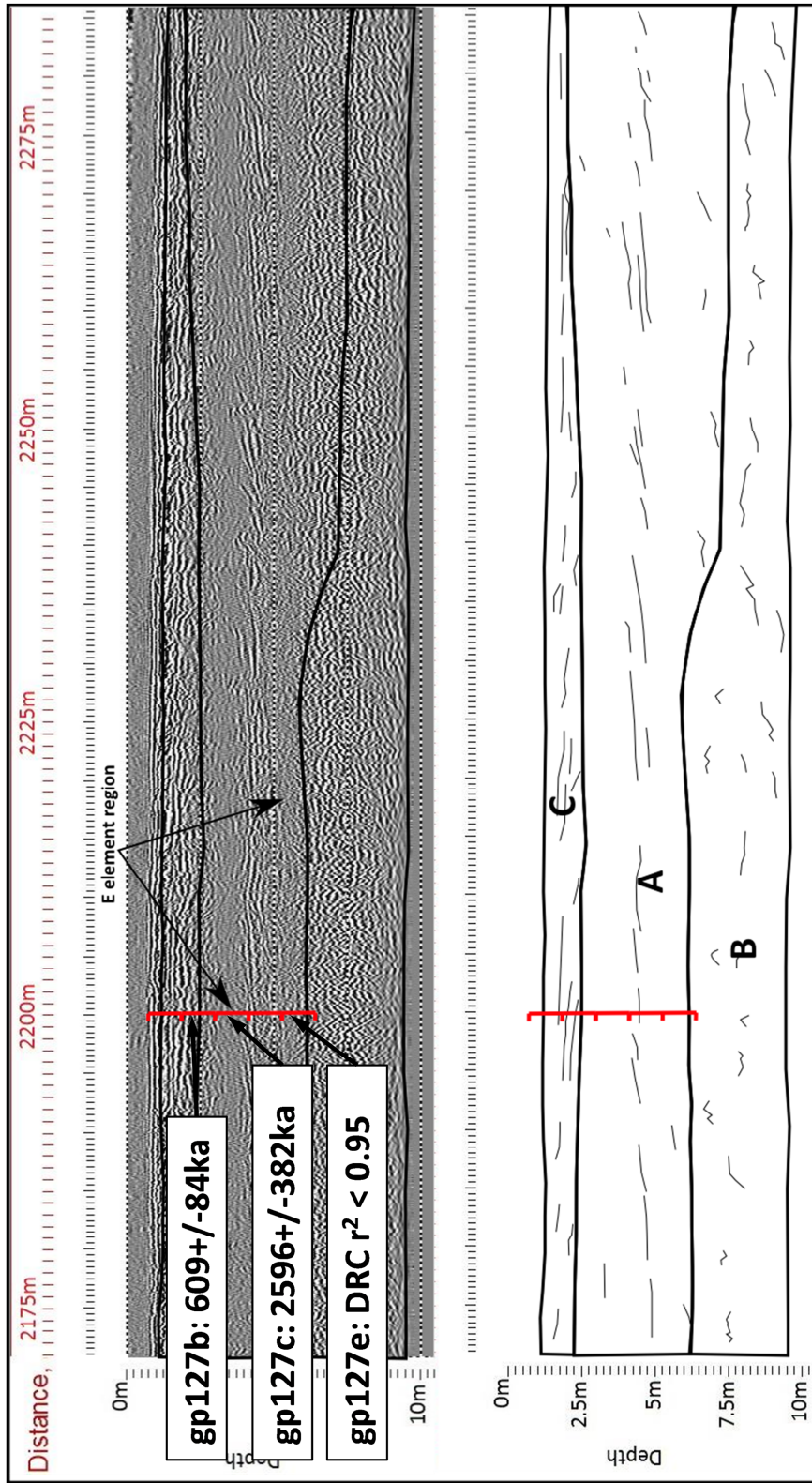


Figure 41: GPR radargram and ESR ages of the Okefenokee ACD. The location of the core gp127 is shown in red. This ACD displays two closely related deposits. The first is defined by the region labeled element A and consist of older ESR ages while the second is defined by the element C region and yielded younger ESR ages. Both of the deposits are consistent lithologically and chronologically with Huddleston's (1988) interpretation of the Cypresshead Formation. Note that due to the low r^2 value of sample gp127e it has been omitted.

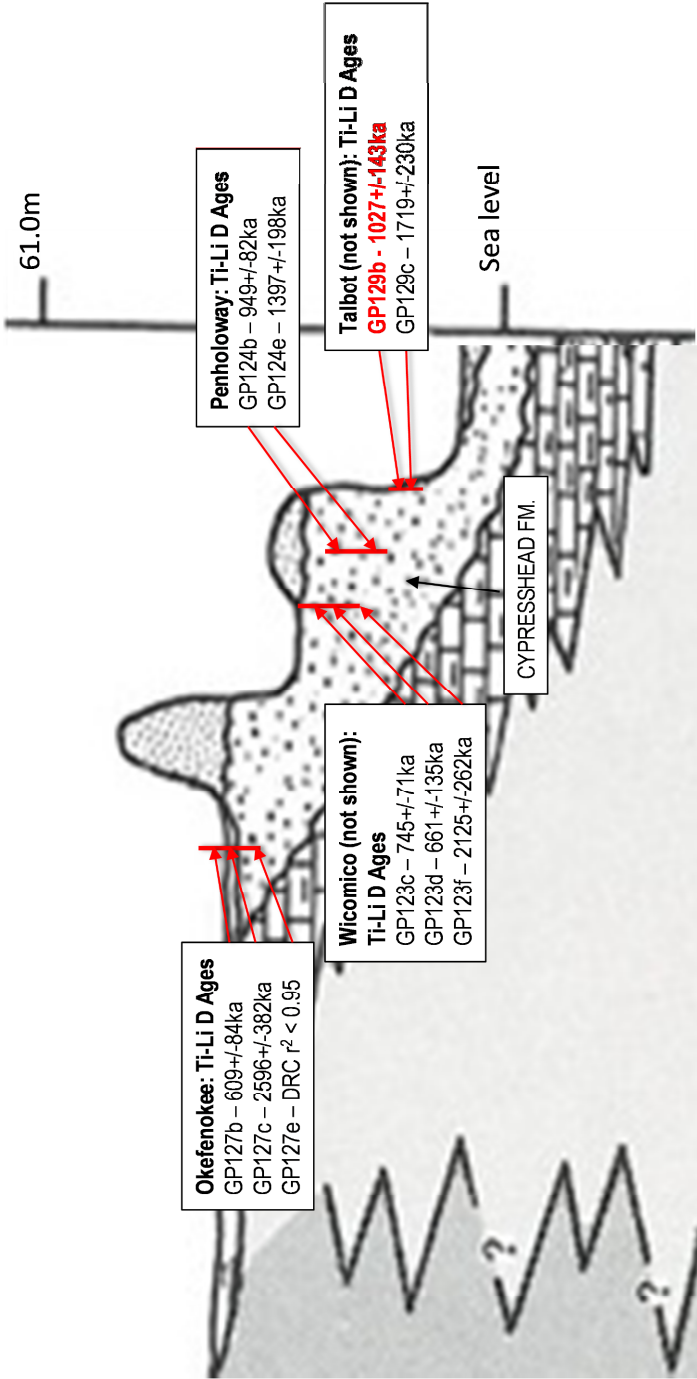


Figure 42: Ti-Li option D (SSE) ESR ages of the upper ACDs of Georgia. All ages shown are attributed to the Cypresshead Formation. The sample shown in red has agreement between the AI (Exp+Lin) age and the Ti-Li option D (SSE), and is considered a more robust age estimate. Note gp127e is excluded due to low r^2 value of the Ti-Li option D DRC fit.

Taken together, the ESR age results from this study show that there are 3 major depositional events. The first includes sample gp1422c (Princess Anne) and all of the Pamlico, gp1421, samples (recall that the age inversion dictates that the age of sample gp1421f be considered the maximum age of the entire deposit). This deposition ranges in age from 243-417ka. The confirmed age of the Al (Exp+Lin) and the Ti-Li D (SSE) on sample gp1421f falls within this age range, supporting this conclusion. These deposits are concluded to represent the deposition of the Satilla Formation. This is consistent with the age range estimated by Hoyt and Hails (1967), Colquhoun (1969), and Huddelston (1998) for the deposition of this formation. The second is from between 433-796ka and is represented by samples gp1422 d and g, gp123 c and d, and gp127b (occurring within the Princess Anne, Wicomico and Okefenokee ADCs). The third consists of samples (from the Talbot, Penholoway, Wicomico and Okefenokee ADCs), which are samples gp129 b and c, gp124 b and e, gp123f, and gp127 c and ranges from 867-2978 ka (3103 ka if the Ti-Li option D (Ti₂)/Al (Exp+Lin) agreement of sample gp129c is accepted). These latter two depositional events are within the time frame of the Cypresshead Formation (Hoyt and Hails, 1967; Colquhoun, 1969; Huddelston, 1998). Core location and elevation data (Figure 43) show that the 433-796 ka group would compose the upper portion of the Cypresshead formation while the group deposited 867-2978(3103) ka would compose the lower portion of the Cypresshead. All of these ages are to be considered maximum age estimates as the incomplete bleaching situation does not allow for confirmed ages to be established. In cases where there is agreement between the Ti-Li signal and the Al (Exp+Lin) the ages can be considered to be more robust.

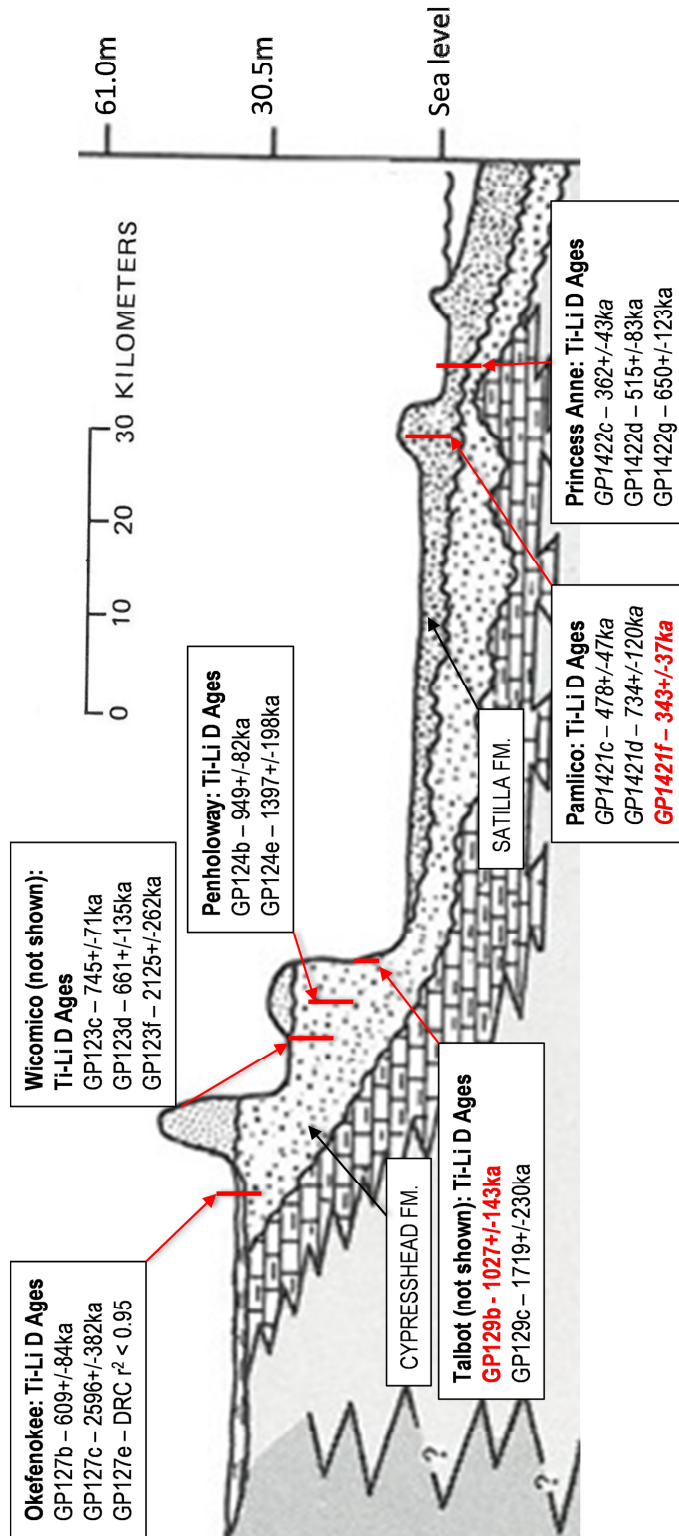


Figure 43: Ages of the ACD samples determined using ESR in this study in relation to the lithology of the Coastal Plain of Georgia according to Huddleston (1988). Sample names and ages shown in italics are Satilla Formation and those in standard text are Cypresshead formation. Ages shown in red have agreement between the Ti-Li option D (SSE) and Al (Exp-Lin) ages. Note that sample gp127e is omitted due to a low r^2 value fit of its' DRC.

4.3.2 Incomplete Bleaching Remediation Test

The following section contains an experimental procedure that does not play a significant role in the interpretation of the ESR results. This section has therefore been placed within the context of the discussion of the data. The presentation of this data is meant to stimulate further research in using these methods.

The non-zero Ti-Li ESR signal measured in the modern coastal deposits of Georgia is unlike the results of Burdette et.al. (2012) from Florida which show complete zeroing of the Ti-Li signal. The source of the sediment for both coastlines is the same (see Chapter 1). The sediments of the Georgia coast are much closer to the source than those in Florida. This suggests that the bleaching of the Florida ESR signal, in particular the Ti-Li signal, occurred during longshore transport of the sediments. As the deposits in Florida are composed of sediments that have a longer longshore transport history they were completely bleached while those in Georgia were not.

Do values reported in Table 4, show that the Al signal would saturate between 2580-46180 Gy while the Ti-Li signal would saturate between 900Gy-4878 Gy (this include both option A and D measurement methods). Saturation at below 5000 Gy is low for the Ti-Li signal which typically saturates at around 10000 Gy (Duval and Guilarte, 2014).

Due to the presence of a non-zero modern signal at Jekyll Island, an experiment was conducted to attempt to remove this “relict” signal from the ESR signals in the ACDs. The goal of this was to ascertain if the removal of the relic signals would result in better agreement between the Al and Ti-Li signals. For the samples measured at Osaka University the average signal intensity of all the signals (Al, Ti-Li A and D, and Ti-H) in the 0d (dune) and 0s (swash zone) samples were subtracted from all of the signal intensities in the ACDs. For the samples measured at FSU (under different measurement conditions that make the direct subtraction above impossible) the percent difference between the bleach and natural of the modern samples was applied to the bleach of the FSU samples and then this value removed from the ACD signals. Due to the above discussion in section 4.3.1 only the option D Ti-Li signals were analyzed from FSU.

Results of this procedure are shown in Table 15. This procedure assumes that each of the ACDs was deposited under the same conditions as the modern barriers (which evidence in section 4.2 above suggest otherwise) and experienced that same degree of incomplete bleaching (i.e. sunlight exposure time prior to burial).

After applying this method two samples show agreement between the Al and Ti-Li signals, sample gp124b and gp124e. Sample gp124b yields an average age (between the Al (SSE) and Ti-Li option D (SSE)) of 614 ± 141 ka while gp124e has an average age (same method) of 847 ± 304 ka. The age confirmation created by this method of gp124b would fall into the age range of the upper Cypresshead group stated above. The age estimate of gp124e would still be grouped within the lower Cypresshead (within error). Within its error range it could also be grouped with the upper Cypresshead deposition as well. This evidence, if accepted would suggest that there was continuous deposition between the upper and lower Cypresshead.

As sample 4b was measured at FSU and required a more elaborate signal removal method this age is less reliable. No other samples show agreement indicating that the assumptions stated above are not true. Samples measured at FSU show significant variations between the Al and Ti-Li signals with some samples the Al D_E being less than the Ti-Li or the Ti-Li resulting in a negative D_E . This could be due to the more elaborate method required to remove the relict signal. Due to the measurement conditions used at FSU there was significant difficulty in determining the signal intensity of the Ti-Li signals in the bleached aliquots of these samples. This is the most likely reason for the negative D_E values in the Ti-Li signals. Further experimentation is needed to determine if this method is useful in ESR dating of incompletely bleached coastal deposits.

Modern Removed (SSE)													
Sample	D _E						Age (ka)						Avg
	Al	Ti-Li (optA)	Ti-Li (optD)	Ti-H	Al	Ti-Li (optA)	Ti-Li (optD)	Ti-H	Ti-Li (optA)	Ti-Li (optD)	Ti-H		
gp1422c	447.37+/- 75.35	103.85+/- 8.52	71.68+/-6.62 (-)148.28+/- 20.43	105.28+/- 16.76	492.26+/-87.10	114.27+/- 11.47	78.87+/-8.58	115.84+/- 19.50					
gp1422d	550.67+/- 197.53		(-)554.80+/- 52.35		654.03+/-234.77	na	0.00	na					
gp1422g	679.59+/- 157.59		113.50+/-9.61 523.26+/- 81.08	45.02+/-7.96	553.89+/-131.19	na	0.00	na					
gp1421c	624.21+/- 165.01	156.88+/- 11.49			761.90+/-203.71	191.48+/- 17.47	138.54+/- 13.92	54.95+/- 10.08					
gp1421d	34.71+/-9.06 64.94+/- 12.03		81.08 (-)95.88+/- 35.71		48.70+/-12.84	na	734.13+/- 119.52	na					
gp1421f	206.43+/- 25.74		(-)207.04+/- 30.24		78.12+/-14.94	na	0.00	na					
gp129b	237.00+/- 35.29	562.47+/- 79.65	563.80+/- 67.98	42.97+/-17.29	440.00+/-60.09	na	0.00	na					
gp129c	451.98+/- 93.51		456.01+/- 33.87		534.02+/-84.52	1267.37+/- 192.25	1270.37+/- 169.05	96.82+/- 38.66					
gp124b	304.89+/- 100.64	278.84+/- 42.42	330.30+/- 43.50	323.12+/- 156.72	610.79+/-128.65	na	616.24+/- 54.91	na				614+/- 141	
gp124e	3379.57+/- 1323.97	1052.34+/- 84.53	1070.10+/- 82.28	373.43+/- 90.14	812.54+/-267.38	743.11+/- 120.68	880.26+/- 127.06	861.12+/- 411.93				847+/- 304	
gp123c	2129.12+/- 538.49	616.38+/- 112.00	660.92+/- 132.36	399.59+/- 102.79	2137.37+/- 841.26	665.54+/- 64.85	676.77+/- 64.07	236.17+/- 58.21					
gp123d	1870.80+/- 359.51	747.15+/- 99.42	809.36+/- 93.82	403.50+/- 106.93	1897.57+/- 489.45	549.35+/- 104.31	589.04+/- 122.20	356.13+/- 93.35					
gp123f	2041.41+/- 548.18	364.36+/- 30.83	380.60+/- 41.61	220.68+/- 88.11	4354.71+/- 858.97	1739.16+/- 248.70	1883.97+/- 240.90	939.24+/- 250.06					
gp127b	1089.00+/- 249.74	651.61+/- 86.84	502.23+/- 60.47	371.55+/- 93.44	2988.50+/- 831.92	533.40+/- 63.50	557.17+/- 76.49	323.06+/- 130.27					
gp127c	3133.02+/- 924.50	1133.99+/- 552.02	1221.64+/- 503.68	367.27+/- 83.26	4158.68+/- 994.47	2488.37+/- 390.36	1917.92+/- 281.59	1418.88+/- 367.67					
gp127e					3868.34+/- 1148.37	1400.14+/- 678.52	1508.36+/- 620.61	453.47+/- 104.60					

Table 15: D_E and age results of the Georgia ACD samples after removal of the modern signal intensity. Note the ages shown in yellow are from samples measured at FSU under different measurement conditions than the modern samples. Therefore significant conversion is needed to apply the removal technique. These ages should be considered with more caution than the others. Only the Ti-Li option D was converted from the FSU data due to the issues with the Ti-Li A signals (see chapters 3 and 4). The Ti-H signal was omitted as well as no measure of its bleached signal (needed for conversion) could be obtained reliably. Note that only two samples show age agreement with this technique, both from the same ACD (gp124, Penholway). The results of this test yield younger ages than the standard method.

4.3.3 Ti-H (Yoshida, 1986) Signal

The Ti-H quartz ESR signal bleaches considerably faster than the Ti-Li signal (Tissoux et.al., 2007) and could potentially determine the depositional age of a deposit that was exposed to less sunlight than necessary to bleach the Ti-Li signal fully. The additive dose plan of the samples measured at Osaka University was designed to measure the Ti-H as well as the Al and Ti-Li signals. In many studies additive dose steps are too large or the first additive doses that are applied are too high. As a result few additive dose points are within the useful range (<+1000 Gy) of the Ti-H signal. This makes fitting of the Ti-H signal difficult with a SSE equation resulting in large DRC r^2 values for this signal. The Osaka samples received additive doses of +200, +400, +600, +800, and +1000 Gy allowing for at least four points within the range of Ti-H stability. Additive doses up to +3000 Gy were used to fit the curve. This was done ensure that the saturation condition of the signal was met. Even with this methodology error estimates remain high as too few data points are present at the <1000 Gy portion of the dose response curve (ie. additive doses close to the natural). For this reason age estimates with DRC r^2 values under 0.95 were accepted in an effort to explore the use of this signal.

All of the Ti-H ages measured (at FSU and Osaka) resulted in D_E lower than that of the Ti-Li signal as was observed in Duval and Guilarte (2014). As all of the Ti-H dose response curves show an increase in intensity with additive doses up to +1000 Gy it can be concluded that the Ti-H signal is not completely saturated in these samples. Furthermore evidence discussed above regarding the modern samples concludes that it is likely that the Ti-Li signal was not completely bleached.

As shown in Table 25-28 the D_E estimates of samples derived from OSL agree with the D_E estimates derived from the Ti-H signal. Using the homogeneity test, discussed numerous times in this text, the Ti-H signal agrees within a 1σ error to all of the OSL D_E (in samples in which it was possible to obtain a D_E) with the exception of sample gp1421d in which the agreement is only 2σ . In samples gp1422d and gp1421d the Ti-H signal D_E agree with the TT-OSL derived D_E at 1σ as well. These results are similar to those found by Beerten (2006) in which Ti-H ESR ages of materials less than

350 ka agree better with independent ages determined by OSL than the Ti-Li ESR signals. This could indicate that the Ti-H signal shares similar characteristics to the OSL signal.

While one could conclude that the Ti-H signal should be used to determine the age of these deposits, the large error in the D_E estimates (resulting from DRC r^2 values under 0.95), low saturation dose (between 238Gy-2682 Gy in this study as determined by $2*Do$ of the maximum and minimum Do values of all the samples), and unknown behavior of the signal at high additive doses suggest that more research is needed before this method can be considered reliable. The results of these signals will be discussed further.

4.3.4 Ga Ages vs Fl Ages

As only two age agreements between the Al and Ti-Li were found in the Georgia samples (gp1421f Al (Exp+Lin) and Ti-Li option D and gp129b Al (Exp+Lin) and Ti-Li option D), unlike the Florida samples in which nearly all showed Al/Ti-Li agreement as measured by Burdette et.al. (2012), a direct comparison of ages is not feasible as too few Georgia samples could be used. Ti-Li option D (SSE) ages were selected to represent the maximum age of deposition of the Georgia ACDs. Burdette et.al. (2012) used the Ti-Li option A signal without a $1/I^2$ in their study of the Florida coastal deposits. This difference also makes a direct comparison to the Florida samples weak.

Table 16 is an age homogeneity chart, similar to those shown in chapter 3, that shows the homogeneity between the Ti-Li option D (SSE) ages of the deposits in Georgia dated in this study and the Ti-Li ages published by Burdette et.al. (2012) of similar (correlative) deposits in Florida. This table shows that many of the deposit ages in Florida agree with those found in Georgia at both the 1σ and 2σ confidence levels using this signal alone.

Elev. (m)	FL Seq.	Sample	Ti-Li (SSE) (ka)	Ti-Li error (ka)	Princess Anne		Pamlico		Talbot	Penholoway		Wicomico		Okfenokee						
					0.3	-1.6	-4.9	3.3		1.6	-0.8	11.0	9.5	17.0	14.0	21.0	20.3	17.3	40.1	38.8
40.8	Trail Ridge	med-02	760	100	362	515	650	478	734	343	1027	1719	949	1397	745	661	2125	609	2596	1640
40.1	Trail Ridge	med-03	1460	270	43	83	123	47	120	37	143	230	82	198	71	135	262	84	382	672
44	Trail Ridge	dpm-01	2100	420	0.00	0.00	0.00	0.00	0.00	0.00	0.02	0.43	0.01	0.13	0.00	0.00	0.96	0.00	0.38	0.56
43.5	Trail Ridge	dpm-02	3820	2240	0.12	0.14	0.16	0.14	0.17	0.12	0.21	0.35	0.20	0.28	0.17	0.16	0.45	0.15	0.59	0.35
28.9	Trail Ridge	jsf-01	680	140	0.03	0.31	0.87	0.17	0.77	0.02	0.08	0.00	0.10	0.00	0.68	0.92	0.00	0.66	0.00	0.16
24	Trail Ridge	jsf-02	820	130	0.00	0.05	0.34	0.01	0.63	0.00	0.28	0.00	0.40	0.01	0.61	0.40	0.00	0.17	0.00	0.23
21.5	Trail Ridge	gsq-02	1780	530	0.01	0.02	0.04	0.01	0.05	0.01	0.17	0.92	0.12	0.50	0.05	0.04	0.56	0.03	0.21	0.87
20	Effingham	cjr-01	350	60	0.87	0.11	0.03	0.09	0.00	0.92	0.00	0.00	0.00	0.00	0.00	0.04	0.00	0.01	0.00	0.06
18.7	Effingham	cjr-02	1600	270	0.00	0.00	0.00	0.00	0.00	0.00	0.06	0.74	0.02	0.54	0.00	0.00	0.16	0.00	0.03	0.96
15	Effingham	dsg-01	1050	180	0.00	0.01	0.07	0.00	0.14	0.00	0.92	0.02	0.61	0.19	0.11	0.08	0.00	0.03	0.00	0.40
12.9	Chatham	rrg-02	460	50	0.14	0.57	0.15	0.79	0.04	0.06	0.00	0.00	0.00	0.00	0.00	0.16	0.00	0.13	0.00	0.08
9.8	Chatham	she-02	870	160	0.00	0.05	0.28	0.02	0.50	0.00	0.46	0.00	0.66	0.04	0.48	0.32	0.00	0.15	0.00	0.26
9	Chatham	she-03	890	180	0.00	0.06	0.27	0.03	0.47	0.00	0.55	0.00	0.77	0.06	0.45	0.31	0.00	0.16	0.00	0.28
8.8	Chatham	rrg-01	570	110	0.08	0.69	0.63	0.44	0.31	0.05	0.01	0.00	0.01	0.00	0.18	0.60	0.00	0.78	0.00	0.12
8	Effingham	srq-02	620	120	0.04	0.47	0.86	0.27	0.50	0.03	0.03	0.00	0.02	0.00	0.37	0.82	0.00	0.94	0.00	0.14
1	Effingham	srq-03	600	80	0.01	0.46	0.73	0.19	0.35	0.00	0.01	0.00	0.00	0.00	0.18	0.70	0.00	0.94	0.00	0.12
-4.5	Chatham	dsq-02	650	220	0.20	0.57	1.00	0.44	0.74	0.17	0.15	0.00	0.20	0.01	0.68	0.97	0.00	0.86	0.00	0.16
-7	Chatham	dsq-01	950	240	0.02	0.09	0.27	0.05	0.42	0.01	0.78	0.02	1.00	0.15	0.41	0.29	0.00	0.18	0.00	0.33

Table 16: Age agreement between the Ti-Li option D (SSE) signals of the Georgia ACD samples and the Ti-Li ESR signals of the Florida coastal sequences published by Burdette et.al. (2012). Note the sample gp127e is included to complete the data set but should be considered unreliable.

In particular the samples gp1422d and gp1422g, from the Princess Anne ACD, agrees well with low elevation Chatham and Effingham Florida sequences (rrg-01, srq-01 through 03, and dsq-02). In particular is the correlation between the FL dsq-02 sample representing the Chatham sequence and Georgia sample gp1422g representing the Princess Anne ACD, in which there is an exact match in age (shown by a P value of 1.00) at nearly the same elevation. These lower ACD samples show a great many agreements with Florida samples from higher elevations as well.

Age agreements are indicated for the samples gp1421c and gp1421d but as mentioned above these are likely age overestimates as the lower most sample gp1421f is dated to be much younger than those above. Sample gp1421f of the Pamlico ACD does correlate to sample cjr-01 of the Effingham Sequence emplaced at a much higher elevation than the Pamlico samples from Ga. Winker and Howard (1977) note an increase in elevation of the Effingham Sequence between Georgia and Florida.

Georgia upper ACDs (sample gp12 9, 4, 3, and 7) show many correlations to the higher elevation Florida sequences of the Effingham and Trail Ridge. In addition sample gp123c, gp123d, and gp127b show correlation between themselves and the lower elevation Effingham and Chatham Florida samples mentioned above in the discussion of gp1422d and gp1422g.

These results indicate that there is correlation between all of the Georgia samples, with the exception of gp1422c and the gp1421, to all of the Florida ESR samples. It is possible then that the majority of the ESR ages in Burdette et.al. (2012) (exception being cjr-01) represent the ages of emplacement of the Cypresshead Formation or its Florida equivalent. Florida sample cjr-01, gp1422c and the gp1421 samples represent the deposition of the Satilla Formation (or Florida equivalent). This conclusion is supported in the correlation in age of both high elevation and low elevation ACDs/sequences.

4.4 OSL Discussion

4.4.1 Standard OSL

Standard OSL measurement of the lower ACDs resulted in few aliquots accepted. While recycling ratios were acceptable and sensitivity changes were normal, the lack of accepted aliquots is the result of a saturated OSL signal. Those aliquots that were accepted would represent a minimum age of the deposit (ie the youngest grains not saturated). The ages determined by OSL should be considered with caution. The limited number of aliquots accepted results in a poor estimation of the D_E distribution and leads to a less robust determination of the age model to be used (CAM or MAM based on the Bailey and Arnold (2006) Criterion).

The age estimates derived from OSL of these samples are in line with the ages estimated by Hoyt and Hails (1967), Colquhoun (1969), and Huddelston (1998) of these ACDs being formed during the deposition of the Satilla formation during the Pleistocene to Late Pleistocene. The ages are similar (being within the age range or slightly younger) to U-series age studies conducted Szabo (1985) and Wehmiller et.al. (2004) and OSL studies by Willis (2006) with a MIS stage 5e depositional age of the Pamlico and slightly younger (80-90ka) deposition of the Princess Anne. These ages do not agree with the ages of the correlative Chatham Formation in Florida as determined by Burdette et.al. (2012) with ESR to between 860-1090 ka in age. They agree with Markewich et.al. (2013) estimates of the age of the Princess Anne at 109-123 ka, but are younger than the stated age of the Pamlico at 243-191 ka.

As stated in section 4.3.3 above the OSL ages do display agreement with the Ti-H ESR measurements of the respective samples.

4.4.2 OSL Saturation Work

Typical D_0 values found in quartz OSL range between 50-100 Gy (Wintle and Murray, 2006). In this study the OSL D_0 value range from 37-52 Gy, much lower than the typical quartz. As $2 * D_0$ can be used as a proxy for the saturation dose, these results

indicate that the maximum recordable OSL dose the GA quartz can obtain is approximately 100 Gy (half the normal dose). This reduces the age range that OSL can be effectively used on these deposits to less than 115 ka (using an average dose rate of 0.87 Gy/ka)

Pietsch et.al. (2008) and Jeong and Choi (2012) suggest that significant transport, associated with numerous irradiation and bleaching events increases the sensitivity of quartz. The low D_0 values associated with the GA quartz could be associated with limited depositional cycles. Jeong and Choi (2012) also indicate that the source of the quartz determines how it behaves when exposed to OSL testing. They state that while sedimentary rock-sourced quartz shows great sensitivity, quartz from igneous and metamorphic host rock do not. As the material found in the GA ACDs is sourced from igneous and metamorphic rock in the GA highlands this too could account for the low saturation values observed.

4.4.3 TT-OSL

TT-OSL measurements increased the number of accepted aliquots in a sample but still resulted in general saturation conditions of the TT-OSL signal. In samples gp1421d there is no agreement between the OSL (MAM) and TT-OSL based on the result of the homogeneity test. In sample gp1422d both the OSL and TT-OSL ages agree. In both samples TT-OSL ages agree with the Ti-H ESR age. Furthermore TT-OSL, OSL, and Ti-H ESR ages all agree in sample gp1422d.

TT-OSL results of these samples display the sample's low saturation dose (low D_0 value) characteristics found in both the ESR and OSL dose response curves. Typical TT-OSL have D_0 values in the 50-100s Gy while the GA ACD TT-OSL range from 46-51 Gy. As in OSL, this limits the maximum dose that the TT-OSL signal can record and therefore its usefulness for determining the age of older materials. As the TT-OSL ages agree with the OSL ages, agreements between the TT-OSL and other studies are the same as the agreements as those stated for the OSL portion of this project.

4.5 Summary and Conclusions

4.5.1 Ages ACDs Based on ESR and OSL (objective 1)

Based on the age estimates from previous works (excluding Burdette et.al. 2012) as well as the age estimates from the OSL and TT-OSL experiments in this work, and the strong ESR signal observed in the modern Georgia coastal samples as well as the numerous age inversions seen in the ESR data the following conclusions can be reached. The ESR ages provided in this study do not accurately reflect the formation of the Georgia ACD shoreline events as was the goal of this study. They are an over estimate brought about by an incomplete bleaching of the ESR signals prior to the formation of the ACD. Using the assumption of reasonably complete zeroing of the Ti-Li D signal, the ages do however appear to reflect the depositional age of the geological formations (the Cypresshead and Satilla Formations) that underlies and form the subsurface of the ACDs. The ESR age estimates for the deposition of these formations based on this assumption is consistent with other geological evidence published previously by others. It can be concluded that although the formation of the ACDs did not fully reset the Al ESR signals, tentative correlations based on the assumed near zeroing of the Ti-Li D option signal provide some indications of the ages of various events in the history of these formations and that the samples do not necessarily reflect clear indications of sea level fluctuations with full resetting at shoreline formation events on the Georgia Coastal Plain. Voinchet et.al. (2007) and Tissoux et. al. (2007) have both shown that fluvial transport is effective at bleaching the Ti-H, Ti-Li, and Al signals in ESR. It is therefore more likely that some bleaching of the ESR signal occurred during transport of the quartz to the Georgia coast. In cases such as the Pamlico ACD where the youngest age is the lower-most sample, mixing of older sediments transported down from higher on the coastal plain (or older ACDs) could account for the age inversions observed. The use of ESR on the Georgia Coastal Plain will be discussed further in section 4.5.4.

OSL and TT-OSL ages estimates, as well as Ti-H ESR age estimates seem to correlate better with other ages estimates in previous works in Georgia and along the

Atlantic coast. Due to the limited information provided by the OSL and TT-OSL data these results must be considered with caution (more in section 4.5.4). Likewise the use of the Ti-H signal in quartz ESR-OD requires more research and the ages provided by that method must also be considered skeptically (more in section 4.5.4).

While the initial goal of determining the depositional age of the series of ACDs along the Georgia Coastal Plain proved challenging, ESR was useful in estimating the depositional age of events within the coastal geological formations in Georgia. Considering only the Ti-Li option d ESR ages, the maximum depositional age of the Satilla Formation is between 243-417 ka. This would indicate that the Satilla Formation was being deposited during MIS 11 until the beginning of MIS 7 or later. The ESR data show the deposition of the Cypresshead Formation possibly took place in two distinct pulses. The early deposition occurred at a maximum age of 867-2978(3103) ka followed by a second at 433-796 ka. It is possible that deposition was continuous between these two phases. The GPR boundaries between these two age groups does not suggest significant erosion but does suggest a change of some sort or a short break in deposition. These ages are consistent with estimate of others (Hoyt and Hails, 1967; Colquhoun, 1969; Huddelston, 1988), in that the Cypresshead was deposited during the Late Pliocene to Early Pleistocene (recall the Pilo-Pleistocene boundary was changed in 2009, after the publication of these previous works, from 1.81 Ma to its current 2.86 Ma so that while Epoch name may not now be accurate the age estimate is still valid), and the Satilla Formation deposited during the Pleistocene to Late Pleistocene.

4.5.2 GPR Stratigraphy and Sediment Analysis (objective 2)

GPR proves a valuable tool for sampling of the Georgia ACDs. GPR penetration is deep and allowed for targeting of specific sites of interest. The radargrams showed facies that were interpreted to be of shoreline features such as beach face deposits and overwash deposits (shown in Figure 24 element C and A respectively) as well as channel features (shown in Figure 26) and dunes (shown in Figure 25). The interpretation of these features is strengthened by the GPR studies by other of the modern Georgia barrier

islands which show similar features and radar facies (shown in Figure 35). The discovery of potential ravinement surfaces in the Pamlico, Talbot and Okefenokee ACDs radargrams show that GPR can be used to help locate sea level indicators in the subsurface in Georgia. These results show GPR is viable tool for the exploration of the Georgia ACD and should be used in further studies of these deposits.

Furthermore correlation between radar facies Element E regions and the humate that prevented geoprobe penetration could be useful to future researches. GPR scans of their potential core sites could be used to locate the problematic humate and another location could be selected or a more robust drill brought in to complete the job. This research could be a benefit to any group planning on doing subsurface work in Georgia, both academic research and industrial. A GPR survey of the project site to identify and map the extent of potential subsurface humate regions could save time, money and resources.

GPR radargrams of the upper and lower ACDs appear quite different. While the upper ACDs show little structure the lower ACD show more. This is consistent with Hails and Hoyt (1969b), Howard and Scott (1983) and Huddlestun (1988) in that the ACDs lack structure, and were modified by post-depositional processes. The lower ACDs radargrams show more structure suggesting that less time has passed for post-depositional process to occur. What structures can be seen appear in both the upper and lower ACDs suggesting similar depositional processes.

Sediments in the cores of the ACDs appear similar. This is particularly true for the upper ACDs. Sediment lithology of these ACDs is consistent with the Cypresshead Formation as described by Huddlestun (1988). The lower ACDs do show clay layers similar to those attributed to the Satilla formation by Huddlestun (1988). This is particularly true for the Pamlico core. The ESR data from the Princess Anne core shows that the upper portion could belong to the Satilla Formation while material in the lower portion of the core could belong to the Cypresshead Formation.

Sediments in the Georgia cores do appear to be less mature (containing clays and mica, less sorted) than those described by Burdette (2010) in Florida. This has

implications for the amount of transport and exposure experienced by the quartz in the sediment.

4.5.3 Georgia and Florida deposit correlations (objective 3)

Due to the lack of agreement between the Al and Ti-Li signals of the Georgia ESR measurements and the differences between the ESR methodological approach employed in this work and Burdette et.al. (2012) there are limited comparisons that can be made between the Florida deposits dated by Burdette et.al. (2012) and the correlative deposits in Georgia. A comparison of the ages derived from the Ti-Li signals allows for the maximum age of the Georgia samples to be tentatively compared to the ages of the Florida samples as the Al ages of the Georgia samples can be considered over estimates. Based on the group associations discussed above the deposition of both the Satilla and the upper Cypresshead occurred after the deposition of the Chatham Sequence (860-1090ka). The lower Cypresshead group correlates to the deposition of the Effingham and Trail Ridge sequences in Florida.

As Burdette et.al. (2012) found evidence for complete bleaching of the Al and Ti-Li ESR signals in the modern coastal deposits of Florida and the sediment source for both is the Georgia Highlands (ie. the source of the quartz is the same) the bleaching of the relict signals of the sediment must occur during littoral transport alongshore to the south. Sediment maturity differences between Georgia and Florida support the hypothesis that the sediments are reworked as they travel longshore. This would allow for multiple exposures to sunlight. Even if the relict ESR signal is not fully bleached after a cycle of exposure and burial, the next cycle could remove the signal associated with the previous burial as well as a portion of the relic signal. Over multiple cycles this could effectively zero the relict ESR signals.

4.5.4 Suitability of OSL and ESR-OD in Georgia (objective 4)

This is the first study that attempts to use ESR to date sediments in Georgia. This study also makes use of OSL and TT-OSL. The results of this project can be used by

others who attempt to use these methods in Georgia. Of interest to note is that in all three dating methods that were attempted in this study (ESR, OSL, TT-OSL) all samples showed a significantly lower than typical saturation dose ($2 \cdot D_0$). In all methods these low saturation values limit the effective range in which these methods can be used and increase the D_E error estimates in sample age ranges that have been found suitable in other locations.

4.5.4.1 Using OSL in Georgia

OSL geochronological methods work well in Georgia, though OSL should be used with caution, because of the limited range of the method. Although this study did not yield any robust OSL ages the quartz did produce good regeneration curves and recovered dose well. While OSL is possible to use on Georgia sands, future researchers are cautioned that the D_0 values and therefore low saturation doses of the Georgia sand may limit the age range that OSL is effective. This low saturation dose is likely associated with the proximal source of the sediments not allowing for many sensitization cycles to occur.

To determine the age of deposits expected to be outside realm of traditional OSL TT-OSL was attempted. The results of this work again show a significantly lower D_0 value than expected. This limits the effective range of TT-OSL. While few studies have been attempted to determine the sensitivity changes with dose and bleaching with TT-OSL it is possible that the low maturity of the sediments affects the TT-OSL signal as it does the OSL signal.

4.5.4.2 Using ESR in Georgia

As stated above the low saturation dose of the ESR method limits its use in Georgia. Furthermore the presence of a relict ESR signal in both the AL and Ti-Li signals of the modern Georgia barrier islands calls in to question the extent of bleaching that occurred during formation of the ACDs. As no agreement was found in the Al (SSE) and Ti-Li (SSE) signals there are no ages that can be fully confirmed. For this reason the

ages reported in this work are from the Ti-Li option D (SSE) signal and should be considered maximum age estimates, though analysis of the correlations using the assumption of near or complete zeroing of the Ti-Li D signal provided intriguing correlations. Although there are two samples that showed agreement between the Al (Exp+Lin) and the Ti-LiD (SSE), the fact that only two of the 16 did agree using this technique suggest that bleaching is still a significant issue when working with ESR on Georgia coastal deposits. As deposits in Florida did not have this problem (Burdette et.al., 2012) it can be concluded that the sediments were bleached during longshore transport from their source in Georgia to their depositional sites in Florida.

The experimental technique to remove the modern relic signal from the ACDs met with limited success. Two samples did show an age agreement between the Al (SSE) and Ti-Li D (SSE) after this technique was applied but the negative D_E estimates in some samples and the continued non-agreement shows that this technique needs refinement. Having stated this, this technique does show promise and further experimentation could show that accurate age estimates are possible for samples that are incompletely bleached using modern relic dose analogs.

The Ti-H signal measured in this study is unique in that the dose response curve incorporated a number of low additive dose intervals to construct a dose response curve for this low saturating signal. Even with 5 doses below the typical saturating dose (1000 Gy) of this signal D_e error was high (up to 87% in one case) owing to a low r^2 value of the DRC. Despite this, there does appear to be some correlation between the OSL, TT-OSL and Ti-H ESR signals. With additional additive doses under +1000 Gy it may be possible to use Ti-H to confidently date sediments. As this signal bleaches quickly (Yoshida, 1986) it could be used instead of the Al signal to confirm Ti-Li ages where bleaching times maybe less than optimal to fully rest the Al signal. The low saturation dose would limit use of this signal to younger sediments.

Future researchers should be cautious when working with ESR in Georgia. Incomplete bleaching and low signal saturation doses create challenges to working with ESR on the ACD sediments of Georgia. It is apparent that both the Al and Ti-Li signals

have issues with incomplete bleaching while the inability of the Ti-H to register high dose values limits its usefulness in the older deposits along the Georgia coast.

4.5.5 Future work

Future work into the use of the Ti-H signal is required before it can become a useful ESR signal. An additive dose plan that includes more low dose steps would allow for better fitting of the signal (higher r^2 values) and reduced error. More work is needed to confirm that longshore transport is in fact producing better bleached sediments further down drift.

Low D_0 values are pervasive in this study. Future work in confirming that cycles of irradiation and bleaching raise the D_0 to normal levels would show that the low D_0 values are due to low cycling and not an inherent characteristic of the quartz. These experiments would make use of OSL, TT-OSL, and ESR to determine if there are any similarities between saturation dose changes with cycling between all the methods. Similar changes between the methods would suggest that the physics involved in the creation of these signals may share some common processes.

Specific to Georgia, expansion of the TT-OSL dating would provide age confirmations of either the ESR or OSL ages. Low D_0 values of the Georgia sands could limit the use of this method to the lower ACDs.

4.5.6 Closing Remarks

This was the first study to attempt ESR-OD on coastal deposits in Georgia. The goal of determining the age of the ACDs of Georgia using ESR-OD was not reached in this study due to the incomplete bleaching of the ESR signals. This makes drawing conclusions about the sea level history of Georgia from this data impossible. Maximum ages estimates for the age of the Satilla and Cypresshead Formations underlying the ACDs was determined from the ESR results. ESR ages derived from the Ti-Li option D (SSE) ages indicate that the Satilla Formation was deposited during or after 243-417 ka while the Cypresshead Formation was deposited in two events during or after 867-2978

ka and during or after 433-796 ka. These age estimates agree with previous geochronological work in the area further confirming the depositional age of these deposits.

Data collected with ESR, OSL, and TT-OSL indicates that the quartz of southern coastal Georgia exhibits a low saturation dose. This characteristic limits the age range in which these methods can be used with confidence in this environment. Further luminescence geochronological studies of the Georgia ACD must take this in to account. The Ti-H signal shows potential as a geochronological tool through a specific additive dose regime is need to use the signal to its potential.

GPR proved useful in targeting lithologies as well as selecting core sites. Coastal features similar to those found in the modern barrier islands of Georgia were identifiable in the ACDs validating the use of GPR in the study of the paleo-coastal region of Georgia. GPR reflection data and coring data has made the identification of potential humate horizons viable with GPR. This data has potential use for many aspects of geological investigation and geotechnical within the Georgia coastal region.

References Cited

- Adamiec, G., Bailey, R.M., Wang, X.L. and Wintle, A.G., 2008, The mechanism of thermally transferred optically stimulated luminescence in quartz: *Journal of Physics D: Applied Physics*, no. 41, pp. 14.
- Adamiec, G., Duller, G.A.T., Roberts, H.M. and Wintle, A.G., 2010, Improving the TT-OSL SAR protocol through source trap characterization: *Radiation Measurements*, no. 45, p. 768-777.
- Aitken, M.J., and Smith, B.W., 1988, Optical dating: recuperation after bleaching: *Quaternary Science Reviews*, vol. 7, p. 387-393.
- Anderson, A., Roberts, R., Dickinson, W., Clark, G., Burley, D., de Biran, A., Hope, G. and Nunn, P., 2006, Times of sand: sedimentary history and archaeology at the Sigatoka Dunes, Fiji: *Geoarchaeology*, vol. 21, p. 131-154.
- Arnold, L.J. and Roberts, R.G., 2009, Stochastic modelling of multi-grain equivalent dose (De) distributions: Implications for OSL dating of sediment mixtures: *Quaternary Geochronology*, no. 4, pp. 204-230.
- Arnold, L.J., Bailey, R.M., and Tucker, G.E., 2007, Statistical treatment of fluvial dose distributions from southern Colorado arroyo deposits: *Quaternary Geochronology*, no. 2, pp. 162-167.
- Arnold, L.J., Demuro, M., Parés, J.M., Pérez-González, A., Arsuaga, J.L., de Castro, J.M.B. and Carbonell, E., 2014, Evaluating the suitability of extended-range luminescence dating techniques over early and Middle Pleistocene timescales: Published datasets and case studies from Atapuerca, Spain: *Quaternary International*, pp. 1-24.
- Bailey, R.W. and Arnold, L.J., 2006, Statistical modelling of single grain quartz De distributions and an assessment of procedures for estimating burial dose: *Quaternary Science Reviews*, no. 25, pp. 2475-2502.
- Baker, P.L., 1991. Response of ground-penetrating radar to bounding surfaces and lithofacies variation in sand barrier sequences. *Exploration Geophysics*, vol. 22, pp. 19-22.
- Banerjee, D., Bøtter-Jensen, L. and Murray, A.S., 2000, Retrospective dosimetry: estimation of the dose to quartz using the single-aliquot regenerative-dose protocol: *Applied Radiation and Isotopes*, no. 52, pp. 831-844.
- Bateman, M., Murton, J.B. and Boulter, C., 2010, The source of De variability in periglacial sand wedges: depositional processes versus measurement issues: *Quaternary Geochronology*, vol. 5, p. 250-256.
- Buhay, W.M., Schwarcz, H.P. and Grün, R., 1988, ESR dating of fault gouge: the effect of grain size: *Quaternary Science Reviews*, vol. 7, p. 515-522.
- Burdette, K., Rink, W.J., Mallinson, D., Parham, P. and Means, G. , 2012, Electron spin resonance optical dating of marine, estuarine, and aeolian sediments in Florida, USA.: *Quaternary Research*.
- Burdette, K., Rink, W.J., Mallinson, D.J., Parham, P.R., Reinhardt, E.G., 2010, Geologic investigation and optical dating of the Merritt Island sand ridge sequence, Eastern Florida, USA: *Southeastern Geology*, vol. 47, no. 4, pp. 175-190.

- Carr, A.S., Bateman, M.D. and Holmes, P.J., 2007, Developing a 150ka luminescence chronology for the barrier dunes of the southern Cape, South Africa: *Quaternary Geochronology*, vol. 2, p. 110-116.
- Clark, W.Z. Jr., and Zisa, A.C., 1976, Physiographic map of Georgia: Georgia Department of Natural Resources, Environmental Protection Division, Atlanta, GA.
- Cohen, K.M., Finney, S.C., Gibbard, P.L. and Fan, J.X., 2013, The ICS international chronostratigraphic chart: Episodes, no. 36, vol. 3, p. 199-204.
- Colquhoun, D.J., Johnson, G.H., Peebles, P.C., Huddleston, P.F., and Scott, Thomas, 1991, Quaternary geology of the Atlantic Coastal Plain: New Jersey, Delmarva Peninsula, western shore of Maryland, Virginia, and North Carolina, Cape Fear Arch, northeastern South Carolina, central South Carolina, Georgia, Florida, in Morrison, R.B., ed., *Quaternary nonglacial geology; Conterminous U.S., The Geology of North America Volume K-2: Boulder, Colorado*, Geological Society of America, p. 629-650.
- Cooke, C.W., 1925, The coastal plain, *Physical geography of Georgia: Georgia Geological Survey Bulletin*, no. 42, p. 19-54.
- Cooke, C.W., 1931, Seven coastal terraces in the southwestern states: *Washington Academy of Science Journal*, vol. 21, p. 503-513.
- Cooke, C.W., 1945, *Geology of Florida: Florida Geological Survey Bulletin*, no. 29, pp.342.
- Cornin, T.M., Bybell, L.M., Poore, R.Z., Blackwelder, B.W., Liddicoat, J.C., Hazel, J.E., 1984, Age and correlation of emerged Pliocene and Pleistocene deposits, U.S. Atlantic coastal plain: *Palaeogeography, Palaeoclimatology, Palaeoecology*, vol. 47, p. 21-51.
- Costas, S., Alejo, I., Rial, F., Lorenzo, H. and Nombela, M.A., 2006, Cyclical evolution of a modern transgressive sand barrier in northwestern Spain elucidated by GPR and aerial photos: *Journal of Sedimentary Research*, vol., 76, p. 1077-1092.
- Cunningham, Alastair C., Wallinga, Jakob, and Minderhoud, Philip S.J., 2011, Expectations of scatter in equivalent-dose distributions when using multi-grain aliquots for OSL dating: *Geochronometria*, no. 38, vol. 4, pp. 424-431.
- Davis, J.L. and Annan, A.P., 1989, Ground-penetrating radar for high-resolution mapping of soil and rock stratigraphy: *Geophysical Prospecting*, no. 37, p. 531-551.
- Doering, J.A., 1960, Quaternary surface formation of Southern part of Atlantic Coastal Plain: *The Journal of Geology*, v. 68, no. 2, pp. 182-202.
- DuBar, J.R., Johnson, H.S., Thom, B. and Hatchell, W.O., 1974, Neogene stratigraphy and morphology, south flank of the Cape Fear Arch, North and South Carolina, *in Post-Miocene Stratigraphy, Central and Southern Atlantic Coastal Plain* Oaks, R.Q. and DuBar, J.R. (ed.): Utah State University Press, Logan, UT, p. 139-173.
- Duller, G.A.T., 2008, *Luminescence dating: guidelines on using luminescence dating in archaeology*: Swindon: English Heritage, p. 44.
- Duller, G.T.A., 2015, *Luminescence dating in Encyclopedia of Scientific Dating Methods*, Rink, W.J. and Thompson, J. (eds.): Springer Netherlands.
- Duller, Geoff, 2013, *Luminescence Analyst version 4.10*: Aberystwyth Luminescence Research Laboratory, Aberystwyth University, United Kingdom.
- Duval, M. and Guilarte, V., 2014, ESR dosimetry of optically bleached quartz grains extracted from Plio-Quaternary sediments: evaluating some key aspects of the ESR signals associated to the Ti-centers: *Radiation Measurements*, vol. 78, p. 28-41.

- Duval, M., Guilarte Moreno, V. and Grün, R., 2013, ESR dosimetry of fossil enamel: some comments about measurement precision, long-term signal fading and dose-response curve fitting: *Radiation Protection Doseimetry*, vol. 157 (4), pp. 463-476.
- Duval, M., 2012, Dose response curve of the ESR signal of the Aluminum center in quartz grains extracted from sediments: *Ancient TL*, vol. 30, no. 2, p. 41-50.
- Galbraith, R.F., 2003, A simple homogeneity test for estimates of dose obtained using OSL: *Ancient TL*, vol. 21, no. 2, pp.75-77.
- Galbraith, R.F. and Roberts, R.G., 2012, Statistical aspects of equivalent dose error calculation and display in OSL dating: an overview and some recommendations: *Quaternary Geochronology*, vol. 11, p. 1-27.
- Galbraith, R.F., Roberts, R.G., Laslett, G.M., Yoshida, H. and Olley, J.M., 1999, Optical dating of single and multiple grains of quartz from Jinmium Rock Shelter, Northern Australia: Part I, experimental design and statistical models: *Archaeometry*, no. 41, vol. 2, pp. 339-364.
- Georgia Department of Natural Resources, 1979, *Geologic Map of Georgia*: Georgia Geological Survey, Atlanta GA, 1:500,000 scale.
- Grün, R. and Brumby, S., 1994, The assessment of errors in past radiation doses extrapolated from ESR/TL dose response data: *Radiation Measurements*, vol. 23, no. 2/3, p. 307-315.
- Grün, R. and MacDonald, P.D.M., 1989, Non-linear fitting of TL/ESR dose-response curves: *Applied Radiation Measurements*, vol. 40, no. 10-12, p. 1077-1080.
- Grün, R., 1989, Electron spin resonance (ESR) dating: *Quaternary International*, vol. 1, p. 65-109.
- Guhl, A., Bertran, P., Zielhofer, C. and Fitzsimmons, K.E., 2013, Optically stimulated luminescence (OSL) dating of sand-filled wedge structures and their fine-grained host sediment from Jonzac, SW France: *Boreas*, vol. 42, p. 317-332.
- Hails, J.R. and Hoyt, J.H., 1969, The significance and limitations of statistical parameters for distinguishing ancient and modern sedimentary environments of the lower Georgia coastal plain: *Journal of Sedimentary Petrology*, vol. 39, no. 2, p. 559-580.
- Hails, J.R. and Hoyt, J.H., 1972, The nature and occurrence of heavy minerals in Pleistocene and Holocene sediments of the Lower Georgia Coastal Plain: *Journal of Sedimentary Petrology*, vol. 2, no. 3, p. 646-666.
- Hails, J.R., and Hoyt, J.H., 1969, An appraisal of the evolution of the lower Atlantic coastal plain of Georgia, U.S.A: *Transactions of the Institute of British Geographers*, no. 46, pp. 53-68.
- Hayden, B.P. and Dolan, R., 1979, Barrier islands, lagoons, and marshes: *Journal of Sedimentary Petrology*, vol. 49, no. 4, p. 1061-1072.
- Henning, G.J. and Grün, R., 1983, ESR dating in Quaternary geology: *Quaternary Science Reviews*, vol. 2, p. 157-238.
- Herrick, S.M. and Vorhis, R.C., 1963, *Subsurface geology of the Georgia Coastal Plain*: The Geological Survey, Information Circular 25, Georgia State Division of Conservation, Department of Mines, Mining and Geology, Atlanta, GA.
- Hollin, J.T., and Hearty, P.J., 1990, South Carolina interglacial sites and stage 5 sea levels: *Journal of Quaternary Research*, v. 33, pp. 1-17.

- Howard, J.D. and Frey, R.W., 1985, Physical and biogenic aspects of backbarrier sedimentary sequences, Georgia Coast, U.S.A.: *Marine Geology*, no. 63, pp. 77-127.
- Howard, J.D., and Scott, R.M., 1983, Comparison of Pleistocene and Holocene barrier islands beach-to-offshore sequences, Georgia and Northeast Florida coast, U.S.A.: *Sedimentary Geology*, v. 34, pp. 167-183.
- Hoyt, J.H., and Hails, J.R., 1967, Pleistocene shoreline sediments in coastal Georgia: deposition and modification: *Science*, v. 155, iss. 3769, pp. 1541-1543.
- Hoyt, J.H., Henry, V.J. Jr. and Weimer, R.J., 1968, Age of Late Pleistocene shoreline deposits, coastal Georgia: *Means of Correlation of Quaternary Successions*, University of Utah Press, Salt Lake City, UT, p 381-393.
- Huddleston, P.F., 1988, A revision of the lithostratigraphic units of the Coastal Plain of Georgia, The Miocene through Holocene: Georgia Geologic Survey Department of Natural Resources Bulletin, no. 104, p. 162
- Ikeya, M., 1993, *New Applications of Electron Spin Resonance – Dating, Dosimetry and Microscopy*: World Scientific, Singapore.
- Jeong, G.Y. and Choi, J.-H., 2012, Variations in quartz OSL components with lithology, weathering and transportation: *Quaternary Geochronology*, vol. 10, p. 320-326.
- Johannes, R.E., 1980, The ecological significance of the submarine discharge of groundwater: *Marine Ecology Progress Series*, vol. 3, p. 365-373.
- Jol, H.M., Lawton, D.C., Smith, D.G., 2002. Ground Penetrating Radar: 2-D and 3-D subsurface imaging of a coastal barrier spit, Long Beach, WA, USA. *Geomorphology*, vol. 53, pp. 165-181.
- Jol, H.M., Smith, D.G., Meyers, R.A., 1996, Digital Ground Penetrating Radar (GPR): A new geophysical tool for coastal barrier research (examples from the Atlantic, Gulf and Pacific Coast, U.S.A.). *Journal of Coastal Research*, vol. 12, no. 4, pp. 960-968.
- Jonas, M., 1997, Concepts and methods of ESR dating: *Radiation Measurements*, no. 5/6, vol. 27, p. 943-973.
- Kellam, J.A., Mallery, M., and Laney, M.K., 1991, Heavy mineral bearing sands from the Wicomico to the Princess Anne paleobarrier complexes along the Georgia Coastal Plain: Georgia Department of Natural Resources, Geological Survey Bulletin 111, Atlanta, GA.
- Kellam, M.F. ed., 1986, *Environmental geological atlas of coastal Georgia: Geologic Atlas 5*: Georgia Department of Natural Resources, Geological Survey, Atlanta, GA.
- Krantz, D.E., 1991, A chronology of Pliocene sea-level fluctuations: the U.S. middle Atlantic Coastal Plain record: *Quaternary Science Reviews*, v. 10, pp. 163-174.
- Kreutzer, Sebastian, Schmidt, Christoph, Fuchs, Margret C., Dietze, Michael, Burow, Christoph and Fuchs, Markus, 2014, Package for Luminescence Dating data analysis version 0.3.2: R package, CRAN Repository, <http://CRAN.R-project.org/package=Luminescence>.
- Leigh, D.S., Srivastava, P., Brook, G.A., 2004, Late Pleistocene braided rivers of the Atlantic Coastal Plain, USA: *Quaternary Science Reviews*, v. 23, pp. 65-84.
- Lin, M., Yin, G., Ding, Y., Cui, Y., Chen, K., Wu, C., Xu, L., 2006. Reliability study on ESR dating of the aluminum center in quartz. *Radiation Measurements* 41, 1045-1049.
- MacNeil, F.S., 1949, Pleistocene shorelines in Florida and Georgia: U.S. Geological Survey Professional Paper, no. 221-F, p. 95-106.

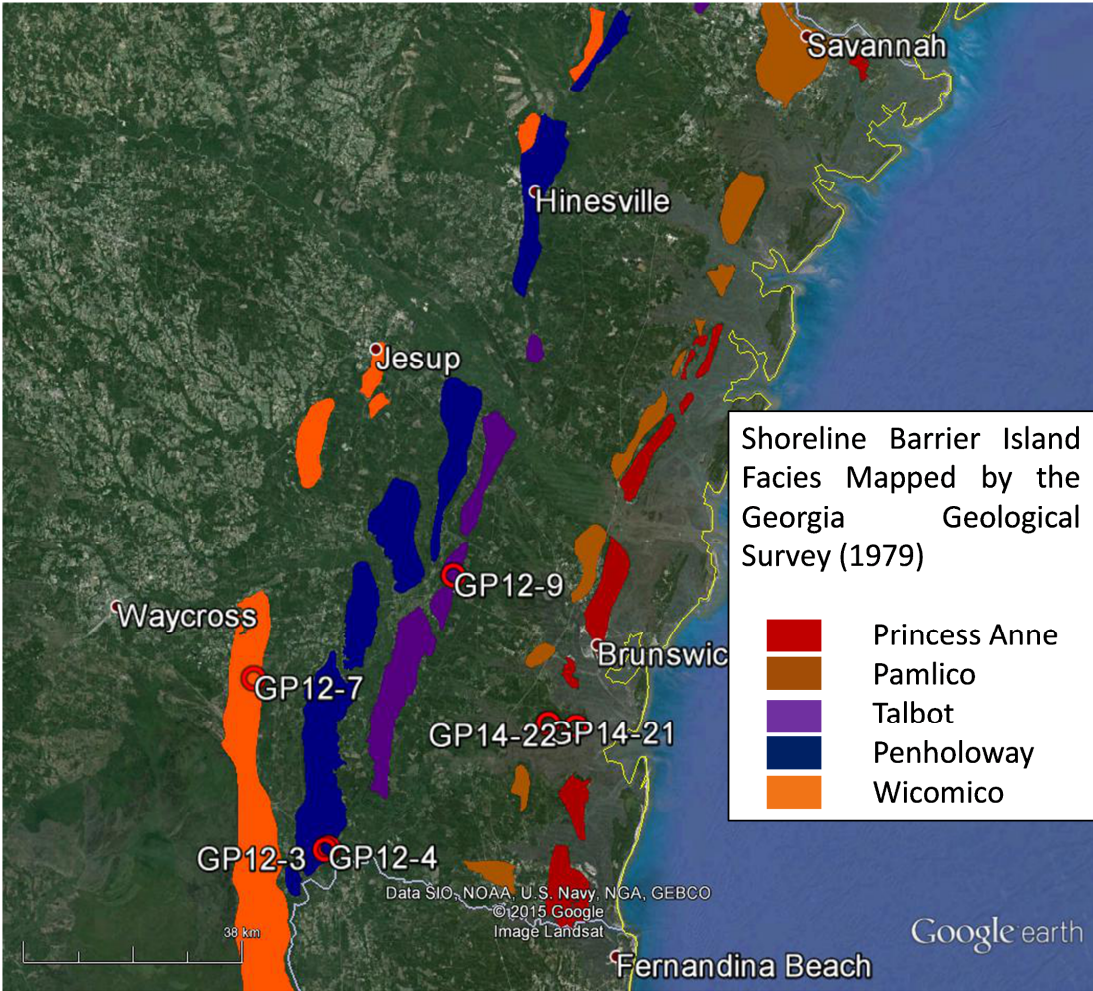
- Mallinson, D.J., Mahan, S., Moore, C., 2008, High resolution shallow geologic characterization of a Late Pleistocene eolian environment using ground penetrating radar and optically stimulated luminescence techniques: North Carolina, USA. *Southeastern Geology*, vol. 45, no. 3, pp. 161-177.
- Mallinson, D.J., Smith, C.W., Culver, S.J., Riggs, S.R., Ames, D., 2010, Geological characteristics and special distribution of paleo-inlet channels beneath the outer banks barrier islands, North Carolina, USA. *Estuarine, Coastal and Shelf Science*, vol. 88, pp. 175-189.
- Markewich, H.W., Pavich, M.J., Schultz, A.P., Mahan, S.A., Aleman-Gonzalez, W.B., Bierman, P.R., 2013, Geochronologic evidence for a possible MIS-11 emergent barrier/beach-ridge in southeastern Georgia, USA:
- Marple, R.T. and Talwani, P., 2000, Evidence for a buried fault system in the Coastal Plain of the Carolinas and Virginia – Implications for neotectonics in the southeastern United States: *GSA Bulletin*, no. 2, vol. 112, pp. 200-220.
- Martens, J.H., 1935, Beach sands between Charleston, South Carolina and Miami, Florida: *Bulletin of the Geological Society of America*, vol. 46, p. 1563-1596.
- McCartan, L., Owens, J.P., Blackwelder, B.W., Szabo, B.J., Belknap, D.F., Kriausakul, N., Mitterer, R.M., Wehmiller, J.F., 1982, Comparison of amino acid racemization geochronometry with lithostratigraphy, biostratigraphy, uranium-series coral dating, and magnetostratigraphy in the Atlantic Coastal Plain of the Southeastern United States: *Quaternary Research*, vol. 18, pp. 337-359.
- Mercier, Norbert, 1998, ANATOL version 0.72: LSCE – Domaine du CNRS, Gif-sur-Yvette, France.
- Murray A.S., Wintle, A.G., 2003. The single aliquot regenerative dose protocol: potential for improvements in reliability. *Radiation Measurements* 37, 377-381.
- Murray, A.S., Olley, J.M., 2002. Precision and accuracy in the optically stimulated luminescence dating of sedimentary quartz: a status review. *Geochronometria* 21, 1-16.
- Murray, A.S., Wintle A. G., 2000. Luminescence dating of quartz using an improved single-aliquot regenerative-dose procedure. *Radiation Measurements* 32, 57-73.
- Neal, A., 2004, Ground-penetrating radar and its use in sedimentology: principles, problems and progress. *Earth-Science Reviews*, vol. 66, pp. 261-330.
- Neiheisel, J., 1962, Heavy-mineral investigation of recent and Pleistocene sands of Lower Coastal plain of Georgia: *Geological Society of America Bulletin*, vol. 73, p. 365-374.
- Oertel, G.F, 1975, Post Pleistocene island and inlet adjustment along the Georgia coast: *Journal of Sedimentary Petrology*, v. 45, no. 1, pp. 150-159.
- Olhoeft, G.R., 1998, Electrical, magnetic and geometric properties that determine ground penetrating radar performance: *Proceedings of GPR 1998, Seventh International Conference on Ground Penetrating Radar*, The University of Kansas, Lawrence, KS, p. 177-182.
- Pagnois, V., Wintle, A.G., Chen, R. and Wang, X.L., 2008, A theoretical model for a new dating protocol for quartz based on thermally transferred OSL (TT-OSL): *Radiation Measurements*, no. 43, p. 704-708.

- Parham, P.P., Riggs, S.R., Culver, S.J., Mallinson, D.J., Rink, W.J. and Burdette, K., 2013, Quaternary coastal lithofacies, sequence development and stratigraphy in a passive margin setting, North Carolina and Virginia, USA: *Sedimentology*, vol. 60, p. 503-547.
- Pietsch, T.J., Olley, J.M. and Nanson, G.C., 2008, Fluvial transport as a natural luminescence sensitiser of quartz: *Quaternary Geochronology*, vol. 3, p. 365-376.
- Pirkle, F.L., Pirkle, W.A. and Rich, F.J., 2013, Heavy-mineral mining in the Atlantic Coastal Plain and what deposit locations tell us about ancient shorelines: *Journal of Coastal Research*, vol. 69, p. 154-175.
- Porat, N., Duller, G.A.T., Roberts, H.M. and Wintle, A.G., 2009, A simplified SAR protocol for TT-OSL: *Radiation Measurements*, no. 44, p. 538-542.
- Powers, M.H., 1997, Modeling frequency-dependent GPR: *The Leading Edge*, no. 16, vol. 11, p. 1657-1662.
- Preusser, F., Chithambo, M., Götte, T., Martini, M., Ramseyer, K., Sendezera, E.J., Susino, G.J. and Wintle, A.G., 2009, Quartz as a natural luminescence dosimeter: *Earth-Science Reviews*, no. 97, p. 196-226.
- Preusser, F., Chithambo, M.L., Gotte, T., Martini, M., Ramseyer, K., Sandezera, E.J., Susino, G.J., Wintle, A.G., 2009, Quartz as a natural luminescence dosimeter: *Earth-Science Reviews*, vol. 97, pp. 196-226.
- Preusser, F., Degering, D., Fuchs, M., Hilgers, A., Kadereit, A., Klasen, N., Krbetschek, M., Richter, D. and Spencer, J.Q.G., 2008: *Quaternary Science Journal*, vol. 57, no. 1-2, p. 95-149.
- Rhea, M.W., 1986, Comparison of the Quaternary Shoreline Systems in Georgia: Morphology, Drainage, and Inferred Processes of Formation: Masters Thesis, Brown University, Athens, GA.
- Rink, W.J., 1997, Electron spin resonance (ESR) dating and ESR applications in Quaternary science and archaeometry: *Radiation Measurements*, vol. 27, no. 5-6, pp. 975-1025.
- Rink, W.J. and Thompson, J. (eds.), 2015, *Encyclopedia of Dating Methods*: Springer Netherlands.
- Rink, W.J., Bartoll, J., Schwarcz, H.P., Shane, P., Bar-Yosef, O., 2007, Testing the reliability of ESR dating of optically exposed buried quartz sediments: *Radiation Measurements*, vol. 42, pp. 1618-1626.
- Schultz, G., 2001, Characterizing heterogeneity of subsurface aquifers in coastal Georgia using complementary observations: *Geological Society of America Annual Meeting*, November 5-8.
- Scott, T.W., Swift, D.J.P., Whittecar, G.R., Brook, G.A., 2010, Glacioisostatic influences on Virginia's late Pleistocene coastal plain deposits: *Geomorphology*, vol. 116, pp. 175-188.
- Sheriff, R.E., 1977, Limitations on resolution of seismic reflections and geologic detail derivable from them: *AAPG Memoir*, no. 26, p. 3-14.
- Sheriff, R.E., 1997, Seismic resolution a key element: *AAPG Explorer*, no. 18, vol. 10, p. 44-51.
- Siddall, M., Rohling, E. J., Almogi-Labin, A., Hemleben, Ch., Meischner, D., Schmelzer, I., Smeed, D. A., 2003. Sea-level fluctuations during the last glacial cycle. *Nature* 423, 853-858.

- Stevens, T., Buylaert, J.-P. and Murray, A.S., 2009, Toward development of a broadly-applicable SAR TT-OSL dating protocol for quartz: *Radiation Measurements*, no. 44, p.639-645.
- Swanson, V.E. and Palacas, J.G., 1965, Humate in coastal sands of northwest Florida: United States Geological Survey Technical Report 1214-B, Washington, D.C., pp. 26.
- Szabo, B.J., 1988, Uranium-series dating of fossil corals from marine sediments of southeastern United States Atlantic Coastal Plain: *Geological Society of America Bulletin*, vol. 96, p. 398-406.
- Tanaka, K., Hataya, R., Spooner, N.A., Questiaux, D.G., Saito, Y. and Hashimoto, T., 1997, Dating of marine terrace sediments by ESR, TL and OSL methods and their applicabilities: *Quaternary Science Reviews (Quaternary Geochronology)*, vol. 16, p. 257-264.
- Thompson V.D. and Thomas, D.H. (eds.), 2013, Life among the tides, recent archaeology on the Georgia Bight: *Anthropological Papers of the American Museum of Natural History*, no. 98, pp. 494.
- Tissoux, H., Falguères, C., Voinchet, P., Toyoda, S., Bahain, J.J. and Despriée, J., 2007, Potential use of Ti-center ESR dating of fluvial sediments: *Quaternary Geochronology*, vol. 2, p. 367-372.
- Tissoux, H., Toyoda, S., Falguères, C., Voinchet, P., Takada, M., Bahain, J.J. and Despriée, J., 2008, ESR dating of sedimentary quartz from two Pleistocene deposits using Al and Ti-centers: *Geochronometria*, no. 30, p. 23-31.
- Tissoux, H., Valladas, H., Voinchet, P., Reyss, J.L., Mercier, N., Falgueres, C., Bahain, J.J., Zoller, L., Antonie, P., 2010, OSL and ESR studies of Aeolian quartz from the Upper Pleistocene loess sequence of Nussloch ,Germany: *Quaternary Geochronology*, vol. 5, pp. 131-136.
- Toyoda, S., Voinchet, P., Falgueres, C., Dolo, J.M., Laurent, M., 2000. Bleaching of ESR signals by sunlight: a laboratory experiment for establishing the ESR dating of sediments. *Applied Radiation and Isotopes* 52, 1357-1362.
- Tsukamoto, S., Duller, G.A.T. and Wintle, A.G., 2008, Characteristics of thermally transferred optically stimulated luminescence (TT-OSL) in quartz and its potential for dating sediments: *Radiation Measurements*, vol. 43, p. 1204-1218.
- Veatch, J.O., and Stephenson, L.W., 1911, Preliminary report on the geology of the Coastal Plain of Georgia: *Georgia Geological Survey Bulletin*, no. 26, pp. 466.
- Voinchet, P., Falguères, C., Laurent, M., Toyoda, S., Bahain, J.J. and Dolo, J.M., 2003, Artificial optical bleaching of the Aluminium center in quartz implications to ESR dating of sediments: *Quaternary Science Reviews*, no. 22, p. 1335-1338.
- Walther R. and Zilles, D., 1994, ESR studies on bleached sedimentary quartz: *Quaternary Geochronology (Quaternary Science Reviews)*, vol. 13, p. 611-614.
- Wang, X.L., Wintle, A.G. and Lu, Y.C., 2006, thermally transferred luminescence in fine-grained quartz from Chinese loess: basic observations: *Radiation Measurements*, no. 41, p. 649-658.
- Wang, X.L., Wintle, A.G. and Lu, Y.C., 2007, Testing a single-aliquot protocol for recuperated OSL dating: *Radiation Measurements*, no. 42, p. 380-391.

- Wehmiller, J.F., 2012, United States Quaternary coastal sequences and molluscan racemization geochronology – What have they meant for each other over the past 45 years: *Quaternary Geochronology*, in press, p. 18.
- Wehmiller, J.F., Harris, W.B., Boutin, B.S., Farrell, K.M., 2012, Calibration of amino acid racemization (AAR) kinetics in United States mid-Atlantic Coastal Plain Quaternary mollusks using $^{87}\text{Sr}/^{86}\text{Sr}$ analysis: Evaluation of kinetic models and estimation of regional Late Pleistocene temperature history: *Quaternary Geochronology*, no. 7, pp. 21-36.
- Wehmiller, J.F., Simmons, K.R., Cheng, H., Edwards, R.L., Martin-McNaughton, J., York, L.L., Krantz, D.E., Shen, C.-C., 2004, Uranium-series coral ages from the US Atlantic Coastal Plain-the “80 ka problem” revisited: *Quaternary International*, no. 120, pp. 3 -14.
- Wehmiller, J.F., Thieler, E.R., Miller, D., Pellerito, V., Bakeman Keeney, V., Riggs, S.R., Culver, S., Mallinson, D., Farrell, K.M., York, L.L., Pierson, J., Parham, P.R., 2010, Aminostratigraphy of surface and subsurface Quaternary sediments, North Carolina coastal plain, USA: *Quaternary Geochronology*, no. 5, pp. 459-492.
- Willis, R.A., 2006, Genetic stratigraphy and geochronology of last interglacial shorelines of the central coast of South Carolina: Masters Thesis, Louisiana State University, Baton Rouge, LA.
- Winker, C.D., and Howard, J.D., 1977, Correlation of tectonically deformed shorelines on the southern Atlantic coastal plain: *Geology*, v. 5, pp. 123-127.
- Wintle, A.G. and Murray, A.S., 2006, A review of quartz optically simulated luminescence characteristics and their relevance in single-aliquot regeneration dating protocols: *Radiation Measurements*, no. 41, p. 369-391.
- Yokoyama, Y., Falgueres, C., Quaegebeur, J.P., 1985. ESR dating of quartz from Quaternary sediments: first attempt. *Nuclear Tracks and Radiation Measurements* 10, 921.
- Yoshida, H., 1996, Quaternary dating studies using ESR signals, emphasis on shell, coral, tooth enamel and quartz: Doctor of Philosophy Thesis, The Australian National University, Canberra, Australia.

Appendix 1 : Locations



A1-F1: Location of the Georgia ACDs according to the Georgia Geological Survey Map of 1979. The location of the core sample sites are shown as red circles. Note the lack of the Okefenokee ACD and the location of the Wicomico ACD in its place. The reclassification of these ACDs as mapped by Rhea (1986) and described by Huddleston (1988) is used in this study.

Table A1-T1

Sample	ACD Name	Latitude (°N)	Longitude (°W)	Surface Elevation (m)
Os	J.I. swash	31.049981	81.408327	0
Od	J.I. dune	31.050085	81.408722	1
gp1422c	PA	31.024775	81.530049	3
gp1422d	P A	31.024775	81.530049	3
gp1422g	P A	31.024775	81.530049	3
gp1421c	pam	31.029803	81.580026	6
gp1421d	pam	31.029803	81.580026	6
gp1421f	pam	31.029803	81.580026	6
gp129b	tal	31.258100	81.747990	13
gp129c	tal	31.258100	81.747990	13
gp124b	pen	30.840250	81.976120	19
gp124e	pen	30.840250	81.976120	19
gp123c	wic	30.837270	81.982080	24
gp123d	wic	30.837270	81.982080	24
gp123f	wic	30.837270	81.982080	24
gp127b	oke	31.101642	82.107803	42
gp127c	oke	31.101642	82.107803	42
gp127e	oke	31.101642	82.107803	42

A1-T1: Location of the ACD sample sites in Georgia, USA. Locations are given in decimal degrees and elevation in meters above sea level in WGS84 (Google Earth geographic coordinate system).

Appendix 2 : Core logs

The following images are the visually logged core of this project. Shown are the core length, grain size and features, color, a brief description of the lithology and the GPR reflections in the vicinity of the core. Larger format digital images of these cores can be found in the folder titles core logs in the CD accompanying this document.

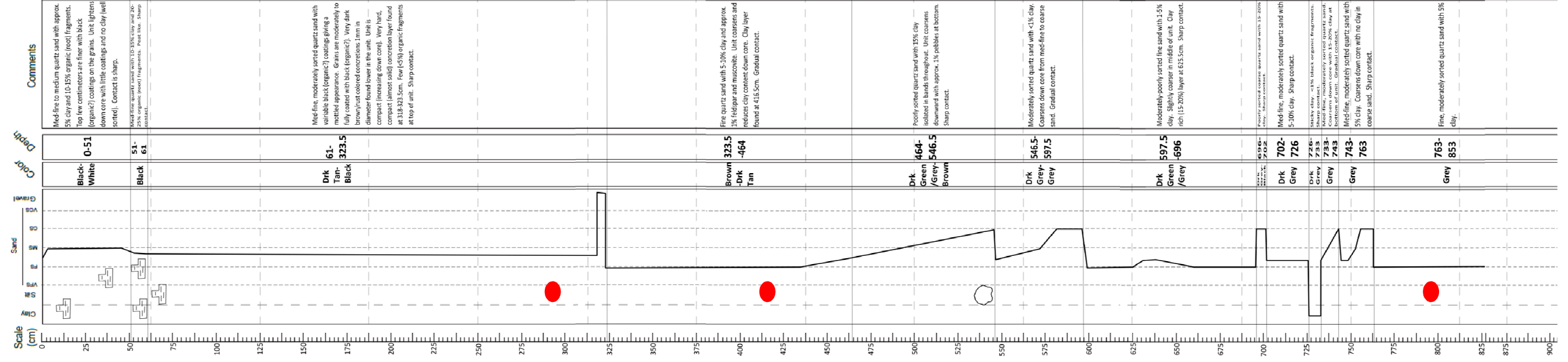


Figure A2-F1: Core of gp1422 of the Princess Anne ACD. Note the number of coarsening upward sequences as well as the clay layers found in the lower portion of the core. The red dots indicate the sample collection sites.

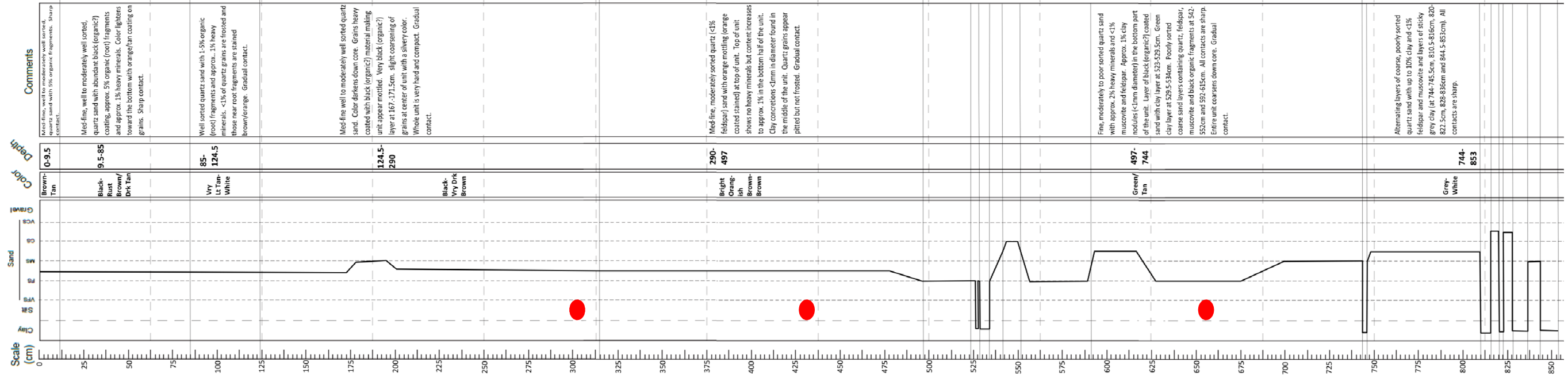


Figure A2-F2: Core of gp1421 of the Pamlico ACD. Note the numerous clay layers found in the middle portion and lower portion of this core. The red dots indicate the sample collection sites.

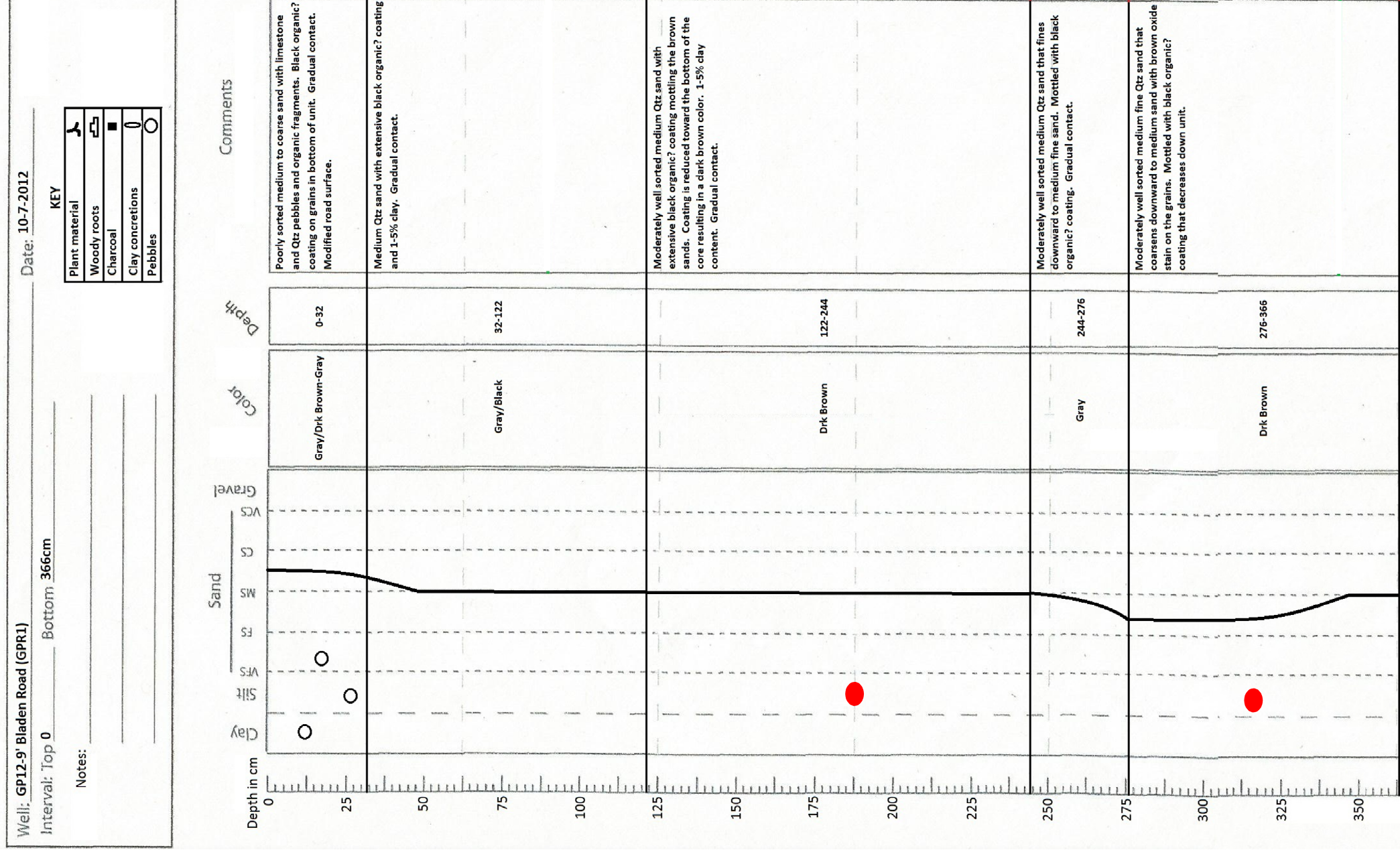


Figure A2-F3: Core of gp129 of the Talbot ACD. This core is short due to drill refusal at humate layer. The red dots indicate the sample collection sites.

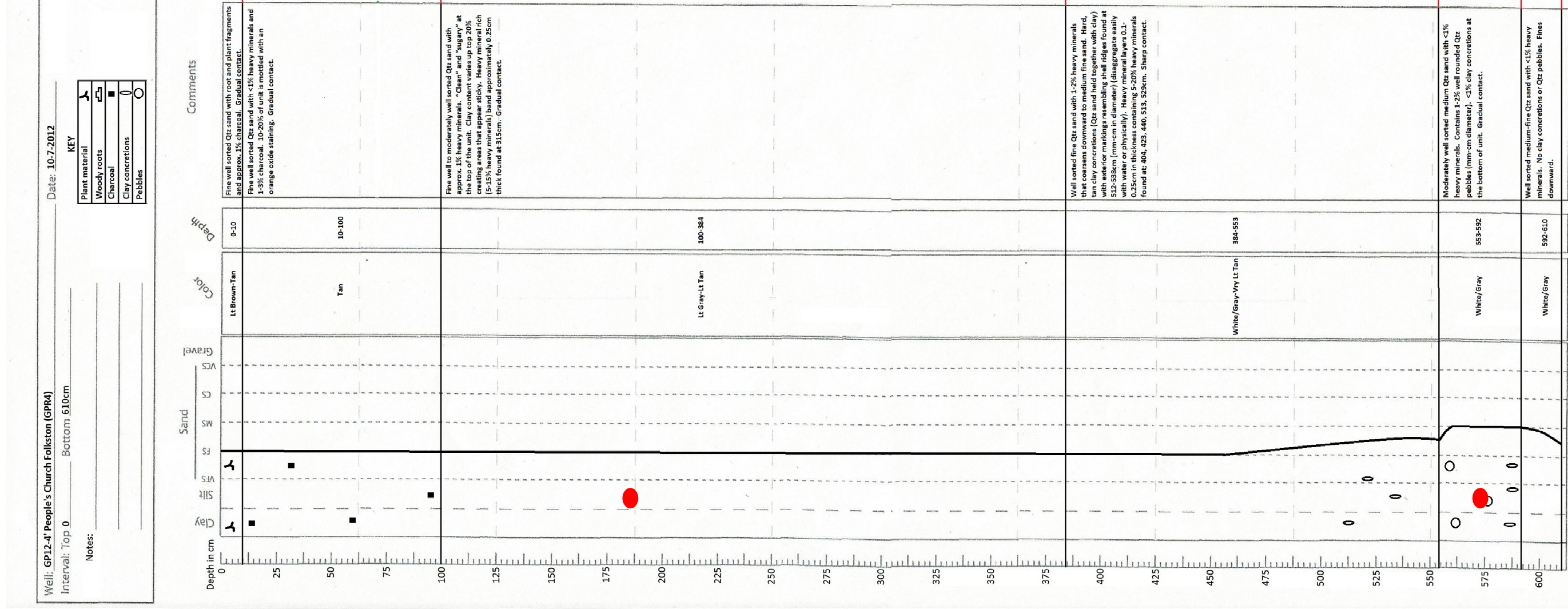


Figure A2-F4: Core of gp124 of the Penholoway ACD. The red dots indicate the sample collection sites.

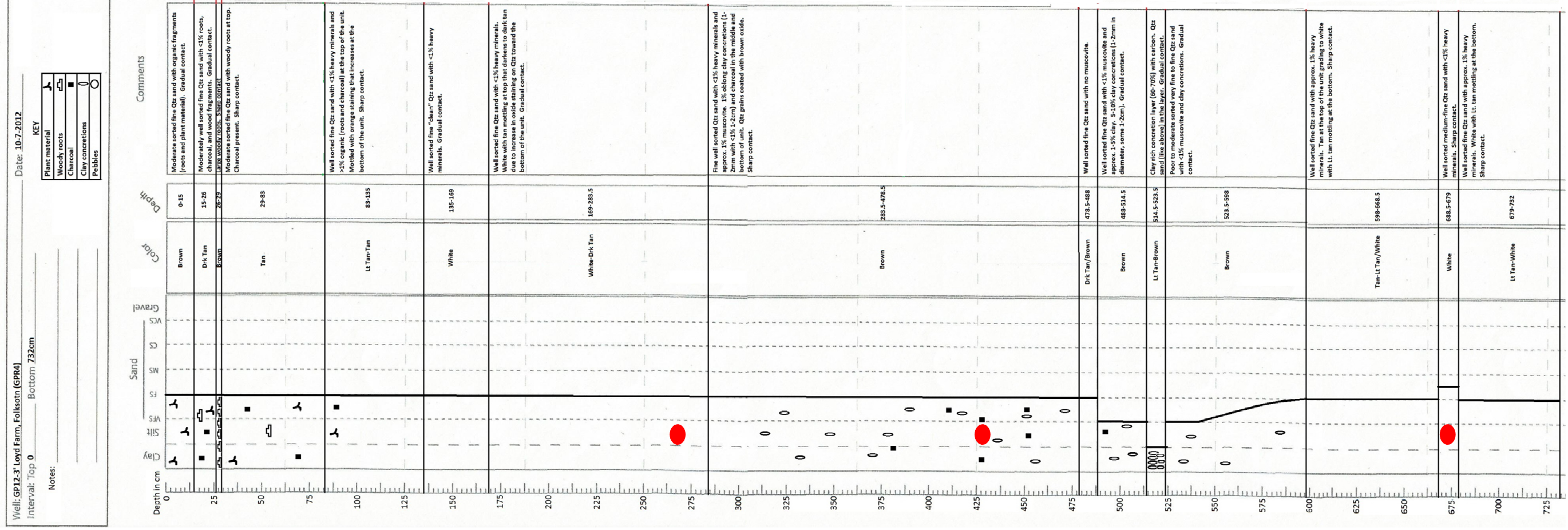


Figure: A2-F5: Core of gp123 of the Wicomico ACD. Note the layer of clay shell casts. The red dots indicate the sample collection sites.

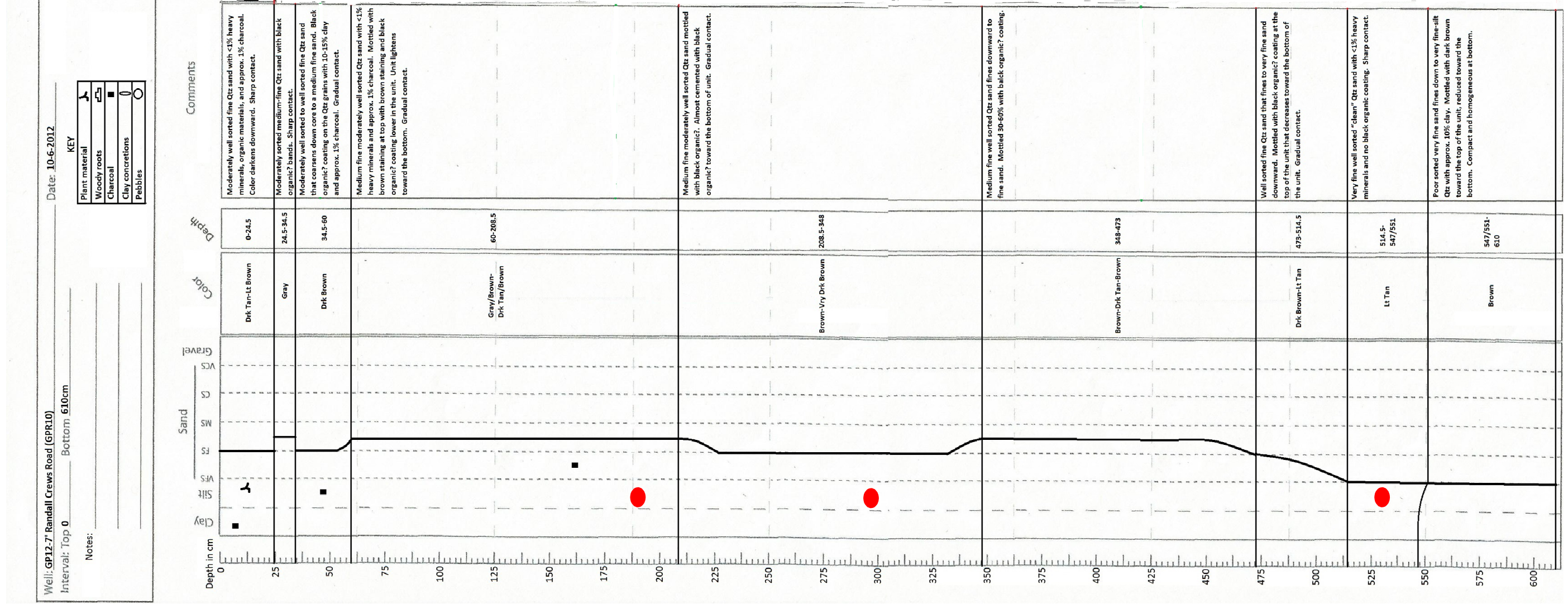


Figure A2-F6: Core of gp127 of the Okfenokee ACD. The red dots indicate the sample collection sites.

Appendix 3: ESR data

Appendix 3 contains information on ESR measurement conditions at both FSU and Osaka University (Table A3-T1), Dose Response Curves (DRCs) for the ESR signals (Figures A3-F1 to A3-F15), and correlation charts correlating the ESR signals within a sample (Table A3-T2 to A3-T15) as well as correlating the ESR signals between samples (Table A3-T16 to A3-T21).

As stated in Chapters 3 and 4 Tables A3-T2 to A3-T15 show the correlation between the different ESR signals measured within each sample. Each chart shows a P value as calculated by Galbraith (2003) and described in Galbraith and Roberts (2012) and Arnold et.al. (2014). Strong correlations with P values over 0.32 (representing correlation at the 1σ confidence level) are highlighted in green. Those values not highlighted do not show any correlation. These values were taken into consideration when determining which samples showed agreement between the ESR signals and in the case of no agreement which age should be used to interpret results.

Tables A3-T15 to A3-T21 show the correlation between ESR signals of the samples of the study. Each chart shows a P value as calculated by Galbraith (2003) and described in Galbraith and Roberts (2012) and Arnold et.al. (2014). Strong correlations with P values over 0.32 (representing correlation at the 1σ confidence level) are highlighted in green while those with correlation have P values of between 0.5 and 0.31 (representing correlation at the 2σ confidence level) are highlighted in yellow. Those values not highlighted do not show any correlation. All ESR signals studied in this project are shown below, with the exception of the Ti-Li option D (SSE) as it is shown in Figure 23. As stated in Chapter 4 the Ti-Li option D signal was considered the most likely signal to represent the maximum age of the samples in this study. As such all correlations between samples as stated in Chapters 3 and 4 are made using the Ti-Li option D signal. The charts of the remaining signals are included in the hopes that it will benefit future ESR research in incomplete signal bleaching.

Raw ESR data, including spectra, intensity measurements and Origins plots can be found in the supplemental data disc included in this work.

Table A3-T1

	Florida State University	Osaka University	
Measurement Conditions		Al	Ti
Temperature (K°)	77	77/83	77/83
Cooling system	dewar	dewar/ gas system	dewar/ gas system
Sample size (g)	0.1	0.1	0.1
Modulation frequency (kHz)	100	100	100
Modulation amplitude (mT)	1.6	1.6	1.6
Time constant (mT/min)	1.28	0.03	0.03
Measurement time (min)	4	8	8
Microwave power (mW)	5	5	5
Rotations	none	5	5

A3-T1: Measurement conditions of the ESR samples at both FSU and Osaka University. Note that at FSU both the Al and Ti signals were measured during the same run while at Osaka University these signals were measured in separate runs with similar measurement conditions.

Princess Anne: GP1422d

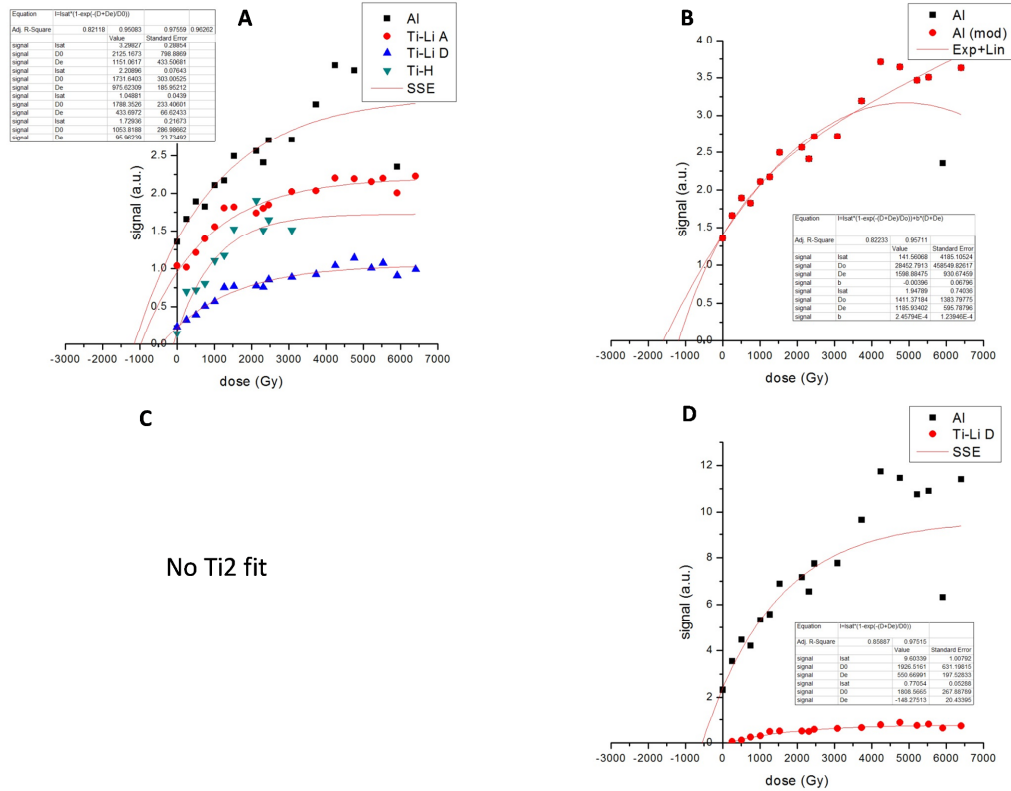


Figure A3-F1: Dose response curve (DRC) of sample gp1422d of the Princess Anne ACD measured at FSU. Part A shows the AI, Ti-Li option A and option D signals, as well as the Ti-H signal fitted with a Single Saturating Exponential (SSE) fit. Shown in B is the Exponential plus Linear (Exp+Lin) fit of both the AI signal as well as a modified AI signal with an outlying dose point removed. C is the DRC of the Ti-Li (option A and D) fitted with the Ti2 curve of Duval and Guilarte (2014) but as this sample did not have aliquots at the high additive dose the curve did not fit. D shows the SSE fit of AI and Ti-Li option D the ESR signals, fitted with a SSE, that have had the calculated relict signal intensity removed (see part 4.3.3.1). Included in each graph is the I_{max}, D₀, D_E, and R squared fit of the curve.

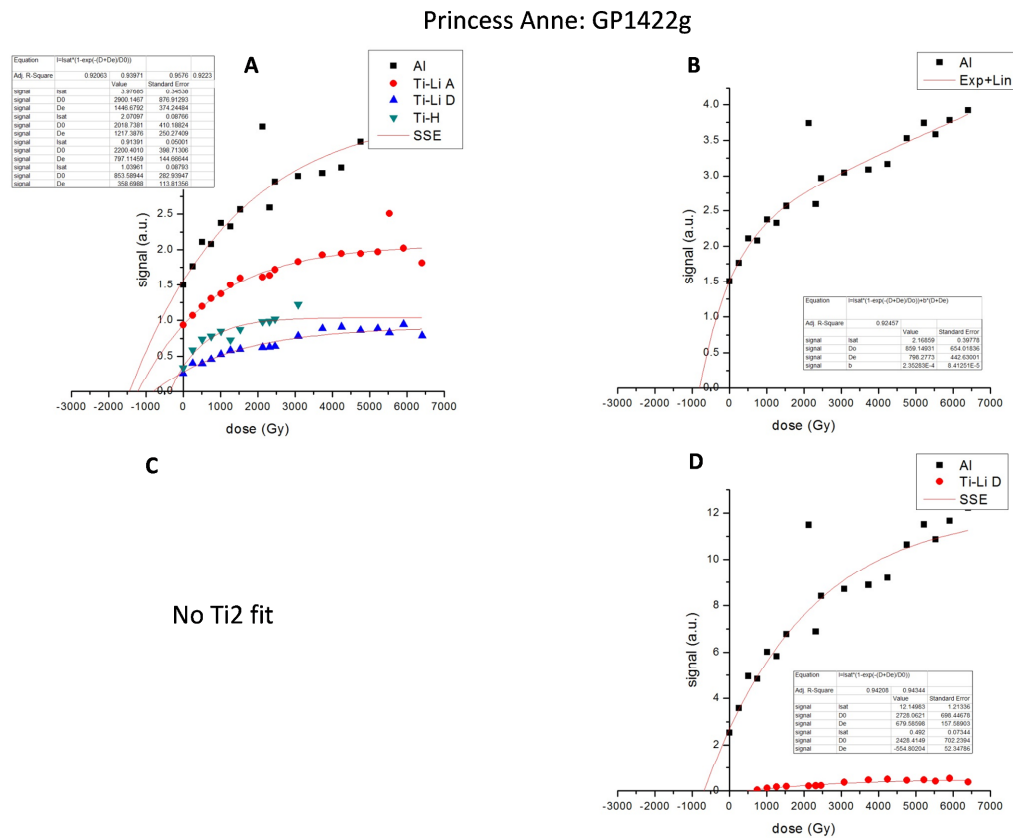


Figure A3-F2: Dose response curve (DRC) of sample gp1422g of the Princess Anne ACD measured at FSU. Part A shows the Al, Ti-Li option A and option D signals, as well as the Ti-H signal fitted with a Single Saturating Exponential (SSE) fit. Shown in B is the Exponential plus Linear (Exp+Lin) fit of the Al signal. C is the DRC of the Ti-Li (option A and D) fitted with the Ti2 curve of Duval and Guilarte (2014) but as this sample did not have aliquots at the high additive dose the curve did not fit. D shows the SSE fit of Al and Ti-Li option D the ESR signals, fitted with a SSE, that have had the calculated relict signal intensity removed (see part 4.3.3.1). Included in each graph is the I_{max} , D_0 , D_E , and R squared fit of the curve.

Pamlico: GP1421c

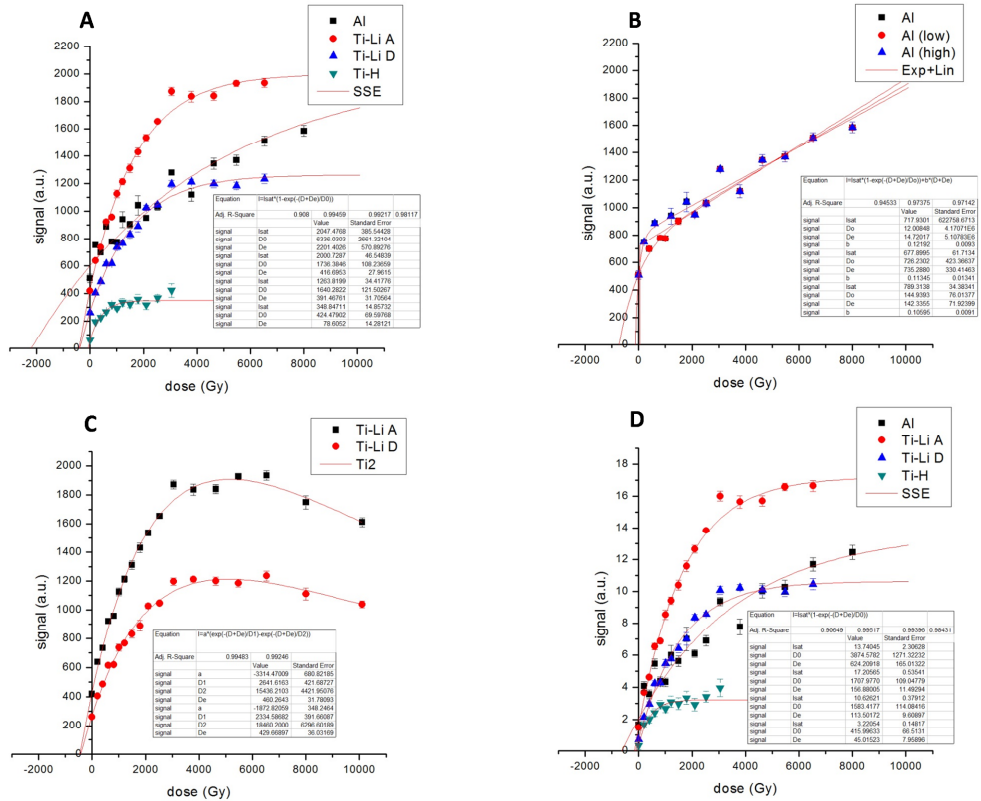


Figure A3-F3: Dose response curve (DRC) of sample gp1421c of the Pamlico ACD measured at Osaka University. Part A shows the AI, Ti-Li option A and option D signals, as well as the Ti-H signal fitted with a Single Saturating Exponential (SSE) fit. Shown in B is the Exponential plus Linear (Exp+Lin) fit of the full AI signal as well as two modifications: the outlying dose points are dropped. C is the DRC of the Ti-Li (option A and D) including points at additive doses over +6500GY and fitted with the Ti2 curve of Duval and Guilarte (2014). D shows the SSE fit of all the ESR signals, fitted with a SSE, that have had the calculated relict signal intensity removed (see part 4.3.3.1). Included in each graph is the I_{max}, D₀, D_E, and R squared fit of the curve.

Pamlico: GP1421d

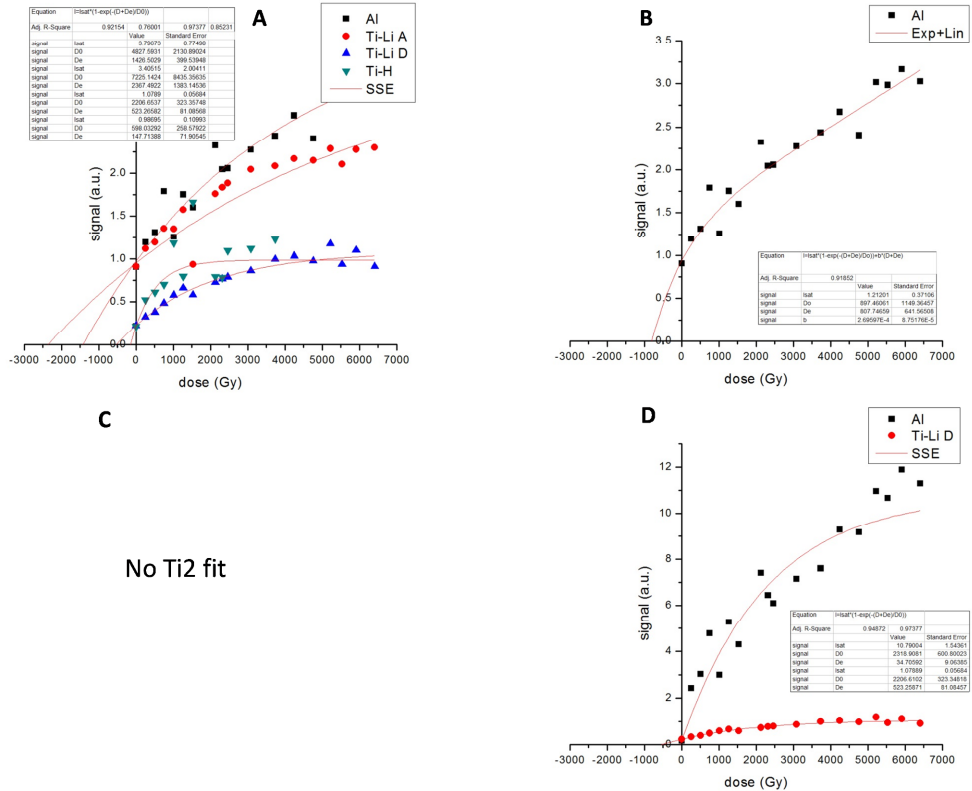


Figure A3-F4: Dose response curve (DRC) of sample gp1421d of the Princess Anne ACD measured at FSU. Part A shows the Al, Ti-Li option A and option D signals, as well as the Ti-H signal fitted with a Single Saturating Exponential (SSE) fit. Shown in B is the Exponential plus Linear (Exp+Lin) fit of the Al signal. C is the DRC of the Ti-Li (option A and D) fitted with the Ti2 curve of Duval and Guilarte (2014) but as this sample did not have aliquots at the high additive dose the curve did not fit. D shows the SSE fit of Al and Ti-Li option D the ESR signals, fitted with a SSE, that have had the calculated relict signal intensity removed (see part 4.3.3.1). Included in each graph is the Imax, Do, DE, and R squared fit of the curve.

Pamlico: GP1421f

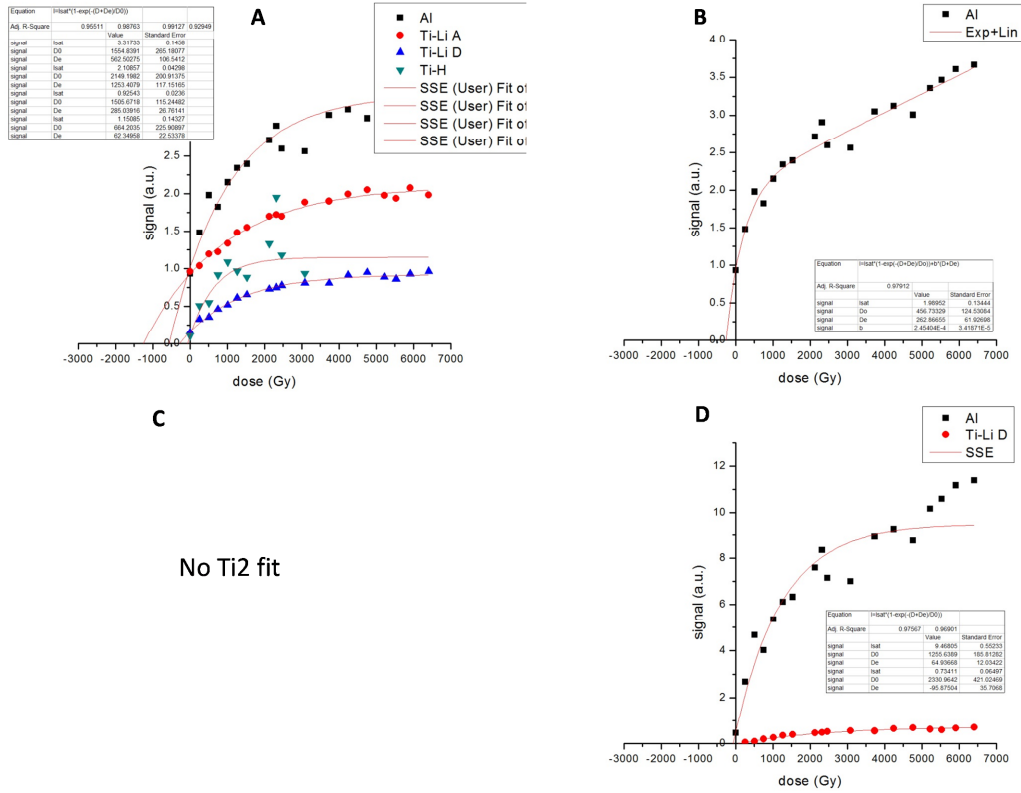


Figure A3-F5: Dose response curve (DRC) of sample gp1421f of the Pamlico ACD measured at FSU. Part A shows the Al, Ti-Li option A and option D signals, as well as the Ti-H signal fitted with a Single Saturating Exponential (SSE) fit. Shown in B is the Exponential plus Linear (Exp+Lin) fit of the Al signal. C is the DRC of the Ti-Li (option A and D) fitted with the Ti2 curve of Duval and Guilarte (2014) but as this sample did not have aliquots at the high additive dose the curve did not fit. D shows the SSE fit of Al and Ti-Li option D the ESR signals, fitted with a SSE, that have had the calculated relic signal intensity removed (see part 4.3.3.1). Included in each graph is the Imax, Do, DE, and R squared fit of the curve.

Talbot: GP129b

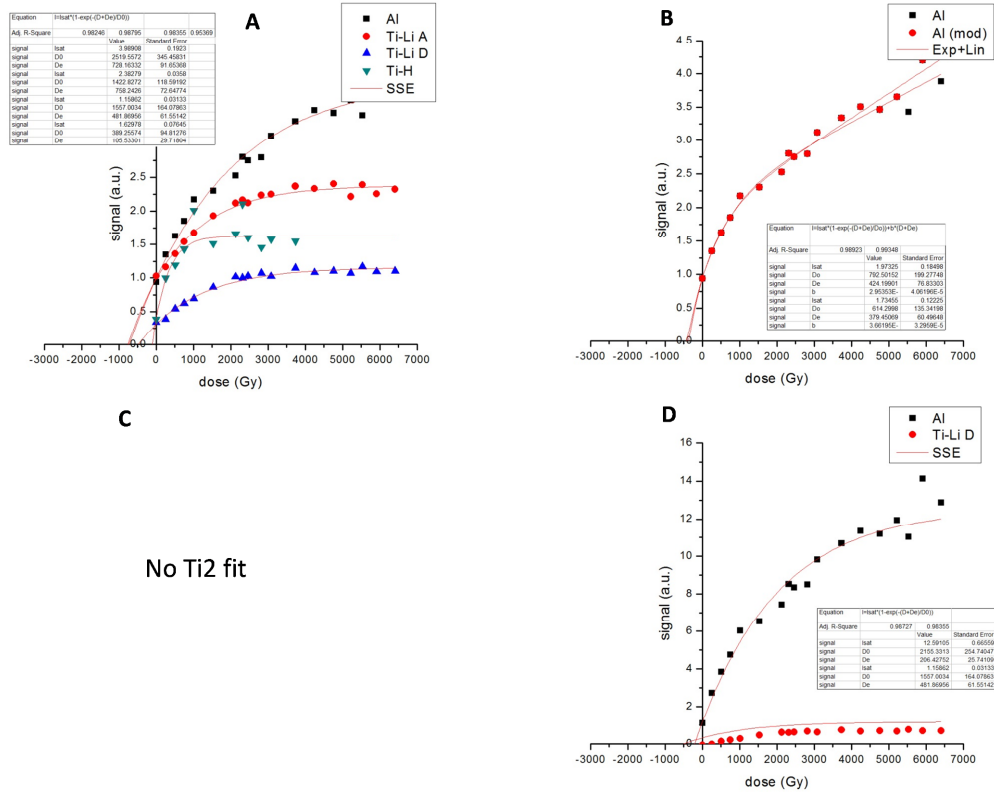


Figure A3-F6: Dose response curve (DRC) of sample gp129b of the Talbot ACD measured at FSU. Part A shows the AI, Ti-Li option A and option D signals, as well as the Ti-H signal fitted with a Single Saturating Exponential (SSE) fit. Shown in B is the Exponential plus Linear (Exp+Lin) fit of both the AI signal as well as a modified AI signal with an outlying dose point removed. C is the DRC of the Ti-Li (option A and D) fitted with the Ti2 curve of Duval and Guilarte (2014) but as this sample did not have aliquots at the high additive dose the curve did not fit. D shows the SSE fit of AI and Ti-Li option D the ESR signals, fitted with a SSE, that have had the calculated relict signal intensity removed (see part 4.3.3.1). Included in each graph is the Imax, Do, DE, and R squared fit of the curve.

Talbot: GP129c

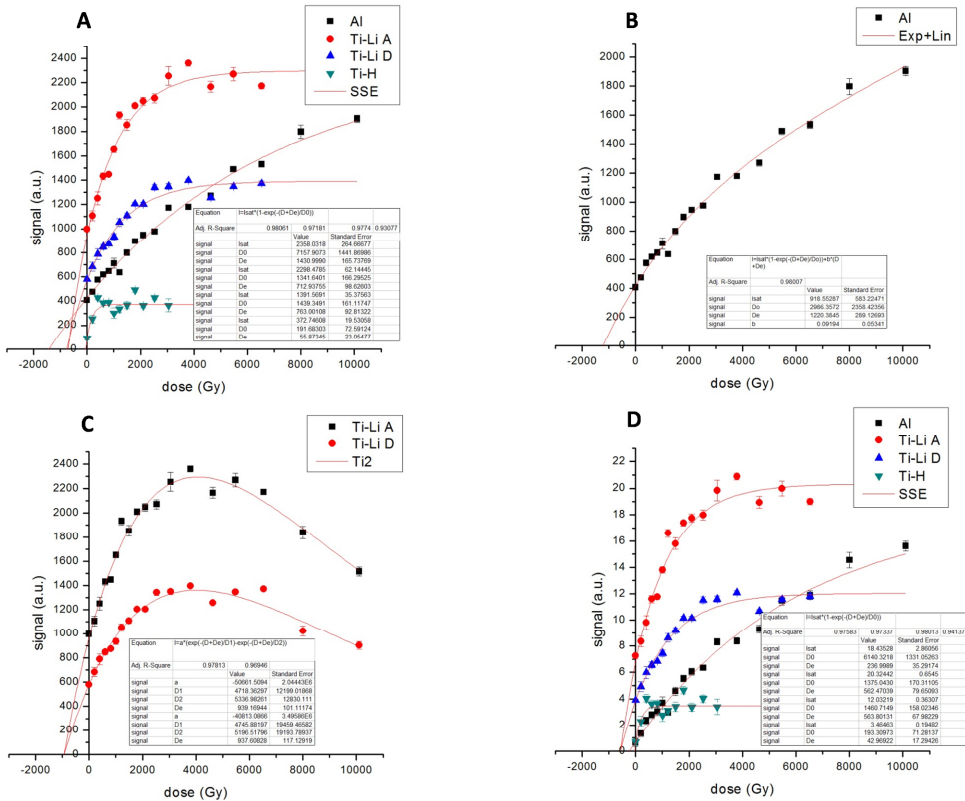


Figure A3-F7: Dose response curve (DRC) of sample gp129c of the Talbot ACD measured at Osaka University. Part A shows the AI, Ti-Li option A and option D signals, as well as the Ti-H signal fitted with a Single Saturating Exponential (SSE) fit. Shown in B is the Exponential plus Linear (Exp+Lin) fit of the AI signal. C is the DRC of the Ti-Li (option A and D) including points at additive doses over +6500GY and fitted with the Ti2 curve of Duval and Guilarte (2014). D shows the SSE fit of all the ESR signals, fitted with a SSE, that have had the calculated relict signal intensity removed (see part 4.3.3.1). Included in each graph is the Imax, Do, De, and R squared fit of the curve.

Penholoway: GP124b

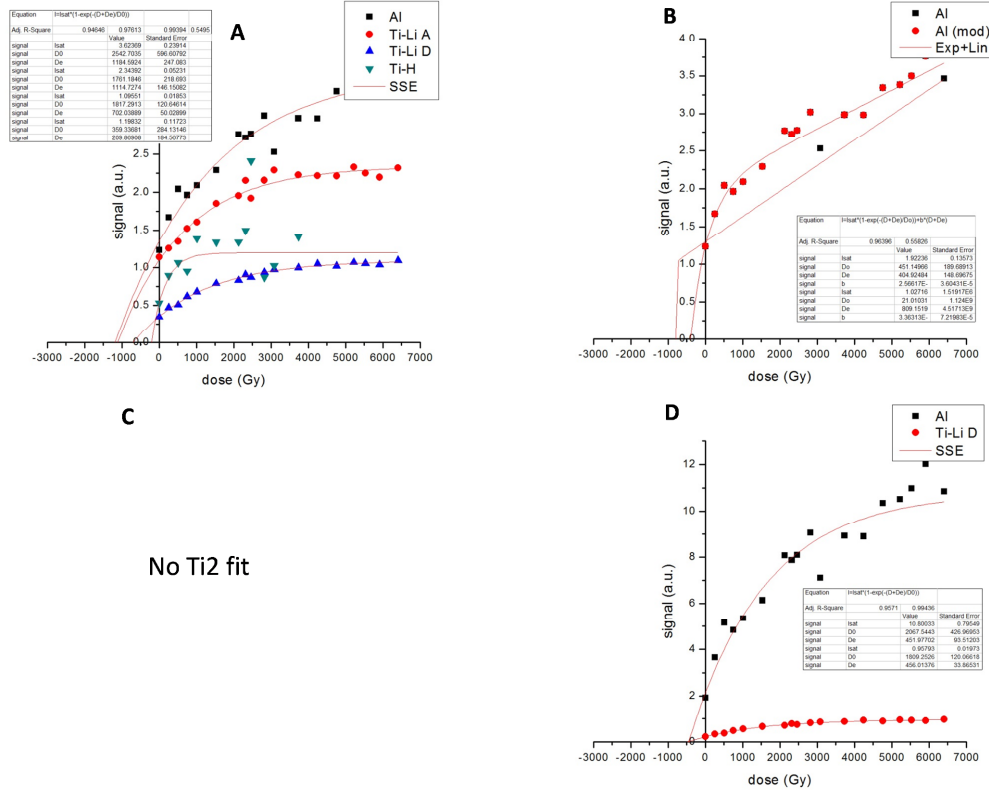


Figure A3-F8: Dose response curve (DRC) of sample gp124b of the Penholoway ACD measured at FSU. Part A shows the Al, Ti-Li option A and option D signals, as well as the Ti-H signal fitted with a Single Saturating Exponential (SSE) fit. Shown in B is the Exponential plus Linear (Exp+Lin) fit of both the Al signal as well as a modified Al signal with an outlying dose point removed. C is the DRC of the Ti-Li (option A and D) fitted with the Ti2 curve of Duval and Guilarte (2014) but as this sample did not have aliquots at the high additive dose the curve did not fit. D shows the SSE fit of Al and Ti-Li option D the ESR signals, fitted with a SSE, that have had the calculated relict signal intensity removed (see part 4.3.3.1). Included in each graph is the I_{max}, D₀, D_E, and R squared fit of the curve.

Wicomico: GP123c

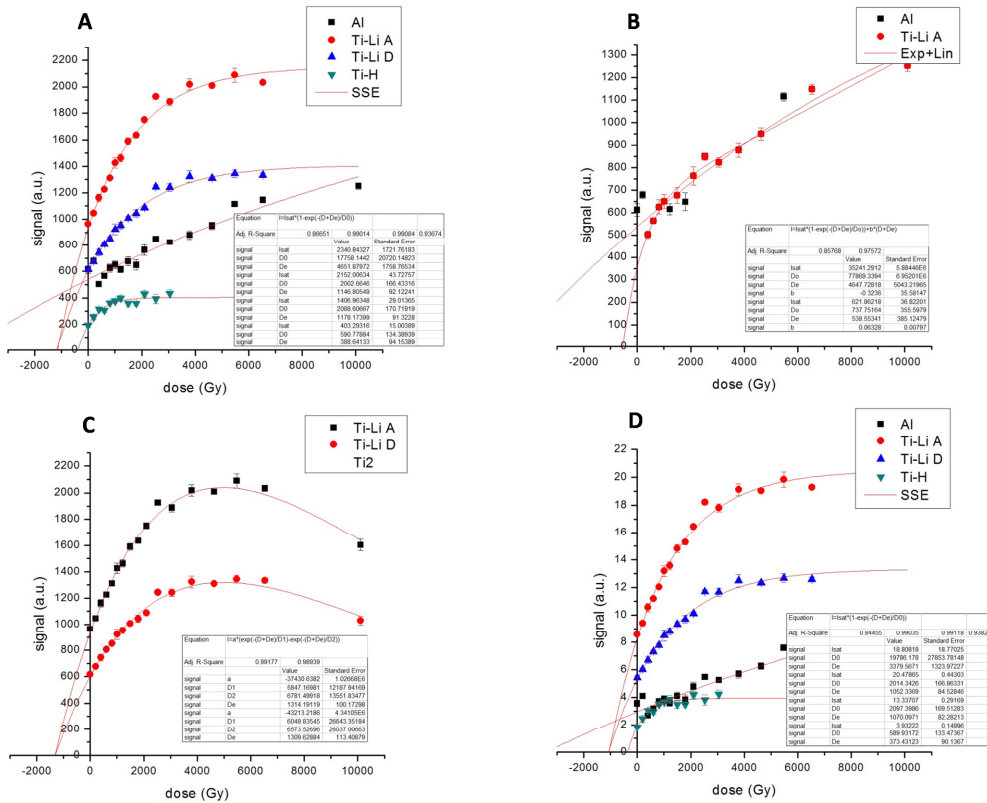


Figure A3-F9: Dose response curve (DRC) of sample gp123c of the Wicomico ACD measured at Osaka University. Part A shows the AI, Ti-Li option A and option D signals, as well as the Ti-H signal fitted with a Single Saturating Exponential (SSE) fit. Shown in B is the Exponential plus Linear (Exp+Lin) fit of the full AI signal as well as modification were outlying dose points were dropped. C is the DRC of the Ti-Li (option A and D) including points at additive doses over +6500GY and fitted with the Ti2 curve of Duval and Guilarte (2014). D shows the SSE fit of all the ESR signals, fitted with a SSE, that have had the calculated relict signal intensity removed (see part 4.3.3.1). Included in each graph is the Imax, Do, De, and R squared fit of the curve.

Wicomico: GP123d

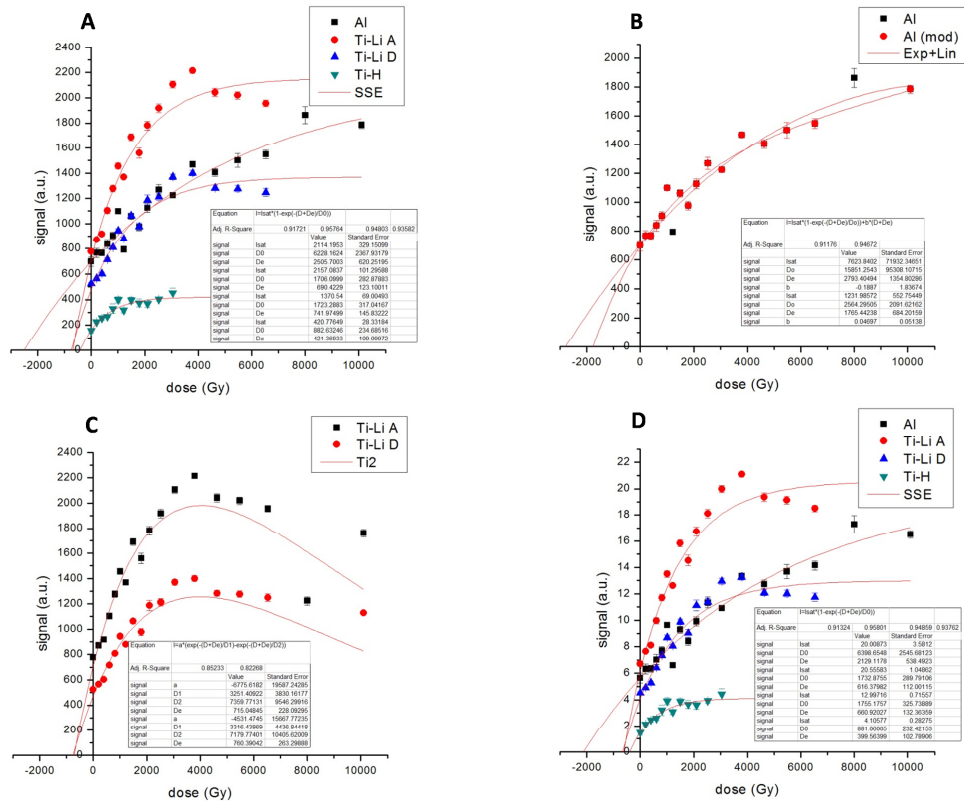


Figure A3-F10: Dose response curve (DRC) of sample gp123d of the Wicomico ACD measured at Osaka University. Part A shows the AI, Ti-Li option A and option D signals, as well as the Ti-H signal fitted with a Single Saturating Exponential (SSE) fit. Shown in B is the Exponential plus Linear (Exp+Lin) fit of the full AI signal as well as modification were outlying dose points were dropped. C is the DRC of the Ti-Li (option A and D) including points at additive doses over +6500Gy and fitted with the Ti2 curve of Duval and Guilarte (2014). D shows the SSE fit of all the ESR signals, fitted with a SSE, that have had the calculated relict signal intensity removed (see part 4.3.3.1). Included in each graph is the Imax, Do, DE, and R squared fit of the curve.

Wicomico: GP123f

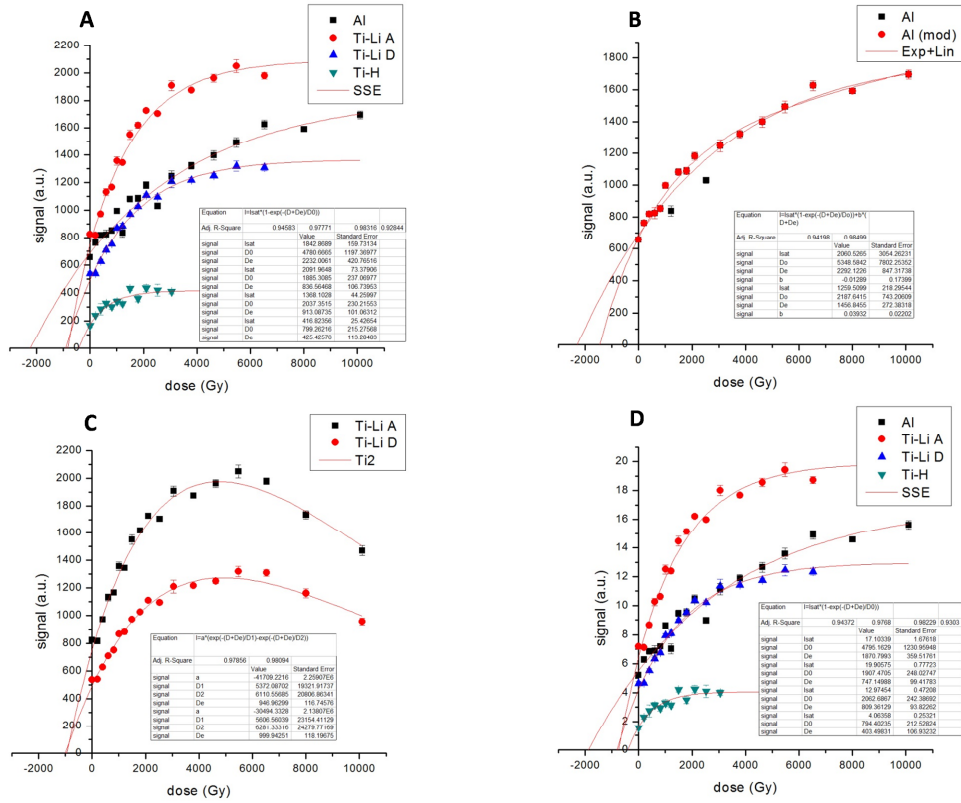


Figure A3-F11: Dose response curve (DRC) of sample gp123f of the Wicomico ACD measured at Osaka University. Part A shows the AI, Ti-Li option A and option D signals, as well as the Ti-H signal fitted with a Single Saturating Exponential (SSE) fit. Shown in B is the Exponential plus Linear (Exp+Lin) fit of the full AI signal as well as a modification where outlying dose points were dropped. C is the DRC of the Ti-Li (option A and D) including points at additive doses over +6500GY and fitted with the Ti2 curve of Duval and Guilarte (2014). D shows the SSE fit of all the ESR signals, fitted with a SSE, that have had the calculated relict signal intensity removed (see part 4.3.3.1). Included in each graph is the I_{max} , D_0 , D_e , and R squared fit of the curve.

Okefenokee: GP127b

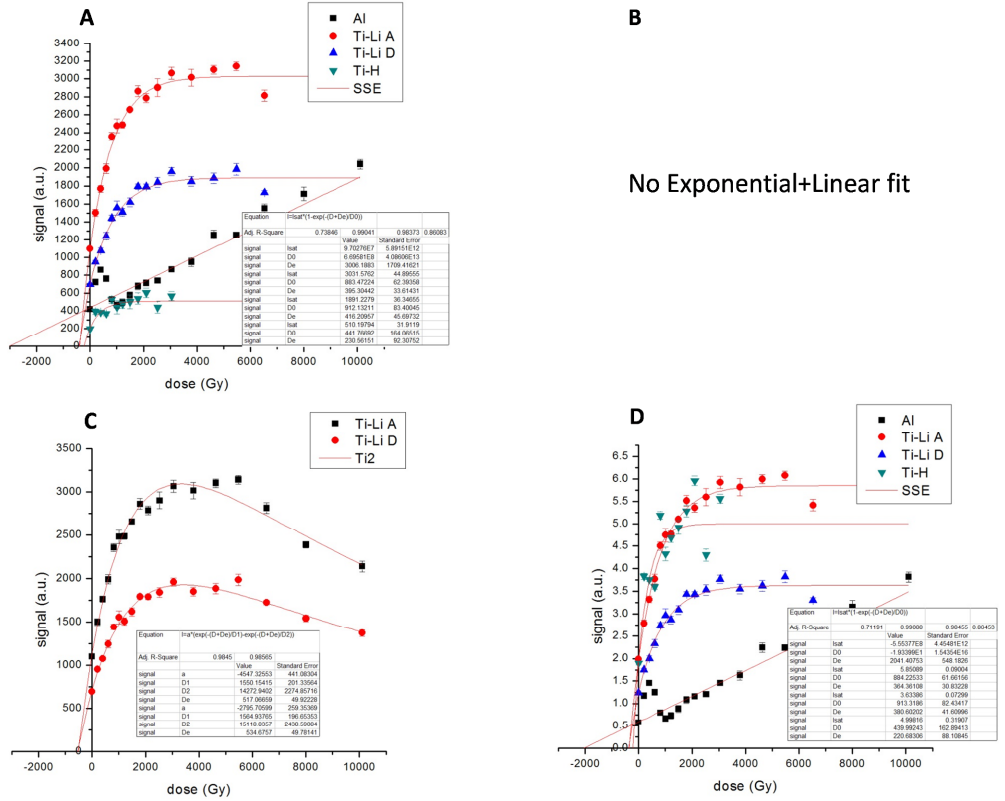


Figure A3-F12: Dose response curve (DRC) of sample gp127b of the Okefenokee ACD measured at Osaka University. Part A shows the Al, Ti-Li option A and option D signals, as well as the Ti-H signal fitted with a Single Saturating Exponential (SSE) fit. Shown in B is the Exponential plus Linear (Exp+Lin) fit of the Al signal, thought this equation did not fit the data for this sample so it is omitted. C is the DRC of the Ti-Li (option A and D) including points at additive doses over +6500GY and fitted with the Ti2 curve of Duval and Guilarte (2014). D shows the SSE fit of all the ESR signals, fitted with a SSE, that have had the calculated relict signal intensity removed (see part 4.3.3.1). Included in each graph is the Imax, Do, De, and R squared fit of the curve.

Okefenokee: GP127c

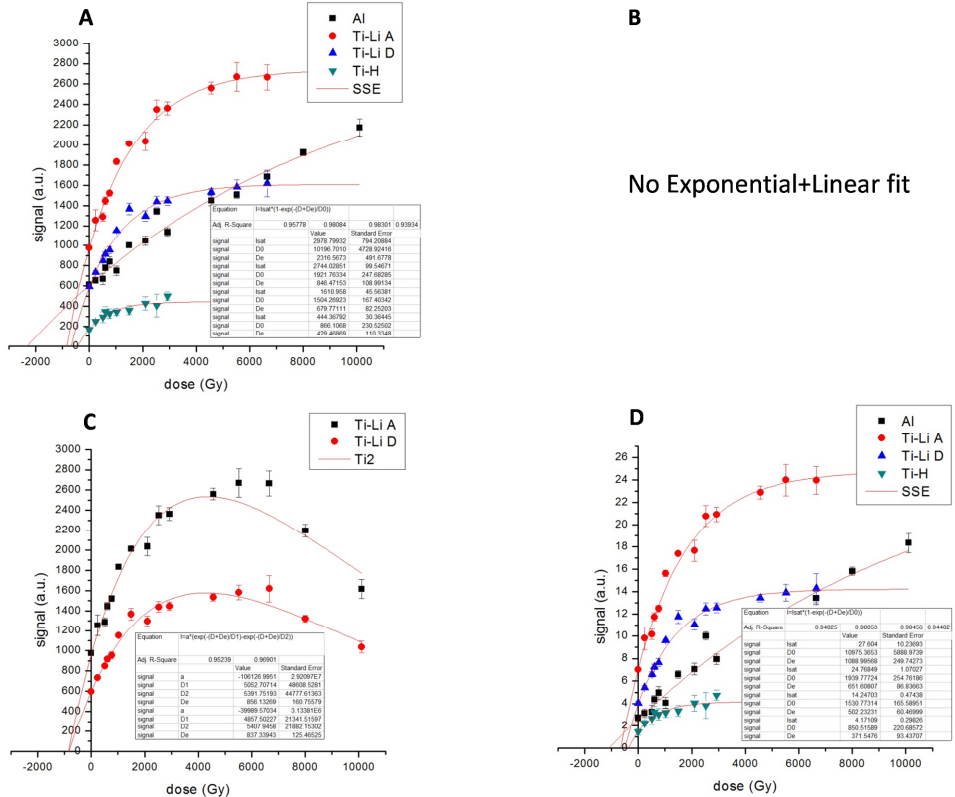


Figure A3-F13: Dose response curve (DRC) of sample gp127c of the Okefenokee ACD measured at Osaka University. Part A shows the AI, Ti-Li option A and option D signals, as well as the Ti-H signal fitted with a Single Saturating Exponential (SSE) fit. Shown in B is the Exponential plus Linear (Exp+Lin) fit of the AI signal, thought this equation did not fit the data for this sample so it is omitted. C is the DRC of the Ti-Li (option A and D) including points at additive doses over +6500GY and fitted with the Ti2 curve of Duval and Guilarte (2014). D shows the SSE fit of all the ESR signals, fitted with a SSE, that have had the calculated relict signal intensity removed (see part 4.3.3.1). Included in each graph is the Imax, Do, DE, and R squared fit of the curve.

Okefenokee: GP127e

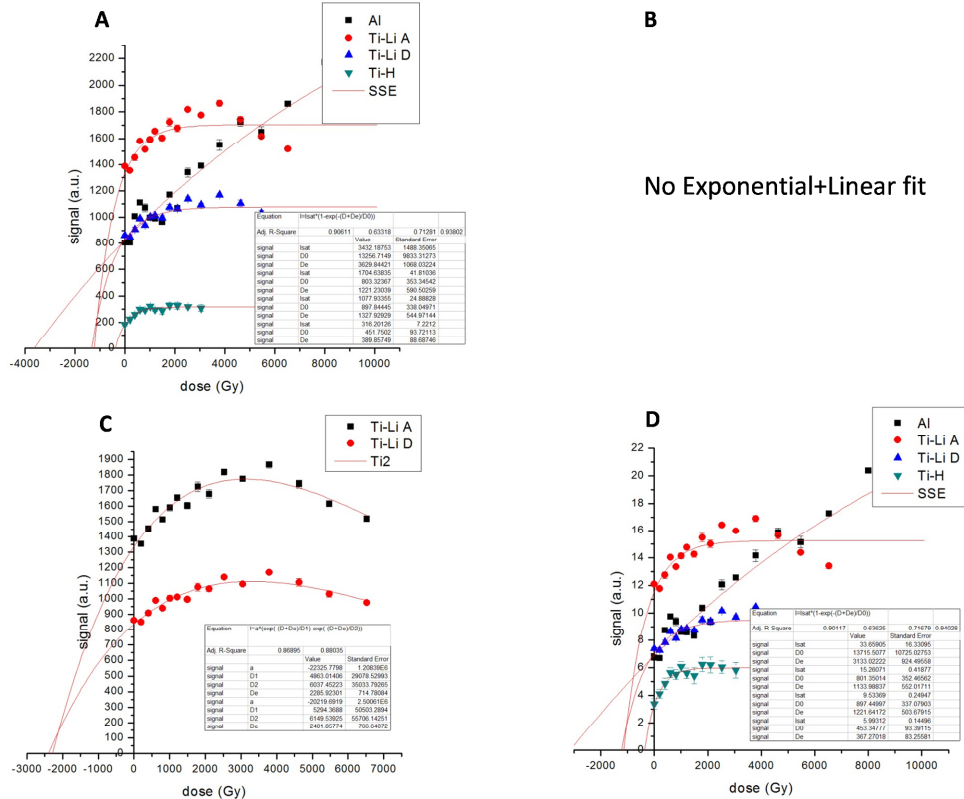


Figure A3-F14: Dose response curve (DRC) of sample gp127e of the Okefenokee ACD measured at Osaka University. Due to the low r^2 values observed in all of this signals this sample has been omitted from final analysis of the Georgia deposits and is included to complete the data set. Part A shows the AI, Ti-Li option A and option D signals, as well as the Ti-H signal fitted with a Single Saturating Exponential (SSE) fit. Shown in B is the Exponential plus Linear (Exp+Lin) fit of the AI signal, thought this equation did not fit the data for this sample so it is omitted. C is the DRC of the Ti-Li (option A and D) including points at additive doses over +6500GY and fitted with the Ti2 curve of Duval and Guilarte (2014). D shows the SSE fit of all the ESR signals, fitted with a SSE, that have had the calculated relict signal intensity removed (see part 4.3.3.1). Included in each graph is the I_{max} , D_0 , D_E , and R squared fit of the curve.

File Calculation Parameters Transfer in ... ?

Quartz Feldspar S-r system a-value

Sample: gp124e
 lin cosmic dose

Grain: 90 - 150 μm
 Etching: Yes Error: 0 %

AGE (ans) Total error 147.4c +/-
 Stat. error 1 %

Paleodose (Gy) 706.46 +/-
Annual dose ($\mu\text{Cyl/a}$) +/-

Doses(%) Internal () External ()

Alpha +/-
 Beta +/-
 Gamma +/-
 Cosmic +/-

Total +/- stat. +/-

Grains: U (ppm) 0.0665 +/- 0.0219 +/-
 Th (ppm) 0.1135 +/- 0.0424 +/-
 K (%) 0 +/- 0 +/-

Environment: U (ppm) 0.41 +/- 0.1 +/-
 Th (ppm) 1.51 +/- 0.1 +/-
 K (%) 0.03164 +/- 0.00112 +/-

Global Systematic Error: 5 %

Water Saturation level (W) : 0.11 Fraction (F) : 0.8 +/- 0.2

Internal:

Alpha
 None
 U, Th contents
 Value : 0.04 +/- 10 % 0 %

Beta
 None
 U, Th, K contents
 by Beta counting or dosimetry
 Beta - absorbed fractions : U 0.106 Th 0.158 K 0.0424
 Dose : 0 +/- 0 0 %

External:

Alpha
 None
 U, Th contents
 by Alpha counting
 Alpha - attenuation factors : U 0 Th 0

Beta
 None
 U, Th, K contents
 by Beta counting or dosimetry
 by Alpha counting
 Nb. alpha /ksec : 0 +/- 0 0 %
 Dose : 0 +/- 0 0 %

Gamma
 None
 U, Th, K contents
 by Beta counting or dosimetry
 by Alpha counting
 Dose : 0 +/- 0 0 %

Cosmic
 U, Th, K contents
 In-situ dosimetry
 Dose : 149.84 +/- 15
 Estimated water content (W.F) during measurement 0

Figure A3-F15: Example of an Anatol dose rate calculation. Note the include Global Systematic Error value of 5% calculated into the dose

22c		% Age err	16%	28%	10%	9%	12%	10%	17%
	Age (ka)	1468.09	1468.09	1111.94	378.77	427.81	361.65	417.07	163.97
	Age err (ka)	237.34	237.34	307.69	39.39	38.11	42.87	41.66	28.62
R squared			AI (SSE)	AI (Exp+Lin)	Ti-Li A (SSE)	Ti-Li A (Ti2)	Ti-Li D (SSE)	Ti-Li D (Ti2)	Ti-H (SSE)
0.9633	1468.09	237.34	1.00						
0.9641	1111.94	307.69	0.36	1.00					
0.9918	378.77	39.39	0.00	0.02	1.00				
0.9953	427.81	38.11	0.00	0.03	0.37	1.00			
0.9882	361.65	42.87	0.00	0.02	0.77	0.25	1.00		
0.9930	417.07	41.66	0.00	0.03	0.50	0.85	0.35	1.00	
0.9799	163.97	28.62	0.00	0.00	0.00	0.00	0.00	0.00	1.00

Table A3-T2: Age correlation table for Princess Anne sample gp1422c. P values are given and highlighted in color blocks for some values. Refer to text for meaning of P values. Green highlighted cells indicate correlation at the 1σ level (P values greater to or equal to 0.32) and yellow highlighted cells indicate correlation at the 2σ level (P values between 0.05 and 0.32). The R squared values are the goodness of fit for each of the signals dose response curve to the ESR data. Note a lack of correlation at the 0.32 confidence level between the Al and Ti signals. There is a strong agreement between the Ti-Li option A and D in both the SEE and Ti2 fits as to be expected (Duval and Guiliarte, 2014).

22d		% Age err	38%	4%	20%	na	16%	25%
R squared	Age (ka)	Age err (ka)	1367.12	1408.54	1158.75	na	515.11	113.97
			514.71	54.00	227.02		82.92	28.54
			AI (SSE)	AI (Exp+Lin)	Ti-Li A (SSE)	Ti-Li A (Ti2)	Ti-Li D (SSE)	Ti-Li D (Ti2)
0.8212	1367.12	514.71	AI (SSE)					
0.9571	1408.54	54.00	AI (Exp+Lin)	1.00				
0.9508	1158.75	227.02	Ti-Li A (SSE)	0.28	1.00			
			Ti-Li A (Ti2)	na	na	na		
0.9756	515.11	82.92	Ti-Li D (SSE)	0.00	0.01	na	1.00	
			Ti-Li D (Ti2)	na	na	na	na	na
0.9626	113.97	28.54	Ti-H (SSE)	0.00	0.00	na	0.00	1.00

Table A3-T3: Age correlation table for Princess Anne sample gp1422d. Note a lack of correlation at the 0.32 confidence level between the AI and Ti signals. There is also a lack of agreement between the Ti-Li option A and option D age determinations. This is counter to the results of Duval and Guiliarte (2014). For this reason the agreement between the AI and Ti-Li option A signal is discounted. The words “na” appear where no correlation is possible due to a lack of ESR signal for a specific fit.

22g		% Age err	26%	55%	21%	na	19%	na	32%
	Age (ka)	1179.09	1179.09	650.62	992.21		649.67		292.35
	Age err (ka)	309.87	309.87	360.04	209.90		122.51		93.53
R squared	Age err (ka)		AI (SSE)	AI (Exp+Lin)	Ti-Li A (SSE)	Ti-Li A (Ti2)	Ti-Li D (SSE)	Ti-Li D (Ti2)	Ti-H (SSE)
0.9206	1179.09	309.87	1.00						
0.9246	650.62	360.04	0.27	1.00					
0.9397	992.21	209.90	0.62	0.41	1.00				
			Ti-Li A (Ti2)	Ti-Li A	Ti-Li A	na	na	na	
0.9576	649.67	122.51	0.11	1.00	0.16	na	1.00		
			Ti-Li D (Ti2)	Ti-Li D	Ti-Li D	na	na	na	
0.9220	292.35	93.53	0.01	0.34	0.00	na	0.02	na	1.00

Table A3-T4: Age correlation table for Princess Anne sample gp1422g. Note a strong correlation between the AI (Exp+Lin) and the Ti-Li option D (SSE) signals. This correlation has been discounted on account of the high error of the AI (Exp+Lin) age estimate. There is also a lack of agreement between the Ti-Li option A and option D age determinations. This is counter to the results of Duval and Guiliarte (2014). For this reason the agreement between the AI and Ti-Li option A signal is discounted. The words “na” appear where no correlation is possible due to a lack of ESR signal for a specific fit.

21c		% Age err	26%	45%	9%	9%	10%	10%	19%
	Age (ka)	2686.98	897.48	897.48	508.62	561.78	477.82	524.45	95.95
	Age err (ka)	705.38	402.13	402.13	43.99	49.43	46.56	52.33	18.05
R squared	Age err (ka)		AI (SSE)	AI (Exp+Lin)	Ti-Li A (SSE)	Ti-Li A (Ti2)	Ti-Li D (SSE)	Ti-Li D (Ti2)	Ti-H (SSE)
0.9080	2686.98	705.38	1.00						
0.9738	897.48	402.13	0.03	1.00					
0.9946	508.62	43.99	0.00	0.34	1.00				
0.9948	561.78	49.43	0.00	0.41	0.42	1.00			
0.9922	477.82	46.56	0.00	0.30	0.63	0.22	1.00		
0.9925	524.45	52.33	0.00	0.36	0.82	0.60	0.51	1.00	
0.9811	95.95	18.05	0.00	0.05	0.00	0.00	0.00	0.00	1.00

Table A3-T5: Age correlation table for Pamlico sample gp1421c. Note a correlation between the Al (Exp+Lin) signal and the Ti signals. This correlation has been discounted due to the high error estimate of the Al (Exp+Lin) age. There is a strong agreement between the Ti-Li option A and D in both the SSE and Ti2 fits as to be expected (Duval and Guiliarte, 2014). The words “na” appear where no correlation is possible due to a lack of ESR signal for a specific fit.

21d		% Age err	28%	79%	58%	na	16%	na	48%
R squared	Age (ka)	Age err (ka)	AI (SSE)	AI (Exp+Lin)	Ti-Li A (SSE)	Ti-Li A (Ti2)	Ti-Li D (SSE)	Ti-Li D (Ti2)	Ti-H (SSE)
0.9215	2001.37	564.78	AI (SSE) 1.00	AI (Exp+Lin) 891.44	Ti-Li A (SSE) 1925.89	Ti-Li A (Ti2) na	Ti-Li D (SSE) 119.54	Ti-Li D (Ti2) na	Ti-H (SSE) 100.33
0.9185	1133.27	891.44	AI (Exp+Lin) 0.41	AI (Exp+Lin) 1.00					
0.7600	3321.57	1925.89	Ti-Li A (SSE) 0.51	Ti-Li A (SSE) 0.30	Ti-Li A (SSE) 1.00				
			Ti-Li A (Ti2) na	Ti-Li A (Ti2) na					
0.9738	734.14	119.54	Ti-Li D (SSE) 0.03	Ti-Li D (SSE) 0.66	Ti-Li D (SSE) 0.18	Ti-Li D (SSE) na	Ti-Li D (SSE) 1.00		
			Ti-Li D (Ti2) na	Ti-Li D (Ti2) na					
0.8523	207.24	100.33	Ti-H (SSE) 0.00	Ti-H (SSE) 0.30	Ti-H (SSE) 0.11	Ti-H (SSE) na	Ti-H (SSE) 0.00	Ti-H (SSE) na	Ti-H (SSE) 1.00

Table A3-T6: Age correlation table for Pamlico gp1421d. Note a strong correlation between the AI (Exp+Lin) and the Ti-Li option D (SSE). This correlation has been discounted on account of the high error of the AI (Exp+Lin) age estimate. There is also a lack of agreement between the Ti-Li option A and option D age determinations. This is counter to the results of Duval and Guiliarte (2014). For this reason the correlation between the AI and Ti-Li option A signals is discounted. The words “na” appear where no correlation is possible due to a lack of ESR signal for a specific fit.

9b		% Age err	14%	17%	11%	na	14%	na	28%
	Age (ka)	1552.06	1552.06	808.79	1616.17	na	1027.09	na	224.93
	Age err (ka)	213.57	213.57	135.74	180.81		143.02		63.66
R squared	Age err (ka)		AI (SSE)	AI (Exp+Lin)	Ti-Li A (SSE)	Ti-Li A (Ti2)	Ti-Li D (SSE)	Ti-Li D (Ti2)	Ti-H (SSE)
0.9825	1552.06	213.57	AI (SSE)	AI (Exp+Lin)	Ti-Li A (SSE)	Ti-Li A (Ti2)	Ti-Li D (SSE)	Ti-Li D (Ti2)	Ti-H (SSE)
0.9935	808.79	135.74	AI	1.00					
0.9880	1616.17	180.81	Ti-Li A (SSE)	0.00	1.00				
			Ti-Li A (Ti2)	na	na	na			
0.9836	1027.09	143.02	Ti-Li D (SSE)	0.27	0.01	na	1.00		
			Ti-Li D (Ti2)	na	na	na	na	na	
0.9536	224.93	63.66	Ti-H (SSE)	0.00	0.00	na	0.00	na	1.00

Table A3-T7: Age correlation table for Talbot gp129b. Note a lack of correlation between the AI and the Ti-Li option D (SSE). There is also a lack of agreement between the Ti-Li option A and option D age determinations. This is counter to the results of Duval and Guiliarte (2014). For this reason the AI Ti-Li option A correlation is not accepted. The words “na” appear where no correlation is possible due to a lack of ESR signal for a specific fit.

R squared		9c		% Age err		13%		24%		15%		12%		13%		14%		41%	
		Age (ka)	Age err (ka)	Age (ka)	Age err (ka)	AI (SSE)	AI (Exp+Lin)	Ti-Li A (SSE)	Ti-Li A (Ti2)	Ti-Li A (SSE)	Ti-Li A (Ti2)	Ti-Li D (SSE)	Ti-Li D (Ti2)	Ti-Li D (SSE)	Ti-Li D (Ti2)	Ti-H (SSE)			
0.9806		3224.38	415.78	3224.38		1.00		1606.42	2116.17	238.98		258.09		1719.22	2112.65			125.89	
0.9801		2749.80	660.52		AI (Exp+Lin)		1.00												
0.9718		1606.42	238.98		Ti-Li A (SSE)		0.10			1.00									
0.9781		2116.17	258.09		Ti-Li A (Ti2)		0.37			0.15			1.00						
0.9774		1719.22	230.38		Ti-Li D (SSE)		0.14		0.73				0.25	1.00					
0.9695		2112.65	289.17		Ti-Li D (Ti2)		0.38		0.18				0.99	0.29	1.00				
0.9307		125.89	51.50		Ti-H (SSE)		0.00		0.00	0.00			0.00	0.00	0.00				1.00

Table A3-T8: Age correlation table for Talbot gp129c. Note a correlation between the AI (Exp+Lin) signal and the Ti2 fit Ti signals. This will be discussed further in section 4. There is agreement between the Ti-Li option A and D in both the SEE and Ti2 fits as to be expected (Duval and Guiliarte, 2014).

4b		% Age err	21%	37%	14%	na	9%	87%
R squared	Age (ka)	Age (ka)	1600.81	547.19	1506.40	na	948.71	283.61
	Age err (ka)	Age err (ka)	339.77	200.52	209.51		82.23	246.93
		AI (SSE)	AI (SSE)	AI (Exp+Lin)	Ti-Li A (SSE)	Ti-Li A (Ti2)	Ti-Li D (SSE)	Ti-H (SSE)
0.9465	1600.81	339.77	1.00					
0.9640	547.19	200.52	0.01	1.00				
0.9761	1506.40	209.51	0.81	0.00	1.00			
		Ti-Li A (Ti2)	na	na	na	na		
0.9939	948.71	82.23	0.06	0.06	0.01	na	1.00	
		Ti-Li D (Ti2)	na	na	na	na	na	na
0.5490	283.61	246.93	0.00	0.41	0.00	na	0.01	1.00

Table A3-T9: Age correlation table for Penholoway gp124b. Note a lack of correlation between the AI and the Ti-Li option D signals. An agreement is seen between the AI and Ti-Li option A signal. There is also a lack of agreement between the Ti-Li option A and option D age determinations. This is counter to the results of Duval and Guiliarte (2014). For this reason the AI Ti-Li option A correlation is not accepted. Correlation exist between the AI (eXp+Lin) and the Ti-H signal but due to the high error on the age estimate of the Ti-H this is discounted. The words “na” appear where no correlation is possible due to a lack of ESR signal for a specific fit.

3c		Age err		AI (SSE)	AI (Exp+Lin)	71%	10%	9%	10%	10%	25%
		Age (ka)	Age err (ka)								
0.8665	2942.02	1118.36	1.00								
0.9757	340.60	242.98	0.02	1.00							
0.9901	725.29	70.68	0.05	0.13	1.00						
0.9918	831.14	78.23	0.06	0.05	0.32	1.00					
0.9908	745.12	70.91	0.05	0.11	0.84	0.42	1.00				
0.9894	828.26	85.00	0.06	0.06	0.35	0.98	0.45	1.00			
0.9367	245.79	60.79	0.02	0.71	0.00	0.00	0.00	0.00	0.00	1.00	1.00

Table A3-T10: Age correlation table for Wicomico gp123c. Note a lack of correlation between the AI signals and the Ti signals. There is agreement between the Ti-Li option A and D in both the SEE and Ti2 fits as to be expected (Duval and Guiliarte, 2014). The agreement in the AI (Exp+Lin) and Ti-H signals is discounted due to the large error in the Ti-H age estimate.

3d		Age err		25%	39%	19%	32%	20%	35%	26%
		Age (ka)	Age err (ka)	2233.20	1573.44	615.33	637.29	661.28	667.70	375.54
				564.42	612.31	114.86	205.26	134.84	236.33	99.04
R squared				AI (SSE)	AI (Exp+Lin)	Ti-Li A (SSE)	Ti-Li A (Ti2)	Ti-Li D (SSE)	Ti-Li D (Ti2)	Ti-H (SSE)
0.9172	2233.20	564.42		1.00						
0.9467	1573.44	612.31		0.43	1.00					
0.9576	615.33	114.86		0.00	0.12	1.00				
0.8523	637.29	205.26		0.01	0.15	0.93	1.00			
0.9480	661.28	134.84		0.01	0.15	0.80	0.92	1.00		
0.8227	667.70	236.33		0.01	0.17	0.84	0.92	0.98	1.00	
0.9358	375.54	99.04		0.00	0.05	0.11	0.25	0.09	0.25	1.00

Table A3-T11: Age correlation table for Wicomico gp123d. Note a lack of correlation between the AI signals and the Ti signals. There is agreement between the Ti-Li option A and D in both the SEE and Ti2 fits as to be expected (Duval and Guiliarte, 2014).

3f		% Age err		8%	19%	14%	13%	12%	13%	27%
		Age (ka)	Age err (ka)	5195.48	3391.15	1947.28	2204.26	2125.42	2327.59	990.28
	Age err (ka)		390.29	AI (SSE)	AI (Exp+Lin)	Ti-Li A (SSE)	Ti-Li A (Ti2)	Ti-Li D (SSE)	Ti-Li D (Ti2)	Ti-H (SSE)
R squared	0.9458	5195.48	390.29	1.00						
	0.9850	3391.15	652.42	AI (SSE)	AI (Exp+Lin)					
	0.9777	1947.28	268.98	0.02	1.00					
	0.9786	2204.26	296.09	0.00	0.04	1.00				
	0.9832	2125.42	262.12	0.00	0.10	0.52	1.00			
	0.9809	2327.59	302.27	0.00	0.07	0.64	0.84	1.00		
	0.9284	990.28	264.85	0.00	0.14	0.35	0.77	0.61	1.00	
				0.00	0.00	0.01	0.00	0.00	0.00	1.00

Table A3-T12: Age correlation table for Wicomico gp123f. Note a lack of correlation between the AI signals and the Ti signals. There is agreement between the Ti-Li option A and D in both the SSE and Ti2 fits as to be expected (Duval and Guiliarte, 2014).

7b		% Age err	57%	na	12%	13%	14%	13%	40%
R squared	Age (ka)	Age err (ka)	AI (SSE)	AI (Exp+Lin)	Ti-Li A (SSE)	Ti-Li A (Ti2)	Ti-Li D (SSE)	Ti-Li D (Ti2)	Ti-H (SSE)
0.7385	4400.88	2498.92	1.00						
0.9904	578.69	69.06	0.13	na	1.00				
0.9845	756.96	96.58	0.15	na	0.13	1.00			
0.9837	609.31	83.87	0.13	na	0.78	0.25	1.00		
0.9857	782.74	97.90	0.15	na	0.09	0.85	0.18	1.00	
0.8608	337.53	136.47	0.10	na	0.11	0.01	0.09	0.01	1.00

Table A3-T13: Age correlation table for Okefenokee gp127b. Note a lack of correlation between the AI signals and the Ti signals. There is agreement between the Ti-Li option A and D in both the SEE and Ti2 fits as to be expected (Duval and Guiliarte, 2014) though in some cases these are weaker than the 0.32 P value threshold. The words “na” appear where no correlation is possible due to a lack of ESR signal for a specific fit.

R squared		7c		% Age err	22%	na	15%	20%	15%	17%	26%
		Age (ka)	Age err (ka)								
		8846.52	1980.68	8846.52	1980.68	na	3232.50	3269.39	2595.91	3197.64	1640.06
				Age err (ka)	1980.68		495.57	661.79	382.32	544.52	433.05
0.9578		AI (SSE)	AI (SSE)	AI (SSE)	1.00	AI (Exp+Lin)	Ti-Li A (SSE)	Ti-Li A (Ti2)	Ti-Li D (SSE)	Ti-Li D (Ti2)	Ti-H (SSE)
		AI (Exp+Lin)	AI (Exp+Lin)	AI (Exp+Lin)	na	na					
0.9808	3232.50	Ti-Li A (SSE)	Ti-Li A (SSE)	Ti-Li A (SSE)	0.01	na	1.00				
0.9524	3269.39	Ti-Li A (Ti2)	Ti-Li A (Ti2)	Ti-Li A (Ti2)	0.01	na	0.96	1.00			
0.9630	2595.91	Ti-Li D (SSE)	Ti-Li D (SSE)	Ti-Li D (SSE)	0.00	na	0.31	0.38	1.00		
0.9690	3197.64	Ti-Li D (Ti2)	Ti-Li D (Ti2)	Ti-Li D (Ti2)	0.01	na	0.96	0.93	0.37	1.00	
0.9393	1640.06	Ti-H (SSE)	Ti-H (SSE)	Ti-H (SSE)	0.00	na	0.02	0.04	0.10	0.03	1.00

Table A3-T14: Age correlation table for Okefenokee gp127c. Note a lack of correlation between the AI signals and the Ti signals. There is agreement between the Ti-Li option A and D in both the SSE and Ti2 fits as to be expected (Duval and Guiliarte, 2014). The words “na” appear where no correlation is possible due to a lack of ESR signal for a specific fit.

<u>Ze</u>		% Age err	30%	na	48%	31%	41%	32%	23%
R squared	Age (ka)	Age err (ka)	AI (SSE)	AI (Exp+Lin)	Ti-Li A (SSE)	Ti-Li A (Ti2)	Ti-Li D (SSE)	Ti-Li D (Ti2)	Ti-H (SSE)
0.9061	4481.76	1326.79	1.00						
			na	na					
0.6332	1507.85	725.88	0.05	na	1.00				
0.8690	2822.42	886.27	0.30	na	0.25	1.00			
0.7128	1639.59	671.54	0.06	na	0.89	0.29	1.00		
0.8804	2965.57	950.00	0.35	na	0.22	0.91	0.25	1.00	
0.9380	481.36	111.40	0.00	na	0.16	0.01	0.09	0.01	1.00

Table A3-T15: Age correlation table for Okefenokee gp127e. Note the correlation between the AI signals and the Ti-Li option D signals but due to the large errors this is discounted. There is agreement between the Ti-Li option A and D in both the SSE and Ti2 fits as to be expected (Duval and Guiliarte, 2014) though in some cases these are weaker than the 0.32 P value threshold. The words “na” appear where no correlation is possible due to a lack of ESR signal for a specific fit.

AI (Exp+Lin)																			
Elev (m)	Age (ka)	Age err (ka)	22c	22d	22g	21c	21d	21f	9b	9c	4b	4e	3c	3d	3f	7b	7c	7e	
0.3	1111.94	307.69	22c	1.00															
-1.6	1408.54	54	22d	0.34	1.00														
-4.9	650.62	360.04	22g	0.33	0.04	1.00													
3.3	897.48	402.13	21c	0.67	0.21	0.65	1.00												
1.6	1133.27	891.44	21d	0.98	0.76	0.62	0.81	1.00											
-0.8	316.23	75.71	21f	0.01	0.00	0.36	0.16	0.36	1.00										
11	808.79	135.74	9b	0.37	0.00	0.68	0.83	0.72	0.00	1.00									
9.5	2749.8	660.52	9c	0.02	0.04	0.01	0.02	0.15	0.00	0.00	1.00								
17	547.19	200.52	4b	0.12	0.00	0.80	0.44	0.52	0.28	0.00	1.00								
14	3665.2	997.11	4e	0.01	0.02	0.00	0.01	0.06	0.00	0.44	0.00	1.00							
21	340.6	242.98	3c	0.05	0.00	0.48	0.24	0.39	0.92	0.00	0.51	0.00	1.00						
20.3	1573.44	612.31	3d	0.50	0.79	0.19	0.36	0.68	0.04	0.22	0.11	0.07	0.06	1.00					
17.3	3391.15	652.42	3f	0.00	0.00	0.00	0.00	0.04	0.00	0.49	0.00	0.82	0.00	0.04	1.00				
40.1			7b	na	na	na	na	na	na	na	na	na	na	na	na	na	na	na	
38.8			7c	na	na	na	na	na	na	na	na	na	na	na	na	na	na	na	
36.3			7e	na	na	na	na	na	na	na	na	na	na	na	na	na	na	na	

A3-T17: Age agreement between the AI (Exp+Lin) signals of the Georgia ACD samples. Those shown in green are strong correlations while those in yellow are weak correlations.

Ti-Li A (SSE)																			
Elev (m)	Age (ka)	Age err (ka)	22c	22d	22g	21c	21d	21f	9b	9c	4b	4e	3c	3d	3f	7b	7c	7e	
0.3	378.77	39.39	22c																
-1.6	1158.75	227.02	22d	1.00															
-4.9	992.21	209.9	22g	0.00	1.00														
3.3	508.62	43.99	21c	0.03	0.00	1.00													
1.6	3321.57	1925.89	21d	0.13	0.26	0.23	0.14	1.00											
-0.8	1507.82	161.78	21f	0.00	0.21	0.05	0.00	0.35	1.00										
11	1616.17	180.81	9b	0.00	0.12	0.02	0.00	0.38	0.66	1.00									
9.5	1606.42	238.98	9c	0.00	0.17	0.05	0.00	0.38	0.73	0.97	1.00								
17	1506.4	209.51	4b	0.00	0.26	0.08	0.00	0.35	1.00	0.69	0.75	1.00							
14	1115.71	176.86	4e	0.00	0.88	0.65	0.00	0.25	0.10	0.05	0.10	0.15	1.00						
21	725.29	70.68	3c	0.00	0.07	0.23	0.01	0.18	0.00	0.00	0.00	0.04	1.00						
20.3	615.33	114.86	3d	0.05	0.03	0.12	0.39	0.16	0.00	0.00	0.00	0.02	0.41	1.00					
17.3	1947.28	268.98	3f	0.00	0.03	0.01	0.00	0.48	0.16	0.31	0.34	0.01	0.00	0.00	1.00				
40.1	578.69	69.06	7b	0.01	0.01	0.06	0.39	0.15	0.00	0.00	0.00	0.00	0.14	0.78	0.00	1.00			
38.8	3232.5	495.57	7c	0.00	0.00	0.00	0.00	0.96	0.00	0.00	0.00	0.00	0.00	0.00	0.02	0.00	1.00		
36.3	1507.85	725.88	7e	0.12	0.65	0.49	0.17	0.38	1.00	0.88	0.90	0.60	0.28	0.22	0.57	0.20	0.05	1.00	

A3-T18: Age agreement between the Ti-Li option A (SSE) signals of the Georgia ACD samples. Those shown in green are strong correlations while those in yellow are weak correlations.

Ti-Li D (Ti2)																			
Elev (m)	Age (ka)	Age err (ka)	22c	22d	22g	21c	21d	21f	9b	9c	4b	4e	3c	3d	3f	7b	7c	7e	
0.3	417.07	41.66	22c	1.00															
-1.6			22d	na	na														
-4.9			22g	na	na														
3.3	524.45	52.33	21c	0.11	na	1.00													
1.6			21d	na	na	na	na												
-0.8			21f	na	na	na	na	na											
11			9b	na	na	na	na	na	na										
9.5	2112.65	289.17	9c	0.00	na	0.00	na	na	na	1.00									
17			4b	na	na	na	na	na	na	na	na								
14	1452.57	229.07	4e	0.00	na	0.00	na	na	na	0.07	na	1.00							
21	828.26	85	3c	0.00	na	0.00	na	na	na	0.00	na	0.01	1.00						
20.3	667.7	236.33	3d	0.30	na	0.55	na	na	na	0.00	na	0.02	0.52	1.00					
17.3	2327.59	302.27	3f	0.00	na	0.00	na	na	na	0.61	na	0.02	0.00	0.00	1.00				
40.1	782.74	97.9	7b	0.00	na	0.02	na	na	na	0.00	na	0.01	0.73	0.65	0.00	1.00			
38.8	3197.64	544.52	7c	0.00	na	0.00	na	na	na	0.08	na	0.00	0.00	0.00	0.16	0.00	1.00		
36.3	2965.57	950	7e	0.01	na	0.01	na	na	na	0.39	na	0.12	0.03	0.02	0.52	0.02	0.83	1.00	

A3-T20: Age agreement between the Ti-Li option D (Ti2) signals of the Georgia ACD samples. Those shown in green are strong correlations while those in yellow are weak correlations.

Appendix 4: OSL results statistics

Following are the results of the statistical analysis of the OSL and TT-OSL measurements. Please note that OSL data from gp1422g is omitted as only 1 aliquot yielded a De. TT-OSL was not conducted on gp1421f.

Raw OSL/TT-OSL data can be found on the supplemental data disc included in this work.

```

summaryED
  Min. 1st Qu.  Median    Mean 3rd Qu.   Max. Std.dev Over Disp
99.79 108.60 115.80 118.80 132.30 134.10 14.14 0.00

mIpED
  5% 10% 15% 20% 25% 30% 50% 70% 90%
pED 99.79 99.79 99.79 102.64 102.64 102.64 108.22 112.81 116.26
Std.pED NA NA NA 2.85 2.85 2.85 3.52 5.34 5.56

homogeneity
chisq.value  p.value homogeneity
0.8706299 0.9900448      Yes

skewness
Skewness Std.Skew significant
-0.22 0.93      No

kurtosis
Kurtosis Std.Kurt significant
-2.02 1.85      No

proposal
[1] "CAM"

[calc_CentralDose]

-----
sample ID:      22G tt-osl
n:              7
log ED:        TRUE

-----
central dose (delta): 114.6669
rse (delta):      0.1266
se (delta):      14.5211

-----
overdispersion (sigma): 0
se (sigma):      -
    
```

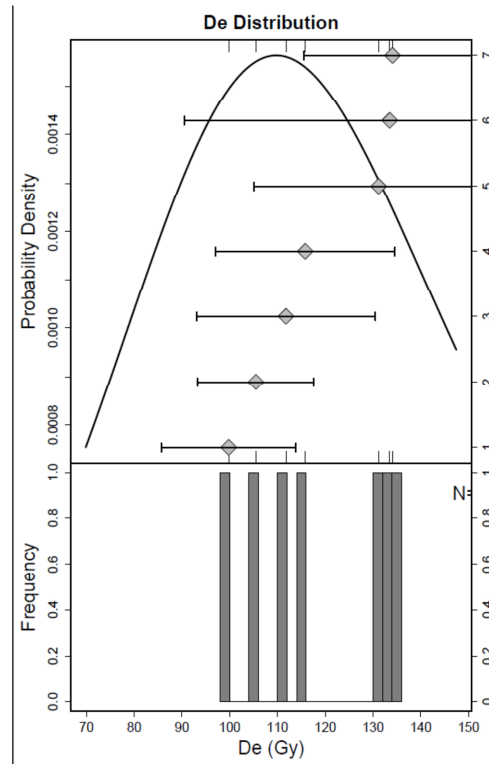


Figure A4-F1: TT-OSL results of sample gp1422g (Princess Anne ACD)

\$summaryED
 Min. 1st Qu. Median Mean 3rd Qu. Max. Std.dev OverDisp
 65.75 79.59 112.50 108.20 131.90 156.00 34.33 0.29

\$smpED
 5% 10% 15% 20% 25% 30% 50% 70% 90%
 pED 65.75 65.75 65.75 71.62 71.62 71.62 84.37 91.88 100.20
 Std.pED NA NA NA 5.87 5.87 5.87 9.98 10.78 12.11

\$homogeneity
 chisq.value p.value homogeneity
 77.58132 1.127813e-14 No

\$skewness
 Skewness Std.Skew significant
 -0.15 0.93 No

\$kurtosis
 Kurtosis Std.Kurt significant
 -1.65 1.85 No

\$proposal
 [1] "CAM"

[calc_CentralDose]

 sample ID: unknown sample
 n: 7
 log ED: TRUE

 central dose (delta): 102.481
 rse (delta): 0.1169
 se (delta): 11.9833

 overdispersion (sigma): 0.2638
 se (sigma): 0.0497

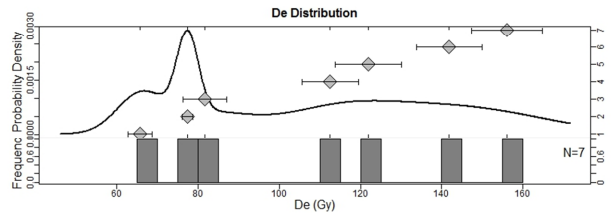


Figure A4-F2: OSL results of sample gp1422d (Princess Anne ACD)

```

summaryED
  Min. 1st Qu. Median Mean 3rd Qu. Max. Std.dev OverDisp
  71.43 92.01 95.54 99.76 111.30 120.30 13.78 0.00

$mpED
  5% 10% 15% 20% 25% 30% 50% 70% 90%
pED 71.43 78.95 78.95 83.08 85.31 85.31 88.96 93.27 96.58
Std.pED NA 7.52 7.52 5.99 4.79 4.79 3.10 3.71 3.74

$homogeneity
chisq.value p.value homogeneity
4.664348 0.9682614 Yes

$skewness
Skewness Std.Skew significant
-0.73 0.68 No

$skurtosis
Kurtosis Std.Kurt significant
-0.25 1.36 No

$proposal
[1] "CAM"

[calc_CentralDose]

-----
sample ID: unknown sample
n: 13
log ED: TRUE

-----
central dose (delta): 93.8318
rse (delta): 0.0697
se (delta): 6.5369

-----
overdispersion (sigma): 0
se (sigma): -
    
```

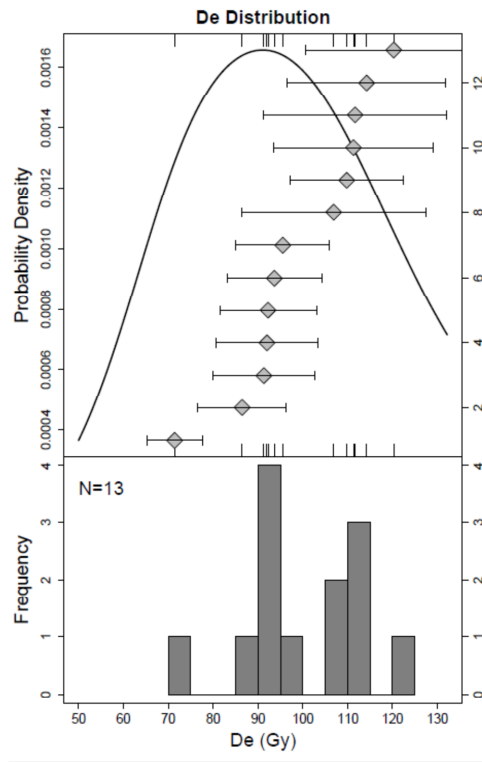


Figure A4-F3: TT-OSL results of sample gp1422d (Princess Anne ACD)

\$summaryED
 Min. 1st Qu. Median Mean 3rd Qu. Max. Std.dev OverDisp
 59.78 70.50 87.56 96.96 121.90 146.50 34.85 0.30

\$mleED
 5% 10% 15% 20% 25% 30% 50% 70% 90%
 pED 59.78 59.78 59.78 63.84 63.84 63.84 72.08 78.31 88.69
 Std.pED NA NA NA 4.06 4.06 4.06 5.84 7.70 12.14

\$homogeneity
 chisq.value p.value homogeneity
 72.51165 1.247286e-13 No

\$skewness
 Skewness Std.Skew significant
 0.2 0.93 No

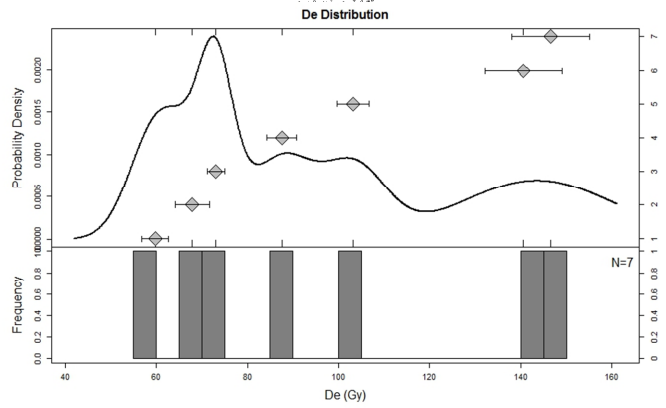
\$kurtosis
 Kurtosis Std.Kurt significant
 -1.4 1.85 No

\$proposal
 [1] "MAM3"

----- meta data -----
 Sample ID: unknown sample
 n: 7
 sigmab: 0.12
 log ED: FALSE
 Lmax: -46.913
 BIC: 99.665

----- final parameter estimates -----
 gamma: 76.0473
 76.047
 sigma: 5
 p0: 0.2281

----- confidence intervals for gamma -----
 95% ci: 70.16 - 81.49 (- 5.88 + 5.45)
 68% ci: 73.08 - 78.86 (- 2.97 + 2.81)



minimum dose:

Figure A4-F4: OSL results of sample gp1421f (Pamlico ACD)

\$summaryED
 Min. 1st Qu. Median Mean 3rd Qu. Max. Std.dev OverDisp
 32.55 44.83 76.64 81.71 95.47 165.30 45.85 0.52

\$smlpED
 5% 10% 15% 20% 25% 30% 50% 70% 90%
 pED 32.55 36.38 36.38 37.79 39.55 39.55 47.72 56.29 67.58
 Std.pED NA 3.83 3.83 2.62 2.56 2.56 5.35 6.99 9.94

\$homogeneity
 chisq.value p.value homogeneity
 567.9231 7.445118e-114 No

\$skewness
 Skewness Std.Skew significant
 0.34 0.68 No

\$kurtosis
 Kurtosis Std.Kurt significant
 -0.69 1.36 No

\$proposal
 [1] "MAM3"

----- final parameter estimates -----
 gamma: 39.5082
 39.508
 sigma: 5
 p0: 0.0764

----- confidence intervals for gamma -----
 95% ci: 37.22 - 41.74 (- 2.29 + 2.23)
 68% ci: 38.36 - 40.65 (- 1.15 + 1.14)

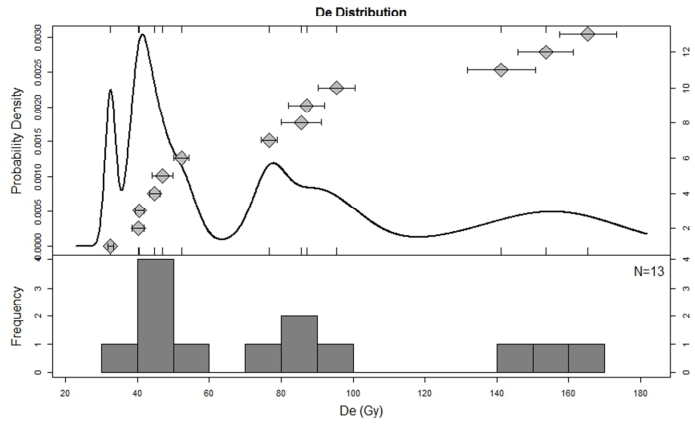


Figure A4-F5: OSL results of sample gp1421d (Pamlico ACD)


```

SummaryED
  Min. 1st Qu. Median Mean 3rd Qu. Max. Std.dev OverDisp
78.86 91.49 102.90 104.20 117.90 137.00 16.91 0.00

$mipED
  5% 10% 15% 20% 25% 30% 50% 70% 90%
pED 78.86 80.61 81.41 83.12 84.64 85.91 91.18 94.63 100.85
Std.pED NA 1.74 1.29 1.93 2.13 2.16 2.56 2.69 3.50

$homogeneity
chisq.value p.value homogeneity
8.652511 0.9672572 Yes

$skewness
Skewness Std.Skew significant
0.12 0.56 No

$kurtosis
Kurtosis Std.Kurt significant
-0.86 1.12 No

$proposal
[1] "CAM"

[calc_CentralDose]
-----
sample ID: unknown sample
n: 19
log ED: TRUE

central dose (delta): 99.6627
rse (delta): 0.0593
se (delta): 5.9082
-----
overdispersion (sigma): 0
se (sigma): -
    
```

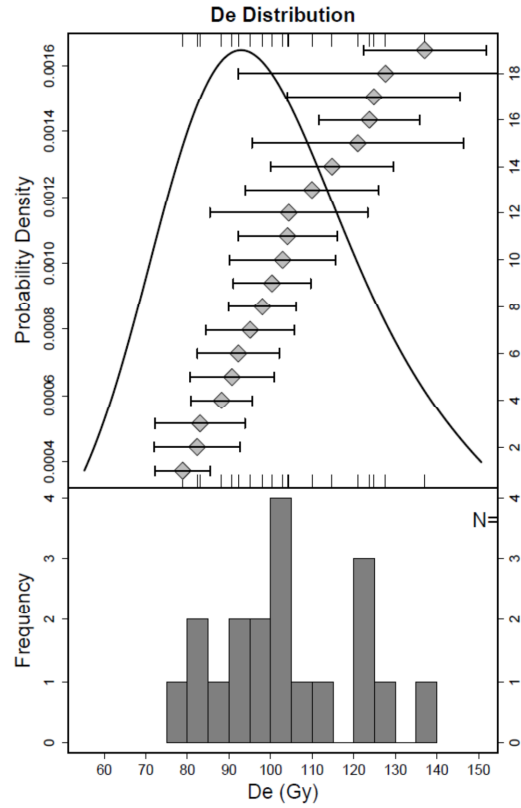


Figure A4-F6: TT-OSL results of sample gp1421d (Pamlico ACD)

Supplemental data

Please refer to the author of this work for access to all the raw data pertaining to this project. This includes raw ESR and OSL data as well as spreadsheets of processed data that were used to create the results and figures in this work. The author can be reached at the email: hendricks.robert.r@gmail.com.